173
Advances in Polymer Science

Advances in Polymer Science

Recently Published and Forthcoming Volumes

Inorganic Polymeric Nanocomposites and Membranes
Vol. 179, 2005

Polymeric and Inorganic Fibres
Vol. 178, 2005

Poly(arylene Ethynylenes)
From Synthesis to Application
Volume Editor: Weder C.
Vol. 177, 2005

Ring Opening Metathesis
Volume Editor: Buchmeister, M.
Vol. 176, 2005

Polymer Particles
Volume Editor: Okubo M.
Vol. 175, 2005

Neutron Spin Echo in Polymer Systems
Authors: Richter, D., Monkenbusch, M., Arbe, A., Colmenero, J.
Vol. 174, 2005

Advanced Computer Simulation Approaches for Soft Matter Sciences I
Volume Editors: Holm, C. Kremer, K.
Vol. 173, 2005

Microlithography · Molecular Imprinting
Vol. 172, 2005

Polymer Synthesis
Vol. 171, 2004

NMR · Coordination Polimerization · Photopolymerization
Vol. 170, 2004

Long-Term Properties of Polyolefins
Volume Editor: Albertsson A.-C.
Vol. 169, 2004

Polymers and Light
Volume Editor: Lippert T. K.
Vol 168, 2004

New Synthetic Methods
Vol. 167, 2004

Polyelectrolytes with Defined Molecular Architecture II
Volume Editor: Schmidt M.
Vol. 166, 2004

Polyelectrolytes with Defined Molecular Architecture I
Volume Editor: Schmidt M.
Vol. 165, 2004

Filler-Reinforced Elastomers · Scanning Force Microscopy
Vol. 164, 2003

Liquid Chromatography · FTIR Microspectroscopy · Microwave Assisted Synthesis
Vol. 163, 2003

Radiation Effects on Polymers for Biological Use
Volume Editor: Kausch H.
Vol. 162, 2003

Polymers for Photonics Applications II
Nonlinear Optical, Photorefractive and Two-Photon Absorption Polymers
Volume Editor: Lee, K.-S.
Vol. 161, 2003

Filled Elastomers · Drug Delivery Systems
Vol. 160, 2002

Statistical, Gradient, Block and Graft Copolymers by Controlled/ Living Radical Polymerizations
Authors: Davis, K.A., Matyjaszewski, Kr.
Vol. 159, 2002

Advanced Computer Simulation Approaches for Soft Matter Sciences I

Volume Editors: Christian Holm · Kurt Kremer

With contributions by
S. Auer ·K. Binder · J. G. Curro · D. Frenkel · G. S. Grest
D. R. Heine · P. H. Hünenberger · L. G. MacDowell · M. Müller
P. Virnau

Springer

This series presents critical reviews of the present and future trends in polymer and biopolymer science including chemistry, physical chemistry, physics and material science. It is adressed to all scientists at universities and in industry who wish to keep abreast of advances in the topics covered.

As a rule, contributions are specially commissioned. The editors and publishers will, however, always be pleased to receive suggestions and supplementary information. Papers are accepted for "Advances in Polymer Science" in English.

In references Advances in Polymer Science is abbeviated Adv Polym Sci and is cited as a journal.

The electronic content of APS may found at springerlink.com

Library of Congress Control Number: 2004109781

ISSN 0065-3195
ISBN 3-540-22058-5 **Springer Berlin Heidelberg New York**
DOI 10.1007/b98052

Springer is a part of Springer Science+Business Media
springeronline.com

Printed in Germany

Cover design: *Design & Production* GmbH, Heidelberg
Typesetting and Production: LE-TEX Jelonek, Schmidt & Vöckler GbR, Leipzig

Printed on acid-free paper 02/3141 YL – 5 4 3 2 1 0

Volume Editors

Dr. Christian Holm
Prof. Dr. Kurt Kremer

MPI für Polymerforschung
55128 Mainz, Germany
holm@mpip-maine.mpg.de
kurt.kremer@mpip-maine.mpg.de

Editorial Board

Advances in Polymer Science
Also Available Electronically

For all customers who have a standing order to Advances in Polymer Science, we offer the electronic version via SpringerLink free of charge. Please contact your librarian who can receive a password for free access to the full articles by registering at:

springerlink.com

If you do not have a subscription, you can still view the tables of contents of the volumes and the abstract of each article by going to the SpringerLink Homepage, clicking on "Browse by Online Libraries", then "Chemical Sciences", and finally choose Advances in Polymer Science.

You will find information about the

– Editorial Board
– Aims and Scope
– Instructions for Authors
– Sample Contribution

at springeronline.com using the search function.

Adv. Polym. Sci. (2005) 173:1–110
DOI:10.1007/b99426

Polymer + Solvent Systems: Phase Diagrams, Interface Free Energies, and Nucleation

Kurt Binder[1], Marcus Müller[1,3], Peter Virnau[1,4], and Luis González MacDowell[2]

[1] Institut für Physik, WA331, Johannes Gutenberg-Universität, Staudinger Weg 7, D-55099 Mainz, Germany
binder@chaplin.physik.uni-mainz.de
[2] Dpto. de Quimica Fisica, Facultad de Ciencias Quimicas, Universidad Complutense, Madrid 28040, Spain
[3] Physics Dept., University of Wisconsin-Wadison, Madison, WI53706-1390, USA
[4] Dept. Phys., Massachusetts Institute of Technology, 77 Mass. Ave., Cambridge, MA 02139-4307, USA

Abstract Some theoretical concepts on polymer + solvent systems and Monte Carlo simulations of corresponding coarse-grained models are briefly reviewed. While the phase diagram of polymers in bad solvents invoking the incompressibility approximation for the polymer solution has been a standard problem of polymer science for a long time, a more complete understanding of compressible polymer solutions, where liquid-liquid phase separation and liquid-vapor transitions compete, has emerged only recently. After giving a phenomenological introduction, we outline and compare three complementary approaches: self-consistent field theory, thermodynamic perturbation theory and grandcanonical Monte Carlo simulation. In order to give a specific example, we focus on the mixture of hexadecane with carbon dioxide. Attention is paid to correlate the description of the phase diagram with the properties of interfaces and the nucleation barrier that needs to be overcome to form a droplet (or bubble, respectively) of critical size, necessary for the decay of the corresponding super-saturated metastable state. Particular emphasis is given to new techniques used for the computer simulation of such phase diagrams where several order parameters compete, and to systematic difficulties that still hamper the prediction of accurate nucleation barriers from the observation of droplets (or bubbles, respectively) in finite volumes. The extent to which real materials can be modeled will also be examined.

Keywords Phase equilibria, Compressible mixtures, Nucleation, Interface properties, Flory-Huggins theory, Self-consistent field theory, Thermodynamic perturbation theory, Computer simulation, Coarse-grained model, Hexadecane, Carbon dioxide

List of Abbreviations and Symbols

MC	Monte Carlo
MD	molecular dynamics
SCF	self-consistent field
TPT1	thermodynamic perturbation theory of 1st order
SAFT	self associating fluid theory
MSA	mean spherical approximation
RHNC	reference hypernetted chain

P-RISM	polymer reference interaction site model
RMPY/HTA	reference molecular Percus Yevick / high temperature approximation
RIS	rotational isomeric state
CO_2	carbon dioxide
$C_{16}H_{34}$	hexadecane

1 Introduction

Understanding the properties of solutions of polymers in solvents of variable quality has been an outstanding problem in polymer science for decades [1, 2, 3, 4, 5]. Theses systems are of fundamental interest as model systems for the statistical mechanics of fluid binary mixtures [6] and also are of enormous practical interest for predicting processing properties of various plastic materials in the chemical industry [7]. A good example is the production of solid polystyrene foam from polystyrene + carbon dioxide mixtures [8, 9, 10, 11]. While in this system phase separation between the polymer and the small, molecular solvent is induced by a pressure jump, other systems show phase separation when the solvent quality is changed by variation of temperature (see e.g. [12]).

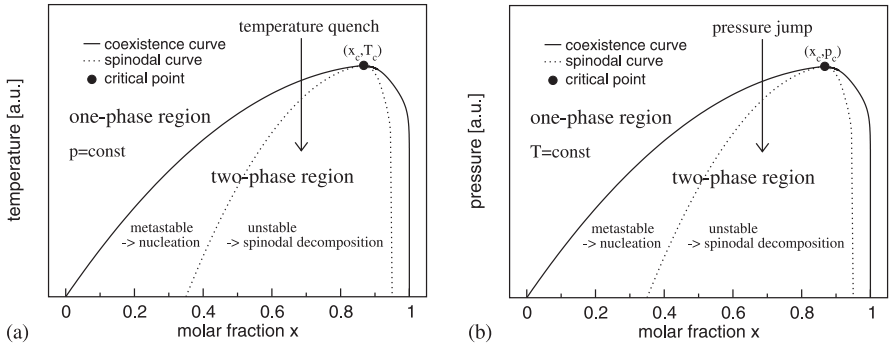

Fig. 1. (**a**) Schematic phase diagram of an incompressible polymer solution. Temperature T and molar fraction x of the solvent are variables, pressure p is constant. The position of the critical point (x_{crit}, T_{crit}) is indicated by a *filled circle*. The coexistence curve is drawn as a *full curve*, while the (mean-field) spinodal is shown as a *dotted curve*. It separates metastable states which can only decay via nucleation and growth from unstable states which decay via spontaneous growth of concentration fluctuations ("spinodal decomposition"). A temperature quench from the one-phase region into the two-phase region is also indicated. (**b**) Schematic isothermal slice of a phase diagram of a compressible polymer solution, using pressure p and molar fraction x of the solvent as variables. A pressure jump from the one-phase region into the two-phase region is indicated. From [16]

Actually, the latter case is conceptually most simple, since it can already be addressed using a special case of the Flory-Huggins theory [1, 2, 13, 14, 15] of

binary polymer mixtures (see Sect. 2). A schematic phase diagram is drawn in Fig. 1 (**a**) [16]. Note that the critical molar fraction of the solvent $x_{\rm crit} \to 1$ when the chain length N of the polymer tends to infinity. In this limit the critical temperature $T_{\rm crit}$ of the polymer solution converges to the Θ temperature. We shall summarize the main facts for this case in Sect. 2.

When one works at temperatures far below the liquid-vapor critical point of the solvent, treating the polymer solution as incompressible is a reasonable approximation. Often, however, many solvents are used in their super-critical region [7], and then it would be completely inappropriate to assume incompressibility: Rather then, pressure is a useful control variable to trigger the phase separation (Fig. 1 (**b**)). While in Fig. 1 (**a**) an equilibrium state in the two phase coexistence region consists of polymer with some dissolved solvent molecules (on the left branch of the coexistence curve) coexisting with essentially pure ($x = 1$) dense solvent of high density in the liquid phase, Fig. 1 (**b**) actually may represent an equilibrium of polymer (with some dissolved solvent molecules) with the solvent ($x = 1$) in the vapor phase, having a much lower density than the polymer-rich phase.

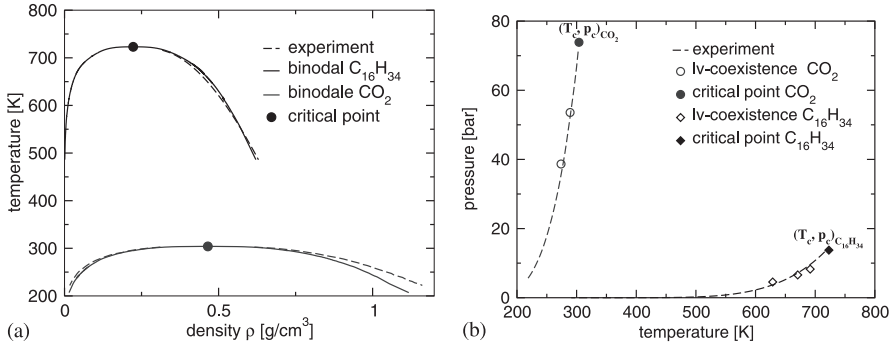

Fig. 2. (**a**) Phase diagrams of pure CO_2 (*lower two curves*) and pure hexadecane (C_{16} H_{34}, *upper two curves*) in the temperature-density plane. Experimental data were taken from [17, 18, 19, 20, 21], simulation data from [22] (see Sect. 5) (**b**) Same as (**a**) but in the pressure-temperature plane. Curves are experimental results [17, 18, 19, 21], simulation data were taken from Virnau et al. [22]

Of course, Fig. 1 only focuses on the simplest cases of the phase behavior. Even when we disregard the solid (crystalline or glassy) phases of the polymer and the solvent from the outset, it is necessary to discuss the global phase diagram of the binary fluid mixture consisting of polymer and solvent in more detail. As is well-known [6, 23, 24], in the space of control parameters – pressure p, temperature T, and molar fraction x of the solvent – several distinct types of phase diagrams may occur, due to different ways in which liquid-vapor transitions and liquid-liquid unmixing interfere with each other. To set the scene, let us consider the model system that will be considered extensively throughout this review, namely the mixture of hexadecane and carbon dioxide. The phase diagrams of these two pure fluids are plotted in

Fig. 2 [17, 18, 19, 20, 21, 22]. In principle, we expect a qualitatively similar behavior for any pair of polymer and solvent. In practice, of course, the liquid-vapor critical point can only be observed for oligomers (such as hexadecane) but not for polymers of high molecular weight, since then T_{crit} would be so high that the polymer chains chemically disintegrate before the critical region is reached. Now the question is how does the phase diagram of the mixed system look like?

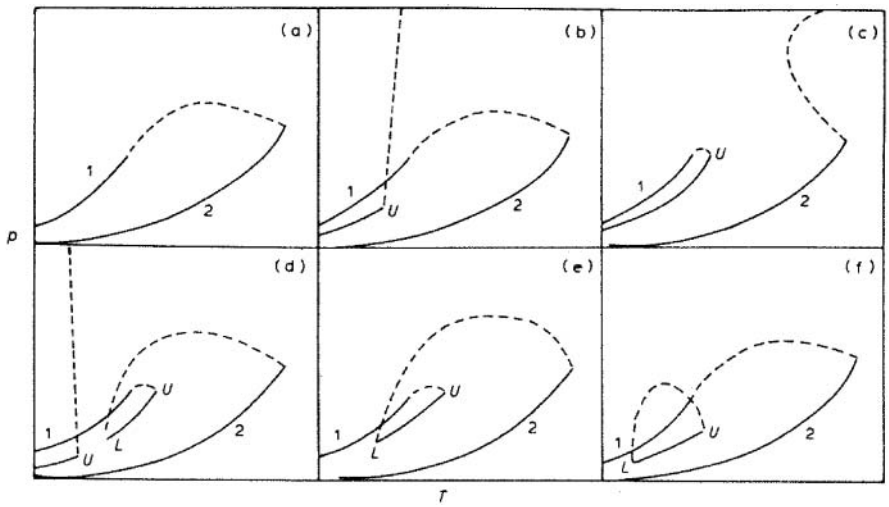

Fig. 3. Schematic phase diagrams of binary fluid mixtures, showing projections of critical lines $(p_{\mathrm{crit}}(x),\ T_{\mathrm{crit}}(x))$ into the pressure-temperature plane (broken lines), while projections of first-order transitions are shown as full lines. From top/left to bottom/down phase diagrams of type I (**a**) to type VI (**f**) in the classification of Van Konynenburg and Scott [24]. For further explanations see text. From [6]

In the simplest case, the critical points $(p_{P\mathrm{crit}}, T_{P\mathrm{crit}})$ and $(p_{S\mathrm{crit}}, T_{S\mathrm{crit}})$ of pure polymer and pure solvent are connected by the critical line $(p_{\mathrm{crit}}(x)\,,\ T_{\mathrm{crit}}(x))$, cf. Fig. 3 (**a**). The graph shows a projection of the phase boundaries of the two pure systems and this critical line into the p-T plane. This phase diagram is called "type I" in the classification of Van Konynenburg and Scott [24]. In this case, phase coexistence is always characterized by a coexistence of a vapor-like phase (with molar fraction x') and a liquid-like phase (with molar fraction x''). While such a phase diagram is often found in experiments for mixtures of chemically very similar molecules, the phase diagrams of polymer + solvent systems are typically more complicated. Oftentimes, they are of type III in this classification [24] (note that more types of phase diagrams do occur [6, 23, 24] than are discussed here). Then, not only liquid-vapor but also liquid-liquid phase separation occurs. The liquid-vapor critical line $(p_{\mathrm{crit}}(x),\ T_{\mathrm{crit}}(x))$ that starts at the critical point of the pure solvent does not extend all the way to the critical point of the pure polymer, but rather ends at a critical end-point, where it joins a triple line. On the triple line the polymer-rich liquid co-

exists with a solvent–rich liquid and with a vapor phase. The phase coexistence with a critical line that starts at the critical point of the pure polymer gradually changes its character from a liquid-vapor phase coexistence – close to the critical point of the pure polymer – to a coexistence between a polymer–rich and solvent–rich liquid at low temperatures and high pressure. Thus, the two parameters, the total density of the fluid and the relative polymer concentration, are coupled in a non-trivial way. Of course, already the correct prediction of such complex phase diagrams from models for the molecular interactions is an ambitious and difficult task. It is even more difficult to assess the interface properties (interfacial tensions between coexisting phases, interface profiles of the two order parameters, nucleation barriers which control the decay rate of metastable states that can be reached in quenching experiments such as schematically shown in Fig. 1).

In the present review we summarize various theoretical approaches to this problem, emphasizing the system hexadecane and carbon dioxide as a representative testing ground. In Sect. 3, a phenomenological treatment of the problem based on the self-consistent (SCF) field approach is given. Here we use a simple expansion of the basic free energy density, and do not attempt a quantitatively accurate description of a specific system, but rather try to model the generic features. In Sect. 4, a rather powerful version of thermodynamic perturbation theory (TPT) adopted to solutions and melts of flexible chain molecules is presented. In [134, 145] Sect. 5, Monte Carlo (MC) methods [145] are developed which allow an estimation of both the phase diagram and the desired properties of interfaces. It will be shown that indeed useful and non-trivial predictions on the behavior of real systems, such as the $C_{16}H_{34}$+CO_2 system, can be made. Sect. 6 then contains some conclusions and an outlook on future work.

2
The Flory-Huggins Model of Incompressible Polymer Solutions and Its Test

2.1
The Flory-Huggins Lattice Model and the Mean-field Approximation

Although the Flory-Huggins lattice model [1, 2, 13, 14] is more than 60 years old and extremely idealized, treating the configurations of the (flexible) polymers as random walks on a lattice, it is still widely used and in fact a useful starting point to expose the basic ideas of thermodynamics of polymer solutions. Each lattice site i is either taken by a monomer ($c_i = 1$) or by a solvent molecule ($c_i = 0$), and the polymer chains are described as self- and mutually avoiding random walks of $N - 1$ steps on a lattice, i.e., we have N (effective) monomers per chain. If two neighboring lattice sites are taken by monomers which are not nearest neighbors along the same chain, an energy ϵ_{PP} is won.

If no further approximations were made, the statistical mechanics of such a model still would be a formidable problem, impossible to solve analytically, only tractable

by Monte Carlo (MC) simulations [5]. To make progress and derive simple analytical expressions for the critical temperature $T_{\rm crit}(N)$ and critical volume fraction $\phi_{\rm crit}(N)$ taken by the monomers ($\phi \equiv \langle c_i \rangle_T$ where $\langle \cdots \rangle_T$ denotes an average in the canonical ensemble of statistical mechanics), Flory and Huggins [13, 14] introduced several additional approximations, that go beyond the simplifications inherent in the use of the lattice model, as it was just formulated: (i) Correlations in the occupancy of lattice sites are ignored. (ii) It is ignored, that on a lattice with coordination number z an inner monomer of a chain can at most have $z-2$ neighboring monomers from other chains, and that a monomer forming a chain end can have at most $z-1$ non-bonded neighbors, and one takes the possible number of non-bonded neighbors (from other chains) equal to z. Writing now $\epsilon = \epsilon_{PS} - (\epsilon_{PP} + \epsilon_{SS})/2$ where ϵ_{PS}, ϵ_{SS} are enthalpies for nearest neighbor pairs of polymer-solvent or solvent-solvent molecules, the enthalpy per lattice site simply is $z\epsilon\phi(1-\phi)$. The last approximation (iii) amounts to ignore that chains must not intersect themselves (or other chains), by treating them as non-reversal random walks, rather than true self-avoiding walks. Then a simple expression for the entropy of mixing of the model results, $S(\phi)/k_B = -(\phi \ln \phi)/N - (1-\phi)\ln(1-\phi)$, again normalized per lattice site. Thus, the free energy density of the system becomes (a is the spacing of the Flory-Huggins lattice, which henceforth is taken as the unit of length in this section, $a = 1$)

$$a^{-3} f(\phi)/k_B T = (\phi/N)\ln\phi + (1-\phi)\ln(1-\phi) + \chi\phi(1-\phi) \quad , \tag{1}$$

where the Flory-Huggins parameter χ is $\chi = z\epsilon/k_B T$. For large N only volume fractions $\phi \ll 1$ matter and hence expanding $\ln(1-\phi)$ the potential $g(\phi) = f(\phi) + k_B T\phi(1-\chi)$ becomes

$$g(\phi)/k_B T \approx \frac{\phi}{N}\ln\phi + \frac{1}{2}b_2\phi^2 + \frac{1}{6}b_3\phi^3 + \cdots , \tag{2}$$

where the virial coefficients are simply $b_2 = 1 - 2\chi$, $b_3 = 1$. In the following we allow for a slightly more general choice where b_3 can differ from unity. The spinodal curve of the polymer solution then is found from the condition $(\partial^2 g(\phi)/\partial\phi^2)_T = 0$, i.e.

$$-b_2 = 2\chi_s(\phi) - 1 = (N\phi)^{-1} + b_3\phi \, . \tag{3}$$

The minimum [] of the spinodal curve in the χ-ϕ plane yields the critical point of the phase separation, which is given by

$$\phi_{\rm crit} = (Nb_3)^{-1/2} \, , \; \chi_{\rm crit}(N) = \left[\frac{1}{2} + (b_3/N)^{1/2}\right] . \tag{4}$$

Noting that the limiting value of $\chi_{\rm crit}(N \to \infty) = 2$ yields the Theta point of the polymer solution, the critical temperature $T_{\rm crit}$ of the polymer solution (note $T_{\rm crit} = z\epsilon/k_B\chi_{\rm crit}$) varies as

$$T_{\rm crit}(N) = \Theta\left[1 - (b_3/N)^{1/2}\right], \quad N \to \infty \quad . \tag{5}$$

The coexistence curve that describes (see Fig. 1) the coexistence between a dilute polymer solution of volume fraction $\phi_{\rm coex}^{(1)}$ and a semidilute polymer solution of volume fraction $\phi_{\rm coex}^{(2)}$ for $T < T_{\rm crit}$, can be found by equating the chemical potentials $\mu = k_B T(\partial g(\phi)/\partial\phi)_T$ and the osmotic pressures [1, 2, 3]

$$\Pi = \phi^2(\partial[g(\phi)/\phi]/\partial\phi)_T = \phi/N + b_2\phi^2/2 + b_3\phi^3/3 \tag{6}$$

of both phases. Near the critical point, where $\Pi_{\rm crit} = b_3^{-1/2} N^{-3/2}/3$, one finds a coexistence curve of mean-field type,

$$\phi_{\rm coex}^{(1,2)} = \phi_{\rm crit} \pm \sqrt{3(\chi - \chi_{\rm crit})/(N^{1/2} b_3^{3/2})}\,. \tag{7}$$

Thus, we can define the "order parameter" ψ of the unmixing transition as

$$\psi = [\phi_{\rm coex}^{(2)} - \phi_{\rm coex}^{(1)}]/2 = \hat{B}(N)\tau^{\beta}, \quad \tau \equiv \chi/\chi_{\rm crit} - 1 \approx 1 - T/T_{\rm crit} \quad , \tag{8}$$

where the critical exponent β takes its mean-field value $\beta_{\rm MF} = 1/2$ and the critical amplitude $\hat{B}(N)$ scales for $N \to \infty$ as

$$\hat{B}(N) = \sqrt{6}\, b_3^{-3/4} N^{-1/4} \quad . \tag{9}$$

It is also of interest not only to consider the uniform order parameter, but also its long wavelength fluctuations. This can be done by introducing the free energy functional [5, 25, 26, 27, 28]

$$\Delta\mathcal{F}/k_B T = \int d\vec{r}\left\{ f\left[\phi(\vec{r})\right] + \frac{a^2}{36\phi(1-\phi)}\left[\nabla\phi(\vec{r})\right]^2 \right\} \quad . \tag{10}$$

Note that the length a (which we choose as our unit of length, as noted above) has the physical meaning of $a^2/[\phi(1-\phi)] = b_P^2/\phi + b_S^2/(1-\phi) \approx b_P^2/\phi$, where b_P is the size of an effective monomeric unit forming the polymer, and b_S the typical size of a solvent molecule. This interpretation can be derived from the random phase approximation [5, 28] (cf. also Sect. 3.5.1). The homogeneous chemical potential μ introduced above can then be generalized as

$$\mu(\vec{r}) \equiv \delta(\Delta\mathcal{F})/\delta\phi(\vec{r})$$
$$= const + k_B T \left\{ (N\phi_0)^{-1} + b_2 + b_3\phi_0 - \frac{a^2}{18\phi_0}\nabla^2 \right\} \delta\phi(\vec{r}), \tag{11}$$

where we have written $\phi(\vec{r}) = \phi_0 + \delta\phi(\vec{r})$ and linearized the functional derivative with respect to $\delta\phi(\vec{r})$. Considering the spatial Fourier components $\delta\phi_{\vec{q}}$, the inverse collective structure factor $S_{coll}(\vec{q})$ [5, 28]) becomes

$$S_{\rm coll}(\vec{q})^{-1} = [(N\phi_0)^{-1} + b_2 + b_3\phi_0][1 + q^2\xi^2] \quad , \tag{12}$$

with a correlation length ξ of local concentration fluctuations,

$$\xi = (a/3\sqrt{2\phi_0})[(N\phi_0)^{-1} + b_2 + b_3\phi_0]^{-1/2} \quad . \tag{13}$$

Comparison with Eq. (3) immediately shows that both $S_{\rm coll}(0)$ and ξ diverge when one approaches the spinodal curve from the one-phase region

$$S_{\rm coll}(0) = [\chi_s(\phi) - \chi]^{-1} \quad , \tag{14}$$

$$\xi = (a/3\sqrt{2}\phi_0)[\chi_s(\phi) - \chi]^{-1/2} \quad . \tag{15}$$

In particular, at the critical point, $\phi_0 = \phi_{\rm crit}$, we find mean-field type power laws analogous to Eq. (9),

$$S_{\rm coll}(0) = \hat{\Gamma}^+(N)(-\tau)^{-\gamma} \quad , \tag{16}$$

$$\xi(\phi_{\rm crit}) = \hat{\xi}^+(N)(-\tau)^{-\nu} \quad , \tag{17}$$

where the exponents γ and ν take their mean-field values $\gamma_{\rm MF} = 1$, $\nu_{\rm MF} = \frac{1}{2}$ and the critical amplitudes scale as

$$\hat{\Gamma}^+(N) = \chi_{\rm crit}^{-1} = 1/2 \quad \text{(independent of N)}\,, \tag{18}$$

$$\hat{\xi}^+(N) = (a/6\phi_{\rm crit}^{1/2}) = (ab_3^{1/4}/6)N^{1/4} \quad . \tag{19}$$

It also is straightforward to work out the corresponding power laws along the coexistence curve [28],

$$S_{\rm coll}^{\rm coex}(0) = \hat{\Gamma}^{-}(N)\tau^{-\gamma} \quad , \quad \hat{\Gamma}^{-}(N) = \frac{1}{2}\hat{\Gamma}^{+}(N) = 1/4 \quad , \tag{20}$$

$$\xi_{\rm coex} = \hat{\xi}^{-}(N)\tau^{-\nu} \, , \, \hat{\xi}^{-}(N) = \frac{1}{\sqrt{2}}\hat{\xi}^{+}(N) \quad . \tag{21}$$

Finally, we recall that Eq. (10) can be used [5, 25, 26, 27, 28] to derive the excess free energy γ due to a flat interface. The result is [29, 30], for $b_3 = 1, a = 1$

$$\gamma / k_B T = (5/3)^{1/2} N^{-1/4} (\chi/\chi_{\rm crit} - 1)^{3/2} \quad ; \tag{22}$$

writing again a general power law $\gamma / k_B T = \hat{\gamma}(N)\tau^{\mu}$ we conclude $\mu_{\rm MF} = 3/2$ and

$$\hat{\gamma}(N) = (5/3)^{1/2} N^{-1/4} \quad . \tag{23}$$

However, it should be noted that even within a mean-field context the validity of these asymptotic power laws is severely restricted. This is noted already from Eqs. (7)–(9), since $\phi_{\rm coex}^{(1,2)} = \phi_{\rm crit} \pm \psi$ implies that $\psi < \phi_{\rm crit}$, since $\phi_{\rm coex}^{(1)}$ must be positive, and thus we conclude that $(\chi/\chi_{\rm crit} - 1)^{1/2} N^{-1/4} < N^{-1/2}$, ignoring prefactors for the moment, or alternatively $(\chi/\chi_{\rm crit} - 1) N^{1/2} < 1$. This shows that already when $|\chi/\chi_{\rm crit} - 1|$ is of order $N^{-1/2}$, the power laws derived in Eqs. (7)–(23) cease to describe the actual functions ψ, $S_{\rm coll}(0)$, ξ and $\gamma / k_B T$, and rather a crossover to a different behavior sets in. This crossover is a consequence of the fact that the limit $N \to \infty$, $T_{\rm crit}(N) \to \Theta$, $\phi_{\rm crit} \to 0$ can be considered as a tricritical point [3, 29, 30, 31, 32, 33]. As expected from the above argument, $\zeta = N^{1/2}(\chi/\chi_{\rm crit} - 1)$ acts as a crossover scaling variable, and hence [3, 29, 30]

$$\psi = N^{-1/2} \tilde{\psi}(\zeta) \, , \, \tilde{\psi}(\zeta \to 0) \propto \zeta^{1/2} \quad , \tag{24}$$

in agreement with Eqs. (7)–(9). In the limit where $\chi/\chi_{\rm crit} - 1 \ll 1$ but $N \to \infty$, the N-dependence must in fact cancel out from Eq. (24), in order to allow for a physically plausible behavior. This readily yields [3, 29, 30], cf. Eq. (5)

$$\tilde{\psi}(\zeta \to \infty) \propto \zeta^{1} \, , \quad \psi \propto (\chi/\chi_{\rm crit}(N \to \infty) - 1) = 1 - T/\Theta \, . \tag{25}$$

Similar crossover formulae can be written down for the other quantities of interest, too. While Eqs. (12)–(19) also remain valid for $\zeta \to \infty$, the behavior of $\xi_{\rm coex}$, $\zeta_{\rm coll}^{\rm coex}(0)$ and $\gamma / k_B T$ gets correspondingly modified by the crossover. A pronounced asymmetry along the dilute branch ($\phi_{\rm coex}^{(1)} \to 0$) is then of particular interest and the concentrated branch of the coexistence curve becomes ($\phi_{\rm coex}^{(2)} \to 2\psi$): One finds $\xi_{\rm coex}^{(1)} \propto N^{1/2}$ while $\xi_{\rm coex}^{(2)} \propto N^{1/2}/\zeta$ as $\zeta \to \infty$, i.e. $\xi_{\rm coex}^{(2)} \propto (1 - T/\Theta)^{-1}$ independent of N. A related asymmetry concerns $S^{\rm coex}(0)$. Finally, we consider $\gamma / k_B T$ which can be written as [29, 30]

$$\gamma / k_B T = N^{-1} \tilde{\gamma}(\zeta) \quad \tilde{\gamma}(\zeta \to 0) \to \zeta^{3/2} \quad , \tag{26}$$

reproducing Eqs. (22), (23), while for $N \to \infty$ at fixed small $1 - T/\Theta$ we must require that N cancels out and thus

$$\tilde{\gamma}(\zeta \to \infty) \to \zeta^2 \quad , \quad \gamma / k_B T \propto (1 - T/\Theta)^2 \, . \tag{27}$$

2.2 Phase Separation Between Polymer and Solvent Beyond Mean-field Theory: Scaling Predictions

From Eqs. (24)–(27) we have seen that the standard mean-field power laws describing the singularities near the critical unmixing point can hold only for $\zeta = N^{1/2}(\chi/\chi_{\rm crit} - 1) \ll 1$. Of course, when $\chi \to \chi_{\rm crit}$ at fixed N, we do expect that mean-field theory breaks down due to the neglect of thermal fluctuations, and in reality a crossover to the critical behavior described by the Ising model universality class [34, 35, 36] sets in. Thus, very close to the critical point, we expect the following critical exponents [35, 36].

$$\beta \approx 0.326(1), \ \gamma = 1.238(2), \ \nu = 0.630(1), \ \mu (= 2\nu) = 1.260(2) \quad . \tag{28}$$

Note that the "hyperscaling relation" $d\nu = \gamma + 2\beta$ (in $d = 3$ dimensions) [34] as well as the Widom [38] scaling relation for the interfacial tension exponent $\mu = (d-1)\nu$ hold here, but are not obeyed for the mean-field exponents [34].

We now discuss at what distance from the critical point the crossover to this Ising-type critical behavior occurs. A simple and qualitative but essentially correct answer to this question is provided by the Ginzburg criterion [39], which is a simple self-consistency check of mean-field theory (for more detailed discussions and derivations of this criterion see e.g. [5, 40]). Basically it says that the standard mean-field description of critical behavior holds if the reduced temperature distance from the critical point, $|\tau|$, exceeds the "Ginzburg number" Gi, which can be written as the following combination of mean-field critical amplitudes [41], in $d = 3$ dimensions

$$Gi = (3/4\pi)^2 \frac{1}{[\hat{B}(N)]^4} \left[\hat{\Gamma}_+(N)\right]^2 \left[a/\hat{\xi}_+(N)\right]^6 \quad . \tag{29}$$

Using Eqs. (9), (18), and (19) we readily recognize that

$$Gi \propto N^{-1/2} \tag{30}$$

and hence the condition for the validity of the mean-field power law would be $|\tau|/Gi \gg 1$, i.e. $N^{1/2}|\tau| \gg 1$. However, as we have seen for $\chi > \chi_{\rm crit} (T < T_{\rm crit})$ this condition means that $\zeta \gg 1$, and hence the crossover towards the tricritical behavior (e.g. Eq. (25) and (27)) has occurred.

We conclude that for polymer solutions the standard mean-field critical (rather than tricritical) behavior never holds, irrespective of how large the chain length N becomes. Of course, this conclusion is opposite to the result for symmetric polymer mixtures (where also Flory-Huggins theory similar to Eq. (1) is the starting point, but we have an entropy of mixing-term $(\phi/N_A)\ln\phi + ([1-\phi]/N_B)\ln[1-\phi]$ with $N_A = N_B$ rather than the expression written in Eq. (1)). There, the Ginzburg criterion shows that standard mean-field theory does become valid in $d = 3$ [3, 5, 42, 43] (though not in $d = 2$ [44]), when $N_A = N_B \to \infty$. This conclusion actually is in agreement with both experiment (e.g. [45]) and simulation [46, 47]. On the other hand, one knows that - apart from logarithmic correction factors – the mean-field description of tricritical behavior is correct [31], and hence one does expect that the part of Sect. 2.1. pertaining to the region $\zeta \gg 1$ is qualitatively correct.

Unfortunately, a full description of the crossover from tricritical behavior to non-mean-field critical behavior is a difficult theoretical problem [48]. Here, we shall not dwell on recent developments based on the renormalization group approach, since this is outside the scope of the present review, but we only mention the phenomenological extension of the crossover scaling description, Eqs. (24)–(27), to incorporate the Ising behavior [3, 30, 49]. There one starts from the observation that the variable appearing in the Ginzburg criterion, $|\tau|Gi \propto N^{1/2}|\tau|$, is simply proportional to the mean-field crossover scaling variable ζ. Thus, the assumption is that there is no need to change the crossover scaling variable, and one only needs to change the behavior of the crossover scaling functions $\tilde{\psi}$, $\tilde{\gamma}(\zeta)$ etc. in the limit of small ζ, in order to incorporate the correct Ising-type critical behavior. Thus, one writes

$$\tilde{\psi}(\zeta \to 0) \propto \zeta^{\beta} \quad , \quad \tilde{\gamma}(\zeta) \propto \zeta^{2\nu} . \tag{31}$$

Then it follows that

$$\hat{B}(N) \propto N^{-x_1} \quad , \quad \hat{\gamma}(N) \propto N^{-x_5} \quad , \tag{32}$$

with

$$x_1 = (1-\beta)/2 \approx 0.34, \quad x_5 = 1 - \nu \approx 0.37 , \tag{33}$$

adopting a notation introduced by Enders et al. [50]. In that work, the phenomenological assumption of power laws with non-trivial exponents for the shift of $T_{\rm crit}(N)$ with N and the critical concentration $\phi_{\rm crit}(N)$ were also made,

$$\phi_{\rm crit}(N) \propto N^{-x_2} , \; \Theta - T_{\rm crit}(N) \propto N^{-x_3} \quad . \tag{34}$$

From Eqs. (4), (5) we read off that the mean-field predictions for these exponents are

$$x_2 = 1/2, \; x_3 = 1/2 \quad . \tag{35}$$

However, experiments have found that [51, 52, 53, 54, 55, 56, 57, 58]

$$x_1 \approx 0.23 - 0.34, \;\; x_2 \approx 0.38, \;\; x_3 \approx 0.47 - 0.50 \quad . \tag{36}$$

One sees that the data for x_1 span the full range from the mean-field result ($x_1 = 1/4$) to the scaling prediction (cf. Eq. (33)), while the data for x_3 are compatible with the mean-field result. However, the experimental results for x_2 seem to indicate a clear discrepancy with the mean-field result $x_2 = 1/2$ (cf. Eq. (35)). Enders et al. then also allowed for a non-mean-field crossover exponent, writing

$$\psi = N^{-x_4} \, \tilde{\psi}(N^{x_4} \tau) \quad , \tag{37}$$

which requires $\tilde{\psi}(\zeta \to \infty) \propto \zeta$ in order to reproduce $\psi \propto 1 - T/\Theta$ for $N \to \infty$ (cf. Eq. (25)) while $\tilde{\psi}(\zeta \to 0) \propto \zeta^{\beta}$ yields $x_1 = x_4(1 - \beta)$. The physical interpretation for Eq. (37) would be the assumption that the radius of gyration of the polymer coils does not scale like $R_{\rm gyr} \propto N^{1/2}$ in the critical region but with a different exponent. However, there is little information from experiment on this issue. With respect to the exponent x_5, experimental results lie in the range [52, 55]

$$x_5 \approx 0.38 - 0.44 \, , \tag{38}$$

close to the scaling prediction, Eq. (33) .

The discrepancy for x_2 between experiment, Eq. (36) and mean-field prediction, Eq. (35), has led to a large theoretical activity, aiming to explain how a different exponent could arise, and to predict what its value should be [58, 59, 60, 61, 62, 63]. We shall come back to this question in the framework of thermodynamic perturbation theory (TPT) in Sect. 4. There is the alternative view that logarithmic corrections to the simple mean-field power laws, Eqs. (4) and (5), are present, namely [64]

$$\phi_{\rm crit}(N) \propto (\ln N)^{1/2}/N^{1/2} \quad , \quad \Theta - T_{\rm crit}(N) \propto N^{-1/2} (\ln N)^{-3/11}, N \to \infty \quad . \tag{39}$$

If Eq. (39) holds asymptotically, it is quite likely that the approach to this asymptotic behavior for large N as a function of N is quite slow, and hence the results, Eqs. (36) and (38), find an explanation as non-universal pre-asymptotic slow crossovers.

Finally we mention that also the collective scattering function $S_{\rm coll}(0)$ and the correlation length $\xi(\phi_{\rm crit})$ must show a crossover scaling

$$S_{\rm coll}(0) = N^{1/2} \, \tilde{S}(\zeta) \quad , \quad \zeta = N^{1/2}(-\tau), \tag{40}$$

where $\tilde{S}(\zeta \to \infty) \propto \zeta^{-1}$ to reproduce Eqs. (14), (16) in the (tricritical) mean-field region, while $\tilde{S}(\zeta \to 0) \propto \zeta^{-\gamma}$ with γ given in Eq. (28). Hence it follows that $\hat{\Gamma}^{+}(N) \propto N^{(1-\gamma)/2}$ must vanish with a power law as $N \to \infty$. Similarly,

$$\xi(\phi_{\rm crit}) = N^{1/2}\tilde{\xi}(\zeta) \quad , \quad \tilde{\xi}(\zeta \to \infty) \propto \zeta^{-1/2} \quad , \tag{41}$$

which reproduces Eqs. (17), (19) in the (tricritical) mean-field region, while $\tilde{\xi}(\zeta \to 0) \propto \zeta^{-\nu}$ with ν given in Eq. (28) as well. This argument shows that $\hat{\xi}^{+}(N) \propto N^{(1-\nu)/2}$ in the Ising-like critical region. We expect that the same power laws (but with different amplitude prefactors, compatible with the known universal critical amplitude ratios [65]) hold for $\hat{\xi}_{\rm coex}(N)$ and $S_{\rm coll}^{\rm coex}$ as well.

2.3 Monte Carlo and Molecular Dynamics Methods

First of all we emphasize that the theory described in the previous sections can be interpreted alternatively as a description for the liquid-vapor transition of a homopolymer in the absence of any solvent: When lattice sites occupied by solvent particles are reinterpreted as vacancies, it is natural to take $\epsilon_{ss} = \epsilon_{ps} = 0$ and $\epsilon = -\epsilon_{pp}/2$. The osmotic pressure Π, Eq. (6), is then simply reinterpreted as the total pressure of the polymeric fluid. Thus, Eq. (6) is nothing but the virial equation of state for the polymeric fluid, with the first term ($\Pi = \phi/N$) representing the ideal gas law (recall that a factor $1/k_BT$ has been absorbed in the definition of Π).

We emphasize this liquid-vapor interpretation of the Flory-Huggins theory here, since many of the computer simulations that we shall discuss actually use this language, in the interest of comparing to experimental data on the liquid-vapor equilibrium of short alkane chains [19, 66, 67, 68, 69], for instance.

As we have seen in the previous sections, the formulation of the theory involves many questionable assumptions, and hence the idea to test them by computer simulation methods [70, 71, 72, 73] is clearly attractive. However, while the first study of the self-avoiding walk problem of single polymer chains [74] has appeared two years after the importance sampling MC method [75] was invented, the study of phase equilibria of multi-chain systems by computer simulation is much more difficult. The first tests of the Flory—Huggins theory were performed in 1987 for a study of phase separation in a strictly symmetric polymer mixture (chain lengths $N_A = N_B = N$) [76], utilizing the possibility to carry out the simulation in the semi-grandcanonical ensemble (where the chemical potential difference $\Delta\mu$ is a central parameter, and MC moves are introduced that transform A into B or vice versa). While later the technique was generalized to asymmetric mixtures [77, 78], the corresponding simulation of the polymer-solvent phase separation is more difficult, since MC simulations in the grandcanonical ensemble (with the chemical potential μ as a control parameter) require MC moves where chains have to be inserted with randomly chosen configurations at random positions into the simulation box that already contains other chains. For long chains, the acceptance rate of such moves becomes negligibly small

already at semidilute concentrations, preventing a naive implementation of such an algorithm [79, 80, 81]. It has been possible to carry out a simulation study of the polymer-solvent critical point [82] for the bond fluctuation model [83, 84] for chains up to a length of $N = 60$ effective monomers. In this model, each effective monomer blocks all eight sites of an elementary cube of a three-dimensional lattice from further occupation, and the length b of the bond vector $\vec{b}$ may take the values $b = 2, \sqrt{5}, \sqrt{6}, 3$, and $\sqrt{10}$ [84]. Applying a combination of "random hopping" and "slithering snake" moves (see [70] for a review of the basic simulation methods for polymers) the configuration of chains for this model can be equilibrated more efficiently than using the ordinary self-avoiding walk (SAW) model, as done in [76]. However, while for the case of symmetric polymer mixtures rather long chain lengths could be studied (up to $N = 512$ [46]), it is clear that the chain length reached for the polymer-solvent case ($N = 60$) [82] may be too short to reach the asymptotic behavior of interest. Actually, much longer chains (up to $N = 2048$) were used by Frauenkron and Grassberger [85], applying the pruned-enriched Rosenbluth method (PERM) to generate the chains in the simulated sample. However, even with these chain lengths it is not yet clear whether a significant test of the theoretical predictions summarized in Sect. 2.2 is possible.

While it is our view, that in principle the finite size scaling analysis [86, 87, 88, 89] of MC simulation results generated in the grandcanonical ensemble (utilizing also histogram extrapolation methods [90, 91, 92] and paying attention to "field mixing" [89, 93, 94]) is the most powerful simulation approach to study the polymer-solvent critical point and the phase equilibrium at temperatures slightly below $T_{\mathrm{crit}}(N)$, other methods can be applied when one is interested in the study of the wellseparated phases at temperatures far below criticality. Actually, the first study of this problem is due to Madden et al. [95, 96] who used the canonical ensemble.

The disadvantage of this method is that the two phases have to coexist in the same simulation cell, including two interfaces (Due to the periodic boundary conditions, the interfaces are oriented parallel to a surface of the cubic simulation box, generating the fluid in a slab-like configuration. Hence, one faces the problem of slow equilibration of interface fluctuations, and to distinguish bulk properties from those of the interface region [97, 98, 99, 100]).

The most popular method to study phase equilibria, however, is the Gibbs ensemble [101, 102, 103]. In this method, one simulates two boxes 1 and 2, where the total number of particles $n = n_1 + n_2$ and the total volume $V = V_1 + V_2$ are kept constant. One considers moves where particles are exchanged between the boxes and the volume is redistributed ($V_1 \to V_1' = V_1 - \Delta V$, $V_2 \to V_2' = V_2 + \Delta V$). If the total density $\rho = n/V$ is chosen such that it falls in between the two branches of the coexistence curve, the system will evolve into an equilibrium state such that one box contains only the fluid with a density according to the liquid branch of the coexistence curve, and the other box contains only the fluid with a density according to the vapor branch. Of course, there is no physical reason which of the boxes should contain the liquid and which should contain the vapor, and in fact, if one simulates long enough, one will observe transitions where the boxes switch the identity of the phases they contain, i.e. the "liquid box" will become the "vapor box" and vice

versa. Nevertheless, one can sample the density distribution and distinguish between the vapor peak and the liquid peak of this distribution, at least for temperatures well below $T_{\rm crit}(N)$. In this method, both boxes automatically establish the equilibrium characterizing two-phase coexistence, i.e. both boxes are at the same chemical potential μ and pressure p on average (note that both μ and p are fluctuating variables in this ensemble).

As it stands, the Gibbs ensemble due to its need for volume exchange moves is well-suited for off-lattice models, and in fact it has been used to calculate phase equilibria for various models of chain molecules [104, 105, 106, 107, 108, 109, 110, 111, 112, 113], making use of the configurational bias method to perform the necessary chain insertions, when one exchanges chains from one box to the other. In particular, the move of a chain from the vapor box to the liquid box is very difficult due to a low acceptance rate. An alternative method constructs the chemical potential in the two coexisting phases explicitly [114], applying the chain increment method [115] to calculate the chemical potential of the chains, and avoid potential sampling difficulties due to the biased insertion moves. However, the results of this method seems to be compatible to the Gibbs ensemble studies [114]. Finally, we mention that the Gibbs ensemble technique has also been extended to lattice homopolymer models [116, 117]. Chain lengths up to $N = 100$ could be treated by this method.

The Gibbs ensemble approach to study liquid-vapor phase equilibria of polymers (or other fluids) as well as polymer-solvent equilibria [112] clearly is a very valuable and efficient method, since it requires comparatively modest computer resources, which in turn allows the study of chemically realistic models of specific systems [109, 112, 118]. Predicting coexistence curves and the rough location of the critical point of alkanes such as $C_{24}H_{50}$ and $C_{48}H_{98}$ complements experiment (the real polymers could never be studied in the critical region due to chemical degradation) but is very useful since it helps to develop a better equation of state also for the experimentally accessible region [106, 107, 109]. On the other hand, it is clear that for a detailed study of critical properties of polymers or other fluids the Gibbs ensemble is not the method of choice, since near the critical point one has to deal with finite size effects [72, 73, 86, 87, 88, 89, 93, 94] which for the Gibbs ensemble are cumbersome to deal with. It now is widely accepted that the use of finite size scaling [72, 73, 87, 88, 89] in conjunction with MC simulations carried out in the grandcanonical ensemble is the most powerful method to study liquid—vapor critical points [119, 120, 121, 122], critical unmixing of binary fluid mixtures [123, 124], and polymer solutions [82, 85]. Another limitation of the Gibbs ensemble occurs far below the critical point, where the configurational bias chain insertion step into the dense polymer fluid has an acceptance rate that is too low (then the grandcanonical ensemble simulations fail as well, of course). This limitation has recently been overcome by Brennan and Madden [113] for the case where the polymer density in the vapor (or solvent, respectively) can be taken to be strictly zero. They developed a strategy to establish an osmotic equilibrium between a pure solvent phase and a polymer–rich phase which produces a polymer–rich phase that should be indistin-

guishable from the corresponding phase of the full binary polymer+solvent system and does not require the insertion and deletion of chain molecules [113].

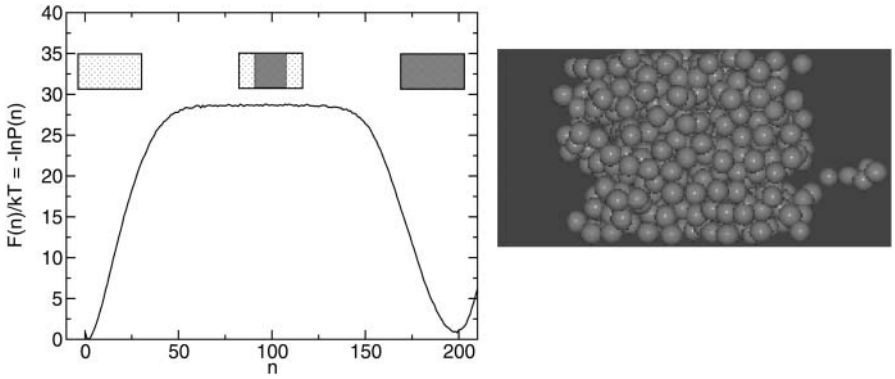

Fig. 4. Free energy $F(n)/k_BT$ plotted versus the number n of chains (using a coarse-grained bead-spring model of hexadecane with $N = 5$ effective monomers, see Sect. 5) at temperature $T = 1.38\epsilon/k_B$ (ϵ sets the scale for the Lennard-Jones energy). The results are for a box geometry $L \times L \times 2L$, with periodic boundary conditions in all three directions, and a choice of $L = 9\sigma$, σ being the range parameter of the Lennard-Jones interaction. The *rectangles* in the main part of the figure show the schematic state of the system: Pure vapor (*left*), liquid-vapor coexistence with a slab-like liquid layer (*middle*) and pure liquid (*right*). A typical snapshot picture of the system in the slab configuration with $n = 100$ polymers is shown *on the right*

An additional bonus of the finite size scaling analysis of grandcanonical simulation data is that information on the interfacial tension between the coexisting phases can be extracted [22, 99, 120, 121, 125, 126, 127, 128, 129, 130]. Figure 4 gives a brief explanation of this method: The idea is to sample the density distribution function $P(\phi)$ at temperatures $T < T_{\text{crit}}$ for densities throughout the full miscibility gap. Doing this by straightforward MC sampling [125] would be extremely inefficient, of course, but accurate data on $P(\phi)$ can in fact be obtained either by multicanonical MC methods [131, 132] or by other "extended ensemble" methods (transition matrix MC [133] was used in [121], while successive umbrella sampling [134] was used for the results presented in Fig. 4). The states of the system at intermediate densities (near $\phi_m = (\phi_{\text{coex}}^{(1)} + \phi_{\text{coex}}^{(2)})/2$, $\phi_{\text{coex}}^{(1)}$, $\phi_{\text{coex}}^{(2)}$ being the densities of the coexisting phases, where $P(\phi)$ has sharp maxima) are dominated by "slab" configurations, where a thin film of liquid extends throughout the simulation box, separated from the surrounding vapor by two planar interfaces, which are oriented parallel to the walls (and are connected in itself via the periodic boundary conditions). If one chooses a cubic $L \times L \times L$ box, these interfaces could be oriented perpendicular either to the x or y or the z axis; however, choosing a box geometry of $L \times L \times 2L$ (cf. Fig. 4) the interfaces orient perpendicular to the direction in which the system is longer, to minimize the interface area. This choice also puts the two interfaces farther apart, thereby reducing their mutual interactions [130]. The effective free energy of the

system then simply is $F(\phi) = -k_B T \ln P(\phi) + \text{const}$, and this quantity is plotted in Fig. 4. Note that for ϕ near ϕ_m, $F(\phi)$ is horizontal, because changing ϕ in this region only changes the volume of the liquid slab but not its total surface area $2L^2$, and for large enough L the two liquid-vapor interfaces can be treated as non-interacting. This interpretation implies that the free energy of interfaces can be found as

$$f_\gamma = \Delta F/(2L^2), \quad \Delta F = F(\phi_m) - [F(\phi^{(1)}\text{coex}) + F(\phi^{(2)}_{\text{coex}})]/2 \quad . \tag{42}$$

This method was used in [22] to obtain the data shown in Fig. 5.

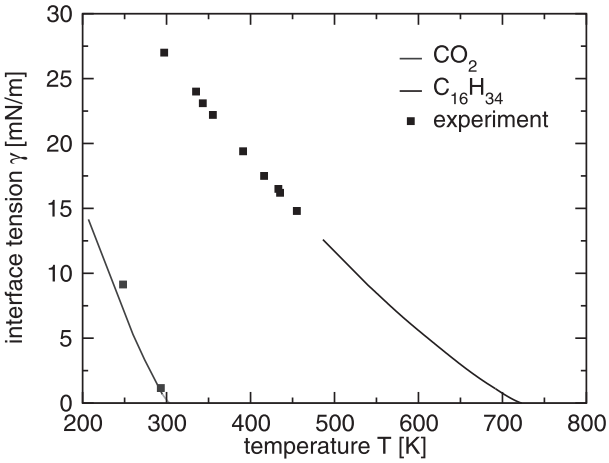

Fig. 5. Interfacial free energy of pure CO_2 and of $C_{16}H_{34}$ plotted versus temperature. Experimental data from Dee and Sauer [135, 136] are included. Data for CO_2 were taken from [137]

At this point, we emphasize that the use of Eq. (42) is not the traditional standard method to estimate interfacial tensions from computer simulations: Usually, one simulates a system prepared in a slab configuration such as shown in Fig. 4, using the canonical (nVT) ensemble or the microcanonical ensemble (when one carries out Molecular Dynamics (MD) rather than MC simulations). The interface free energy is then found from the anisotropy of the pressure tensor [138, 139]

$$\gamma = \frac{1}{2}\int \mathrm{d}z\, [\Pi_N(z) - \Pi_T(z)],$$
$$\Pi_N(z) = \Pi_{zz}(z) \qquad \Pi_T(z) = [\Pi_{xx}(z) + \Pi_{yy}(z)]/2\ , \tag{43}$$

where we have assumed that the interfaces are normal to the z-axis, and the integration is extended in this direction over the entire box. The pressure tensor requires to evaluate the forces between particles $\vec{F}_{ij} = -\partial U(\vec{r}_{ij})/\partial \vec{r}_{ij}$. If we assume pairwise potentials,

$$\Pi_{\alpha\beta}(z) = \phi(z) k_B T \, \delta_{\alpha\beta} + \frac{1}{2L^2} \sum_{i \neq j} (\vec{r}_{ij})_\alpha (\vec{F}_{ij})_\beta \Theta[z - z_i)/z_{ij}] \Theta[z_j - z)/z_{ij}]/z_{ij} \, , \tag{44}$$

where z_{ij} is the z-component of $\vec{r}_{ij} = \vec{r}_i - \vec{r}_j$, and $\Theta(\zeta)$ is the Heaviside step function here.

Forces are not required in MC simulations but are routinely calculated in the context of Molecular Dynamics (MD) simulations (where one solves Newton's equation of motion [70, 71]). In these simulations [140, 141, 142], Eqs. (43) and (44) are used and both the liquid-vapor coexistence curve and f_γ are extracted. However, while this method has been used for various chemically realistic models of solvents [140, 141, 142], we are not aware of studies of liquid-vapor coexistence curves for polymeric systems by this method yet. Already for small molecules such as CO_2, only a rather rough estimation of the coexistence curve is possible [142]. Therefore, we shall not discuss the MD method in this article further. An interesting comparison between the MD approach (using Eq. (43)) and the grandcanonical MC method (using Eq. (42)) for a square well fluid is given in [121]. In agreement with our own experience [99] they find that the grandcanonical method is superior to measuring the interfacial tension by the anisotropy of the pressure, at least for not too low temperatures.

In the next section, we briefly describe some results obtained [82, 85] for lattice models of critical unmixing of polymers, which have some relevance for the theories summarized in the previous sections. We do not give a more detailed account of the simulation techniques applied in those papers, however, because they are well documented in the literature [70, 71, 72, 73, 77, 78, 81, 82, 85, 91]. The extensions of these techniques needed to cope with the complications due to competing order parameters (as they occur in polymer+solvent systems when both liquid-vapor unmixing and fluid-fluid unmixing is possible) are deferred to Sect. 5.

2.4 Comparison Between Computer Simulation Results and Analytical Predictions

Due to the strong asymmetry of the coexistence curve for large N, it is mandatory to include "field mixing" [82, 85, 89, 93, 94, 119] in the finite size scaling analysis (i.e., energy density and particle number density need to be treated as coupled parameters, and the "order parameter" M of the transition needs to be constructed as a suitable linear combination, as described in the quoted references). If this is done, one finds an excellent agreement of the rescaled order parameter distribution $P_L(x)$ at criticality versus the rescaled order parameter $x = a_m^{-1} L^{\beta/\nu}(M - M_{\text{crit}})$, with that of the three-dimensional Ising model (Fig. 6). Here, a_m is a normalization constant, and M_{crit} the value of the order parameter M precisely at the critical point in the limit $L \to \infty$. The Ising model exponents, as quoted in Eq. (28), were used in this analysis, too. Within statistical errors, very good agreement with the scaled order parameter distribution of the Ising model is found, which is not a big surprise, of course, since the applied

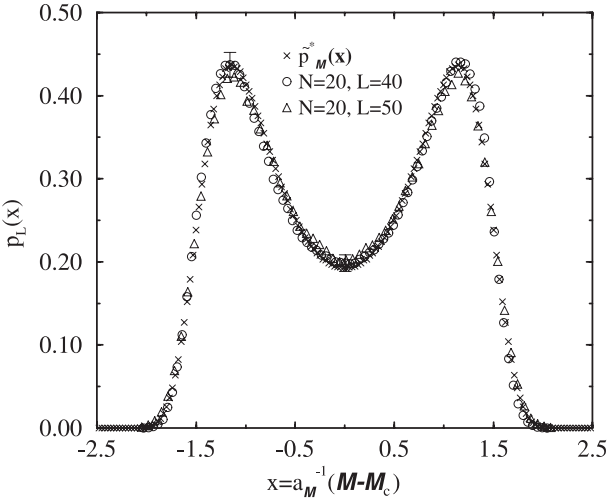

Fig. 6. The order parameter distribution function $P_L(x)$, where x is the rescaled order parameter $x = a_{\rm M}^{-1} L^{\beta/\gamma}(M - M_c)$, for the bond fluctuation model with $N = 20$. The *crosses* represent the Ising model order parameter distribution. From Wilding et al. [82]

chain length is still rather short. But Frauenkron and Grassberger [85] obtained a similar good agreement also for somewhat longer chains, such as $N = 128$ and $N = 256$, using the simpler self-avoiding walk model on the simple cubic lattice.

The chain length dependence of the critical parameters is of particular interest. When one fits the MC data for $T_{\rm crit}(N) - \Theta$ and $\phi_{\rm crit}(N)$ to simple power laws, one finds

$$T_{\rm crit}(N) - \Theta \propto N^{-1/2} \quad , \quad \phi_{\rm crit}(N) \propto N^{-0.38} \quad . \tag{45}$$

Exactly the same conclusion emerges from the bond fluctuation model study of Wilding et al. [82] that used $20 \le N \le 60$, and the SAW model study of Frauenkron and Grassberger [85] that used much longer chains ($N \le 2048$). Equation (45) is nicely compatible with experiment, but it is not consistent with the theoretical expectations. Of course, the possibility that simple power laws do not apply and rather logarithmic corrections need to be considered (e.g. Eq. (39)) is not ruled out. In order to test for such logarithmic corrections, both very large values of N and a range of several decades in N would be required. However, it remains then to explain why the asymptotic power law for the relation for $T_{\rm crit}(N) - \Theta$ is readily seen for small N and for various models as well as in experiment, while the other relation for $\phi_{\rm crit}(N)$ is not. In addition, if the exponent 0.38 is an effective exponent, it is strange that it shows up in an almost universal manner - two different lattice models for very different ranges of N, and various experiments with rather good accuracy yield the same number.

At least the simulations are rather definite on another point that has been controversial among the theories described in Sect. 2.2: It has been shown [82, 85]

that the chain configurations at criticality are definitely not collapsed, but do follow Gaussian chain statistics for larger N, i.e. the mean square radius of gyration for large N scales linearly with N [82, 85] (very short chains are slightly swollen rather than contracted [82], so chain contraction as an origin of the anomalous power law in Eq. (45) is definitely ruled out).

Another point which still needs to be addressed by the simulations is the crossover between critical and tricritical behavior. Wilding et al. [82] noted that the Ising critical region (describing the shape of the coexistence curve for $T < T_{\rm crit}(N)$ in terms of the critical exponent $\beta \approx 0.326$, Eq. (28)) is considerably narrower than for other systems (e.g., the simple Lennard-Jones fluid), but an analysis of the critical vs. tricritical behavior is still lacking. These crossover phenomena in polymer solutions have recently been studied experimentally by Hager et al. [143] and Anisimov et al. [144]. Thus, we conclude this section by stating that even in the study of unmixing of those polymer solutions which can be approximated as incompressible, there are still many unsolved questions.

3 Self-consistent Field Theory for Compressible Polymer Solutions

3.1 Hexadecane and Carbon Dioxide: A Model for a Compressible Polymer Mixture

While the Flory-Huggins mean-field theory [13, 14, 15] of Sect. 2.1 describes the generic, qualitative behavior of incompressible polymer + solvent mixtures, it invokes three important simplifications that restrict its application:

1. In compressible polymer-solvent mixtures there are two coupled order parameters – the density and the composition – and in addition to liquid-vapor phase coexistence also liquid-liquid phase separation can occur [6, 7, 24, 21]. The interplay between composition and density gives rise to six distinct types of phase diagrams according to the classification of Van Konynenburg and Scott [24] (see also Fig. 3).
2. Spatial inhomogeneities are only captured by a square gradient term in the free energy functional [3]. While this is appropriate in the vicinity of the critical point (or the spinodal), where the width of interfaces grows very large [146], this approximation becomes less accurate away from the critical point, where the "intrinsic" width (i.e., without accounting for capillary waves [100, 147]) of the interface is on the order of the interparticle distance in the liquid.
3. Being a mean-field approach, the Flory-Huggins theory neglects fluctuations which are important in the vicinity of the critical point or the spinodal (cf. Sect. 2), i.e., just where the square gradient approximation is useful.

The first approximation might prevent the Flory-Huggins theory even from capturing the *qualitative* behavior of compressible systems. In this section, we will present

a self-consistent field (SCF) theory which makes a first step towards improving the first two issues. We expect the theory to correctly describe the qualitative behavior of compressible polymer-solvent mixtures; yet the mean-field character of the description and deficiencies in describing the structure on short length scales will remain. Importantly, the computational scheme can be systematically improved albeit at the expense of computational complexity.

As illustrated by the qualitatively different types of phase diagrams in the classification of Van Konynenburg and Scott [24] the thermodynamic properties of polymer + solvent mixtures exhibit a great deal of variability. Rather than exploring the complete parameter space of polymer + solvent mixtures, we shall focus on phase diagrams of type III and often refer to a specific, experimentally accessible model system: a mixture of hexadecane $C_{16}H_{34}$ and carbon dioxide CO_2. In particular, we will investigate the super-critical region of the solvent, which corresponds to parameters commonly used in processing polymers (e.g., foaming [8, 9, 10, 11]). In this region of parameter space, the solubility can be adjusted over a wide range by varying the pressure. On the one hand, this polymer + solvent mixture already exhibits many characteristics (e.g., three phase coexistence) which cannot be explained by the Flory-Huggins theory. On the other hand, the chemical structure is rather simple (e.g., simple monomer structure, no branching) and there are no strong specific interactions. Additional complications (e.g., crystallization or glass transition) occur far below the solvent critical temperature. Moreover, much is known of the phase behavior, both of the pure components as well as of the mixture. Importantly, directing a great deal of experimental expertise towards observing *homogeneous* bubble nucleation, Rathke and co-workers [148] have determined nucleation rates and the onset of bubble nucleation for this model system.

In the following we represent the hexadecane+carbon dioxide mixture by a coarse-grained model, which does not faithfully represent the atomistic details, but rather uses a few coarse-grained parameters that are adjusted to mimic the specific substances. This coarse-graining procedure results in a significant reduction of the number of degrees of freedom which makes the model computationally tractable. We do not derive the coarse-grained model, but rather use physical intuition. Where possible, we then compare our MC simulation to experimental results to evaluate the limitation of our model.

A solvent molecule, CO_2, is represented by a single particle. Solvent particles interact via a truncated Lennard—Jones potential

$$V_{\mathrm{LJ}}(r) = \begin{cases} 4\epsilon_{SS}\left(\left(\frac{\sigma_{SS}}{r}\right)^{12} - \left(\frac{\sigma_{SS}}{r}\right)^{6} + \frac{127}{16384}\right) & \text{for} \quad r < 2\cdot\sqrt[6]{2}\sigma_{SS} \\ 0 & \text{for} \quad r \geq 2\cdot\sqrt[6]{2}\sigma_{SS}, \end{cases} \tag{46}$$

where r denotes the distance between the particles. Obviously, this is a crude representation, which ignores all internal degrees of freedom of CO_2. Additionally, the completely spherical interaction potential not even faithfully describes intermolecular interactions, because CO_2 molecules have a quadrupole moment.

In the same spirit of a rough but effective description, we represent a hexadecane molecule by a chain of $N_P = 5$ segments. Again, segments interact via a truncated

Lennard-Jones potential that is characterized by an energy parameter ϵ_{PP} and segment size σ_{PP}. Monomers along a chain are bonded together via FENE (finitely extensible non-linear elastic) springs [149]:

$$V_{\text{FENE}}(r) = -33.75\epsilon \cdot \ln\left[1 - \left(\frac{r}{R_{PP}}\right)^2\right] \tag{47}$$

with $R_{PP} = 1.5\sigma_{PP}$. No bond angle or torsional potentials are included in our model, and we do not attempt to match experimental data for the radius of gyration of hexadecane. In our model the statistical segment length b is about $1.22\sigma_{PP}$ [99]. In any case, these values would rather sensitively depend on the thermodynamic state [112, 150, 151]. Since an effective segment corresponds to a small number of CH_2 units of hexadecane (literally, 3.2), we expect a flexible chain model to yield qualitatively reasonable results. Importantly, this modeling preserves roughly the geometrical size ratio between solvent and polymer segment, which determines the intermolecular packing. The comparison between the critical properties of alkanes and the predictions of the TPT1 in Sect. 4.3.2 lends further support to our coarse-grained description.

Table 1. Critical points of the pure components in MC simulation and experiment

	$T_{S\text{crit}}$	$\phi_{S\text{crit}}$	$p_{S\text{crit}}$	$T_{P\text{crit}}$	$\phi_{P\text{crit}}$	$p_{P\text{crit}}$
MC	$0.999\,\epsilon_{SS}/k_B$	$0.32\,\sigma_{SS}^{-3}$	$0.088\,\epsilon_{SS}/\sigma_{SS}^3$	$1.725\,\epsilon_{PP}/k_B$	$0.27\,\sigma_{PP}^{-3}$	$0.022\,\epsilon_{PP}/\sigma_{SS}^3$
	$0.725\,\epsilon_{PP}/k_B$	$0.59\,\sigma_{PP}^{-3}$	$0.118\,\epsilon_{PP}/\sigma_{SS}^3$			
EXP	304K	0.464 g/cm^3	73.87 bar	723K	0.219 g/cm^3	13.98 bar
	ϵ_{PP}/k_B=419.15K, $\epsilon_{PP}/\sigma_{PP}^3$=625.45 bar, $\epsilon_{PP}/\sigma_{PP}^2$=28.29 mN/m					

In the following we shall measure all lengths in units of the Lennard-Jones diameter $\sigma \equiv \sigma_{PP}$ and all energies in units of the Lennard-Jones well-depth $\epsilon \equiv \epsilon_{PP}$ of the polymer. The parameters of the Lennard-Jones potentials of the pure components are identified by matching the critical density ϕ_{crit} and temperature T_{crit} of pure carbon dioxide and hexadecane. The values from the simulations in reduced Lennard-Jones units and from the experiments are compiled in Table 1. Comparing simulation and experiments we identify $\sigma = 4.52 \cdot 10^{-10}$m and $\epsilon = 5.79 \cdot 10^{-21}$J. The ratio of the critical densities of CO_2 and hexadecane yields $\sigma_{SS} = 0.816\sigma$, and from the ratio of critical temperatures we obtain $\epsilon_{SS} = 0.726\epsilon$.

The comparison between the phase behavior (cf. Fig. 2) and the interface properties (cf. Fig. 5) of the pure components demonstrates that our crude coarse-grained model reproduces the properties of the pure components reasonably well, especially those of the polymer. It is therefore a good starting point for exploring the properties of polymer + solvent mixtures.

To complete the definition of our coarse-grained model, we also use a truncated Lennard-Jones potential between segments of different species. For the size parameter, we use a simple mixing rule

$$\sigma_{SP} = \frac{\sigma_{SS} + \sigma_{PP}}{2} \tag{48}$$

while we take

$$\epsilon_{SP} = \xi \sqrt{\epsilon_{SS} \epsilon_{PP}} \tag{49}$$

for the interactions between unlike segments. For $\xi = 1$ we recover the Lorentz-Berthelot mixing rule. In order to reproduce the experimental observations, however, we have to depart from the Lorentz-Berthelot mixing rule. We shall demonstrate in the following two sections that even the qualitative topology of the phase diagram sensitively depends on the mixing parameter ξ.

3.2 Self-consistent Field Theory

In the remainder of this section we describe the behavior of the coarse-grained model in the framework of the SCF theory. To allow for an analytical treatment, the SCF calculations use an even simpler model, which only reproduces the properties of the polymer model on long-length scales.

To describe a compressible mixture of two molecules – solvent S and polymer P – we use two independent (segmental) number densities ϕ_S and ϕ_P. The pressure depends on both densities and to capture the qualitative behavior we parameterize the equation of state by a virial expression that only retains terms up to third order [152]:

$$\begin{aligned} \frac{p}{k_B T} = \phi_S + \frac{\phi_P}{N} + \frac{\upsilon}{k_B T} \left[\frac{1}{2}(\phi_S + \phi_P)^2 - \frac{\tilde{\chi}}{4}(\phi_S - \phi_P)^2 + \frac{\zeta}{2}(\phi_S^2 - \phi_P^2) \right] \\ + \frac{2w_{SSS}}{3}\phi_S^3 + \frac{w_{SSP}}{3}\phi_S^2\phi_P + \frac{w_{SPP}}{3}\phi_S\phi_P^2 + \frac{2w_{PPP}}{3}\phi_P^3. \end{aligned} \tag{50}$$

The first two terms correspond to an ideal gas. υ parameterizes the average excluded volume per segment, and ζ their difference. $\tilde{\chi}$ characterizes the repulsive interaction between the solvent and the polymer and is proportional to the Flory-Huggins parameter. w_{SSS}, w_{SSP}, w_{SPP}, and w_{PPP} are third order virial coefficients and mimic the (mainly entropic) repulsion of the segments at short distances. Obviously, this is only a very crude description of the equation of state of compressible polymer-solvent mixtures: (i) At low polymer concentration (semi-dilute solutions) one expects the osmotic pressure of the polymer to exhibit a characteristic power-law and the second virial coefficient to depend on the chain length N like $\upsilon \sim R_e^3 \sim N^{3\nu_{\mathrm{SAW}}}$, where R_e is the end-to-end distance and $\nu_{\mathrm{SAW}} = 0.588$ the exponent that characterizes the chain extension in dilute solution. (ii) At high density, higher order virial coefficients become important, too. Even for a one-component monomeric fluid (e.g., a Lennard-Jones system or hard sphere fluid) such an equation would yield at best a qualitative approximation. Therefore, we should consider this expression as an effective description only, and the parameters shall be identified to give a reasonable description of the equation of state over the relevant regime of densities and not only be fitted to the low-density behavior. In principle, all parameters of the equation of state

υ, $\tilde{\chi}$, ζ, w_{SSS}, w_{SSP}, w_{SPP}, and w_{PPP} depend on temperature. In the following, we assume the second virial contributions to be purely enthalpic and the third order contributions to be purely entropic, i.e., the second and third virial coefficients of the pure polymer are $B_2(T) = \upsilon N^2(1-\tilde{\chi}/2-\zeta)/2k_BT$ and $B_3(T) = 2w_{PPP}N^3/3$, respectively. The chain length dependence of the virial coefficients coincides with the Flory-Huggins theory. The temperature dependence however differs: In the Flory-Huggins theory one takes $B_2(T) = N^2(1-\Theta/T)$ which accounts for the vanishing second virial coefficient at the Θ-temperature, while the second virial coefficient in the SCF calculations is purely enthalpic. In the super-critical regime of the solvent, $T \approx T_{S\text{crit}} \ll \Theta$, the difference between the two assumptions becomes less important. In spite of its simplicity, this phenomenological form is flexible enough to describe the various types of phase diagrams. Moreover, it is straightforward to improve the equation of state by considering higher order terms.

We also mention an alternative approach by Hong and Noolandi [153]: In their SCF calculations of a compressible polymer mixture three species – polymer A, polymer/solvent S, and vacancy V – are introduced and incompressibility is enforced, i.e., $\phi_A+\phi_S+\phi_V = 1$. This approach is a generalization of the Flory-Huggins theory, and by similar arguments as discussed in Sect. 2 one can identify the behavior of an incompressible ternary mixture with the behavior of a compressible binary mixture. The translational entropy of the vacancies in junction with the incompressibility constraint generates an infinite sequence of virial coefficients. Hence, this approach can describe the liquid (A) - liquid (S) immiscibility at high pressures and low densities of vacancies, whereas our third order virial expansion will become quantitatively unreliable at high densities. There is, however, quite a conceptual difference: The third order virial coefficients in our equation of state arise from the packing of segments in the fluid, while in the Flory-Huggins approach higher order virial coefficients stem from the translational entropy of vacancies. Therefore, we prefer our more flexible equation of state to describe the behavior at low pressure.

To investigate the properties of spatially inhomogeneous systems, we start from the grandcanonical partition function:

$$\mathcal{Z} = \sum_{n_S,n_P=0}^{\infty} \frac{e^{\mu_S n_S/k_BT}}{n_S!}\frac{e^{\mu_P N n_P/k_BT}}{n_P!}\int \mathcal{D}\mathcal{P}_S\mathcal{D}\mathcal{P}_P \exp\left(-\frac{\mathcal{E}\left[\hat{\phi}_S,\hat{\phi}_P\right]}{k_BT}\right), \quad (51)$$

where we sum over all numbers of molecules n_S and n_P, and μ_S and μ_P denote the chemical potentials per segment. $\mathcal{E}$ denotes the interaction free energy functional for which we assume the following form

$$\frac{\mathcal{E}[\phi_S,\phi_P]}{k_BT} = \int \mathrm{d}\mathbf{r}\left\{\frac{\upsilon}{k_BT}\left[\frac{1}{2}(\phi_S+\phi_P)^2 - \frac{\tilde{\chi}}{4}(\phi_S-\phi_P)^2 + \frac{\zeta}{2}(\phi_S^2-\phi_P^2)\right]\right.$$
$$\left. + \frac{w_{SSS}}{3}\phi_S^3 + w_{SSP}\phi_S^2\phi_P + w_{SPP}\phi_S\phi_P^2 + \frac{w_{PPP}}{3}\phi_P^3\right\}. \quad (52)$$

Equation (52) is compatible with the equation of state (50). Note that this interaction functional is strictly local, i.e., we implicitly assume the range of segmental interactions to be small compared to the width w of the liquid-vapor interface,

which is the smallest length scale of interest. Far away from the critical point, the width of the interface is comparable to the size of a segment and this assumption becomes quantitatively inaccurate; also packing effects at high densities are not properly represented. Non-local free energy functionals have also been explored [99, 154, 155, 156, 157, 158, 159] and it turns out that a decomposition into a short-ranged repulsive contribution, which determines the packing inside the fluid, and an attractive contribution is essential to provide a quantitatively accurate description. Without such a decomposition, the theory tends to underestimate the interfacial tension [99, 154] (cf. also Fig. 38). Nevertheless, we expect this interaction functional to describe the qualitative behavior correctly.

$\hat{\phi}_P(\mathbf{r}) = \sum_{i=1}^{n_P} \int_0^N \mathrm{d}s\ \delta(\mathbf{r} - \mathbf{r}_i(s))$ denotes the microscopic segment number density, which depends on the position $\mathbf{r}_i(s)$ of the sth segment on polymer i. For computational convenience, we model polymers as Gaussian chains and

$$\mathcal{P}_P[\mathbf{r}] \sim \exp\left[-\frac{3}{2b^2}\int_0^N \mathrm{d}s\ \left(\frac{\mathrm{d}\mathbf{r}}{\mathrm{d}s}\right)^2\right] \tag{53}$$

characterizes the probability distribution of the unperturbed molecular conformations. b is the statistical segment length, and the end-to-end distance of the polymers is given by $R_e = b\sqrt{N}$. This sets the length scale of a spatially varying density profile for the pure polymer system. There are two limitations: (i) Chain conformations depend on the thermodynamic parameters (i.e., solvent quality, density, and concentration), but in the SCF calculations the chain extension in a spatially homogeneous system always remains Gaussian with $R_e = b\sqrt{N}$. This approximation also excludes any contribution of conformational entropy on the bulk phase behavior.[1] (ii) Note that we assume the conformational statistics of the polymer to be Gaussian on *all* length scales, i.e., we do not represent the local conformations due to bending and torsional potentials and there are no details of the chemical architecture (e.g., side groups) which would be included into a chemically realistic modeling.

In this important aspect, polymer + solvent mixtures differ qualitatively from binary polymer blends: In the latter class of systems, the Flory-Huggins parameter which parameterizes the segmental interactions is small ($\chi \sim O(1/N)$),[2] the interface width is much larger than the statistical segment length, and a rather universal behavior is observed which depends on only two parameters – the segmental repulsion χ and the coil size R_e. In polymer solutions, however, interactions are strong on the segmental scale ($\chi \sim O(1)$), the width of the liquid-vapor interface is comparable to the statistical segment length, and details of the local structure (molecular architecture and interactions) are important. They cannot be described quantitatively by just a small number of coarse-grained parameters. A quantitatively accurate description is outside the scope of the SCF approach presented here, but we shall mention possible improvements at the end of this section.

[1] The SCFT does describe the variation of chain conformations in the vicinity of spatial inhomogeneities.

[2] For a symmetric polymer blend phase separation occurs already for $\chi > \chi_{\mathrm{crit}} = 2/N \ll 1$

Since the interactions are strictly local, it is not possible to represent the solvent as a structureless point particle. In the following we assume that the size of the solvent particle is comparable to the size of a polymer segment. To deal with solvent and polymer on the same footing, we describe the spatial distribution of the density of a solvent particle by that of a single polymer segment, i.e., we set $N_S = 1$ and $b_S = b$.

Specifying the segmental interaction free energy functional, and the spatial characteristics of the polymer and solvent molecules we have completely defined the model that we employ in our SCF calculations. Even though it involves rather drastic simplifications, it cannot be solved exactly and we shall use a mean-field approximation to proceed. Introducing auxiliary fields W_S, W_P and densities Φ_S, Φ_P we can rewrite the grandcanonical partition function in the form [153, 160, 161]:

$$\mathcal{Z} = \int \mathcal{D}W_S \mathcal{D}W_P \; \mathcal{D}\Phi_S \mathcal{D}\Phi_P \; \exp\left(-\frac{\mathcal{G}[W_S, W_P, \Phi_S, \Phi_P]}{k_B T}\right), \tag{54}$$

with

$$\begin{aligned}\frac{\mathcal{G}[W_S, W_P, \Phi_S, \Phi_P]}{k_B T} = &\frac{\mathcal{E}[\Phi_S, \Phi_P]}{k_B T} \\ &- e^{\mu_S/k_B T} V Q_S[W_S] - e^{\mu_P N/k_B T} V Q_P[W_P] \\ &- \int \mathrm{d}\mathbf{r}\; (W_S \Phi_S + W_P \Phi_P).\end{aligned} \tag{55}$$

$Q_P[W_P]$ is the partition function of the polymer in the external field W_P [162].

$$Q_P[W_P] = \frac{1}{V} \int \mathcal{D}_1 \mathcal{P}_{P1} \; \exp\left(-\int_0^N \mathrm{d}s \; W_P(\mathbf{r}(s))\right), \tag{56}$$

where $\mathcal{D}_1$ sums over all conformations of a single polymer. An analog expression holds for Q_S.

A critical bubble or interface corresponds to a saddle point of the unconstraint grandcanonical free energy functional $\mathcal{G}$, but, unfortunately, the corresponding solution is unstable with respect to small perturbations: If the radius of the nucleus is too large, the bubble will grow indefinitely and the solution will ultimately converge to the stable gas. If the extension of the bubble is too small, it will eventually vanish. Finding the saddle point in the grandcanonical ensemble is a difficult task due to the numerical instabilities associated with the growth or shrinkage of a near-critical bubble. The iterative solution of the SCF equations will first converge towards the metastable critical nucleus, but eventually grow or shrink. Oxtoby and Evans [163] used the convergence properties of the numerical solution to identify the critical bubble.

To circumvent this difficulty we constrain the polymer density at R_0 to equal a predefined value ϕ_P^0 (crossing criterion) via a Lagrange multiplier Ψ:

$$\int \mathrm{d}\mathbf{r}\; \delta(|\mathbf{r}| - R_0)(\phi_P(\mathbf{r}) - \phi_P^0) = 0. \tag{57}$$

Typically, we use the mean of the polymer densities $\phi_P^0 = (\phi_{P\text{coex}}^{(1)} + \phi_{P\text{coex}}^{(2)})/2$ at coexistence. This is a reasonable choice close to coexistence, but fails in the ultimate vicinity of the spinodal, where the density of the spinodal $\phi_P^0 = \phi_{P\text{spin}}$ has to be employed. We emphasize that our results for the nucleation barrier, interface free energy, and the excess of polymer or solvent at a spatial inhomogeneity are independent from the value ϕ_P^0 or the specific way the constraint is imposed [164].

The constraint grandcanonical free energy functional $\tilde{\mathcal{G}}$

$$\frac{\tilde{\mathcal{G}}[W_S, W_P, \Phi_S, \Phi_P, \Psi|R_0]}{k_BT} = \frac{\mathcal{G}[W_S, W_P, \Phi_S, \Phi_P]}{k_BT} - \Psi \int \mathrm{d}\mathbf{r}\, \delta(|\mathbf{r}| - R_0)(\Phi_B(\mathbf{r}) - \phi_P^0) \tag{58}$$

has a saddle point for each value of R_0, and the corresponding solution is numerically stable. Ψ represents an additional external chemical potential which acts on the polymer on the sphere of radius R_0. We adjust Ψ to fulfill the constraint (57) and denote this value by $\psi(R_0)$. In mean-field approximation, we extremize $\tilde{G}$ with respect to its five arguments. These saddle point values are denoted by w_S, w_P, ϕ_S, ϕ_P, and ψ and obey the self–consistent set of equations:

$$\begin{aligned}
\phi_S(\mathbf{r}) &= -e^{\mu_S/k_BT} V \frac{\mathcal{D}Q_S}{\mathcal{D}w_S} \\
\phi_P(\mathbf{r}) &= -e^{\mu_P N/k_BT} V \frac{\mathcal{D}Q_P}{\mathcal{D}w_P} \\
w_S(\mathbf{r}) &= \frac{\mathcal{D}\mathcal{E}}{\mathcal{D}\phi_S} \\
w_P(\mathbf{r}) &= \frac{\mathcal{D}\mathcal{E}}{\mathcal{D}\phi_P} - \psi\delta(|\mathbf{r}| - R_c) \\
\phi_P(|\mathbf{r}| = R_0) &= \phi_P^0 \qquad \text{(constraint Eq. (57))}.
\end{aligned} \tag{59}$$

The first two equations show that the densities are given by the density of a single molecule in an external field (within the grandcanonical ensemble) while the next two equations relate the external fields to the local densities. Inserting the values at the saddle point in Eqs.(55) and (58) we obtain:

$$\begin{aligned}
\frac{\tilde{G}(R_0)}{k_BT} &= \frac{\tilde{\mathcal{G}}[w_S, w_P, \phi_S, \phi_P, \psi|R_0]}{k_BT} \\
&= \int \mathrm{d}\mathbf{r} \left\{ -\frac{v}{k_BT}\left[\frac{1}{2}(\phi_S + \phi_P)^2 - \frac{\tilde{\chi}}{4}(\phi_S - \phi_P)^2 + \frac{\zeta}{2}(\phi_S^2 - \phi_P^2)\right] \right. \\
&\quad - \frac{2w_{SSS}}{3}\phi_S^3 - \frac{w_{SSP}}{3}\phi_S^2\phi_P - \frac{w_{SPP}}{3}\phi_S\phi_P^2 - \frac{2w_{PPP}}{3}\phi_P^3 \\
&\quad \left. -\phi_S - \frac{\phi_P}{N} + \psi\delta(|\mathbf{r}| - R_c)\phi_P \right\}.
\end{aligned} \tag{60}$$

For the spatially homogeneous system $G = -pV$ ($\psi = 0$) and we recover the equation of state (50), of course.

If we fix the chemical potential to a value which corresponds to the coexistence of a polymer-rich and a polymer-poor phase, and consider a planar interface, ψ will vanish by virtue of translational invariance. In spherical geometry, there is a critical radius R_c at which $\psi(R_c) = 0$. Its value depends on the deviation of the chemical potentials from their coexistence values. In both cases, $\psi = 0$, and the value and derivatives of the constraint free energy functional $\tilde{\mathcal{G}}$ with respect to W_S, W_P, ϕ_S, ϕ_P coincide with those of the original free energy functional $\mathcal{G}$. Consequentially, a saddle point of $\tilde{\mathcal{G}}$ is simultaneously a saddle point of $\mathcal{G}$, i.e., the condition $\psi = 0$ characterizes a planar interface or a critical nucleus. This condition is equivalent to

$$\frac{\mathrm{d}\tilde{G}(R_0)}{\mathrm{d}R_0} = -4\pi R_0^2 \psi \left.\frac{\mathrm{d}\phi_P}{\mathrm{d}r}\right|_{R_0} \stackrel{!}{=} 0 \qquad \Longleftrightarrow \qquad \psi \stackrel{!}{=} 0 \tag{61}$$

but easier to implement numerically.[3] The structure and free energy of the interface or critical bubble is independent from the way the constraint is enforced (e.g., whether the excess of the stable phase (integral criterion) or the density at a certain radius (crossing criterion) is fixed). This is no longer valid for sub-critical or supercritical bubbles ($\psi \neq 0$), where the profiles as well as the free energy depends on how one prevents the bubble to shrink or grow. This limits the application of the constraint grandcanonical ensemble to near-critical bubbles.

To calculate the segment densities it is useful to introduce the end segment distribution

$$q_P(\mathbf{r}, t) = \int_0^t \mathcal{D}[\mathbf{r}]\delta(\mathbf{r} - \mathbf{r}(t)) \exp\left[-\frac{3}{2b^2}\int_{s=0}^t \mathrm{d}s \left(\frac{\mathrm{d}\mathbf{r}}{\mathrm{d}s}\right)^2 - \int_{s=0}^t \mathrm{d}s\; w_P(\mathbf{r}(s))\right]. \tag{62}$$

It obeys the modified diffusion equation:

$$\frac{\partial q_P(\mathbf{r}, t)}{\partial t} = \frac{b^2}{6}\Delta q_P(\mathbf{r}, t) - w_P q_P(\mathbf{r}, t) \qquad \text{with} \qquad q_P(\mathbf{r}, 0) = 1. \tag{63}$$

Then, we can calculate the segment density ϕ_P and the single chain partition function Q_P[153, 160, 161, 162]:

$$\begin{aligned}
\phi_P(\mathbf{r}) &= e^{\mu_P N/k_B T} \int_0^N \mathrm{d}s\; q_P(\mathbf{r}, s) q_P(\mathbf{r}, N - s) \\
Q_P &= \frac{1}{V}\int \mathrm{d}\mathbf{r}\; q_P(\mathbf{r}, s) q_P(\mathbf{r}, N - s) \qquad \forall s \\
&= \frac{1}{V}\int \mathrm{d}\mathbf{r}\; q_P(\mathbf{r}, N) = \frac{e^{\mu_P N/k_B T}}{NV}\int \mathrm{d}\mathbf{r}\; \phi_P(\mathbf{r}).
\end{aligned} \tag{64}$$

In order to calculate the properties of a spherical bubble, we consider a spherical shell of size $R - D \leq |\mathbf{r}| \leq R + D$. The width D is chosen large enough for the

[3] We do not solve the whole set of equations for different values of R_0 but rather add one equation to the set of $2M + 1$.

profiles to reach their limiting values at the boundaries. Following Matsen [161], we expand all spatial dependencies normal to the interface in a cos–series with M terms. For example, the monomer density takes the form $\phi_P(r) = \sum_{i=1}^{M} \phi_{Pi} f_i(r)$ with

$$f_i(r) = \mathcal{N}_i \cos\left(\frac{(i-1)\pi(r-R+D)}{2D}\right), \tag{65}$$

and normalization factors $\mathcal{N}_1 = 1$ and $\mathcal{N}_i = \sqrt{2}$ for $i \geq 2$. Up to $M = 128$ basis functions have been employed in our calculations. Using this set of basis functions the diffusion equation in spherical coordinates

$$\frac{\partial q_P(r,t)}{\partial t} = \frac{b^2}{6}\left(\frac{\partial^2}{\partial r^2} + \frac{2}{r}\frac{\partial}{\partial r}\right) q_P(r,t) - w_P(r) q_P(r,t) \tag{66}$$

transforms into a matrix equation [161]:

$$\frac{\partial q_{Pi}(t)}{\partial t} = \mathcal{A}_{ik} q_{Pk}(t) \qquad \text{with} \tag{67}$$

$$\mathcal{A}_{ik} = -\frac{b^2\pi^2(k-1)^2}{24D^2}\delta_{i,k} + \frac{2(k-1)\pi b^2}{12DR}\sum_j \Gamma'_{ikj}\mathcal{R}_j^{-1} - \sum_j \Gamma_{ikj} w_{Pj}$$

$$\mathcal{R}_j^m = \frac{1}{2D}\int_{-D}^{D} \mathrm{d}r \ \left(\frac{r}{R}\right)^m f_j$$

$$\Gamma_{ikj} = \frac{1}{2D}\int_{-D}^{D} \mathrm{d}r \ f_i f_k f_j$$

$$= \frac{\mathcal{N}_i\mathcal{N}_j\mathcal{N}_k}{4}\left(\delta_{i+j+k,3} + \delta_{i+j-k,1} + \delta_{i-j+k,1} + \delta_{i-j-k,-1}\right)$$

$$\Gamma'_{ikj} = \frac{1}{2D}\int_{-D}^{D} \mathrm{d}r \ f_i \ \mathcal{N}_k \sin\left(\frac{(k-1)\pi(r+D)}{2D}\right) f_j$$

$$= \begin{cases} \frac{\mathcal{N}_i\mathcal{N}_j\mathcal{N}_k}{2\pi}\left(\frac{1}{i+k+j-3} + \frac{1}{i+k-j-1} - \frac{1}{i-k+j-1} - \frac{1}{i-k-j+1}\right) \\ \qquad \text{if } i+j+k \text{ even} \\ 0 \\ \qquad \text{if } i+j+k \text{ odd} \end{cases}$$

In planar symmetry the matrix $\mathcal{A}_{ij}$ is symmetric and real, i.e., it possesses real eigenvalues. In spherical geometry $\mathcal{A}_{ij}$ is not normal, but it can still be decomposed into

$$\mathcal{A}_{ij} = \sum_k O_{ik}\lambda_k O_{kj}^{-1} \tag{68}$$

Eigenvalues $\{\lambda_k\}$ are obtained via a HQR–algorithm [165] and (right) eigenvectors are found via inverse iteration using the eigenvectors of the planar problem as starting values. As $\mathcal{A}_{ij}$ is a real matrix the eigenvalues $\{\lambda_k\}$ are real or they occur in pairs, which are complex conjugated. This decomposition enables us to rewrite Eq. (64) into:

$$q_{Pi}(t) = \sum_k O_{ik} \exp(\lambda_k t) O^{-1}_{k1} \qquad \text{and}$$

$$\phi_{Pi} = e^{\mu_P N/k_B T} \sum_{jk} \Gamma_{ijk} \int_0^N \mathrm{d}t \; q_{Pj}(t) q_{Pk}(N-t). \tag{69}$$

Similarly, we proceed for the solvent component.

Given the fields w_{Si} and w_{Pi}, we calculate the densities $\phi_{Si}[\{w_{Si}\}]$ and $\phi_{Pi}[\{w_{Pi}\}]$ according to the procedure outlined above. Then, we adjust the $2M$ fields, w_{Si} and w_{Pi}, and the two parameters R_c and Ψ via a Newton–Broydon scheme as to fulfill the remaining $2M + 2$ self–consistent equations:

$$\begin{aligned}
w_{Si} &= \frac{v}{k_B T}\left((\phi_{Si} + \phi_{Pi}) - \frac{\tilde{\chi}}{2}(\phi_{Si} - \phi_{Pi}) + \zeta\phi_{Si}\right) \\
&\quad + \sum_{jk} \Gamma_{ijk}\left(w_{SSS}\phi_{Sj}\phi_{Sk} + 2w_{SSP}\phi_{Sj}\phi_{Pk} + w_{SPP}\phi_{Pj}\phi_{Pk}\right) \\
w_{Pi} &= \frac{v}{k_B T}\left((\phi_{Si} + \phi_{Pi}) + \frac{\tilde{\chi}}{2}(\phi_{Si} - \phi_{Pi}) - \zeta\phi_{Pi}\right) \\
&\quad + \sum_{jk} \Gamma_{ijk}\left(w_{PPP}\phi_{Pj}\phi_{Pk} + w_{SSP}\phi_{Sj}\phi_{Pk} + 2w_{SPP}\phi_{Sj}\phi_{Pk}\right) - \frac{1}{2}\psi c_i \\
c_1\phi_P^0 &= \sum_i c_i \phi_{Pi} \qquad \text{with} \qquad c_i = \frac{1}{D} f_i(R_c) \\
\psi &= 0.
\end{aligned} \tag{70}$$

This computational scheme allows us to calculate both the free energy and the profiles of interfaces and critical bubbles in compressible polymer mixtures within mean-field approximation.

Although, this SCF theory goes clearly beyond the Flory-Huggins theory, we expect it only to capture the qualitative behavior correctly due to (i) a coarse description of the local structure and (ii) the mean-field approximation.

In principle, it is straightforward to incorporate a better description of the local structure which is required to model a specific chemical substance: Instead of using the Gaussian chain model, one can calculate the density of a single chain in an external field by brute force enumeration techniques [99, 154, 155, 166, 167, 168, 169] over a large representative sample of molecular conformations. These configurations can be generated from the Rotational-Isomeric-State [1, 170] model or extracted from detailed, atomistic modeling. On parallel computers one can use 10^7 chain conformation without excessive computational effort. Likewise, one could use a weighted density functional instead of the local one to incorporate information about packing effects and the range of repulsive and attractive interactions. Another important challenge is to include a realistic description of the equation of state. To calculate interface properties, our calculations require input also for a hypothetical homogeneous state at densities at which the system phase separates. This information cannot be obtained from experiments, and one has to rely either on an *ad-hoc*

extrapolation from the accessible one-phase region into the miscibility gap or has to resort to a systematic, microscopic derivation of the equation of state. A powerful method to achieve this goal – thermodynamic perturbation theory (TPT) – will be discussed in the following Sect. 4. Incorporating the dependence of the chain conformations in the bulk on the thermodynamic state is more difficult. From the various methods [171, 172, 173], to date none has been applied to spatially inhomogeneous systems. Computer simulations, however, indicate that the effects might be quite pronounced for super-critical solvents [112, 150].

The second caveat – the mean-field approximation – is also difficult to remedy (see article *Incorporating fluctuations and dynamics into SCF calculations for polymer blends* in this same volume). The mean-field treatment neglects fluctuations around the most probable configuration. Thus, composition fluctuations or fluctuations of the shape of interfaces or bubbles (i.e., capillary waves) are not considered. We expect those fluctuations to be important when their energy is comparable to thermal fluctuations (e.g., in the vicinity of spinodals or critical points) or when structures (droplets or bubbles) become so small that their excess free energy is comparable to the thermal energy scale $k_B T$. In principle, computer simulations are well suited to evaluate the role of fluctuations and we shall discuss them in Sects. 4 and 5. In the following application of the SCF theory to polymer + solvent systems, we shall mention fluctuation effects where we expect them to change the qualitative behavior.

3.3 Modeling a Type III-phase Diagram of a Polymer + Solvent System

The grandcanonical free energy density of the homogeneous system gives the equation of state. For a spatially homogenous system the saddle point equations become particularly simple. Using

$$Q_{P\mathrm{hom}} = \mathcal{Z}_{\mathrm{conf}} \exp(-N w_P), \tag{71}$$

where $\mathcal{Z}_{\mathrm{conf}} = (1/V) \int \mathcal{D}_1 \mathcal{P}_{P1}$ denotes the number of conformations of a single molecule, we obtain for the chemical potential per segment:

$$\begin{aligned} \frac{\mu_P}{k_B T} &= -\frac{1}{N} \ln \mathcal{Z}_{\mathrm{conf}} + \frac{1}{N} \ln \frac{\phi_P}{N} + w_P \\ &= -\frac{1}{N} \ln \mathcal{Z}_{\mathrm{conf}} + \frac{1}{N} \ln \frac{\phi_P}{N} + \frac{v}{k_B T} \left[(\phi_S + \phi_P) + \frac{\tilde{\chi}}{2} (\phi_S - \phi_P) - \zeta \phi_P \right] \\ &\quad + w_{PPP} \phi_P^2 + w_{SSP} \phi_S^2 + 2 w_{SPP} \phi_S \phi_P \end{aligned} \tag{72}$$

and a similar expression for the solvent. Using the chemical potentials and the equation of state, we can calculate the canonical free energy density f as a function of its natural variables:

$$f \equiv \frac{F_{\rm hom}(\phi_S,\phi_P)}{Vk_BT} = -\frac{p}{k_BT} + \frac{\mu_S\phi_S + \mu_P\phi_P}{k_BT}$$
$$= \phi_S \ln\frac{\phi_S}{e} + \frac{\phi_P}{N}\ln\frac{\phi_P}{Ne\mathcal{Z}_{\rm conf}}$$
$$+\frac{v}{k_BT}\left[\frac{1}{2}(\phi_S+\phi_P)^2 - \frac{\tilde{\chi}}{4}(\phi_S-\phi_P)^2 + \frac{\zeta}{2}(\phi_S^2-\phi_P^2)\right]$$
$$+\frac{w_{SSS}}{3}\phi_S^3 + w_{SSP}\phi_S^2\phi_P + w_{SPP}\phi_S\phi_P^2 + \frac{w_{PPP}}{3}\phi_P^3. \quad (73)$$

This expression is similar to Eq. (2), but generalizes the result to two independent densities.

Two phases – $(\phi_S^{(1)},\phi_P^{(1)})$ and $(\phi_S^{(2)},\phi_P^{(2)})$ – coexist, if they have identical pressure (i.e., Gibbs free energy) at the same value of the chemical potentials. If we fix the temperature, there is a coexistence curve $\mu_{S\rm coex}(\mu_P)$ implicitly given by:

$$p\left[\phi_S^{(1)}(\mu_{S\rm coex},\mu_P),\phi_P^{(1)}(\mu_{S\rm coex},\mu_P)\right]$$
$$= p\left[\phi_S^{(2)}(\mu_{S\rm coex},\mu_P),\phi_P^{(2)}(\mu_{S\rm coex},\mu_P)\right]. \quad (74)$$

The spinodals mark the limit of stability of a homogeneous state. They are found by requiring that the determinant for the second derivatives of the canonical free energy density f with respect to the densities (i.e., the stability matrix) vanishes:

$$\frac{\partial\mu_S}{\partial\phi_S}\frac{\partial\mu_P}{\partial\phi_P} = \frac{\partial\mu_P}{\partial\phi_S}\frac{\partial\mu_S}{\partial\phi_P}. \quad (75)$$

At the spinodal one eigenvalue of the stability matrix is zero and the corresponding eigenvalue defines an unstable linear combination c of densities. Using the derivatives of the free energy at the spinodal

$$\alpha = \sqrt{\frac{\partial\mu_P}{\partial\phi_P}}\bigg|_{\rm spin} \qquad \text{and} \qquad \beta = -\sqrt{\frac{\partial\mu_S}{\partial\phi_S}}\bigg|_{\rm spin} \quad (76)$$

we calculate the unstable linear combination c and its orthogonal $\bar{c}$:

$$c = \frac{\alpha\phi_S + \beta\phi_P}{\alpha^2+\beta^2} \qquad \text{and} \qquad \bar{c} = \frac{\beta\phi_S - \alpha\phi_P}{\alpha^2+\beta^2}. \quad (77)$$

The second derivative of the canonical free energy density f with respect to c vanishes at the spinodal. If additionally the third derivative becomes zero, there is a critical point. Expressed in terms of ϕ_S and ϕ_P this condition takes the form:

$$\sqrt{\frac{\partial\mu_P}{\partial\phi_P}}\left[\frac{\partial\mu_P}{\partial\phi_P}\frac{\partial^2\mu_S}{\partial\phi_S^2} + 3\frac{\partial\mu_S}{\partial\phi_S}\frac{\partial^2\mu_P}{\partial\phi_S\partial\phi_P}\right] =$$
$$\sqrt{\frac{\partial\mu_S}{\partial\phi_S}}\left[\frac{\partial\mu_S}{\partial\phi_S}\frac{\partial^2\mu_P}{\partial\phi_P^2} + 3\frac{\partial\mu_P}{\partial\phi_P}\frac{\partial^2\mu_S}{\partial\phi_S\partial\phi_P}\right]. \quad (78)$$

For the pure solvent the equation of state yields the critical points:

$$\phi_{S\mathrm{crit}} = \frac{1}{\sqrt{2w_{SSS}}} \qquad \text{and} \qquad \frac{|\upsilon(1-\tilde{\chi}/2+\zeta)|}{k_B T_{S\mathrm{crit}}} = 2\sqrt{2w_{SSS}}. \tag{79}$$

$w_{SSS}^{1/6}$ and $\upsilon/\sqrt{w_{SSS}}$ set the units of length and energy.

In the following, we choose our parameters to resemble our coarse-grained model for a mixture of carbon dioxide and hexadecane. Accordingly, we use $N = 5$ for our numerical calculations. In the coarse-grained model segments of the polymer interact via a Lennard-Jones potential which is characterized by a length scale σ and an energy scale ϵ. In our SCF calculations, we will also use these Lennard-Jones units in the following. In analogy to the identification of the Lennard-Jones parameters we determine the parameters of the pure components to reproduce the critical densities and temperatures obtained from experiment. This procedure is somewhat inconsistent, because we match the calculations to the experimental data just at the point where mean-field theory is at its worse. For small molecules, which interact only with a few neighbors, we expect the mean-field treatment to overestimate the critical temperature. We shall quantify this point in Sect. 4 where we compare the results of TPT and MC simulations. Here we caution the reader that such an identification imparts a significant uncertainty onto the parameters of the SCF calculations. A fact that again limits the SCF calculations to qualitative predictions only. Of course, other schemes of determining the parameters of our phenomenological equation of state could be envisaged: For instance, if we were interested in a specific temperature, we might choose the coefficients as to reproduce the density and compressibility of the polymer liquid at the liquid—vapor coexistence of the pure fluid [99].

Identifying $w_{SSS} = 1.451\sigma^6 = 1.2 \cdot 10^{-56} m^6$, we match the critical density of CO_2, $\phi_{S\mathrm{crit}} = 6.4 \cdot 10^{27}\ \mathrm{m}^{-3}$. Choosing $\upsilon = -2.24924\epsilon\sigma^3 = -1.2 \cdot 10^{-48}\ \mathrm{Jm}^3$, and $1 - \tilde{\chi}/2 + \zeta = 1.1$ (cf. below) we reproduce the critical temperature of pure CO_2, $T_{S\mathrm{crit}} = 304$ K.

To specify all length scales, we furthermore set the statistical segment lengths to $b = b_S = \sigma$. This is consistent with a fully flexible chain model, but in the simulation model we find $b \approx 1.22\sigma$ [99] due to the restriction of bond angles by excluded volume. Our choice does not affect the bulk phase behavior, it does, however, influence the properties of spatially inhomogeneous systems, i.e., interfacial tension and profiles or nucleation barriers. We do not attempt to tune those parameters as to reproduce the temperature-dependent conformational statistics of hexadecane.

The ratio of the critical temperatures and densities of the pure solvent and the polymer determines the second and third order coefficient of the polymer

$$\frac{w_{PPP}}{w_{SSS}} = \frac{1}{N}\left(\frac{\phi_{S\mathrm{crit}}}{\phi_{P\mathrm{crit}}}\right)^2 \qquad \text{and} \qquad \frac{1-\tilde{\chi}/2-\zeta}{1-\tilde{\chi}/2+\zeta} = \sqrt{\frac{w_{PPP}}{N w_{SSS}}}\left(\frac{T_{P\mathrm{crit}}}{T_{S\mathrm{crit}}}\right). \tag{80}$$

Of course, being a mean-field theory, our SCF calculations reduce to the Flory-Huggins prediction $\phi_{P\mathrm{crit}} \sim 1/\sqrt{N}$ for the pure polymer. Using $\phi_{S\mathrm{crit}}/\phi_{P\mathrm{crit}} = 2.17$,

we obtain $w_{PPP} = 1.37157\sigma^6$. The second equation and the experimental ratio $T_{S\text{crit}}/T_{P\text{crit}} = 0.42$ result in the relation $\zeta = -0.017(1 - \tilde{\chi}/2)$. Note that the third order virial expansion fixes the ratio between the critical pressure and the ideal gas value to $p_{\text{crit}}/k_B T\phi_{\text{crit}} = 1/3N$. For carbon dioxide and hexadecane one experimentally obtains 0.277 and 0.048, respectively, i.e., the critical pressure is overestimated by 39% for the polymer. As we shall see in Sect. 4, this is a quite generic feature of a mean-field equation of state.

To reduce the number of variables further we assume that the third order coefficients obey a simple mixing rule:

$$w_{SSP} = (w_{SSS}^2 w_{PPP})^{1/3} \qquad \text{and} \qquad w_{SPP} = (w_{SSS} w_{PPP}^2)^{1/3}. \tag{81}$$

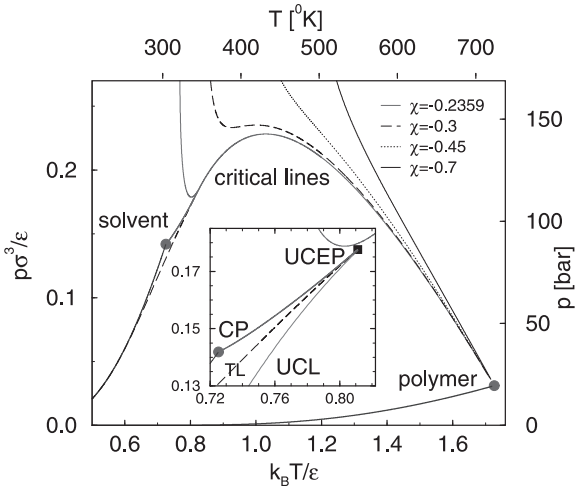

Fig. 7. Coexistence lines of the pure components and critical lines as a function of temperature and pressure. Critical lines, which emerge from the critical point of the pure polymer are shown for different values of $\tilde{\chi}$ as indicated in the key. The *solid line*, which emerges from the critical point of the solvent, and the *dashed line* denote the critical line and the triple line for $\tilde{\chi} = -0.2359$. The *inset* presents an enlarged view of the vicinity of the critical point (CP) of the volatile solvent at $\tilde{\chi} = -0.2359$. The critical line, which emerges from the critical point of the solvent ends in an upper critical end point (UCEP). At the UCEP it joins the triple line (TL) and *not* the critical line which starts at the critical point of the pure polymer. The (hidden) continuation of the liquid—liquid critical points which form an unstable critical line (UCL) is also shown. Adapted from [164]

This leaves us with a single parameter $\tilde{\chi}$ with which we describe deviations from the Berthelot mixing rule:

$$\xi \equiv \frac{|v_{AB}|}{\sqrt{|v_{AA} v_{BB}|}} = \frac{2 + \tilde{\chi}}{\sqrt{(2 - \tilde{\chi})^2 - 4\zeta^2}}, \tag{82}$$

where $v_{SS} = v(1 - \tilde{\chi}/2 + \zeta)$ and $v_{AB} = v(2 + \tilde{\chi})$ and $v_{PP} = v(1 - \tilde{\chi}/2 - \zeta)$ denote the strength of binary interactions. For $\tilde{\chi} = -\zeta^2/2$ the Berthelot mixing rule, $\xi = 1$, is fulfilled, and this corresponds to $\tilde{\chi} = -0.00015$. In this case, the phase diagram is of type I, i.e., there is a line of critical points that joins the critical points of the pure solvent and the pure polymer. The experimental phase diagram of hexadecane and carbon dioxide belongs to type III (down to tridecane) while one finds phase diagrams of type I or type II for shorter alkanes [6, 23]. To reproduce this experimental observation, we reduce the attraction between polymer and solvent by decreasing $\tilde{\chi}$. The dependence of the phase behavior on this parameter is illustrated in Fig. 7. For small negative values $\tilde{\chi}$, we always find phase diagrams of type I. For large negative values of $\tilde{\chi}$ the phase diagram is of type III, i.e., the critical line which emerges from the critical point of the pure polymer P rapidly moves to higher pressure upon decreasing temperature and does not reach the critical point of the solvent S. At intermediate (negative) values of $\tilde{\chi}$ the critical line develops an s–shape. The value $\tilde{\chi} = -0.2359$ or $\xi = 0.789$ corresponds to a phase diagram of type III, but a minuscule increase would change the type of phase diagram, and we choose this value for the following calculations. The parameters of our equation of state are compiled in Table 2. The phase behavior in the vicinity of the critical point of the solvent is presented in the inset of Fig. 7 for that value of $\tilde{\chi}$. The critical line which emerges from the critical point of the solvent ends in an upper critical end point (UCEP). There it connects to a triple line, on which a polymer–rich phase coexists with a solvent–rich vapor and a solvent–rich liquid.

Table 2. Critical pressure of the pure components and parameters of the equation of state, Eq. (50). The critical densities and temperatures agree by construction with the Lennard-Jones data in Table 1

component	w_{iii}/σ^6	N	b/σ
S: CO_2	1.451	1	1
P: $C_{16}H_{34}$	1.37157	5	1
$v = -2.24924\epsilon\sigma^3$			
$\chi = -0.2359$			
$\zeta = -0.0193562$			

The temperature dependence of the phase behavior is shown in Fig. 8(**a**), where we present the binodals at a fixed temperature as a function of pressure and molar fraction of the solvent, $x = \phi_S/(\phi_S + \phi_P/N)$. At low pressure we find a coexistence between an almost pure polymer–rich phase and a low density solvent–vapor. Upon increasing pressure, we can load the polymer–rich phase with solvent and the molar fraction x of the polymer–rich phase increases. At high temperatures, this phase coexistence ends in a critical point. At low temperatures, we encounter a triple point, where a polymer–rich phase coexists with an almost pure solvent–vapor and

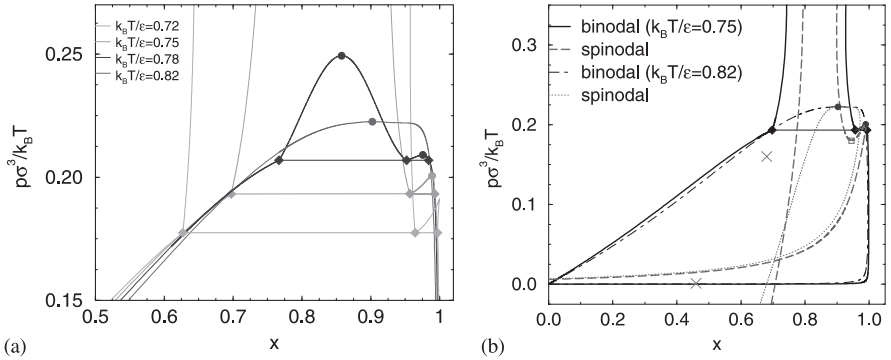

Fig. 8. (**a**) Phase diagram as a function of pressure p and molar fraction x for various temperatures T as indicated in the key. Triple points are marked by *horizontal lines* and *diamonds*, critical points are marked by *circles*. $k_BT/\epsilon = 0.72$ is below the critical temperature of the solvent. (**b**) Phase diagram as a function of pressure and molar fraction for $k_BT/\epsilon = 0.75$ (*thick lines*) and $k_BT/\epsilon = 0.82$ (*thin lines*). Binodals are represented as *solid lines*, spinodals are drawn with *dashed lines*. The triple point for $k_BT/\epsilon = 0.75$ is marked by a *horizontal line* and *diamonds*. Critical points are marked by *circles*. *Crosses* mark the location at which we study the temperature variation in Fig.18. The *open square* marks the unstable liquid-liquid critical point for $k_BT/\epsilon = 0.75$. From [164]

a solvent–rich liquid. Above the pressure p_{triple} of the triple point, the polymer–rich phase coexists with a solvent–rich liquid.

Binodals and spinodals for temperatures $k_BT/\epsilon = 0.75$ and $k_BT/\epsilon = 0.82$ are shown in Fig. 8(**b**). As we increase the pressure above the triple line for $k_BT/\epsilon = 0.75$, the miscibility gap first narrows but then widens again for $p\sigma^3/k_BT > 0.325$, because the segregation between polymer–rich and solvent–rich liquid increases as we increase the pressure/density. This behavior is an artifact of our simple equation of state, because in the experiment on CO_2 and hexadecane one observes that the liquid—liquid phase coexistence terminates in a critical point at high pressure (about $p_{\text{crit}} = 165$ bar at $T = 40°\text{C}$) [148]. At such large densities the simple representation via a third order polynomial in the densities cannot be expected to be reliable anymore. The spinodal of the solvent–rich phase touches the binodal at the critical point of the solvent–vapor and the polymer–rich liquid, but always remains at positive pressure. The spinodal of the polymer–rich phase depends for positive pressure only weakly on the molar fraction; notably the spinodal stays in the regime $x > 0.6$ for all positive pressures. The spinodal extends, however, further to negative pressures and for large negative pressures (not shown in the figure) it also tends towards $x = 0$. Unlike the solvent–rich phase, the polymer–rich phase can support negative pressure as a metastable state. The bubble formation or cavitation of a liquid under tensile stress ($p < 0$) can be realized experimentally. Of course, there is no such analog of a metastable state for a temperature quench.

Comparing $k_BT/\epsilon = 0.82$ with $k_BT/\epsilon = 0.75$ we find that the binodals below $p < p_{\text{triple}}(k_BT/\epsilon = 0.75)$ depend only very little on temperature, but spinodals

exhibit a much stronger variation with temperature. The distance between binodal and spinodal increases upon increasing temperature at high pressure, but the regime where we expect nucleation to occur narrows with increasing temperature at low pressure.

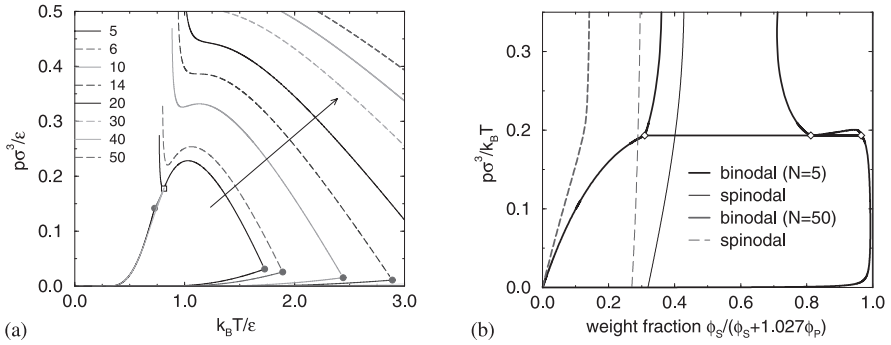

Fig. 9. Dependence of the phase diagram on chain length N of the polymer. (**a**) coexistence line of the pure components and critical lines which emerge from the critical point of the pure polymer. The critical line which begins at the solvent critical point and the triple line is only shown for $N = 5$. The values of N are given in the key, and the *arrow* indicates an increase in chain length. (**b**) Binodals and spinodals for chain length $N = 5$ and $N = 50$ as a function of pressure and mass fraction of solvent at $k_B T/\epsilon = 0.75$

The chain length N of the polymer enters the calculation of the bulk phase behavior only via the (trivial) reduction of the translational entropy due to the bonding of the segments to chains; a non-trivial dependence of the virial coefficients on the chain length is absent. Therefore, we can extend our calculations to long chain lengths. In Fig. 9(**a**) we show the phase behavior in the pressure-temperature plane. In accord with experiments [23], increasing chain length has a qualitatively similar effect as decreasing $\tilde{\chi}$, i.e., the polymer and the solvent become more unlike. This behavior agrees qualitatively with TPT (cf. Sect. 4.5) and experiments [23].

The binodal and spinodals as a function of the solvent weight fraction are presented in panel (**a**) of Fig. 9, where we have used the ratio of the molar masses of hexadecane and carbon dioxide. This representation is more convenient for large molecular masses, because the molar faction x of the coexisting phases is very close to unity. For long polymers and pressures far below the triple pressure, the polymer–rich phase at saturation contains only a few weight-percent of the super-critical solvent, and this amount decreases upon increasing molecular mass. Moreover, both binodals and spinodals depend only on mass fraction, but become fairly independent from pressure for large N.

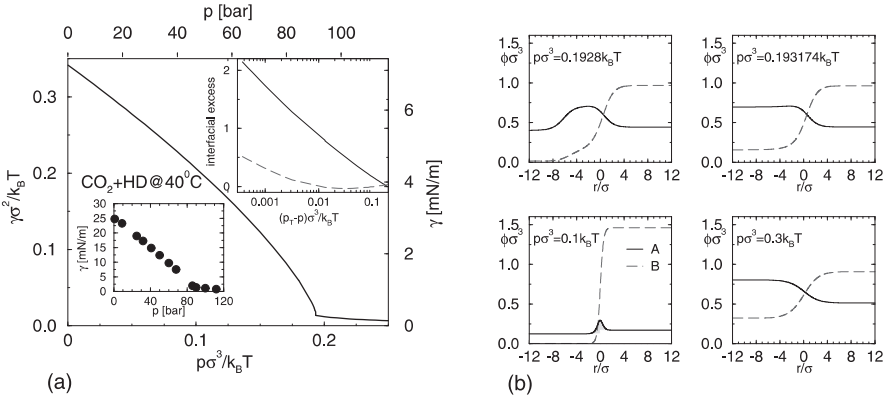

Fig. 10. (**a**) Interfacial tension between polymer–rich phase and solvent–rich phase as a function of pressure p at temperature $k_BT/\epsilon = 0.75$ which corresponds to $T = 314K$. For $p < p_{\text{triple}} = 0.193174 k_BT/\sigma^3$ the polymer–rich phase coexists with a solvent–vapor, while beyond the triple pressure it coexists with a solvent–rich liquid. The jump of the interfacial tension at the triple point is hardly visible on the scale of the figure. The *insets* show the logarithmic divergence of the interfacial excess as one approaches the triple pressure from below and the experimental values of the interfacial tension at $T = 40^o$C$= 313.15$K. (**b**) Density profiles between coexisting phases at various pressures as indicated in the keys. From [164]

3.4 Profiles Across Interfaces

In this paragraph we focus on the properties of interfaces between coexisting phases, i.e., planar interfaces between macroscopic domains. Let $\mathcal{A}$ denote the area of the (planar) interface, so we calculate the free energy that an interface costs per unit area, the interfacial tension γ, via:

$$\gamma = \frac{G + p^{\text{coex}} V}{\mathcal{A}}. \tag{83}$$

The results of our calculations at temperature $kT/\epsilon = 0.75$ are displayed in Fig. 10 (**a**). Upon increasing pressure the interfacial tension decreases. At the triple pressure $p_{\text{triple}}\sigma^3/k_BT = 0.193174$ there is a small jump, because for lower pressure we consider the interface between the polymer–rich phase and the solvent–vapor, while for higher pressure the polymer–rich phase coexists with a solvent–rich liquid. Upon increasing pressure further, the interfacial tension decreases, passes through a minimum, and then increases again at high pressure as the miscibility gap becomes wider again (not shown in the figure). Comparing our results to experimental data (cf. left inset in panel (**a**)), we note that we underestimate the interfacial tension by about a factor of 3.5. Unfortunately, MC simulations cannot access this part of the parameter space, but the simulation data shown in Fig. 5 for the pure polymer can be extrapolated towards lower temperatures and match the experimental data at around $T = 450$ K. Therefore we conclude that these deviations of the SCF calculations are

not related to the coarse-grained representation as such, but due to the additional assumptions in the SCF model: (i) the simple equation of state, (ii) the approximation of a fully flexible chain model $b = \sigma$, and (iii) the local character of the interaction free energy functional. Indeed, a comparison of MC results for the bead-spring model with chain length $N = 10$ and SCF calculations suggests, that a non-local density functional is crucial for obtaining quantitative accurate predictions. Nevertheless, the qualitative behavior – strong reduction of the interfacial tension upon approaching the triple point – agrees with the experimental findings.

The density profiles across the interface are depicted in Fig. 10(**b**). At low pressure the coexisting phases differ in the density of polymers. The density of the volatile solvent is almost equal in both phases, and very low. At the center of the interface there is a small excess of solvent. Upon increasing pressure, the density of solvent increases both in the vapor and in the liquid. The density of the polymer in the liquid decreases in turn. The interfacial excess of solvent increases and the profile becomes asymmetric; most of the excess is found on the vapor side of the interface. The interfacial excess per unit area can be defined by

$$\Omega_S^{\rm int} \equiv \frac{1}{\mathcal{A}} \left(\int {\rm d}\mathbf{r}\, \phi_S(\mathbf{r}) - \phi_{S{\rm coex}}^{(1)} V_1 - \phi_{S{\rm coex}}^{(2)} V_2 \right), \tag{84}$$

where V_1 and V_2 are the volumes associated with the two phases. Obviously, Ω_S depends on the choice of the interface position and we have defined the position as the point where the density of the polymer equals the mean of the densities at coexistence. Upon approaching the triple line from low pressure, a layer of liquid solvent forms at the interface and the interfacial excess of solvent diverges (cf. Fig. 10(**a**) inset). This indicates that the solvent in its liquid state wets the interface between solvent–vapor and polymer–rich liquid. The interfacial excess increases logarithmically as the triple pressure is approached. This logarithmic increase of the wetting layer of liquid solvent is a consequence of the short–ranged interactions in our model [174]. With (more realistic) van der Waals interactions between molecules, i.e., intermolecular potentials that exhibit a power law tail proportional to r^{-6} at large distances, one expects an increase of the interfacial excess as $t^{-1/3}$ when the distance t to the triple point goes to zero. Note also that throughout our mean-field calculations of interface profiles we disregard capillary wave broadening (cf. Ref. [100, 147]).

3.5 Bubble Nucleation

Having calculated the binodals and spinodals in the bulk and properties of planar interfaces, we now turn to the quasi-equilibrium properties of bubbles, which form upon reducing the pressure in the polymer–rich phase. Quasi–equilibrium means that the bubble is in chemical and mechanical equilibrium with its surrounding, the mother phase. The mother phase itself corresponds to a metastable state inside the miscibility gap between the binodal and the spinodal. Such a critical bubble extremizes the free energy among all configurations. In the simulations (cf. Sect. 5) such

bubbles are observable in finite volumes when densities are fixed (canonical ensemble). In the SCF calculations, we use the grandcanonical ensemble and observe only critical bubbles.

In principle, the transition from the metastable, super-saturated liquid to the thermodynamically stable vapor phase is a non–equilibrium phenomenon and a kinetic theory or computer simulations are well suited to tackle the problem [175]. This holds *a fortiori* if there is a large disparity in the dynamical behavior between the components. One species might be very mobile (e.g., the super-critical solvent) while the other might be rather viscous (e.g., a polymer near its glass transition). These effects are expected to be particularly pronounced in the late stages of phase separation where viscoelastic effects [176, 177, 178] become important. If the kinetics is sufficiently slow, however, one can hope to describe the early stages of phase separation via the evolution of an isolated bubble and use the amount of the stable vapor phase as a reaction coordinate. The critical bubble corresponds to a saddle point of the free energy along the reaction path. This concept forms the basis of many versions of nucleation theory and we shall adopt it in the following as well.

The surrounding of the bubble, the mother phase, is characterized by its pressure $p = p_{\text{out}}$ and molar fraction x. Since bubble (inner phase) and mother phase (outer phase) can exchange particles, the grandcanonical ensemble is appropriate and we employ chemical potentials $\mu_S(p, x)$ and $\mu_P(p, x)$ as to reproduce the pressure and composition of the mother phase. We use the total excess of polymer with respect to the mother phase

$$\Delta_B^{\text{nuc}} \equiv \int \mathrm{d}\mathbf{r} \ (\phi_P(\mathbf{r}) - \phi_{P\text{out}}) \tag{85}$$

to define the radius of the bubble as

$$R_{\text{nuc}} \equiv \left(\frac{3\Delta_{P\text{nuc}}}{4\pi(\phi_{P\text{in}} - \phi_{P\text{out}})} \right)^{1/3}, \tag{86}$$

where $\phi_{P\text{in}}$ and $\phi_{P\text{out}}$ denote the polymer segment densities at the center of the bubble and in the mother phase, respectively. This definition is independent from the constraint we impose to stabilize a bubble of a given size. The critical bubble does neither grow nor shrink (i.e., $\psi = 0$) and its free energy of formation is given by:

$$\Delta G^\star \equiv G(R_c) + p_{\text{out}} V. \tag{87}$$

In Fig. 11 (**a**) we present the phase diagram at temperature $k_B T/\epsilon = 0.75$ as a function of molar fraction and pressure. Binodal, spinodal, and three lines of constant nucleation free energy are shown. At the binodal the nucleation barrier diverges. As we increase the molar fraction and move away from the binodal at constant pressure the nucleation barrier decreases, and at the spinodal it vanishes.

If the nucleation free energy is of the order of $200 k_B T$ or larger, the rate of homogeneous nucleation will be unmeasurably small. Using nucleation theory we can estimate the nucleation rate J per unit volume

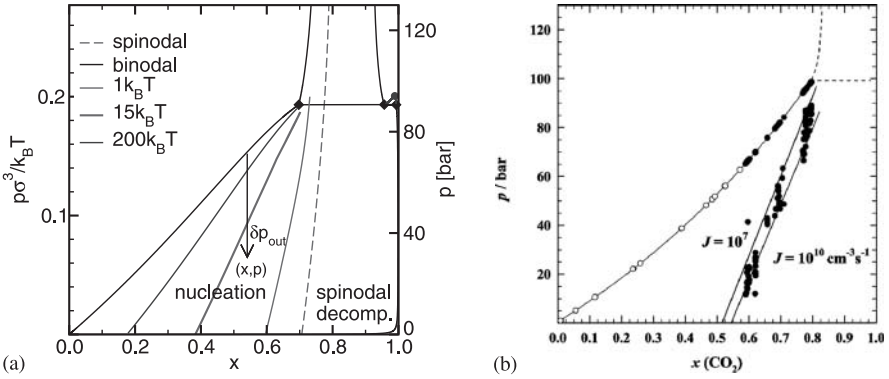

Fig. 11. (**a**) Phase diagram at temperature $k_BT/\epsilon = 0.75 \approx 41°\text{C}$ as a function of pressure p and molar fraction x. Lines of constant nucleation barrier are shown. A pressure jump, which would result in bubble nucleation, is indicated schematically. From [164]. (**b**) Nucleation behavior of a hexadecane + carbon dioxide mixture at $T = 40°\text{C}$. The binodal and the triple line are indicated by *solid* and *horizontal dashed lines*, respectively. *Full circles* mark the starting and ending point at which (homogeneous) bubble nucleation can be induced by a pressure jump. *Open circles* indicate starting points at which no bubble formation could be observed. The *lines* inside the miscibility gap indicate the location where the nucleation rate is $J = 10^7$ and $10^{10}/(\text{cm}^3\text{s})$, respectively. Courtesy of B. Rathke (adapted from [148])

$$J = K \exp(-\Delta G^\star / k_B T), \tag{88}$$

where K is a kinetic prefactor, which has been the subject of considerable debate [179]. If we use a typical value $K = 10^{32}/(\text{cm}^3\text{s})$ (the precise value does not matter here), then a nucleation barrier of $\Delta G^\star = 114 k_B T$ would mean that one could wait the age of the universe (about 10^{10} years) to observe a single nucleation event in a cubic centimeter of solution. Clearly, under these circumstances the system will choose alternative pathways of phase separation, e.g., nucleation may occur at the wall of the container or the surface of an impurity (heterogeneous nucleation). In the simplest case of heterogeneous nucleation at a planar surface, the barrier is reduced by a factor of

$$\frac{\Delta G^\star_{\text{hetero}}}{\Delta G^\star} = \frac{(2+\cos\Theta)(1-\cos\Theta)^2}{4}, \tag{89}$$

where Θ denotes the contact angle between the liquid-vapor interface and the surface.

If the nucleation barrier is on the order of $1 k_B T$ or smaller, "spinodal nucleation" occurs. In this case, the concept of a single bubble being a well-defined transition state breaks down. Since the free energy of the bubble is on the order of thermal fluctuations we expect many bubbles to form simultaneously in the system, and the situation is qualitatively similar to the behavior across the spinodal. In fact, thermal fluctuations destroy the meaning of a spinodal as a sharp boundary between metastable and unstable states, and for nucleation barriers which are comparable to

k_BT there is a gradual, very broad crossover from nucleation to spontaneous phase separation [175]. This is one instance, where mean-field theory fails, and thermal fluctuations alter the qualitative behavior. A theory which takes due account of fluctuations is required to obtain information about the kinetics of the phase transition in this regime. Nevertheless, the SCF theory provides a useful estimate for its limit of validity and the onset of "spinodal nucleation" [180, 181].

Thus, the concept of a single critical bubble as a transition state is pertinent to experiments only in a small fraction of the phase diagram in the middle between binodal and spinodal, namely for barriers of – say – $15k_BT$ or larger. The curve, which marks a nucleation barrier of $15k_BT$, can be taken as a rough estimate of a cloud point curve, where an onset of strong homogeneous nucleation would be observed on experimental time scales. Of course, the choice of the specific value $15k_BT$ is somewhat arbitrary and depends on what precisely is meant by "experimental timescale".

In panel (**b**) of Fig. 11 we reproduce experimental data from Rathke and coworkers [148], studying the onset of nucleation and measuring the nucleation rate in hexadecane + CO_2 mixtures at 40°C. Our crude and coarse-grained SCF calculations are able to reproduce some qualitative features of this careful, experimental study: The topology of the phase diagram, i.e., the location of binodals and the triple line are similar. Most notably, the experiment observes bubble nucleation where the SCF calculations predict barriers on the order of a few tens of k_BT, and the line of constant nucleation barrier is closer to the binodal at higher pressure (close to the triple line) and is further inside the miscibility gap at lower pressure.

3.5.1 *Comparison to Classical Nucleation Theory and Cahn–Hilliard Theory*

In the following we compare our results of the SCF calculations to a simple form of classical nucleation theory. Namely we assume that the free energy of a bubble of radius R is given by a balance between a surface and a volume contribution:

$$\Delta G_{\mathrm{CNT}}(R) = 4\pi\gamma R^2 - \frac{4\pi}{3}\Delta p R^3, \tag{90}$$

where γ denotes the interfacial tension of a planar interface between the coexisting phases at pressure p, and Δp is the pressure difference between the interior of the bubble and the mother phase. We estimate the pressure inside the bubble by calculating the densities at the center of the bubble and using the bulk equation of state. This procedure is close in spirit to the classical nucleation theory [182], where it is assumed that the bubble is a macroscopic object and the properties of the vapor inside the bubble are describable by the thermodynamics of the (homogeneous) bulk system. Maximizing ΔG_{CNT} with respect to the bubble radius, we obtain [147]

$$R^\star_{\mathrm{CNT}} = \frac{2\gamma}{\Delta p} \qquad \text{and} \qquad \Delta G^\star_{\mathrm{CNT}} = \frac{16\pi}{3}\frac{\gamma^3}{\Delta p^2} \tag{91}$$

for the size and excess free energy of a critical bubble. Unless explicitely noted otherwise, we use Δp for calculating the classical nucleation barrier.

Unfortunately, the densities or the pressure inside the bubble are not easily accessible experimentally. Therefore we also try to relate Δp to the distance from the coexistence curve (cf. arrow in Fig. 11). We consider a pressure change $\delta p_{\rm out}$ from the coexistence curve at constant molar fraction x. In an experiment, this change corresponds to the isothermal expansion of a polymer—liquid which has been saturated with solvent. The pressure in the mother phase is then given by $p_{\rm out} = p_{\rm coex} + \delta p_{\rm out}$ and the pressure inside the bubble is $p_{\rm in} = p_{\rm coex} + \delta p_{\rm in}$. The change of the pressure is related to the change in the chemical potentials via:

$$\phi_S \delta\mu_S = \frac{\phi_S^2 \frac{\partial \mu_S}{\partial \phi_S} + \phi_S \phi_P \frac{\partial \mu_S}{\partial \phi_P}}{\phi_S^2 \frac{\partial \mu_S}{\partial \phi_S} + 2\phi_S \phi_P \frac{\partial \mu_S}{\partial \phi_P} + \phi_P^2 \frac{\partial \mu_P}{\partial \phi_P}} \delta p \tag{92}$$

and

$$\frac{\phi_S \delta\mu_S}{\phi_P \delta\mu_P} = \frac{\phi_S^2 \frac{\partial \mu_S}{\partial \phi_S} + \phi_S \phi_P \frac{\partial \mu_S}{\partial \phi_P}}{\phi_P^2 \frac{\partial \mu_P}{\partial \phi_P} + \phi_S \phi_P \frac{\partial \mu_S}{\partial \phi_P}}. \tag{93}$$

If the mother phase is a dense polymer–rich liquid, its compressibility will be small and the term $\phi_P^2 \partial \mu_P / \partial \phi_P$ will be large compared to derivatives of the chemical potential μ_S of the super-critical solvent with respect to the densities. Hence, $\phi_{S\rm out} \delta\mu_S \ll \phi_{P\rm out} \delta\mu_P$. Using the Gibbs–Duhem relation, we then find:

$$\delta p_{\rm out} = \phi_{S\rm out} \delta\mu_S + \phi_{P\rm out} \delta\mu_P \approx \phi_{P\rm out} \delta\mu_P \tag{94}$$

i.e., if we change the chemical potentials at fixed molar fraction, the super-critical solvent will give a small contribution to the pressure change but the almost incompressible polymer liquid will give a large contribution. The pressure change of the interior of the bubble can be calculated to:

$$\delta p_{\rm in} = \phi_{S\rm in} \delta\mu_S + \phi_{P\rm in} \delta\mu_P \approx \frac{\phi_{P\rm in}}{\phi_{P\rm out}} \delta p_{\rm out} \approx 0. \tag{95}$$

The first term is small compared to $\delta p_{\rm out}$ even if the solvent density inside the bubble and in the mother phase are comparable. The second term is small, if the polymer density inside the bubble is much smaller than in the polymer–rich liquid, i.e., $\phi_{P\rm in} \ll \phi_{P\rm out}$. Provided that the polymer–rich liquid (mother phase) is nearly incompressible and the vapor inside the bubble has a low polymer density, we obtain the approximation $\Delta p = \delta p_{\rm in} - \delta p_{\rm out} \approx |\delta p_{\rm out}|$. This latter quantity can be readily obtained from the phase diagram and the information can be used to estimate the nucleation barrier in the framework of the classical nucleation theory. Of course, this approximation is only valid for small pressure changes, and it obviously breaks down for changes across the triple line.

In Fig. 12, we compare the results for the free energy of formation $\Delta G^\star$ of the critical bubble as obtained from the SCF calculations with classical nucleation theory. We fix temperature $k_B T/\epsilon = 0.75$ and pressure $p\sigma^3/k_B T = 0.1$ and study

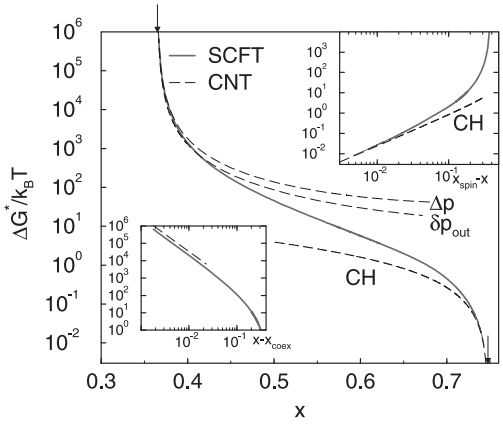

Fig. 12. Nucleation barrier $\Delta G^\star$ versus molar fraction x. The *solid line* corresponds to the SCF calculations, *dashed lines* correspond to the classical nucleation theory using the pressure difference Δp between interior of the bubble and mother phase or the distance δp_{out} from the coexistence curve as illustrated in Fig. 11. The *dashed line* (CH) close to the spinodal corresponds to the predictions of the Cahn–Hilliard theory. The *arrow on the top* marks the binodal, the *arrow on the bottom* marks the spinodal. The *left inset* presents the behavior in the vicinity of the binodal; the *dashed line* marks the power law $\Delta G^\star \sim (x - x_{\text{bin}})^{-2}$. The *right inset* shows the behavior close to the spinodal; the *dashed line* (CH) is the prediction of the Cahn–Hilliard theory. From [164]

the behavior as a function of molar fraction x of the solvent. We use both Δp as obtained from the densities inside and outside of the bubble and the approximation $\Delta p \approx \delta p_{\text{out}}$. The classical nucleation theory provides an accurate description in the vicinity of the binodal. There, the pressure difference depends linearly on the difference from the binodal, and the nucleation barrier diverges like $\Delta G^\star \sim (x - x_{\text{bin}})^{-2}$. The Figure shows that the SCF calculations and classical nucleation theory agree in the ultimate vicinity of the binodal. However, classical nucleation theory becomes gradually inaccurate in predicting nucleation barriers smaller than $O(10^2 k_B T)$. Approximating Δp by δp_{out} appears to provide a slightly better description due to cancellation of errors. Independent from this approximation, classical nucleation theory tends to overestimate the nucleation free energy for $\Delta G^\star \sim 10^2 k_B T$, i.e., it is not quantitatively accurate in the experimentally relevant regime. Ultimately, classical nucleation theory fails to predict the vanishing of the nucleation barrier at the spinodal.

The SCF theory describes the vanishing of the nucleation barrier at the spinodal [163, 183, 164] and is free of the thermodynamic inconsistency of the classical nucleation theory. In the vicinity of the spinodal, the density difference between the inside and the outside of the bubble becomes small, the bubble size large, and its interface to the mother phase very broad. These effects make the behavior in the vicinity of the spinodal amenable to an analytic description, the Cahn–Hilliard theory [146]. While the theory was originally formulated for systems with a single order

parameter, it can be straightforwardly applied to a compressible binary mixture by recognizing that only the unstable linear combination c of the two densities is important in the ultimate vicinity of the spinodal, while the other combination $\bar{c}$ remains to a first approximation constant across the interface between the bubble and the mother phase. Therefore, we can approximately describe the bubble by a single density c, and use the results of Cahn and Hilliard [146] for a one–component system. Analogous to Eq. (10) we can write down a square gradient expansion for the SCF free energy [27, 28]

$$\frac{\mathcal{F}[\phi_S,\phi_P]}{k_BT} = \int \mathrm{d}\mathbf{r}\, \left\{ f(\phi_S,\phi_P) + \frac{b^2}{36}\frac{(\nabla\phi_S)^2}{\phi_S} + \frac{b^2}{36}\frac{(\nabla\phi_P)^2}{\phi_P} \right\}, \tag{96}$$

which is appropriate because the interface of the bubble is very broad in the vicinity of the spinodal. f denotes the canonical free energy density and is given by Eq. (73). Rewriting this free energy in terms of the densities c and $\bar{c}$, we can cast the free energy in the Cahn–Hilliard form:

$$\begin{aligned}\frac{\mathcal{F}[c]}{k_BT} \approx \int \mathrm{d}\mathbf{r}\, \Big\{ & 3\xi_{\mathrm{CH}}\tau(c-c_0)^2 - \xi_{\mathrm{CH}}(c-c_0)^3 + \kappa_{\mathrm{CH}}(\nabla c)^2 \\ & + \text{linear terms in } c + O(\bar{c}-\bar{c}_0)\Big\}, \end{aligned} \tag{97}$$

where c_0 is the density far away from the bubble in the mother phase and the coefficients are given by:

$$\begin{aligned}\xi_{\mathrm{CH}} &= -\frac{1}{6}\frac{\partial^3 f}{\partial c^3} \\ &= -\frac{1}{6}\left\{ \alpha^3\frac{\partial^2\mu_S}{\partial\phi_S^2} + 3\alpha^2\beta\frac{\partial^2\mu_S}{\partial\phi_S\partial\phi_P} + 3\alpha\beta^2\frac{\partial^2\mu_P}{\partial\phi_S\partial\phi_P} + \beta^3\frac{\partial^2\mu_P}{\partial\phi_P^2} \right\}\Big|_{\mathrm{spin}} \\ \kappa_{\mathrm{CH}} &= \frac{b^2}{36}\left\{ \frac{\alpha^2}{\phi_S} + \frac{\beta^2}{\phi_P} \right\}\Big|_{\mathrm{spin}} \\ 3\xi_{\mathrm{CH}}\tau &= \frac{1}{2}\left\{ \alpha^2\frac{\partial\mu_S}{\partial\phi_S} + 2\alpha\beta\frac{\partial\mu_S}{\partial\phi_P} + \beta^2\frac{\partial\mu_P}{\partial\phi_P} \right\}\Big|_{\mathrm{spin}}. \end{aligned} \tag{98}$$

The definitions of α and β are given in Eq. (76). τ measures the distance from the spinodal and the condition $\tau = 0$ yields Eq. (75). Comparing this expression with the calculation of Cahn and Hilliard [146] we can read off the nucleation barrier:

$$\frac{\Delta G^\star_{\mathrm{CH}}}{k_BT} \approx 197\, \xi_{\mathrm{CH}}^{-1/2}\, \kappa_{\mathrm{CH}}^{3/2}\, \tau^{3/2} \sim (x - x_{\mathrm{spin}})^{3/2}. \tag{99}$$

The radius of the critical nucleus diverges according to:

$$R^\star_{\mathrm{CH}} \sim (x - x_{\mathrm{spin}})^{-1/2}. \tag{100}$$

In the vicinity of the spinodal the Cahn–Hilliard theory and the full SCF calculations agree quantitatively, as shown in the inset of Fig. 12. At smaller supersaturation, however, the interface becomes steeper and the square gradient approximation breaks down. Additionally, the variation of the densities across the interface

can no longer be described by a single linear combination of densities. This leads to deviations between the SCF calculations and the Cahn–Hilliard theory for nucleation barriers as small as $0.1k_BT$. Therefore, also the Cahn–Hilliard theory only is of limited use for describing the experimental range of nucleation rates, because it is only valid in the regime of "spinodal nucleation" where both SCF calculations and Cahn–Hilliard theory fail, and thermal fluctuations are important.

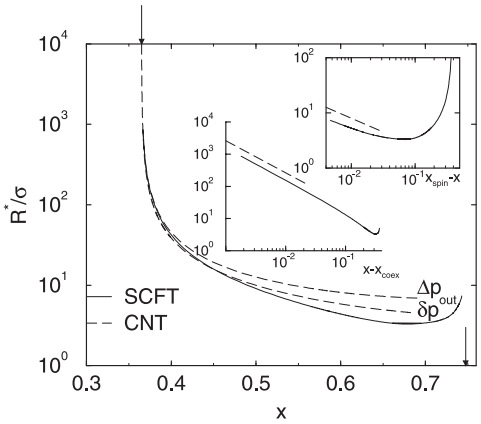

Fig. 13. Size of the critical bubble as determined from the excess of polymer for the same parameters as in Fig. 12. The *dashed line* in the *right inset* marks the power law $R^\star \sim (x - x_{\rm spin})^{-1/2}$. From [164]

In Fig. 13 we show the size of the critical bubble. Both at the binodal and the spinodal the size of the critical bubble diverges as expected from classical nucleation theory and Cahn–Hilliard theory, respectively. The insets show that both analytical approaches agree quantitatively with the SCF calculations in the limits $x \to x_{\rm bin}$ and $x \to x_{\rm spin}$, respectively. Between binodal and spinodal the critical size has a minimum. At the minimum, the size of the critical bubble is only a few segment diameters. For the parameters used in the present calculations, the minimum corresponds to rather small nucleation barriers and is close to the regime of "spinodal nucleation". For most practically relevant nucleation barriers the size of the critical bubble decreases upon increasing molar fraction.

In Fig. 14 we show the radial density profiles of the solvent and polymer across the interface of the critical bubble. In the vicinity of the binodal ($x = 0.4$) the bubble is large and the interface between the bubble's interior and the mother phase resembles the planar interface between macroscopically coexisting phases. For comparison we have also included the profile of a planar interface. Upon increasing molar fraction x, the solvent density increases in both regions. The excess of solvent at the interface also increases slightly. The polymer density decreases in the mother phase and increases in the interior of the bubble. The interface profile broadens gradually. Upon approaching the spinodal further, the solvent density inside the bubble becomes

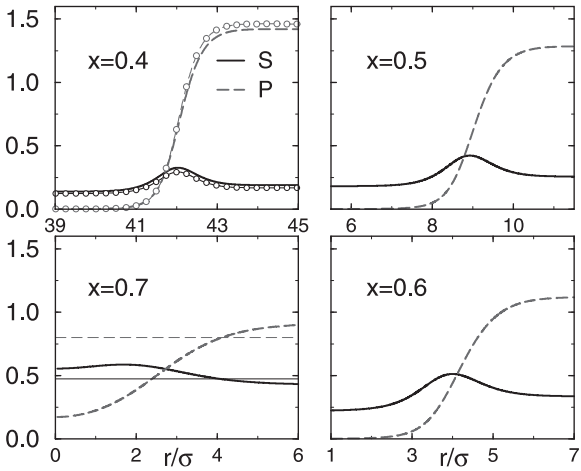

Fig. 14. Interface profiles as a function of the radial distance from the center of the critical bubble at various molar fractions x as indicated in the key at temperature $k_BT/\epsilon = 0.75$ and pressure $p\sigma^3/k_BT = 0.1$. For comparison we show the profiles of a planar interface as *thin lines* with *circles* at $x = 0.4$. The spinodal values are marked by *horizontal lines* for $x = 0.7$. From [164]

larger than in the mother phase. At this stage the density inside the bubble is quite comparable to the density of the mother phase [184]. Clearly, the interface of the bubble in the vicinity of the spinodal bears little resemblance with a planar interface; a fact which illustrates the qualitative failure of the classical nucleation theory in the vicinity of the spinodal.

To summarize, classical nucleation theory is quantitatively accurate only for barriers of $10^2 k_BT$ or larger while Cahn–Hilliard theory is accurate for barriers smaller than $1k_BT$. Unfortunately, the regimes of validity of these analytical approaches do not overlap and there is no obvious way how to interpolate between them or to extrapolate their results into the regime of experimentally relevant nucleation barriers. It is exactly in this regime that density functional methods [163, 184, 186] or SCF calculations [164, 183] are most useful. Our system shares this qualitative behavior in the vicinity of the binodal and the spinodal with pure fluids and incompressible mixtures [163, 183, 184]. The concept of a single spherical bubble as a unique transition state is applicable in a rather small fraction of the region between binodal and spinodal only. Nevertheless, the knowledge of the phase behavior (including the spinodal lines) already yields a rough, but valuable impression of the qualitative nucleation behavior.

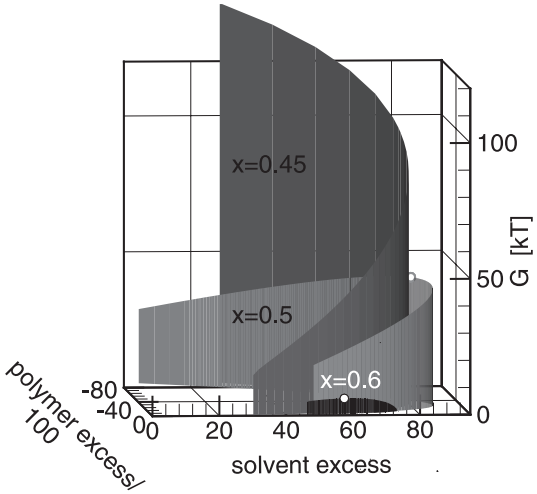

Fig. 15. Excess free energy G of a bubble as a function of the excess of solvent and polymer at temperature $k_BT/\epsilon = 0.75$ and pressure $p\sigma^3/k_BT = 0.1$. Different values of the molar fraction x are indicated in the key. For $x = 0.6$ and 0.5 the critical bubble is included and marked by a *circle*, for $x = 0.45$ only sub-critical data are shown. From [164]

3.5.2
Nucleation in the Vicinity of the Triple Line

In the previous Sect. 3.5.1 we have focused on the rather universal behavior in the vicinity of the binodal and the spinodal. In this section we shall highlight features that are specific to compressible polymer + solvent systems.

In a compressible binary mixture, the composition inside a bubble does not necessarily coincide with the composition of the vapor phase. This additional parameter is chosen as to minimize the free energy of the bubble and depends on the bubble's size. In Fig. 15 we plot the free energy ΔG of the bubble as a function of the excess $\Delta_{S\mathrm{nuc}}$ of the solvent component and the excess $\Delta_{P\mathrm{nuc}}$ of the polymer. The critical bubble corresponds to a maximum of a curve. The values of ΔG away from the maximum depend on the way the size of the bubble is held constant. Such a dependence is rather weak in the vicinity of the maximum, but it gives rise to unphysical density profiles (and convergence problems in the numerical procedure) for very small bubble sizes. Those small sizes are excluded from Fig. 15.

The wings correspond to the lowest free energy path in the $\Delta_{S\mathrm{nuc}}$–$\Delta_{P\mathrm{nuc}}$ plane. The polymer excess is negative, because the vapor inside the bubble has a lower polymer density than the polymer–rich mother phase. $|\Delta_{P\mathrm{nuc}}|$ is proportional to the volume of the bubble. If the composition of the bubble was independent from its size, the projection of the curve into the $\Delta_{S\mathrm{nuc}}$–$\Delta_{P\mathrm{nuc}}$–plane would be straight lines and their slope would be given by the composition of the vapor. This is not all what we observe for bubbles of small and medium sizes. The solvent excess first increases with the size of the bubble (or $|\Delta_{P\mathrm{nuc}}|$), passes through a maximum, and then de-

creases. Small bubbles contain more of the volatile solvent than one would expect from the composition of the vapor phase. Only for very large bubbles (not shown), we find that $\Delta_{S\mathrm{nuc}}$ decreases roughly linearly with $\Delta_{P\mathrm{nuc}}$.

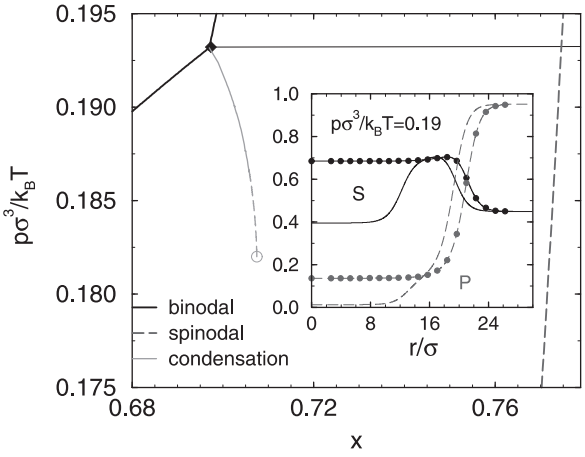

Fig. 16. Condensation of the solvent–vapor into a solvent–rich fluid in the critical bubble at temperature $k_BT/\epsilon = 0.75$. The *dashed line* is extrapolated from the SCF data and the critical point, at which the line of capillary condensation ends, is marked by an *open circle*. Binodal, spinodal, and triple line are shown as reference. The *inset* presents the radial density profiles at $p\sigma^3/k_BT = 0.19$. *Lines* with *circles* refer to the condensed state, while *lines* correspond to the state with solvent–vapor inside the nucleus. From [164]

Upon approaching the triple line the composition of small bubbles differs more strongly from the composition of the vapor. This effect is related to the thick wetting layer of liquid solvent that builds up at the interface between the polymer-liquid and the solvent–vapor. The polymer-rich liquid prefers the solvent in its metastable liquid state rather than the thermodynamically stable vapor. Analogous to capillary condensation, the solvent–vapor might condense into a solvent–rich liquid due to the confined geometry of the bubble. This is observed in our SCF calculations in the ultimate vicinity of the triple line. The density profiles at the "bubble condensation" point for $p\sigma^3/k_BT = 0.19$ are presented in the inset of Fig. 16. For molar fractions $x < 0.70258$ the critical bubble is filled with almost pure solvent–vapor, while for larger values of x, the solvent has condensed to a liquid inside the bubble. At the condensation point both critical bubbles – the one with vapor inside and the one with liquid inside – have the same free energy of formation $\Delta G^\star$. The effective interfacial tension γ_{eff} between the solvent liquid with respect to the polymer is lower than for the solvent–vapor. At constant nucleation barrier, the radius $R^\star \sim \gamma_{\mathrm{eff}}/\Delta p \sim \sqrt{\Delta G^\star/\gamma_{\mathrm{eff}}}$ in the condensed state is larger than in the state where the bubble is filled with vapor, in agreement with the data in the inset of Fig. 16.

As we approach the triple pressure, the free energy difference between metastable liquid solvent and stable solvent–vapor decreases, and "bubble condensation" occurs

for larger bubbles and closer to the binodal (cf. Fig. 16). Above p_{triple} the solvent–rich liquid coexists with the polymer–rich liquid, and then, of course, critical "bubbles" are always filled with liquid solvent. Likewise, if we decrease the pressure away from the triple line, the line of capillary condensation ends in a critical point within mean-field approximation. This behavior is generic in the vicinity of a triple point, and similar effects have been observed in the framework of Cahn–Hilliard theory for droplet nucleation in the presence of a metastable crystalline phase [192] and in simulations [193]. More generally, the condensation inside the bubble into a metastable liquid solvent is an example of Ostwald's rule [194]: The nucleus needs not to be formed by the thermodynamically most stable phase (i.e. the solvent–vapor in our model), but might consist in the phase that is closest in free energy to the mother phase.

At this stage, we point out a qualitative effect of thermal fluctuations: The condensation inside the bubble is a sharp first order transition which ends in a critical point only within mean-field approximation. Since the bubble is only of finite size no true phase transition can occur, because in the vicinity of the transition the free energy difference between the stable and the unstable states is finite. Therefore one can always find the critical nucleus in the metastable state with a small but finite probability, and the transition is rounded. The consideration of fluctuations will replace the sharp transition by a rather rapid but continuous variation of the density inside the bubble.

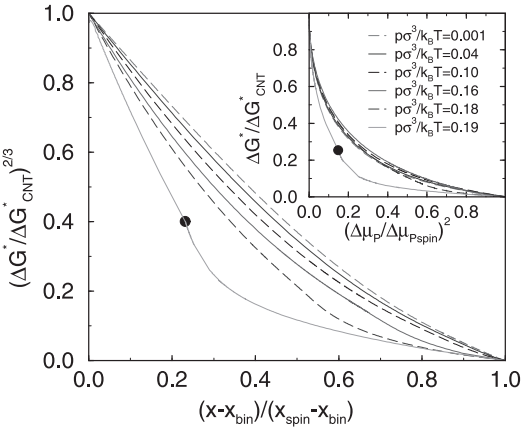

Fig. 17. Ratio between our SCF results for the nucleation barrier $\Delta G^\star$ and the predictions of the classical theory (using Δp) as a function of the reduced distance from the binodal. *Curves* correspond to different pressures as indicated in the key. The *circle* marks the condensation of the solvent–vapor into a solvent–rich liquid inside the critical bubble. The *inset* shows the data for all pressures versus the scaled distance in the chemical potential of the polymer. From [164]

The classical nucleation theory agrees with the SCF calculations in the vicinity of the binodal, but fails to predict the vanishing of the nucleation barrier at the spinodal. To compare the behavior at different pressures, to correlate data from different systems, or to gauge the deviations from classical nucleation theory for systems for which no detailed calculations are available, it is useful to compare data in a rescaled form [185, 186, 187, 188, 189, 190]. For $x \to x_{\rm spin}$ the ratio $\Delta G^\star/\Delta G^\star_{\rm CNT}$ vanishes with the scaled distance $\tilde{x} = (x - x_{\rm bin})/(x_{\rm spin} - x_{\rm bin})$ between the binodal and the spinodal like $\tilde{x}^{3/2}$, while $\Delta G^\star/\Delta G^\star_{\rm CNT} \to 1$ for $\tilde{x} \to 0$. To quantify the deviations from the classical nucleation theory, we plot $(\Delta G^\star/\Delta G^\star_{\rm CNT})^{2/3}$ versus the scaled distance $\tilde{x}$ in Fig. 17 for different pressures at $k_BT/\epsilon = 0.75$. For low pressures the density of the vapor is very small and there is also almost no solvent dissolved in the polymer–rich liquid. The behavior of the compressible mixture is determined by the pure non-volatile polymer, i.e., the behavior is similar to a one-component compressible system. In this case we heuristically find that $(\Delta G^\star/\Delta G^\star_{\rm CNT})^{2/3}$ decreases roughly linearly with $\tilde{x}$ over the entire range between binodal and spinodal. As we increase the pressure, more of the solvent enters the polymer–rich liquid and deviations from the classical nucleation theory gradually become larger as the character of a compressible binary mixture becomes more prominent. In the ultimate vicinity of the triple pressure $p_{\rm triple}\sigma^3/k_BT = 0.193174$, deviations become quite pronounced due to the condensation of the liquid inside the critical bubble. Another common scaled data representation is obtained by using $\Delta\mu/\Delta\mu_{\rm spin} \equiv (\mu - \mu_{\rm coex})/(\mu_{\rm spin} - \mu_{\rm coex})$ to parameterize the region between binodal and spinodal. Plotting the ratio $\Delta G^\star/\Delta G^\star_{\rm CNT}$ versus $(\Delta\mu/\Delta\mu_{\rm spin})^2$ results in an effective collapse of the data over a wide range of pressures $p\sigma^3/k_BT \le 0.18$ (cf. inset), but, there are systematic deviations, that become pronounced in the vicinity of the triple pressure. Qualitatively, the behavior is similar to bubble nucleation in a Lennard–Jones liquid [186, 188], but the ratio $\Delta G^\star/\Delta G^\star_{\rm CNT}$ is somewhat smaller than for a Lennard–Jones liquid, where it was found to decrease linearly to a first approximation, i.e., $\Delta G^\star/\Delta G^\star_{\rm CNT} \sim 1 - (\Delta\mu/\Delta\mu_{\rm spin})^2$ [185, 190, 191]. Intriguingly such a scaling is also born out of a kinetic approach [187]. In the ultimate vicinity of the spinodal, however, one expects $G^\star/\Delta G^\star_{\rm CNT} \sim (1 - \Delta\mu/\Delta\mu_{\rm spin})^{3/2}$.

3.5.3
Temperature Dependence and "Foam Diagrams"

Talanquer and co–workers [195, 196] have considered the nucleation of bubbles in binary mixtures. Intuitively [197], one would expect that the nucleation rate increased with increasing temperature (as it does, e.g., in a compressible one-component polymer solution), but they have found the inverse behavior for certain parameters [195, 196], i.e., a decrease of the nucleation rate with increasing temperature at fixed composition and pressure. Intriguingly, there is no qualitative difference between the structure of critical bubbles with normal and inverse nucleation rate behavior [196]. In Fig. 18 (**a**) we present the temperature dependence of the nucleation barrier at low pressure $p\sigma^3/k_BT = 0.001$ and high pressure $p\sigma^3/k_BT = 0.16$.

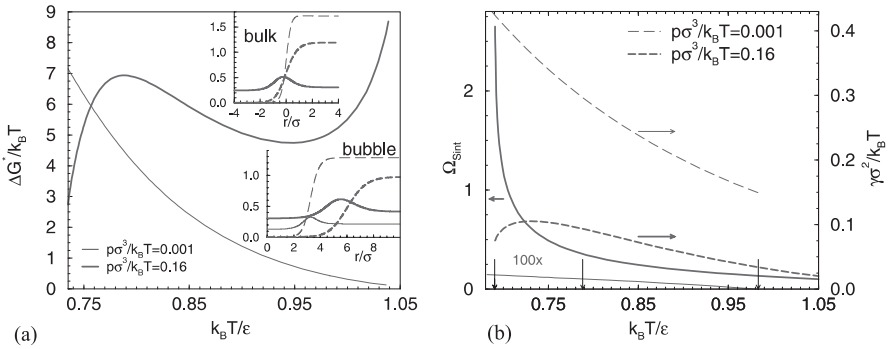

Fig. 18. (**a**) Temperature dependence of the nucleation barrier at fixed pressure $p = 0.001 k_B T$ and $p = 0.16 k_B T$ and composition $x = 0.46$ and $x = 0.68$, respectively. For higher pressure the nucleation barrier exhibits a maximum as a function of temperature, while it decreases with increasing temperature for low pressure as expected. *Insets* show the radial density profiles of critical bubbles (*left*) and planar interfaces (*right*) at temperature $k_B T/\epsilon = 0.7573$. (**b**) The temperature variation of the interfacial excess of solvent and the interfacial tension at bulk coexistence. The interfacial excess for $p\sigma^3/k_B T = 0.001$ is increased by a factor 100. The triple temperature $k_B T_{\text{triple}}/\epsilon = 0.6903$ for the higher pressure $p\sigma^3/k_B T = 0.16$, the temperature at which the nucleation barrier is maximal (at $p\sigma^3/k_B T = 0.16$), and the liquid–vapor coexistence of the pure solvent at $p\sigma^3/k_B T = 0.001$ are indicated by *arrows*. From [164]

The former corresponds effectively to a one-component compressible polymer solution, while the character of a compressible binary mixture becomes more apparent at higher pressures in the vicinity of the triple line. The composition is held constant, and the temperature is varied. From Fig. 8 (**b**) we conclude that the composition of the coexisting phases remains almost constant in the temperature interval $0.75 < k_B T/\epsilon < 0.82$ for both pressures. At low pressure, the nucleation barrier decreases monotonously with temperature as expected. At higher pressure, however, the nucleation barrier exhibits a non-monotonous dependence on temperature: $\Delta G^\star$ exhibits both a maximum and a minimum upon increasing temperature at fixed molar fraction. The inset compares the radial density distributions of the critical bubbles and planar interfaces at $k_B T/\epsilon = 0.7573$. In both cases the solvent density at the center of the bubble is higher than at coexistence and there is an enrichment of solvent at the interface of the bubble. However, there are no qualitative differences in the structure, in agreement with the observation of Talanquer and co–workers [196] for binary Lennard–Jones mixtures.

To obtain further information, we plot the interfacial tension γ and the excess of solvent at the interface between coexisting phases in the bulk in panel (**b**). At low pressure, γ decreases with temperature and there is almost no excess of solvent at the interface. At high pressure, also the interfacial tension exhibits a maximum as a function of temperature and there is a pronounced interfacial excess. In our specific model, this non-monotonous temperature dependence of the interfacial tension can

be related to the phase behavior (cf. Fig. 19 or 7). If we decrease the temperature at $p\sigma^3/k_BT = 0.16$ we will encounter a triple point at $k_BT_{\text{triple}}/\epsilon = 0.690251$. In the ultimate vicinity of the triple temperature $T > T_{\text{triple}}$ there is a pronounced enrichment of liquid solvent at the interface and the interfacial tension is particularly low. Increasing the temperature, we decrease the interfacial excess of solvent rapidly and increase the interfacial tension. Only when the distance from the triple temperature is large enough for the interfacial excess to be small, the normal decrease of γ with temperature sets in. For low pressure $p\sigma^3/k_BT = 0.001$, no substantial interfacial excess builds up and we simply observe the normal decrease of γ with increasing temperature. A maximum in the interfacial tension imparts – in the framework of classical nucleation theory – a non-monotonous temperature dependence onto the nucleation barrier. Similarly, a non-monotonic behavior of the nucleation barrier has been observed in polydisperse colloids [198], albeit not as a function of temperature but as a function of super-saturation, and it has also been related to a non-monotonic behavior of the interfacial free energy.

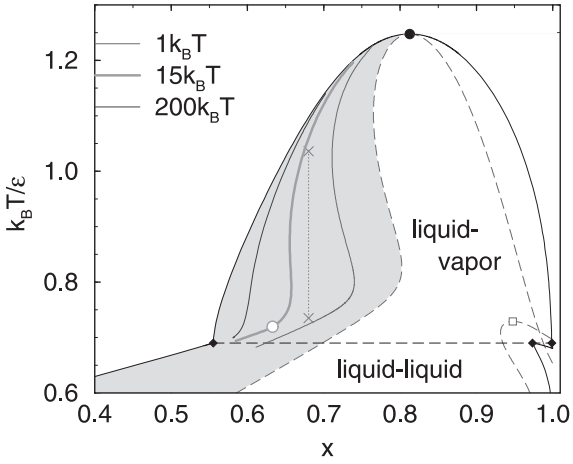

Fig. 19. Binodals (*solid lines*) and spinodals (*dashed lines*) in the temperature–composition plane at $p\sigma^3/k_BT = 0.16$. The critical point is marked by a *filled circle*, *diamonds*, and a *horizontal dashed line* mark the triple point. The unstable liquid–liquid critical point is indicated by a square. Above the triple point, lines of constant nucleation barriers are shown. An *open circle* on the line of nucleation barriers $15k_BT$ marks the condensation of solvent–vapor into a solvent–rich liquid inside the critical nucleus. The *dotted vertical line* at $x = 0.68$ (ending in *crosses*) marks the path at which the nucleation barrier is examined in Fig. 18. From [164]

It is instructive, however, to set our finding also in context of the phase diagram. In Fig. 19 we plot binodals and spinodals as a function of composition x and temperature T at constant $p\sigma^3/k_BT = 0.16$. For the composition $x = 0.68$ the spinodal of the polymer–rich liquid is located at $k_BT_{\text{spin}}/\epsilon = 0.675239$, i.e., just 2% below the triple temperature. In the SCF calculations the nucleation barrier vanishes at T_{spin},

and the nucleation barrier increases steeply with temperature ultimately above T_{spin}. It passes through a maximum, and then exhibits the expected "normal" decrease with temperature. Upon increasing temperature further, however, we approach the binodal, which is located at $k_B T_{\text{bin}}/\epsilon = 1.097$. At this point, the nucleation barrier diverges; i.e., the nucleation barrier passes through a minimum and then grows. This sequence of a maximum and a minimum in the nucleation barrier upon increasing temperature is, indeed, what we observe in our SCF calculations. It can be qualitatively inferred from the location of the binodal and the spinodal. In Fig. 19 we show lines of constant nucleation barrier, too. The line of high nucleation barriers $\Delta G^\star = 200 k_B T$ closely follows the binodal, while the line of low nucleation barriers $\Delta G^\star = 1 k_B T$ has a similar s-shape as the spinodal. Unlike the diagram at constant temperature (cf. Fig. 11), however, the relative distance $\tilde{x}$ of lines, which mark constant nucleation barriers, from binodal and spinodal strongly depends on temperature.

The binodals of the liquid-vapor phase coexistence as a function of molar fraction and temperature resemble the binodals of a one-component system as a function of density and temperature: At high temperature, there is a critical point. Upon decreasing temperature the polymer-rich phase becomes more concentrated in polymer, while the solvent concentration increases in the vapor phase. The spinodal of the polymer liquid, however, exhibits a non-monotonous temperature dependence of the composition. This dependence is parallel to the non-monotonous behavior of the nucleation barrier as we increase temperature. In fact, at the pressure considered, and even more so at lower pressures (cf. Fig. 20), there exists an extended temperature region, where the polymer-fraction at the spinodal of the liquid decreases upon increasing temperature.

The reason for this s-shaped form of the spinodal is an unstable liquid—liquid critical point. Below the triple temperature, there exists a polymer-rich liquid and a solvent-rich liquid. Both binodal and spinodal of the polymer-rich phase become richer in solvent upon increasing temperature. This tendency of the polymer-rich spinodal persists also above the triple temperature, the spinodal runs towards the (unstable) critical point of the liquid—liquid phase coexistence, which would terminate the liquid—liquid phase coexistence if it was not pre-emptied by liquid-vapor coexistence. The unstable critical points are marked by a square in Figs. 19 and 20 (**a-c**). The influence of the unstable liquid—liquid critical point is also detectable in the combination c of densities which becomes unstable at the spinodal. Initially, spinodal decomposition leads to a liquid–liquid phase separation. This effect also matches the observation slightly above the triple temperature that the critical bubble is not filled with solvent-vapor – the thermodynamically stable phase – but rather with liquid solvent. Only at temperatures farther above the triple temperature, the spinodal adopts the normal behavior and approaches the liquid-vapor critical point. In this region the unstable mode also changes from liquid-liquid to liquid-vapor.

The qualitatively different T–x–diagrams in Fig. 20 suggest a large sensitivity of the nucleation behavior on pressure. Below the critical pressure of the non-volatile polymer (**a**), the diagram contains a triple line, but no (stable) critical point. The spinodal has a triangular shape: At low temperatures the solvent molar fraction increases

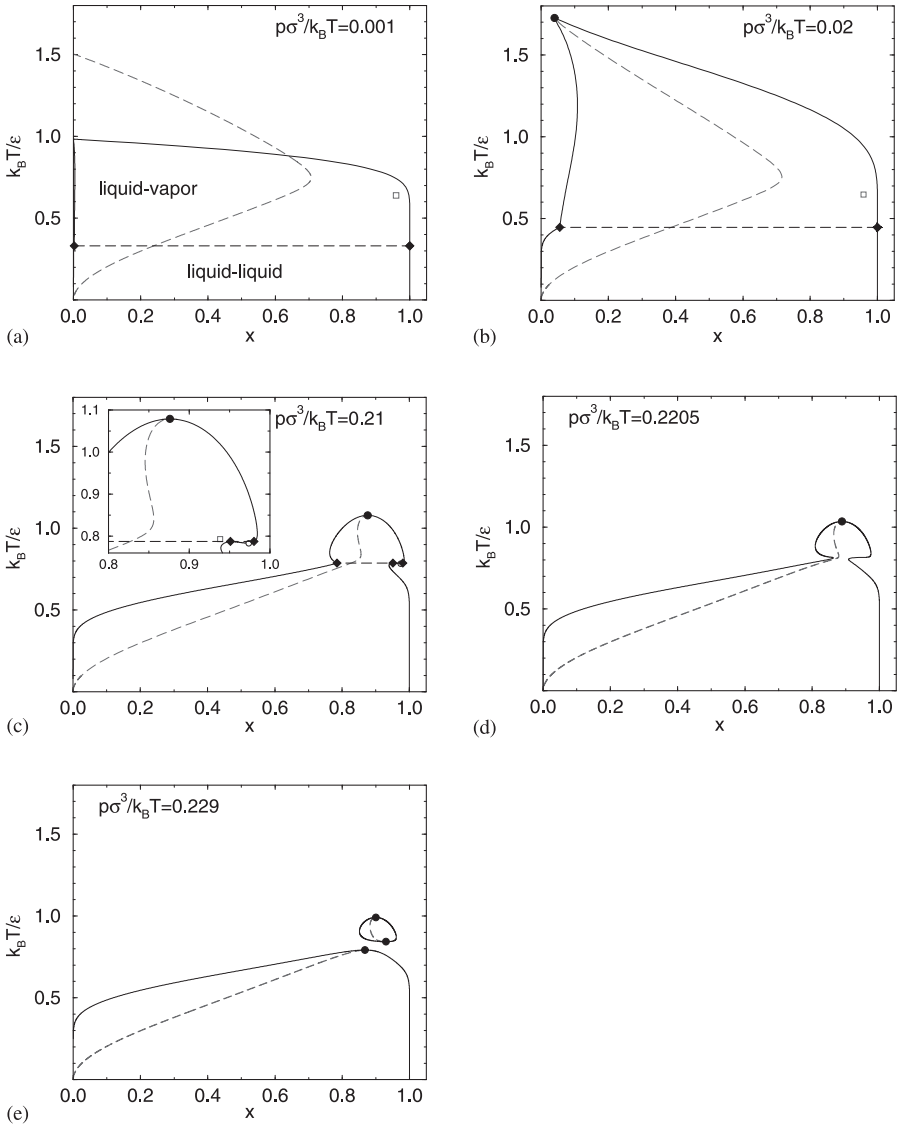

Fig. 20. Binodals and spinodals of the polymer–rich phase in the temperature–composition plane at various pressures as indicated in the key. Critical points are marked by *circles*, triple lines are shown as *diamonds* and *horizontal lines*. Unstable liquid–liquid critical points are indicated by *open squares*. The different pressures correspond to pressures below the critical pressure of the non-volatile component ($p = 0.001 k_B T/\sigma^3 < p_{P\mathrm{crit}} = 0.018 k_B T/\sigma^3$ (**a**)), above this threshold ($p = 0.02 k_B T/\sigma^3$ (**b**)), above the critical pressure of the solvent ($p = 0.21 k_B T/\sigma^3 > p_{S\mathrm{crit}} = 0.1957 k_B T/\sigma^3$ (**c**)), above the UCEP ($p = 0.2205 k_B T/\sigma^3$ (**d**) and $0.229 k_B T/\sigma^3$ (**e**)). At even higher pressure, there is only a single two–phase region which terminates in a critical point (not shown). From [164]

with temperature towards the unstable liquid—liquid critical point and above the vicinity of the unstable critical temperature, the molar fraction decreases with temperature. The behavior above the critical pressure of the polymer is similar, except that the spinodal does not reach $x = 0$ but terminates in a liquid—vapor critical point. As the pressure increases, the critical point shifts to larger molar fractions (cf. panel (**b**) and Fig. 19). Increasing the pressure even more, the triple line shortens and moves to larger temperatures (see panel (**c**)). Eventually (panel (**d**)) the triple line disappears but the binodal continues to constrict. This leads to the formation of an isobaric cut though the phase diagram which contains three critical points. At very large pressure, the critical points at the higher temperature merge and we are left with a single miscibility gap that ends in a single critical point.

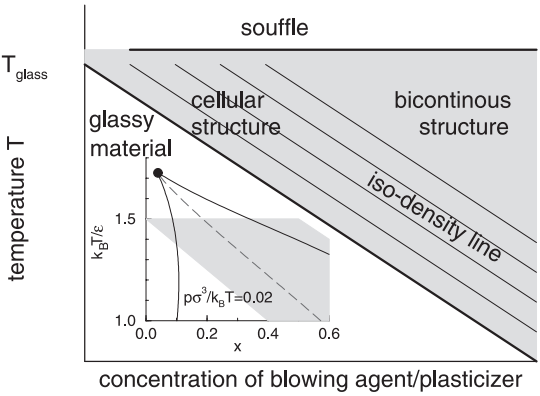

Fig. 21. Qualitative representation of the properties of polystyrene foams using carbon dioxide as a blowing agent and plasticizer. The *inset* shows a part of Fig. 20 (**b**) Redrawn from Krause et al. [11]

We close this section on SCF calculations by trying to relate our findings qualitatively to the experimental observations by Krause and co-workers [11]. In these experiments, one saturates a thin film of polystyrene with carbon dioxide at low temperature and high pressure. Then, one suddenly quenches the polymer—solvent mixture into a super-saturated state by increasing temperature (and/or decreasing pressure) and observes the nucleation and growth of vapor bubbles at a fixed temperature and low (atmospheric) pressure. Carbon dioxide not only acts as a blowing agent, but also plasticizes the glassy polymer. The decrease of the glass transition temperature depends on the concentration of the dissolved CO_2. Stable foams are produced in the narrow temperature window below the glass transition temperature of the pure polymer and above the glass transition temperature of the CO_2 saturated polystyrene. If the temperature was lower, no bubbles form because the material would be solid. If the temperature was too high, bubbles would form but the final foam would be liquid and collapse like a souffle. Therefore only a small triangular region of the entire $T-x$ plane results in useful foams. This is illustrated schematically in Fig. 21. Krause and

co-workers mapped out the structure and density of foams in the $T - x$ plane and compiled their results in "foam diagrams" [11]. Generally, the density of the foam decreases as the polymer becomes more saturated with the blowing agent. Of course, the experiment observes the late stages of phase separation, while we have considered only the mechanisms in the earliest stages. Nevertheless, a smaller density of the foam is partially the result of a larger nucleation rate and, hence, a smaller nucleation barrier. Therefore, the supersaturation of the mixture is higher for larger values of x. Interestingly, one finds (i) that the iso-density lines shift to smaller saturation upon increasing temperature and (ii) that there is a characteristic molar fraction at which the foam density and structure suddenly changes. It is tempting to relate the qualitative behavior of the iso-density lines to the lines of constant nucleation barrier and the change of the foam structure to a change in the mechanism of phase separation from nucleation to spinodal decomposition. The location of the spinodal in the $T - x$ diagrams of Fig. 20 (**a**) and (**b**) lends at least qualitative support to this speculation.

4 Equation of State of Compressible Polymer Solutions

4.1 Introduction

We have already considered two different approaches to the equation of state of polymer–solvent mixtures, the well-known Flory-Huggins theory and a parametric equation of state employed in the context of Self Consistent Field Theory. As noted in Sect. 2.1, the Flory-Huggins model can only describe the behavior of a polymer solution in those special cases where the solvent may be considered essentially incompressible, such that its properties are equal both in the polymer–rich and polymer–poor phases. Typically, a polymer–solvent mixture does have a much more complex phase behavior than that predicted by the Flory–Huggins theory, provided one probes a large region of the pressure–temperature plane [6]. In order to remedy this deficiency, in Sect. 3.2 we have considered a simple parametric equation of state which is capable of showing a rich variety of phase behavior, including phase diagrams of type I to V in the Scott—Van Konynenburg classification. Unfortunately, despite its qualitative agreement, this equation is not particularly accurate, even when the parameters are adjusted to quantitatively describe some chosen substance. Actually, despite some early attempts [199, 200, 201, 202, 203, 204, 205], the development of an accurate equation of state in terms of a well–defined and realistic polymer model has been a difficult problem of statistical mechanics since a long time ago. However, in the mid eighties and early nineties a great progress has been made, and different approaches have been developed in order to describe the thermodynamics of coarse–grained off-lattice polymer models.

One such approach is based on integral equation theories [206, 207, 208, 209, 210, 211]. Possibly the most popular of these attempts is the P-RISM theory of Curro and Schweizer [206, 207]. Typically, these integral equation theories allow to include fine chemical details, such as bond lengths and angles, and yield a rather reasonable

description of the site—site correlation functions and structure factor. However, it is found that small errors in the determination of the structure have a very large effect in the equation of state, and the results depend dramatically on the closures employed to solve the integral equations [212, 213].

Another popular approach is that of Hall and coworkers, who have attempted to extend the Flory-Huggins ideas to off–lattice polymer solutions, yielding first the Generalized Flory and then the Generalized Flory Dimer theories [214, 215]. The GFD theory provides a simple and tractable equation of state and produces rather accurate results for hard sphere chains. The drawback of this approach is that there is no unique way to extend it to more complicated cases, such as mixtures of polymer + solvent [216], heteropolymers [217], systems with attractive interactions [218]; and it is difficult to include chemical details in a straightforward manner [212, 219, 220].

An interesting approach towards an accurate and rigorous equation of state for polymers has its footing in a rather different field, namely, that of chemical equilibrium of simple fluids. In a series of papers, Wertheim developed a perturbation theory especially devised to deal with the equation of state of associating fluids [221, 222, 223, 224]. By studying the chemical association of spherical monomers in the limit of infinite association, it was found that this theoretical treatment yields results for dimers [225], or even, polydisperse polymers of arbitrary length [226]. An important feature in this perturbation theory is that it is formal and rigorous so that the results may be improved successively by adding higher order perturbation contributions. In practice, most of the time one considers only the first order contribution, TPT1, although some results have been reported at the level of second order perturbations (TPT2) [226, 227, 228]. Already at the level of first order the theory is quite accurate, but more importantly, of an enormous versatility. This was shown by Jackson, Chapman, and Gubbins [229, 230], who reformulated and generalized the complex functional formalism of Wertheim in such a way that one can consider the equation of state of simple associating fluids [231, 232, 233]; chains of different length [234, 235, 236, 237, 238, 239], including associating chains [240]; heteropolymers [241, 242]; mixtures of polymer and solvent [243, 244]; and of polymer plus colloids [245], all based on a single unified framework. Very recently, Vega et al. have shown that the formalism of TPT1 is not only applicable to the liquid phase, but it also provides an appropriate framework to describe solid phases of polymers [246, 247, 248]. Another very powerful feature of TPT1 is that it can be applied in a straightforward manner to chains made of attractive interaction sites [231, 233, 249]. Incorporating the dispersive forces right away into the reference system has proven to be very successful, and accurate results have been obtained for Lennard–Jones [234, 236, 238, 240, 250], square well [237, 251] and Yukawa chains [252]. Also the phase coexistence of pure polymer chains and mixtures has been studied and fairly good agreement has been found [238, 240, 244, 250].

The versatility and simplicity of the theory has made this approach rather attractive for engineering applications. Actually, the first engineering application of TPT1, known as the Self-Associating-Fluid-Theory, or SAFT [253, 254], is now employed many times as an alternative name for TPT1. Since the development of SAFT,

however, many different TPT1 versions have appeared, the difference between them being the different liquid state theories which are employed to describe the reference fluid. These equations of state have been employed to describe pure chain molecules [254, 255, 256], as well as their mixtures [257, 258, 259, 260, 261, 262, 263, 264, 265, 266, 267]. Many other different applications have been reported and the interested reader is referred to a recent review on the subject [268].

4.2 Thermodynamic Perturbation Theory

4.2.1 *Intuitive Approach*

Although the original work of Wertheim is mathematically very involved, the underlying physical idea leading to TPT1 may be described in terms of much simpler arguments [269, 270, 271]. The situation is simplified further if one ignores altogether the possibility of partial association [271]. Consider a reference system, made of n_m free monomers. Then the free energy cost required to bring two such monomers a distance r apart will be given by the potential of mean force $W(r)$ [272]. Now, the potential of mean force is expressed conveniently in terms of the pair correlation function, $W(r) = -k_B T \ln g(r)$. Accordingly, the work required to bond two atoms together will be $W(\ell) = -k_B T \ln g(\ell)$, with ℓ being the bond length. In order to form a chain of N monomers, we will need to make $N - 1$ such bonds. As a result, we may consider that the free energy difference between a fluid containing $n = n_m/N$ polymers, and an analogous reference system with n_m monomers is simply expressed as:

$$F - F_{\text{ref}} = -k_B T (N-1) \ln g(\ell) \tag{101}$$

where F_{ref} stands for the free energy of the reference system of unbonded monomers. A similar argument allows to measure the free energy difference between an ideal gas of polymers and an ideal gas of monomers. The difference in this case is that $g(\ell) = \exp(-\beta u(\ell))$, where u is the pair potential between the reference system of unbonded monomers. We may therefore write:

$$F^{ig} - F^{ig}_{\text{ref}} = -k_B T (N-1) u(\ell) \; . \tag{102}$$

In order to relate the free energy of the polymer chain to that of the reference fluid, we now consider a thermodynamic cycle which is the result of summing four different free energy contributions:

$$[F - F_{\text{ref}}] + [F_{\text{ref}} - F^{\text{ig}}_{\text{ref}}] + [F^{\text{ig}}_{\text{ref}} - F^{\text{ig}}] + [F^{\text{ig}} - F] = 0 \; . \tag{103}$$

Clearly, the four contributions add up to zero. By definition, however, the second and fourth contributions are ΔF and ΔF_{ref}, the residual free energies of the polymer and reference systems, respectively. Substitution of Eq. (101–102) into the above expression then yields:

$$\frac{\Delta F}{nk_BT} = N\frac{\Delta F_{\text{ref}}}{n_m k_B T} - (N-1)\ln y(\ell) \tag{104}$$

where y is the background correlation function, defined as $y = g\, e^{\beta u}$. In this way, we are able to express the residual Helmholtz free energy of the polymer system, ΔF, in terms of the properties of the reference monomer system, namely, the residual free energy, ΔF_{ref}, and the background correlation function, $y(\ell)$. The above result is Wertheim's TPT1 result for the equation of state of pure polymer chains of length N and fixed bond length [226, 230].

In Sects. 4.3 and 4.4, we will make quantitative tests of this equation of state. However, some of its limitations become already apparent. First of all, the above expression only gives residual free energies. This means that no information on the single chain partition function is given. Furthermore, the effect of chain connectivity is included only at the level of two body correlations. This means that the theory cannot correctly predict effects which are related to changes in the configuration of the polymer. Particularly, the trivial linear chain length dependence implies that the ith virial coefficient scales as N^i, independent of the 'solvent' quality (i.e., the temperature). Contrarily, scaling arguments suggest that the virial coefficients of polymers scale such as $N^{(i-1)\nu d}$, where ν is an exponent governing the size of the polymer and varies from $\nu = 0.5$ to $\nu = 0.58$, depending on whether the solvent is marginally bad (low temperature) or good (high temperature). This scaling behavior is well documented for B_2 [273, 274, 275, 276, 277, 278] and B_3 [279, 280], but it is not altogether clear whether it holds for B_4 and higher order coefficients [280]. On the other hand, at high densities the linear dependence of the free energy on chain length is known to be correct [281]. Some attempts to reconcile these two limiting scaling behaviors have been proposed recently [282, 283]. Another limitation of TPT1 is that the perturbation to the unbonded reference monomer system is small only if the packing fraction of the system does not change significantly when forming the chains. Obviously, this can only hold true if the monomers bond tangentially, i.e., provided that there is no significant overlap. Although successful extension to chains of overlapping spheres have been proposed, this is at the cost of employing ad-hoc assumptions which are not valid for chains with attractive interactions [284, 285, 286, 287, 288, 289, 290]. Finally, it is clear that the simple treatment considered here provides no information whatsoever on intra- or intermolecular structure. We note, however, that the original approach by Wertheim is cast in the form of a functional theory which allows to extract information of this kind [227, 291].

4.2.2
Scaling Laws for the Critical Properties

Although quantitative comparison of TPT1 requires to consider some specific liquid state theory for the reference fluid, TPT1 already provides a great deal of information on the critical properties without the need of making any specific assumption concerning the reference fluid. To see this, let us start by assuming that the monomer density, ϕ, becomes small for large chain lengths, as suggested by the Flory–Huggins

theory (cf. Sect. 2.1). In this case, one can describe the equation of state in terms of a truncated virial series.

$$\frac{p}{k_B T} = \frac{\phi}{N} + \frac{B_2(T)}{N^2}\phi^2 + \frac{B_3(T)}{N^3}\phi^3 \; . \tag{105}$$

By applying the conditions for the critical point of pure fluids, we obtain a set of equations for the critical temperature and density:

$$B_2(T_{\rm crit}) + \sqrt{3B_3(T_{\rm crit})} = 0 \tag{106}$$

$$\sqrt{3B_3(T_{\rm crit})}\frac{\phi_{\rm crit}}{N} - 1 = 0 \; . \tag{107}$$

Making a Taylor expansion in powers of the density, the first and second virial coefficients predicted by TPT1 are found to be:

$$\begin{aligned} B_2 &= N^2\left(b_2 - \tfrac{N-1}{N}a_2\right) \\ B_3 &= N^3\left(b_3 - \tfrac{N-1}{N}a_3\right) \end{aligned} \tag{108}$$

where b_2 and b_3 are the second and third virial coefficients of the reference fluid of non–bonded monomers, while a_2 and a_3 are the zeroth and first order coefficients in a density expansion of $\partial \ln \delta / \partial \phi$. Of course, all these quantities are chain length independent.

Now, in order to solve Eq. (106) for the critical temperature we will need to linearize the virial coefficients with respect to the temperature. To do so, let us assume that there is a finite asymptotic critical temperature in the limit of infinite chain length, which we call Θ, in analogy to the polymer + solvent case. We now make a series expansion of B_2 and B_3 in powers of $\Delta T = \Theta - T$ up to first order, and consider the limit of this expression for large N, leading to

$$\begin{aligned} B_2(T) &= N^2\left(C_2 - C_2'\Delta T\right) \\ B_3(T) &= N^3\left(C_3 - C_3'\Delta T\right) \end{aligned} \tag{109}$$

where $C_2 = b_2(\Theta) - a_2(\Theta)$ and $C_3 = b_3(\Theta) - a_3(\Theta)$ while C_2' and C_3' are the corresponding derivatives with respect to temperature. Substitution of the linearized virial coefficients into the condition for the critical temperature leads to a quadratic equation for ΔT. Solving this equation yields $\Delta T_{\rm crit}(N)$, defined as $\Theta - T_{\rm crit}(N)$:

$$\Delta T_{\rm crit}(N) - \frac{C_2}{C_2'} = \pm\frac{1}{2C_2'^2}\left(12C_2'^2C_3 - 12C_2C_2'C_3' + 9C_3'^2\frac{1}{N}\right)^{1/2} \; \frac{1}{N^{1/2}} \; - \frac{3C_3'}{2C_2'^2} \; \frac{1}{N} \; . \tag{110}$$

This equation shows that $\Delta T_{\rm crit}(N)$ must reach an asymptotic finite value, since the right-hand-side term should ultimately vanish for large N. The requirement for $T_{\rm crit}(N)$ to attain a finite asymptotic critical temperature equal to Θ is then obeyed provided that C_2 vanishes. If we now notice that

$$\lim_{N\to\infty} B_2(\Theta) = N^2 C_2 \ . \tag{111}$$

we arrive at the conclusion that indeed C_2 must vanish at the Boyle temperature of the infinitely long polymer, T_B^{∞}, thus identifying the Θ temperature with the Boyle temperature of the infinitely long polymer.

The case of the critical density is much simpler. Substitution of the expression for B_3 in the condition for the critical density, Eq. (107), shows that:

$$\phi_{\text{crit}}(N) \propto N^{-1/2} \tag{112}$$

as predicted by the Flory–Huggins theory. Also note that the above arguments apply regardless of the specific form used to describe the reference fluid (thermodynamics and structure).

Another interesting issue is the apparent universality of the compressibility factor as predicted by the truncated virial expansion of Eq. (105). By substitution of Eq. (106–107) into the Eq. (105), it may be shown that Z_{crit} is given by:

$$Z_{\text{crit}}(N) = \frac{N p_{\text{crit}}}{\phi_{\text{crit}} k_B T_{\text{crit}}} = \frac{1}{3} + \frac{B_4}{(3B_3)^{3/2}} + \cdots \ . \tag{113}$$

This result is independent on whatever assumption is made concerning the actual N dependence of the virial coefficients, as long as the ratio of B_i to $B_3^{3/2}$ vanishes (with $i > 3$). In the case of TPT1 this is indeed the case, such that a finite asymptotic critical compressibility factor of about $1/3$ is predicted in the limit of infinite chain length, irrespective of the nature of the polymer. This implies that the critical pressure should decay as $N^{-3/2}$.

An interesting result follows when one considers that the Θ temperature is also the Boyle temperature of the infinitely long polymer. From the expression of B_2, Eq.109, we see that this temperature is attained when the following condition is obeyed:

$$b_2(\Theta) - a_2(\Theta) = 0 \ . \tag{114}$$

By employing results from liquid state theory, Vega et al. show that one can transform the above equation further, in the following manner [271]:

$$b_2(\Theta) - \frac{2}{3} b_2^{md}(\Theta) = 0 \tag{115}$$

where b_2^{md} is simply the crossed second virial coefficient between a monomer and a dimer. Hence it is possible to determine the Θ temperature of a polymer from the low density virial coefficients of a simple fluid.

Before closing this section, it is interesting to discuss the similarity of these predictions with those obtained from the Flory–Huggins theory. It is clear that for both T_{crit} and ϕ_{crit} the chain length dependence is the same. Also note that the leading terms of the expansion Eq. (110) are of order $N^{-1/2}$ and N^{-1}, just as predicted by the Flory–Huggins theory. In this case, there is one difference, however. Namely, the

value taken by the coefficients. It is very usual to employ a Flory–Schulz plot in order to extrapolate Θ temperatures from short chain data, and there it is assumed that the ratio of the $N^{-1/2}$ to the N^{-1} coefficient is 2. From TPT1, however, it is observed that there is no particular reason to assume that this ratio should be precisely 2. Actually, according to TPT1 this ratio takes a non-trivial value which should depend on the monomer properties.

Recently, Chatterjee and Schweizer [292] have analyzed the behavior of the critical point of infinite chain lengths using the P-RISM theory. For two of the closures employed, the same behavior as that predicted by TPT1 is observed, at least concerning (i) vanishing critical density and (ii) finite critical temperature. The power laws are, however, different. The critical monomer density is predicted to vanish with a weaker dependence which may be either $N^{-1/3}$ or $N^{-1/4}$ depending on whether the RMPY/HTA or the MSA closures are used. The critical temperature is predicted to reach a finite critical value with the same exponents as the critical density. It is pleasing to see that TPT1 is able to give a unique conclusion, independent of the molecular theory used to describe the monomer fluid. Unfortunately, the exact scaling laws for the asymptotic critical properties of a polymer remain a matter of debate. Both Flory–Huggins and TPT1, as well as renormalization arguments by de Gennes [3] predict an exponent of $-1/2$ for ϕ_{crit}. Experiments [51, 53, 55, 57] and simulations [82, 85, 116] have found exponents in the range of about 0.3–0.4, but it is not clear whether the chain lengths considered had attained the scaling regime. As noted in Sect. 2.2, it has been argued that considering long enough chains could lead to the expected $-1/2$ exponent, but that smaller apparent exponents in experiments and simulations result when shorter chain lengths are considered [64, 293, 294].

4.2.3
General Expression for Pure Polymers and Mixtures

Previously we have seen a heuristic derivation of TPT1 for the special case of a pure polymer with fixed bond length. Actually, TPT1 is a much more general theory which allows to describe a wide variety of systems. We will henceforth restrict our attention to the special case of multicomponent mixtures. We will assume that each of the components is a chain molecule, described as an ensemble of N_i identical beads, which interact with each other and with any other bead in the system by means of a site–site potential, V_{ij}. Furthermore, adjacent beads on the same molecule interact by means of a bonding potential, Φ_{ii}. The composition of the mixture may be described by means of the total molecular density, ρ, and the molar fractions of each component, x_i. According to TPT1, the total Helmholtz free energy of the multicomponent mixture may be described in terms of three different contributions [237, 253]:

$$\frac{F}{nk_BT} = \frac{F^{\text{ig}}}{nk_BT} + \frac{F^{\text{mono}}}{nk_BT} + \frac{F^{\text{chain}}}{nk_BT} \tag{116}$$

where n is the total number of molecules in the system. In the above equation, F^{ig} is the free energy of an ideal gas of chains; F^{mono} is the residual free energy of

a mixture of unbonded monomers; and F^{chain} is the free energy required to form the actual chain fluid from the monomer fluid. Let us now consider each of these contributions in turn:

Ideal contribution: The Helmholtz free energy of an ideal gas of molecules is given by,

$$\frac{F^{\text{ig}}}{nk_BT} = \sum x_i \ln \rho x_i \Lambda_i^3 - 1 \tag{117}$$

where $x_i = n_i/n$, the molar fraction, is defined as the ratio of molecules of component i to the total number of molecules in the system; and Λ_i is the 'molecular' thermal wavelength of species i. Note that this thermal wavelength includes the non–trivial single chain partition function, a problem which is not addressed by TPT1. Fortunately, for phase equilibria calculations a lack of knowledge on Λ_i is unimportant, as it takes the same value in each of the coexisting phases.

Monomer contribution: The residual monomer contribution to the free energy is given by:

$$\frac{F^{\text{mono}}}{nk_BT} = \sum x_i N_i \frac{F^{\text{m}}}{n_m k_B T} \tag{118}$$

where F^{m} is the residual free energy of a mixture of unbonded monomers, while n_m is the total number of monomers in the system.

Chain contribution: The free energy required to form the chain fluid from the reference fluid of unbonded monomers is given by:

$$\frac{F^{\text{chain}}}{nk_BT} = -\sum x_i (N_i - 1) \ln \delta_{ii}/\delta_{ii}^0 \tag{119}$$

where $\delta_{ii}(T, \phi, x)$, the 'bonding strength' between monomers of type i, is expressed in terms of the radial distribution function of the monomer fluid, $g_{ii}(r)$, and the bonding potential, Φ_{ii}:

$$\delta_{ii} = \int g_{ii}(r) \exp(-\Phi_{ii}(r)/k_BT) \mathrm{d}\mathbf{r} \tag{120}$$

while $\delta_{ii}^0(T, x)$ is the corresponding quantity evaluated at zero density. When evaluating δ_{ii} one must make sure that the integrand vanishes for distances much larger than the bond distance. Otherwise the integral will not converge. Hence, in those cases where the zero of the bonding potential is set at infinite distance, one adds a $-g_{ii}(r)$ term in the integrand to ensure convergence [230]. This is not required here, because we assume that the bonding potential diverges at large distances.

Note that within the TPT1 theory, the problem of describing the thermodynamics of a system of chain molecules is converted into a much simpler problem, namely,

that of describing the structure and thermodynamics of a mixture of monomers whose total monomer density, ϕ, is given by:

$$\phi = \sum N_i x_i \rho \tag{121}$$

and whose monomer molar fractions, y_i, are given by:

$$y_i = \frac{N_i x_i}{\sum_l N_l x_l} \,. \tag{122}$$

In order to calculate the phase coexistence predicted by TPT1, expressions for the compressibility factor and chemical potential are also required. The compressibility factor is obtained by using the following standard thermodynamic relation:

$$Z = \phi \frac{\partial}{\partial \phi} \frac{A}{n k_B T} \,. \tag{123}$$

The above equation then leads to:

$$Z = 1 + \sum x_i N_i Z^m - \sum x_i (N_i - 1) \phi \frac{\partial \ln \delta_{ii}}{\partial \phi} \tag{124}$$

where Z^m is the residual compressibility factor of the mixture of monomers evaluated at the monomer density. As to the chemical potentials, they are obtained using the following equation [6]:

$$\beta \mu_i = \frac{F}{n k_B T} + Z + (1 - x_i) \Delta_i \tag{125}$$

where

$$\Delta_i = \frac{\partial}{\partial x_i} \frac{F}{n k_B T} \tag{126}$$

Care must be taken when deriving the free energy with respect to molar fraction, because a change in x will result in a change in both the monomer molar fraction and the monomer density. When this is taken into account, one obtains:

$$\Delta_1 = \Delta_1^{\text{ig}} + \Delta_1^{\text{mono}} + \Delta_1^{\text{chain}} \,. \tag{127}$$

The different contributions in the above equation are given by:

$$\Delta_1^{\text{ig}} = \ln x_1 \Lambda_1 - \ln(1 - x_1) \Lambda_2 \tag{128}$$

$$\Delta_1^{\text{mono}} = (N_1 - N_2) \frac{F^m}{n k_B T} + \sum x_i N_i \left[\frac{\partial y_1}{\partial x_1} \Delta_1^m + \frac{\partial \phi}{\partial x_1} \frac{Z^m}{\phi} \right] \tag{129}$$

$$\begin{aligned} \Delta_1^{\text{chain}} = -\Bigg\{ & (N_1 - 1) \ln \frac{\delta_{11}}{\delta_{11}^0} - (N_2 - 1) \ln \frac{\delta_{22}}{\delta_{22}^0} + \\ & \sum x_i N_i \left[\frac{\partial y_1}{\partial x_1} \frac{\partial}{\partial y_1} \ln \frac{\delta_{ii}}{\delta_{ii}^0} + \frac{\partial \phi}{\partial x_1} \frac{\partial}{\partial \phi} \ln \frac{\delta_{ii}}{\delta_{ii}^0} \right] \Bigg\} \end{aligned} \tag{130}$$

where Δ_i^m is obtained from Eq. (126) with F replaced by F^m and x_i replaced by y_i. Similar equations hold for Δ_2, but these are unnecessary, given that $\Delta_2 = -\Delta_1$.

4.2.4
Calculation of the Monomer and Chain Contributions

In the preceding section, we have shown general results for TPT1, i.e., we have written expressions for the free energy, compressibility factor, and chemical potential in terms of the corresponding properties of a reference fluid of unbonded monomers. Depending on the way this reference system is described, one obtains different forms of TPT1. For example, Chapman et al. considered a Carnahan—Starling fluid with a parameterized attractive contribution, leading to the well–known SAFT equation of state [253, 254]. Johnson et al. and Blas and Vega considered a very accurate liquid state theory which results from a fit to Molecular Dynamics data, yielding the soft-SAFT equation of state [234]. Gill-Villegas et al. used a Barker—Henderson perturbation theory, and the resulting TPT1 version is known as SAFT-VR [237]. Other versions have been proposed, such as that of Nikitin et al., who employ the simple van der Waals fluid as a reference [295, 296], or that of Yelash and Kraska, who employ a Carnahan—Starling + mean-field contribution [297]. Although less accurate, the last two versions are to be preferred when a thorough exploration of the phase diagram is sought [294, 298].

In what follows, we will restrict our attention to a mixture of model polymers as described in Sect. 3.1, with the chain length N_i and Lennard–Jones parameters yet unspecified. In this case, the most convenient reference system is a mixture of Lennard–Jones monomers, and the perturbative bonding potential is a FENE potential (Eq.47). Let us now consider how to describe such a reference mixture and how to calculate the monomer and chain contributions.

Monomer contribution: As an alternative to the mentioned TPT1 versions, we will attempt to describe the thermodynamics and structure of the binary reference mixture of monomers by means of a second order perturbation theory, based on an analytical solution of the Mean Spherical Approximation (MSA) of simple fluids [299, 317]. In this theory, the free energy of the mixture of monomers is described perturbatively in terms of the properties of an auxiliary fluid which contains only repulsive interactions. We therefore split the full Lennard—Jones potential, $V_{ij}(r)$ into repulsive and perturbative contributions as suggested by Barker and Henderson [300], so that the repulsive potential, w_{ij}^{rep}, contains all of the positive part of the Lennard—Jones potential, while the perturbation, w_{ij}^{per} contains all of the negative region:

$$w_{ij}^{\text{rep}}(r) = \begin{cases} V_{ij}(r) & r \le t\sigma_{ij} \\ 0 & r > t\sigma_{ij} \end{cases} \quad \text{and} \quad w_{ij}^{\text{per}}(r) = \begin{cases} 0 & r \le t\sigma_{ij} \\ V_{ij}(r) & r > t\sigma_{ij} \end{cases} \tag{131}$$

where t defines the value of r where w_{ij} becomes negative.

The residual free energy of the system may now be expressed as a perturbation expansion to second order, yielding:

$$\frac{F^m}{n_m k_B T} = \frac{F_0}{n_m k_B T} + \frac{F_1}{n_m k_B T} + \frac{F_2}{n_m k_B T} \tag{132}$$

where F_0 is the residual free energy of the reference mixture with repulsive interactions, while F_1 and F_2 are first and second order perturbations [301]:

$$\frac{F_1}{n_m k_B T} = \frac{1}{2}\phi\beta \sum_i \sum_j y_i y_j \int_{t\sigma_{ij}}^{\infty} g_{ij}^0(r) w_{ij}^{\mathrm{per}}(r) 4\pi r^2 \mathrm{d}r \tag{133}$$

$$\frac{F_2}{n_m k_B T} = \phi\beta \sum_i \sum_j y_i y_j \int_{t\sigma_{ij}}^{\infty} g_{ij}^1(r) w_{ij}^{\mathrm{per}}(r) 4\pi r^2 \mathrm{d}r \ . \tag{134}$$

In the above equations, g_{ij}^0 and g_{ij}^1 are zero and first order contributions in a Taylor expansion of the radial distribution function about the repulsive system.

At this stage, we encounter the difficulty of describing the repulsive system defined in Eq. (131), which is not well known. In order to circumvent this problem, we map the repulsive system on a simpler mixture of hard spheres with appropriate diameter. The key step is then to choose the hard sphere diameters such that the error brought about by this mapping is minimized. In a one component fluid, a suitable choice is to determine the diameter according to the Barker–Henderson prescription [300]. Here we just consider the straightforward extension, so that the hard sphere diameter of species i is calculated as:

$$d_{ii} = \int_0^{\infty} (1 - e^{-\beta w_{ii}^{\mathrm{rep}}(r)}) \mathrm{d}r \ . \tag{135}$$

Direct application of this equation to the unlike interactions would lead to a mixture of non–additive hard spheres, and this is rather inconvenient. Therefore, we choose to determine d_{ij} by using the hard sphere diameters of the pure components and requiring additivity:

$$d_{ij} = \frac{1}{2}(d_{ii} + d_{jj}) \ . \tag{136}$$

More rigorous prescriptions for the determination of d_{ii} are possible. However, such treatments lead to composition dependent diameters [301], and we avoid this complication here.

Once the hard sphere fluid has been appropriately defined, the free energy of the repulsive system may be described using the equation of state of hard sphere binary mixtures proposed by Boublik [302]:

$$\frac{F_0}{n_m k_B T} = \frac{6}{\pi\phi}\left[\left(\frac{\zeta_2^3}{\zeta_3^2} - \zeta_0\right)\ln(1-\zeta_3) + \frac{3\zeta_1\zeta_2}{1-\zeta_3} + \frac{\zeta_2^3}{\zeta_3(1-\zeta_3)^2}\right] \tag{137}$$

where the ζ_l coefficients are defined as:

$$\zeta_l = \frac{\pi}{6}\phi \sum_i y_i d_{ii}^l \ . \tag{138}$$

The first and second order perturbation contributions could be evaluated by using rigorous expressions for g_{ij}^0 and g_{ij}^1 as obtained from an integral equation theory. Such an approach has been recently undertaken with good results [301, 303]. Unfortunately, the expressions are quite lengthy and somewhat inconvenient for further differentiation. For this reason, we will evaluate the perturbative contributions of the free energy by using a Van der Waals like one fluid approximation. In this approximation, one considers that the radial distribution function of the Lennard–Jones fluid mixture may be expressed in terms of the radial distribution function of a pure effective Lennard–Jones fluid with composition dependent parameters, σ_y and ϵ_y, yet to be determined. More specifically, one assumes that $g_{ij}(r)$ may be expressed in terms of the radial distribution function of a pure fluid as follows,

$$g_{ij}(r;\phi,T,y) = g\left(r\frac{\sigma_y}{\sigma_{ij}},\phi,T\right). \tag{139}$$

As it is well known, however, the radial distribution function of a Lennard–Jones fluid may be expressed in terms of a universal radial distribution function, $\tilde{g}$, when r, ϕ and T are scaled appropriately. Accordingly, we may write,

$$g_{ij}(r;\phi,T,y) = \tilde{g}\left(\frac{r}{\sigma_{ij}},\phi^*,T^*\right) \tag{140}$$

where $\phi^* = \phi\sigma_y^3$ and $T^* = k_BT/\epsilon_y$. Using this relation in Eq. (133) and Eq. (134), one finds that the first order perturbation contribution may be expressed as follows:

$$\frac{F_1}{N_m k_B T} = \frac{1}{2}\phi\beta\sum_i\sum_j y_i y_j \epsilon_{ij}\sigma_{ij}^3 \int_{t\sigma_{ij}}^{\infty} \tilde{g}^0(r/\sigma_{ij}) w_{ij}^{\text{per}}(r) 4\pi r^2 \mathrm{d}r \tag{141}$$

and similarly for the second order contribution. If we now make a simple change of variables of the form $s \to r/\sigma_{ij}$ it is then found that the perturbation contributions may be expressed in terms of the perturbation contribution of a pure Lennard–Jones fluid at reduced temperature and density T^* and ϕ^*:

$$\frac{F_1(\phi,T,y)}{n_m k_B T} = \frac{F_1(\phi^*,T^*)}{n_m k_B T} \tag{142}$$

and similarly for F_2. The above expression holds provided that σ_y and ϵ_y are chosen such that the following relation is obeyed:

$$\epsilon_y\sigma_y^3 = \sum\sum y_i y_j \sigma_{ij}^3 \epsilon_{ij}\ . \tag{143}$$

The actual value for σ_x is now determined by requiring that the one–fluid theory predicts the same compressibility as the actual fluid mixture [304]. In this way, one obtains:

$$\sigma_y^3 = \sum\sum y_i y_j \sigma_{ij}^3\ . \tag{144}$$

What is now required are closed expressions for the first and second order contributions of a pure fluid. To this end, we employ a theory that we have recently applied successfully to study both bulk [238] and interfacial properties [99]. This theory is based on a perturbation expansion proposed recently for the Lennard–Jones potential [299]. Although the expressions are obtained in a closed analytical form, they are rather lengthy and we refer the reader to the original paper for further details [238].

Chain contribution: Once the thermodynamics of the reference monomer mixture is known, we will now require to determine the bonding contribution, F^{chain}. This is done by employing Eq. (119–120), together with a specific form for the radial distribution function of the mixture, and the bonding potential, which we consider to be of the FENE type (Eq. (47)). In principle, the radial distribution function could be obtained from an integral equation theory. In practice, however, such equations may only be solved by numerical calculations. For this reason, we will employ again a one–fluid approximation for g_{ij}. Substitution of Eq. (140) into Eq. (120), together with the change of variable $s \to r/\sigma_{ii}$, then leads to:

$$\delta_{ii} = 4\pi\sigma_{ii}^3 \int_0^{R_{ii}/\sigma_{ii}} g(s;\phi^*,T^*)\exp(-\Phi_{ii}(s)/k_BT)s^2\mathrm{d}s \tag{145}$$

where R_{ii} is the bond distance at which the FENE potential (Eq.47) diverges (cf. Eq. (47)). Note that the use of Eq. (140) leads to a bonding strength that depends both on the effective fluid temperature, T^*, and the actual temperature of the system, T. For this reason, the one–fluid approximation for g_{ij} does not lead to a one–fluid approximation for the bonding strength (i.e., $\delta_{ii}(\phi, T, x)$ may not be approximated by $\delta(\phi^*, T^*)$). An explicit expression for Eq. (145) is obtained by using the simplified exponential approximation for the radial distribution function of a one–component fluid [299]. This, on its turn, requires knowledge of the MSA solution for $g(r)$, which may be obtained from an analytical solution proposed recently [305]. In this way, a rather lengthy but tractable expression for Eq. (145) is obtained.

4.3 Application to Pure Polymers

4.3.1 *Application to a Pure Model Polymer*

In the previous section we have described how to implement TPT1 for a mixture of Lennard–Jones chains with a FENE bonding potential. Before considering binary mixtures, however, we shall restrict our attention to the particular case of a one component system of polymers. In order to describe the thermodynamic properties of such a system, we will consider two TPT1 implementations, which we denote TPT1-MSA and TPT1-RHNC. In TPT1-MSA, we employ the fully analytic equation of state described in the previous section. In TPT1-RHNC, the Lennard–Jones reference system is described by means of the Reference Hypernetted Chain theory (RHNC). This is an integral equation theory which can only be solved numerically,

but has the advantage of being very accurate. In this way, we will be able to identify whether the limitations in TPT1 are related to a particular way of describing the reference system, or, on the contrary, are related to the approximations inherent to TPT1.

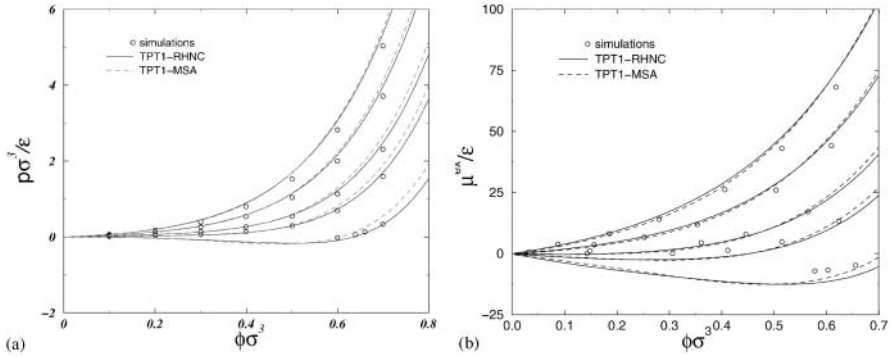

Fig. 22. Pressure (**a**) and chemical potential (**b**) against monomer density for chains of 10 monomers. *Symbols* are nVT simulation data while *lines* are predictions from TPT1; *full line*, RHNC version; *dashed line*, MSA version. From *top* to *bottom*, pressure isotherms at $k_BT/\epsilon = 5, 4, 3, 2.5$ and 1.68 in reduced Lennard-Jones units (adapted from [238])

Let us first examine thermodynamic data for chains of 10 monomers. Figure 22 compares the predictions of TPT1 for several pressure isotherms (k_BT/ϵ=5, 4, 3, 2.5, and 1.68) with simulation results. Both the RHNC and MSA versions of the theory are seen to give rather good estimates; at the highest temperatures, far above the estimated Θ point of our model (see below) as well as at the lowest, a sub-critical isotherm. Overall, the RHNC version seems to describe the isotherms slightly better. Results for the excess chemical potential of the chains are also shown. The agreement is quite satisfactory, though not as good as those for the pressure isotherms, especially at the lowest temperatures and densities. Indeed, the main assumption of TPT1, namely, that the local environment of a monomer in the polymer fluid is similar to that of the reference fluid breaks down in the low density limit. The fluid is then made of isolated clusters of N monomers, rather than of single monomers uniformly distributed in space. Likewise, the theory is unable to describe the density dependence of the single chain internal energy and conformational entropy.

The liquid–vapor coexistence curve of the 10-mer as obtained from simulation and theory is shown in Fig. 23. Both the RHNC and MSA versions overestimate the critical temperature as obtained from simulation by about 15%. Of course, this is expected for any classical theory. On the other hand, far away from the critical point, results from both versions of the theory yield good agreement with simulation. The MSA version is somewhat more convenient, however, because it allows us to calculate the coexistence at low temperatures with no additional cost, while it becomes rather problematic to calculate the coexistence for the RHNC version below

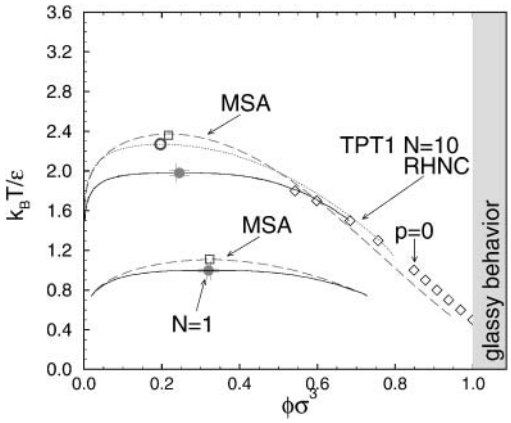

Fig. 23. Liquid–vapor coexistence curves of a 10-mer as obtained from grandcanonical simulations (*solid lines*) and npT simulations at $p = 0$ (*diamonds*), compared with TPT1-RHNC (*dotted line*) and TPT1-MSA (*dashed line*). The *filled circle* presents the critical point as extracted from finite size scaling of the MC data. The *open circle* and the *open square* denote the critical point of the TPT1-RHNC and the TPT1-MSA, respectively. The simulation results and TPT1-MSA calculations for monomers ($N = 1$) are also included (adapted from [238])

the reference fluid critical temperature. The reason for this is that the RHNC integral equation presents a region of no solutions below this point, such that the resulting equation of state is no longer defined inside the liquid-vapor envelope.

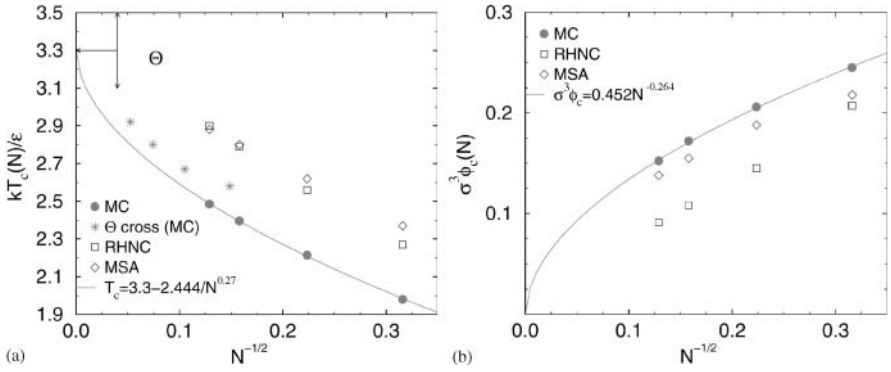

Fig. 24. Critical temperatures (**a**) and critical monomer densities (**b**) in MC simulations and perturbation theory. In panel (**a**) the temperatures of the intersections of $R_e^2(T)/(N-1)$ for neighboring chain lengths are also included. For $N \to \infty$ the values tend to the Θ temperature (adapted from [238])

We have also investigated the critical points of chains with $N = 20, 40$, and 60. Table 3 gives a summary of the simulation results, obtained by finite size scaling,

Table 3. Critical temperature, T_{crit} and critical monomer density, ϕ_{crit} as obtained from simulation (MC) and from TPT1 with either the RHNC version or the MSA version for the structure and thermodynamics of the reference fluid (adapted from [238])

	$k_B T_{\text{crit}}/\epsilon$			$\phi_{\text{crit}}\sigma^3$		
n	(MC)	(RHNC)	(MSA)	(MC)	(RHNC)	(MSA)
1	1.00	1.02	1.11	0.321	0.376	0.323
5	1.72	1.92	2.03	0.270	0.250	0.255
10	1.98	2.27	2.36	0.245	0.207	0.217
20	2.21	2.56	2.62	0.206	0.145	0.184
40	2.40	2.79	2.81	0.172	0.108	0.150
60	2.48	2.90	2.88	0.152	0.091	0.140
∞	~ 3.3	3.44	3.39	–	0	0

together with predictions from TPT1-RHNC and TPT1-MSA. Both versions overestimate the critical temperatures by about 15% for all chain lengths studied. However, the MSA and RHNC predictions seem to converge as the chain length increases. On the other hand, the critical monomer densities are always underestimated, though the MSA version seems to give a much better agreement than the RHNC version. In the latter theory the density decreases much too fast compared to the MC results. The overall behavior of the critical parameters is illustrated in Fig. 24, where both T_{crit} and ϕ_{crit} are plotted against $N^{-1/2}$, the predicted asymptotic scaling law for both of these properties. It is seen that for chain lengths up to 60 monomers, the critical properties are far from reaching their asymptotic behavior, so that the simulations do not allow us to assess unambiguously the predicted scaling laws.

Although the calculation of the critical point of fluids larger than about 100 monomers by computer simulation becomes prohibitively expensive, we can estimate the Θ point of our polymer model by an analysis of the temperature dependence of the polymer extension [238]. Extrapolation of the results gives as an estimate $\Theta \approx 3.32$. As to the theory, fitting the critical temperature predicted by TPT1-RHNC to a power law of the form $T_{\text{crit}} = T_{\text{crit}}^{\infty} + bN^{-1/2} + cN^{-1}$ in the range 10^2 to 10^7 gives $k_B T_{\text{crit}}^{\infty}/\epsilon = 3.44$. On the other hand, by searching for the root in Eq. (114), we find that TPT1-MSA predicts $k_B T_{\text{crit}}^{\infty}/\epsilon = 3.39$.[4] Assuming that the Θ point is indeed the critical point of the infinitely long chain, as suggested by the considerations of Sect. 3, it would seem that TPT1 is capable of giving an excellent prediction for the Θ point of the polymer, even though the actual prediction may vary somewhat depending on the theory used to describe the reference fluid. Similar good agreement has also been found for square well chains [271].

[4] This value is significantly higher than that reported earlier, $k_B T_{\text{crit}}^{\infty}/\epsilon = 3.14$ [238], which was affected by numerical inaccuracy of the equation of state at low densities.

4.3.2 *Application to Alkanes*

Essentially, the equation of state that has been proposed describes the thermodynamics of an idealized model made of tangent Lennard—Jones beads. The parameters of the model are the chain length, N, and the Lennard—Jones range, σ and energy, ϵ, parameters of the interaction sites. Despite of the idealized character of the model, one may still be able to describe real substances if N, σ and ϵ are chosen appropriately, by fitting the theoretical predictions to some well known experimental properties of the substance under consideration. This kind of approach has been applied in a coarse–grained manner for the n-alkane series, by considering N, σ and ϵ as linear functions of the molecular mass [255, 256, 262, 263, 265]. In this section we will propose very simple arguments which allow us to extract more fine chemical information from the parameters of the coarse–grained model. We emphasize, however, that a physical clear significance of the molecular parameters from knowledge of the equation of state may be only obtained unambiguously by using an atomistic molecular model [278, 286, 290, 306].

Table 4. Molecular parameters for TPT1 as obtained from a fit to critical properties. v_i is measured in units of Å^3, while $\epsilon_{ij}\sigma_{ij}^3/k_B$ is given in units of KÅ^3

l_1	l_2	v_1	v_2	$\epsilon_{11}\sigma_{11}^3/k_B$	$\epsilon_{12}\sigma_{12}^3/k_B$	$\epsilon_{22}\sigma_{22}^3/k_B$
1.6250	0.3125	75.44	24.64	6605	4664	2889

Model fitting: As noted above, one could fit a set of N, σ, and ϵ parameters to the coexistence properties of each alkane of the series, and then make a linear regression on the parameters. However, in order to make the theory as predictive as possible, it would be desirable to make the fit from a minimum of information, and in such a way that the N, σ, and ϵ parameters determined for some of the members of the series may be employed to determine those parameters required for the remaining members. This approach is justified, because the building blocks of n-alkanes are just CH_3 and CH_2 units. As a reasonable approximation, one may consider that these units are identical for the different alkanes. Therefore, it will be sufficient to know the properties of a few members of the series in order to determine the energy parameters of CH_3 and CH_2 and then use this information to determine the properties of just any other alkane.

First, let us consider a melt of model polymers with site-site potential u and local monomer density $\phi(\mathbf{r})$. The average internal energy of such melt will be given by:

$$U \propto \int u(\mathbf{r}_1, \mathbf{r}_2)\phi(\mathbf{r}_1)\phi(\mathbf{r}_2)\,\mathrm{d}\mathbf{r}_1\,\mathrm{d}\mathbf{r}_2\ . \tag{146}$$

Considering that the system is uniform and that $u(\mathbf{r}_1, \mathbf{r}_2)$ is a central potential, we may assume that the total energy of the system is about $U \propto V\phi^2\epsilon\sigma^3$, where ϵ and

σ are effective Lennard–Jones parameters. On the other hand, on a more detailed level we may consider that the polymer is made of different sites, say CH_3 and CH_2 sites in the case of an n-alkane. In order to account explicitely for this fact, the total energy should be written as:

$$U \propto \sum_{i,j} \int u_{ij}(\mathbf{r}_1, \mathbf{r}_2)\phi_i(\mathbf{r}_1)\phi_j(\mathbf{r}_2)\, \mathrm{d}\mathbf{r}_1\, \mathrm{d}\mathbf{r}_2 \tag{147}$$

where the sum runs over all possible types of sites; ϕ_i is the total density of site i and u_{ij} is a site–site potential. Roughly speaking, we may consider that the above equation is given by $V \sum_{i,j} \phi_i \phi_j \epsilon_{ij} \sigma_{ij}^3$, where ϵ_{ij} and σ_{ij} are site–site Lennard–Jones parameters. Then, the Lennard–Jones parameters of the effective beads of the idealized model should be related with the alkane interaction sites as follows:

$$N^2 \epsilon \sigma^3 = 4\varepsilon_{11}\sigma_{11}^3 + 4(N_c - 2)\varepsilon_{12}\sigma_{12}^3 + (N_c - 2)^2 \varepsilon_{22}\sigma_{22}^3 \tag{148}$$

where 1 and 2 indexes stand for CH_3 and CH_2 sites, respectively; while N_c is the total number of carbon atoms in the chain. This equation is similar to that used by several authors to correlate the energy of effective alkane beads [239, 255, 262, 263, 265]. A quadratic, instead of linear dependence on N is suggested here.

Using similar arguments for the molecular volume, we express the effective size parameter of the idealized chain as:

$$N\sigma^3 = v_1 + v_2(N_c - 2) \tag{149}$$

where v_1 is related to the molecular volume of ethane, while v_2 is related to the volume increments which result from the addition of CH_2 groups into the chain.

Finally, we assume that the number of 'effective' monomers of the idealized model which are necessary to describe the alkane series follows a linear relation with N_c, so that:

$$N = l_1 + l_2(N_c - 2)\ . \tag{150}$$

In order to be able to obtain N, σ, and ϵ as a function of N_c, we fit some experimental properties of the alkane series so as to obtain the values for $\varepsilon_{11}\sigma_{11}^3$, $\varepsilon_{12}\sigma_{12}^3$, $\varepsilon_{22}\sigma_{22}^3$, v_1, v_2, l_1, and l_2. To achieve this goal, we will consider the critical properties.

According to TPT1, the critical properties of the idealized model are universal functions of the chain length if scaled appropriately, i.e., there exist universal functions, $\tilde{T}_{\mathrm{crit}}$, $\tilde{p}_{\mathrm{crit}}$, and $\tilde{\phi}_{\mathrm{crit}}$ such that:

$$\begin{aligned} \tilde{T}_{\mathrm{crit}}(N) &= \tfrac{k_B}{\epsilon} T_{\mathrm{crit}}(N;\sigma,\epsilon) \\ \tilde{p}_{\mathrm{crit}}(N) &= \tfrac{\sigma^3}{\epsilon} p_{\mathrm{crit}}(N;\sigma,\epsilon)\ . \\ \tilde{\phi}_{\mathrm{crit}}(N) &= \sigma^3 \phi_{\mathrm{crit}}(N;\sigma,\epsilon) \end{aligned} \tag{151}$$

Our strategy is to adjust the products $\epsilon_{11}\sigma_{11}^3$, $\epsilon_{12}\sigma_{12}^3$, and $\epsilon_{22}\sigma_{22}^3$, as well as the parameters l_1 and l_2, v_1 and v_2 by fitting predictions of TPT1-MSA to the critical temperatures and densities of the alkane series. The results of the fit are shown in Table 4.

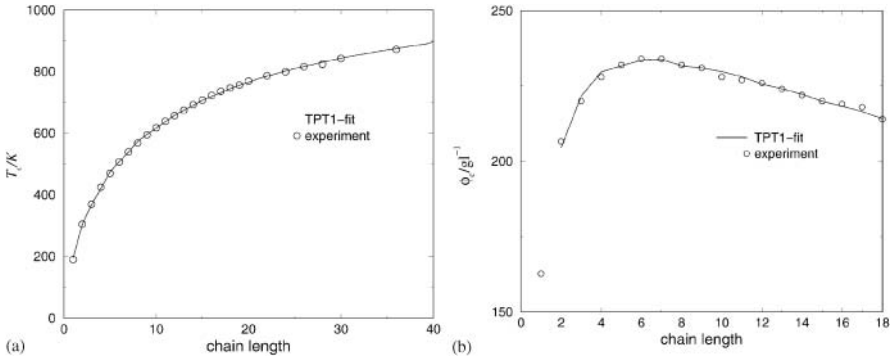

Fig. 25. Critical temperature (**a**) and pressure (**b**) of the n-alkane series as a function of chain length. The *symbols* are results from experiments [307, 308], while the *full lines* are predictions from TPT1

Discussion: Whereas the coarse–grained nature of the molecular model employed does not allow one to expect quantitative agreement with parameters obtained for atomistic models, we do note that the values obtained show qualitative agreement. For the strength parameters, for example, we obtain $\epsilon_{11}\sigma_{11}^3/k_B = 6605\text{K}\text{Å}^3$, $\epsilon_{12}\sigma_{12}^3/k_B = 4664\text{K}\text{Å}^3$ and $\epsilon_{22}\sigma_{22}^3/k_B = 2889\text{K}\text{Å}^3$. These results are consistent with parameters suggested by Vega and López Rodríguez, i.e., $\epsilon_{11}\sigma_{11}^3/k_B = 6278\text{K}\text{Å}^3$, $\epsilon_{12}\sigma_{12}^3/k_B = 4244\text{K}\text{Å}^3$ and $\epsilon_{22}\sigma_{22}^3/k_B = 2868\text{K}\text{Å}^3$, which provide a good fit to second virial calculations [309], and accurately predict critical points with hardly no modification [310, 311]. For the volume parameters similar qualitative trends are observed. Thus, considering that v_1 is the volume of ethane, we may relate a size parameter to the CH_3 group of the order $(1/2v_1)^{1/3} = 3.35$ Å. Similarly, an order of magnitude size parameter for the CH_2 group is $v_2^{1/3} = 2.9$ Å, in reasonable agreement with the typical value of σ in united atom models, of about 3.9 Å [109, 310, 311, 312]. These results are in line with recent findings by Pamies and Vega [265].

In Sect. 3.1 a simple spring–bead model was introduced in order to describe n-hexadecane. Based on simple geometrical arguments for a CO_2 $C_{16}H_{34}$ mixture, it was assumed that a chain of 5 Lennard–Jones sites was appropriate. Considering the fit of Table 4, it is found that TPT1-MSA best describes pure n-hexadecane with an effective chain of 6 beads, somewhat larger than the geometrical estimate. Coincidentally, the increment of effective chain length per carbon atom is 0.3125, which is exactly 5/16, the ratio of effective monomers to actual carbon atoms that we have employed to model hexadecane in Sect. 3.1. As to the Lennard–Jones parameters, the fit for n-hexadecane yields $\epsilon/k_B = 338\text{K}$ and $\sigma = 4.12$ Å, in reasonable agreement with the parameters obtained for the model of Sect. 3.1 from a fit to experimental data ($\epsilon/k_B = 429\text{K}$ and $\sigma = 4.5$ Å).

In Fig. 25 we plot experimental critical temperatures [307, 308] and densities together with the fit obtained from the theory. As it can be seen, the quality of the

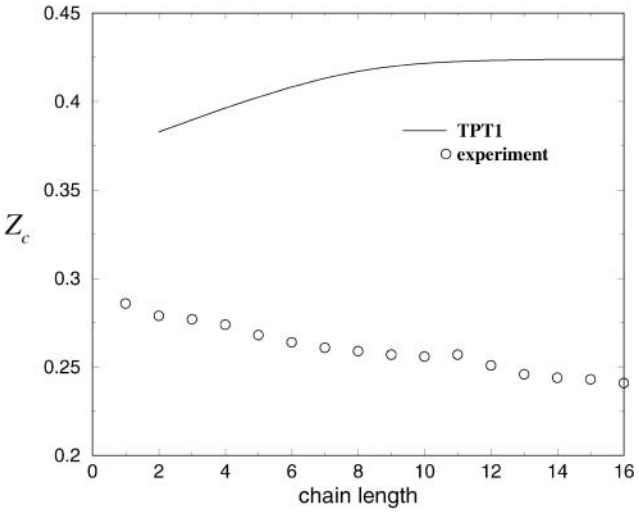

Fig. 26. Critical compressibility factors of the n-alkane series as a function of chain length. The *symbols* are results from experiments [307, 308], while the *full line* is a prediction from TPT1

fit is excellent. TPT1 correctly correlates the critical temperatures, as well as the so-called anomalous behavior of the critical density, ϕ_{crit}, which shows a maximum value for n-hexane. It is interesting to note that when ϕ_{crit} is drawn as a function of N, rather than as a function of N_c, the behavior is rather different, i.e., TPT1 then shows a monotonous decay of the critical density. It has been shown that the occurrence of a maximum in the critical mass density requires the effective chain length to grow at a slower rate than the actual number of monomers [313]. In our approach, this is effectively achieved by means of Eq. (150). In order to correctly predict this behavior without the need of a fit, a fully atomistic molecular model is required [306, 313].

Figure 26 shows the critical compressibility factors as predicted by TPT1. It is seen that TPT1 predicts Z_{crit} which are much too high, as noted recently [314]. Furthermore, given that in the limit of long chain length $Z_{\text{crit}} = 1/3$, it would seem that TPT1 predicts a maximum in Z_{crit} which is not observed experimentally. On the contrary, in experiments it is found that Z_{crit} seems to monotonously approach a plateau from upwards. We do not expect this problem to be related to any particular problem in the reference equation of state, but rather, to deficiencies of TPT1 itself.

Once we have obtained information on the molecular parameters from data of the low-molecular-weight members of the series, we can use TPT1 to predict interesting properties of the longer members. As shown previously, Eq. (115) allows to determine the asymptotic critical temperature from knowledge of monomer—monomer and monomer—dimer second virial coefficients alone. In particular, for the LJ-FENE polymer model described in Sect. 3.1, we have seen that TPT1-MSA predicts a universal asymptotic critical temperature, $\tilde{T}^{\infty}_{\text{crit}} = 3.39$ (cf. Table 3). If we consider that the fit for $\epsilon(N_c)$ has been performed for alkane chains long enough that we

can extrapolate Eq. (148) to $N_c \to \infty$, it can be shown that the ϵ parameter in the asymptotic limit is given by,

$$\frac{\epsilon^{\infty}}{k_B} = \frac{\sigma_{22}^3}{l_2 v_2} \approx 375\text{K} . \tag{152}$$

Using this information, our prediction for the asymptotic critical temperature of polyethylene, T_{crit}^{∞}, should be:

$$T_{\text{crit}}^{\infty} = \frac{k_B \tilde{T}_{\text{crit}}^{\infty}}{\epsilon^{\infty}} = 3.39 \cdot 375 = 1270\text{K} . \tag{153}$$

Blas and Vega [240] have studied the equation of state of a slightly different model by using TPT1. Their model is made of Lennard—Jones beads (full Lennard—Jones, with no truncation) that are rigidly bonded at a distance equal to σ. With this equation they have explored the behavior of alkanes by performing somewhat different fits as the ones proposed here. Their estimated value for ϵ^{∞}, obtained from extrapolation, is $\epsilon^{\infty}/k_B = 280\text{K}$. From knowledge of the monomer and monomer—dimer virial coefficients assumed in their reference equation of state (obtained from a fit to Lennard—Jones molecular dynamics data [315, 234]), one finds that the asymptotic critical temperature consistent with their TPT1 implementation is $\tilde{T}_{\text{crit}}^{\infty} = 4.65$ [271]. This then provides an estimated critical temperature for polyethylene of about 1302K (a recent revised fit by Pamies and Vega only changes this estimate by 1K [265]).

In another study, McCabe and Jackson considered TPT1 as applied to square well chains in order to model the n-alkane series [255]. These authors proposed a linear correlation for the square well strength, ϵ and range parameters, λ. In the limit of infinitely long chains, their correlation yields $\epsilon^{\infty}/k_B = 266\text{K}$ and $\lambda^{\infty} = 1.64$. Fortunately, for the square well chain Eq. (115) provides analytical results for the asymptotic critical temperature [271]. For the above range parameter, one finds $\tilde{T}_{\text{crit}}^{\infty} = 5.03$, so that the estimated critical temperature for polyethylene is found to be about 1339K.

We thus find that several different TPT1 implementations provide similar estimates for the critical temperature of polyethylene, which is roughly predicted to lay between 1270K and 1340K. Note that the fitting procedure proposed allows for the development of a group contribution method for the determination of molecular parameters to be used with TPT1. The method might be particularly useful if employed for binary mixtures, because then the number of possible combinations becomes enormous and a group contribution method is clearly desirable.

4.4 Application to Polymer Solutions

4.4.1 *Application to a Polymer–Solvent System*

In this section we will explore the ability of TPT1 to describe the thermodynamic properties of polymer solutions. In what follows, we will restrict our attention to

the binary mixture that was described in Sect. 3.1, where the first component plays the role of a solvent with $N_S = 1$ and the second component plays the role of a polymer of length $N_P = 5$ (with subscripts S for solvent and P for polymer taken as components 1 and 2, respectively). The choice of Lennard–Jones parameters, $\sigma_{SS}/\sigma_{PP} = 0.816$ and $\epsilon_{SS}/\epsilon_{PP} = 0.726$ is such that the model mimics the behavior of pure CO_2 and hexadecane, but in this section we will rather discuss the thermodynamic properties in reduced Lennard–Jones units of the pentamer. All throughout, we will discuss the TPT1-MSA theory as described in Sects. 4.2.3 and 4.2.4.

Before considering the description of the mixture, let us first address the critical behavior of the pure components alone. Table 3 (see above) summarizes the critical properties for both the monomer and the pentamer as obtained from simulation and theory. The agreement for the monomer is fairly good, as already noted previously [238]. For the pentamer the critical density and temperature are also in fair agreement, but the critical pressure is twice as large as the one obtained in simulations. This failure to predict the critical pressure of the pure pentamer will affect the predictions for the mixtures.

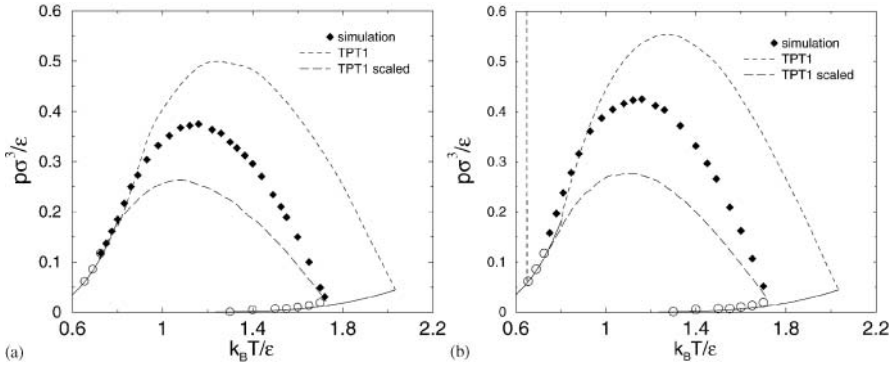

Fig. 27. Pressure—temperature projection of the phase diagram of a binary mixture of pentamer + monomer with $\xi = 1$ (**a**) and $\xi = 0.9$ (**b**). The *filled symbols* are simulation results for the critical line, while the *empty symbols* are simulation results for the vapor—liquid coexistence of the pure components. The *short-dashed line* is the critical line from TPT1, while the *long-dashed line* is the critical line from TPT1 when parameters are rescaled to the critical point of the pure components. *Full lines* are TPT1 predictions for the vapor pressure of the pure components (results from [244])

First, we consider a mixture obeying the Lorenz–Berthelot rules, such that $\xi = 1$ (cf. Eq. (49)). In Fig. 27 we show a p–T projection of the phase diagram as obtained from simulation and theory. The theory correctly predicts the vapor pressure of the pure components. However, the predicted critical temperatures are higher, as expected from a mean field theory. For this reason, the critical line of the mixture is described only in a qualitative manner. Particularly, the predicted critical pressures

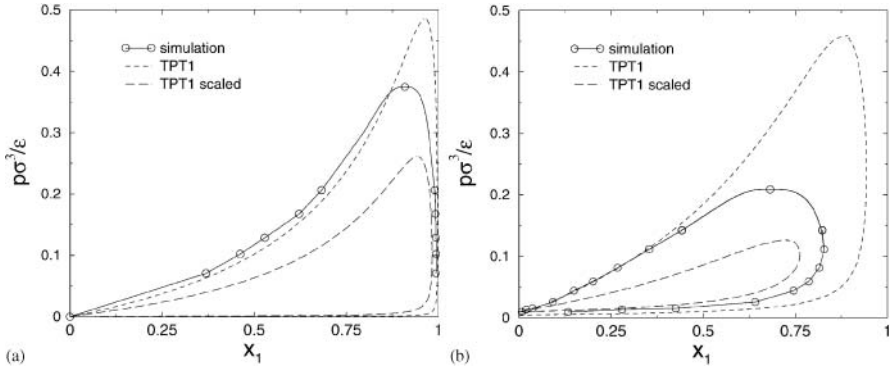

Fig. 28. $p - x$ slice for a pentamer—monomer mixture at $k_BT/\epsilon = 1.16$ and $\xi = 1.0$ (**a**) and $k_BT/\epsilon = 1.55$ and $\xi = 0.9$ (**b**). The *symbols* are simulation results. The *full line* in the neighborhood of the critical point is obtained from scaling analysis. The remaining part of the *full line* is just a guide to the eye. *Short* (TPT1) and *long-dashed* (TPT1 scaled) *lines* are predictions from the theory. (results from [244])

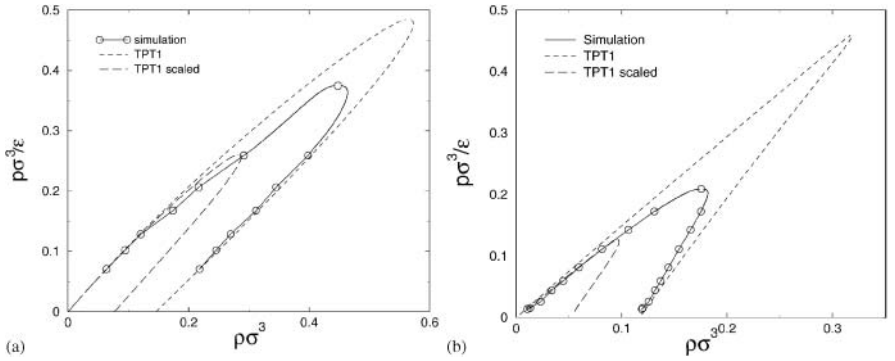

Fig. 29. $p - \rho$ slice for a pentamer—monomer mixture at $k_BT/\epsilon = 1.16$ and $\xi = 1.0$ (**a**) and $k_BT/\epsilon = 1.55$ and $\xi = 0.9$ (**b**). The total density of the system is related to the monomer densities by $\rho = \phi_S + \phi_P/N_P$. Rest of captions as in Fig. 28. (results from [244])

are much too large over a broad range of temperatures. Close to the critical point of the solvent, however, the predicted critical pressures are in good agreement.

One may expect better agreement between the predicted critical line and that obtained from simulation by modifying the LJ parameters so as to enforce agreement for the critical points of the pure components. Such a procedure is frequently employed to predict the high pressure phase behavior of real substances in many TPT1 applications [255, 261, 266]. In Fig. 27 the critical line predicted in this way is shown (dashed line). It is seen that the agreement does not improve noticeably, although the critical line obviously connects the critical points as predicted from simulation. Actually, the effect of rescaling the parameters this way is to decrease the asymmetry of the interactions. As a result, the theory predicts a much greater miscibility than

observed in simulations. Such a problem may probably be remedied by modifying the mixing parameter ξ (cf. Eq. (49)).

We have also considered the detailed phase diagram of this system at a temperature of $k_BT/\epsilon = 1.16$, which is high relative to the critical temperature of the pure monomer but still in a region below the maximum pressure of the critical line. At this temperature, the predictions of the theory for the critical pressures are still fair. Figure 28 shows a p–x slice of the phase diagram. Overall, TPT1 gives a fairly good description of the phase boundaries, though the composition of the liquid phase is somewhat too high and the agreement deteriorates in the neighborhood of the critical point as expected. The corresponding p–ρ slice is shown in Fig. 29. It is seen that the theory yields rather good predictions for the coexisting liquid densities, while agreement with the vapor densities is slightly worse. Together with the predictions from TPT1, we show the theoretical predictions as obtained from the rescaled set of parameters, both in Fig. 28 and in Fig. 29. Again, the agreement is not seen to improve, but rather, to deteriorate, especially if one considers the p–ρ plane.

The mutual solubility may be very much modified by changing the value of ξ that tunes the crossed interactions between the molecules (cf. Eq. (49)). In order to study this effect, we have calculated the phase boundaries of a model as the one described before, but with $\xi = 0.9$. Figure 27 shows a p–T phase diagram for this model. Decreasing ξ from 1 to 0.9 we decrease the solubility, and the critical pressures increase. Our implementation of TPT1 also predicts a considerable increase of immiscibility for this system. On the one hand, the liquid–vapor critical pressures increase with respect to those of the previous system, in agreement with the simulation results. On the other hand, the theory predicts the appearance of liquid–liquid immiscibility at low temperatures. The effect of changing ξ is to shift the presence of liquid–liquid immiscibility all the way from below $k_BT/\epsilon = 0.4$ to about $k_BT/\epsilon = 0.65$. In fact, closer inspection reveals that our theory predicts this system to be of type IV, as a small region of liquid–liquid immiscibility appears in the neighborhood of the critical point of the monomer, with a triple line extending between $k_BT/\epsilon \approx 0.800$ and $k_BT/\epsilon \approx 0.815$ (not shown). This behavior is consistent with the simulation results, which suggest that the phase diagram for this mixture has no longer a continuous critical line joining the critical points of the pure substances. Despite this qualitative agreement, similar trends as observed in Fig. 27 are also seen here, i.e., the predicted critical pressures are usually too large, except in a small region close to the critical point of the first component, where the agreement is rather good. Rescaling of the parameters does not improve much the overall agreement and once more makes the fluid much more miscible.

Next we consider the phase diagram at a fixed temperature of $T = 1.55$, well above the critical point of the monomer. Figure 28 shows a p–x projection of the phase diagram at this temperature. The theory predicts the solubility of the liquid phase in excellent agreement with the simulations up to pressures of about $p\sigma^3/\epsilon \approx 1.15$. On the contrary, the predictions for the composition of the vapor phase are far less satisfactory. The failure of the theory to properly describe the macroscopic fluctuations that occur in the neighborhood of the critical point has a large effect. Particularly, the critical pressure predicted by the theory is more than twice as large

than that obtained from the simulation results. Figure 28 shows the p–ρ projection for this same temperature. In this case both the vapor and liquid coexistence densities are well predicted by the theory away from the critical point. The predicted critical density, however, is much too large.

The reasons for the disagreement found between TPT1 and simulation may be divided into two main groups. On the one hand, there are approximations related to the description of the equation of state of the reference system, i.e., the Lennard–Jones mixture of monomers. On the other hand, there are those other approximations related to deficiencies of TPT1 itself. However, the equation of state of the reference system was tested and found to be rather accurate [244]. For this reason, it is believed that most of the disagreement is probably related to approximations inherent to TPT1. Particularly, there seem to be at least two reasons which may result in a poorer description of the pentamer—monomer properties relative to that of the reference Lennard—Jones mixture. On the one hand, it is well known that TPT1 is unable to correctly predict the virial coefficients of chain molecules, and is therefore not accurate at low concentration [280]. Such a conclusion holds whether the chain is found in vacuum or in solution and may therefore explain the poor agreement found in Fig. 28 for the composition of the vapor phase. On the other hand, TPT1 not only requires knowledge of the equation of state of the reference system, but also of the radial distribution function. In our implementation we have used a simple one-fluid approximation, which is known to be fairly accurate for the equation of state but may be less so for $g(r)$, especially for non–symmetric mixtures of monomers. We further note that a true test of the approximations involved in TPT1 would require knowledge of the exact thermodynamics and structure of the mixture. While this can be obtained in principle from simulation, the large range of states that would be required to study (scanning both density and composition would be required for each temperature) makes this approach rather difficult.

4.4.2 *Application to Solutions of n-Alkanes in CO_2*

The theoretical description of mixtures of CO_2 and hydrocarbons has recently attracted some attention and different versions of TPT1 have been employed to describe this system [264, 266, 316]. In Sect. 1 we saw that the simple models considered above provide a reasonable description of hexadecane and carbon dioxide. We can therefore expect that the chosen set of σ and ϵ parameters should also allow to describe n-alkane + CO_2 mixtures, provided that the chain length is chosen appropriately. In this way, we could address interesting questions concerning the chain length dependence of the polymer/solvent phase diagram. As found previously, for short enough chains the phase diagram exhibits a type I behavior. As the chain length increases, it then becomes of type II and there is some evidence that further increase could switch the behavior to type III. The question then arises as to whether there is any further evolution of the phase behavior with chain length, and particularly, whether there is an asymptotic global phase behavior in the limit of infinite chain length [294].

The study of the whole phase diagram of the polymer solution for larger chains becomes an extremely computationally expensive problem. Fortunately, the comparison of computer simulations and TPT1 for moderate chains gives us some confidence in the reliability of TPT1. Therefore, we will now try to explore this issue with the help of TPT1. Furthermore, we will extend our study to the case of the n-alkane + CO_2 mixture. We will consider σ and ϵ parameters as employed in the simulations, with $\xi = 0.886$. For the effective chain length, we will assume an increase of $5/16$ per monomer (as suggested by the fit of Sect. 4.3.2). By making this assumptions, we can now calculate the critical lines from TPT1. Figure 30 shows the phase diagram obtained for different n-alkanes, ranging from C_{16} to C_{112}. In this case it is clearly observed that all of the phase diagrams are of type III, and that the minimum and maximum of the critical line for moderate chain lengths gradually disappears. In all cases, however, there is a region where the critical line becomes almost vertical, running towards infinite critical pressure at almost constant critical temperature. This kind of criticality corresponds to that of a solute in a dense, incompressible solvent, similar to what is considered in a Flory—Huggins lattice model. Despite of this, the figure does not appear to show any evidence of an asymptotic behavior of the critical line. However, a closer inspection strongly suggests an asymptotic behavior for the vertical portion of the critical lines. In Fig. 30 we show a Flory–Schulz plot of the critical points as determined at a pressure of 1600 bar (as long as it is high enough, the choice of pressure is unimportant, since the critical lines are almost vertical). It is seen that the results for the critical temperature at constant pressure are compatible with a scaling law of the Flory—Schulz type, with an intercept of 0.00111 in the $1/T$ axis. Notwithstanding some caution related to the small chain lengths considered, this result is a strong evidence suggesting an asymptotic behavior for the vertical portion of the critical line, since the data is compatible with the occurrence of a line of Theta points at $T \approx 900$K. A similar behavior has been observed by Yelash and Kraska in a recent study [298]. Note however that this would be a rather different Theta point than those which are typically measured in experiments. Such measurements are usually performed at ambient pressure and occur at moderate temperatures. More importantly, they occur well below the critical point of the solvent. On the contrary, what is predicted here is a supercritical Θ point, occurring above the critical pressure and temperature of the solvent.

This example illustrates the similarity and difference of using an accurate equation of state instead of the simpler Flory—Huggins theory. The latter almost completely ignores the solvent, apart from its effect on the solute. Therefore, one does not know what the pressure of the system is, and there is no distinction between sub– or super–critical solvents. Only the requirement that it should behave as an incompressible fluid is built in. By using an equation of state of the kind that allows to include the solvent explicitely, one is able to accurately locate the behavior observed in the context of the phase diagram of the solvent. This has allowed us to suggest the existence of a Θ point at unexpected conditions.

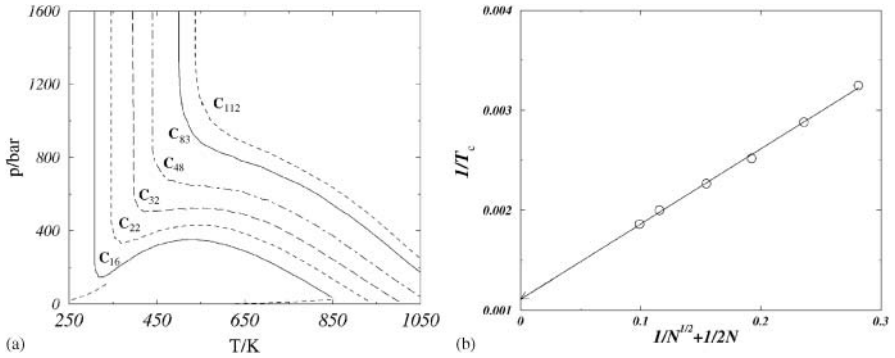

Fig. 30. Panel (**a**) shows the pressure-temperature projection of mixtures of n-alkanes and CO_2 for several chain lengths. At high pressures, all such lines become almost vertical, a feature characteristic of liquid-liquid immiscibility. In panel (**b**) the critical temperatures at 1600 bar are used to plot a Flory—Schulz plot in order to show the occurrence of a high pressure Θ point

5
Monte Carlo Simulations in the Grandcanonical Ensemble

5.1
Technique

MC simulations are well-suited to determine the phase behavior and properties of bubbles directly (i.e., without further approximations). Even in the framework of a coarse–grained polymer model these simulations pose an enormous computational and methodological challenge, but they are absolutely crucial for assessing the validity of the maze of approximations involved in the previous methods. They elucidate the role of fluctuations [70, 71, 72, 73] (both of the composition and at interfaces) and provide – at least in principle – direct information about the kinetics of phase separation. The last two topics cannot be addresses within the SCF theory or TPT1-equation of state, which are mean-field theories for thermal equilibrium.

Similar to our SCF calculations we perform our simulations in the grandcanonical ensemble, i.e., we fix the volume V, temperature T, and chemical potentials μ_S and μ_P of both species, but the number of particles in the simulation cell fluctuates. Particle insertions and deletions are implemented via the configuration bias MC method [104, 105, 106, 107, 108, 109]. Additionally, the polymer conformations are updated by local monomer displacements and slithering snake movements [99].

In order to extract the phase behavior and the properties of bubbles from the simulation data, one faces two problems: (i) The insertion of whole chains has a rather small acceptance rate at high densities and is considerably more computationally demanding than the corresponding MC move in a simple liquid (e.g., a Lennard–Jones monomer fluid or a lattice model). This gives rise to protracted long relaxation times and restricts us to rather small system sizes. In the vicinity of critical points in the

phase diagram, the correlation length of fluctuations exceeds the system size and a careful analysis of simulation data is necessary to extract the behavior in the thermodynamic limit. Fortunately, many finite size scaling techniques [86, 87, 88, 89] from simple fluids can be carried over to polymer + solvent mixtures as well. However, also the size of a bubble in the simulation cell is rather limited; a fact which gives rise to unusual finite size effects [318, 319]. (ii) In order to measure the free energy difference between coexisting phases the system has to tunnel between the two coexisting states. Unfortunately, those states are separated by a large barrier, and pre-weighting techniques [131, 132, 134] have to be applied to facilitate transitions from one phase to the other and to sample the different regions of densities efficiently.

Much of the analysis of the simulation data relies on the joint distribution function which is accumulated in the course of the simulation. In the grandcanonical simulations one samples the partition function

$$\mathcal{Z}_{\mathrm{MC}} = \sum_{n_S,n_P=0}^{\infty} \frac{e^{\mu_S n_S/k_BT}}{n_S!} \frac{e^{\mu_P N n_P/k_BT}}{n_P!} e^{w(n_S,n_P)} \int \Pi_{n_S,n_P} \mathrm{d}^3\mathbf{r} \, \exp\left(-\frac{\mathcal{E}}{k_BT}\right), \tag{154}$$

where $\mathcal{E}$ denotes the sum of the Lennard—Jones interactions between the effective segments and the FENE-potential along the backbone of the coarse-grained chains (cf. Sect. 3.1). $w(n_S, n_P)$ is a pre-weighting function [131, 132] that is chosen such that the system explores the whole phase space that corresponds to the two (or three) coexisting phases within a single simulation run.

The probability distribution P_{MC} of observing n_S solvent particles and n_P polymers in the simulation is related to the distribution function P_{GC} in the grandcanonical ensemble via:

$$P_{\mathrm{GC}}(n_S, n_P|\mu_S, \mu_P) \sim e^{-w(n_S,n_P)} P_{\mathrm{MC}}(n_S, n_P|\mu_S, \mu_P). \tag{155}$$

Hence, the bias that the pre-weighting function imparts onto the distribution can be easily removed to calculate thermodynamic averages in the grandcanonical ensemble. Ideally, one chooses $w(n_S, n_P) = -\ln P_{\mathrm{GC}}(n_S, n_P|\mu_S, \mu_P)$, because all combinations of n_S and n_P would be sampled with equal probability. In principle, this scheme would allow us to construct an entire isothermal slice of the phase diagram from a single simulation run.

It is difficult, however, to choose a good pre-weighting function, because the probability distribution P_{GC} is not known *a priori*. While there has been recent progress in efficiently and systematically extracting pre-weighting functions from simulations [134, 320], it turns out that two-dimensional reweighting functions are still difficult to obtain with good statistics for the polymer + solvent mixture under consideration. Therefore, we used in the present study only one-dimensional reweighting functions, i.e., $w(n_S, n_P) = w(n_S)$ or $w(n_S, n_P) = w(n_p)$, respectively.

In the vicinity of phase coexistence, the probability distribution exhibits two peaks at segment densities that correspond to the two coexisting phases. The statistical weight in each peak is related to the pressure:

$$\frac{p^{(1)}V}{k_BT} = \ln \sum_{(n_S,n_P)\in(1)} \frac{e^{\mu_S n_S/k_BT}}{n_S!} \frac{e^{\mu_P N n_P/k_BT}}{n_P!} \int \Pi_{n_S,n_P} \mathrm{d}^3\mathbf{r} \, \exp\left(-\frac{\mathcal{E}}{k_BT}\right)$$
$$= \ln \mathcal{Z}_{\mathrm{GC}} + \ln \sum_{(n_S,n_P)\in(1)} P_{\mathrm{GC}}(n_S, n_P|\mu_S, \mu_P), \tag{156}$$

where the summation is extended over all particle numbers (n_S, n_P) which correspond to phase (1). If the system is large and the transition of first order, the peaks are describable by a Gaussian distribution. The wings of the distribution yield only an exponentially small contribution to the pressure such that the details of dividing the $n_S - n_P$-plane into the two phases imparts only a negligible error. In practice, we project the joint distribution onto one particle number such that the projection exhibits a clear double peak structure, i.e., we use n_P in the vicinity of the critical point of the pure polymer and n_S whenever the two phases basically consist of S-gas and S-liquid with little or no polymers present. The mean of the projected distribution is then used to distinguish between both phases.

In the grandcanonical ensemble two phases coexist at fixed temperature T, if $p^{(1)}(\mu_S^{\mathrm{coex}}, \mu_P^{\mathrm{coex}}) = p^{(2)}(\mu_S^{\mathrm{coex}}, \mu_P^{\mathrm{coex}})$. Using Eq. (156) one obtains the equal-weight-rule of phase coexistence:

$$\sum_{(n_S,n_P)\in(1)} P_{\mathrm{GC}}(n_S, n_P|\mu_S^{\mathrm{coex}}, \mu_P^{\mathrm{coex}}) = \sum_{(n_S,n_P)\in(2)} P_{\mathrm{GC}}(n_S, n_P|\mu_S^{\mathrm{coex}}, \mu_P^{\mathrm{coex}}). \tag{157}$$

Locating phase coexistence as a function of the two chemical potentials is facilitated by using histogram reweighting of the distribution functions. The joint distributions at two different values of chemical potentials (μ_S, μ_P) and (μ'_S, μ'_P) are related via:

$$P_{\mathrm{MC}}(n_S, n_P|\mu'_S, \mu'_P) \sim e^{(\mu'_S-\mu_S)n_S/k_BT} e^{(\mu'_P-\mu_P)Nn_P/k_BT} P_{\mathrm{MC}}(n_S, n_P|\mu'_S, \mu'_P). \tag{158}$$

Similarly, one can use the joint histogram of energy and particle numbers to extrapolate the results of the simulation to neighboring temperatures [90, 91]. This technique allows us to estimate first order phase coexistence from the simulation data. In the vicinity of critical points, the probability distribution adopts a universal form that characterizes the class of transition [93]. As the critical point is also a point on the spinodal, the construction in Sect.3.3 shows that one can define two linear combinations of densities, such that one, c, distinguishes between the two coexisting phases and exhibits critical behavior, while the other, $\bar{c}$, is (almost) identical in both phases and exhibits only Gaussian fluctuations. Therefore, a single scalar order parameter characterizes the transition which belongs to the 3D Ising universality class. Thus, one can use the same finite-size scaling techniques as in the pure polymer system [82] (cf. Sect.2.4) and map the distribution function onto the bimodal 3D Ising distribution (cf. Fig. 6). In the limit of large system size, the two peaks converge towards the critical density. For the small systems studied in our simulations, the two peaks

are quite separated and yield some information about the concentration of the two coexisting phases slightly below the critical point.

5.2 Phase Diagrams

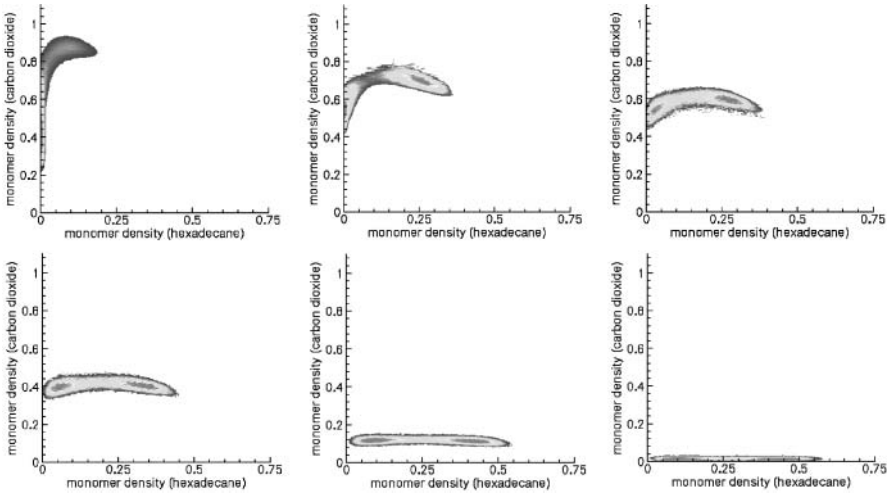

Fig. 31. Joint probability distribution of solvent and polymer density along the critical line in a finite-sized simulation cell for $\xi = 1$. The distributions correspond to temperatures $T =$ 314K, 356K, 398K, 486K, 650K, and 713K from *up/left* to *down/bottom*. For temperatures $T = 314$K and 356K the box size is $L = 6.74\sigma_P$ while $L = 9\sigma_P$ was employed for other temperatures

The joint probability distribution at our finite-size estimate of the critical points is shown in Fig. 31 for a mixture with $\xi = 1$. At high temperature, in the vicinity of the critical point of the pure polymer, the distribution exhibits a two peak structure in ϕ_P, but the number of solvent particles ϕ_S remains small in both phases, i.e., $c \approx \phi_P$. As we follow the critical line towards lower temperatures, ϕ_S increases roughly to the same degree in both phases for $T > 400$K. Upon decreasing temperature further, we observe how the direction defined by c gradually rotates counterclockwise and at $T = 314$K, just slightly above the critical point of the solvent, the two coexisting phases differ in their solvent density and hardly contain any polymer, i.e., $c \approx \phi_S$. This indicates that the critical line connects the two critical points of the pure components, and that the character of the phase transition gradually changes from a liquid—vapor coexistence of the polymer at high temperatures to a liquid—vapor coexistence of the solvent at low temperatures.

The gradual change of the molar fraction x along the critical line is presented in Fig. 32(**a**). At high temperature, the critical molar fraction is small, it increases

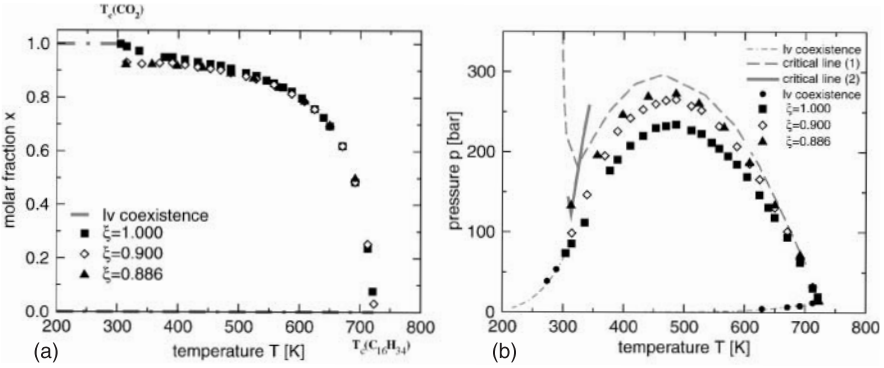

Fig. 32. (**a**) Critical lines of the polymer + solvent mixture as a function of temperature and molar fraction for three values of the mixing parameter $\xi = 1, 0.9$ and 0.886 as indicated in the key. Liquid–vapor coexistence of the pure components are indicated by *dashed horizontal lines*. (**b**) Phase diagram of the mixture as a function of temperature and pressures for different values of ξ. *Squares* correspond to $\xi = 1$, *diamonds* show the results for $\xi = 0.9$, and *triangles* represent $\xi = 0.866$. The simulation results for the liquid—vapor coexistence of the pure components are shown by *circles*. *Thick lines* mark two experimental observations of the critical lines in hexadecane and CO_2 from [321, 322], respectively. *Thin lines* indicate the experimental liquid—vapor coexistence of the pure fluid

upon decrease of temperature, and it reaches $x = 1$ at the critical temperature of the solvent. The behavior in Figs. 31 and 32 is characteristic of a type I phase diagram, and this behavior agrees with the predictions of the virial expansion of the SCF calculations (Sect. 3) and the more accurate TPT1 (Sect. 4) for $\xi = 1$, but it disagrees with the phase behavior of hexadecane and carbon dioxide.

The equation of state predicts that the phase behavior is highly sensitive to the mixing parameter ξ; decreasing ξ we reduce the compatibility between polymer and solvent and induce a liquid–liquid phase separation between the polymer and the solvent. In Fig. 32 (**a**), we study the molar fraction of the critical line for two additional values of ξ. At high temperature, the critical lines hardly depend on the mixing parameter ξ. In the vicinity of the critical temperature of the solvent, however, the critical lines for $\xi = 0.9$ and 0.866 do not reach the critical point of the pure solvent; at $T_{S\text{crit}}$ the critical mixtures still contain about 10% molar of polymer.

The phase behavior as a function of temperature and pressure is compared to experimental data in panel (**b**) of Fig. 32. One clearly observes that the critical line does not connect to the critical point of CO_2, an indication for type III phase behavior. One also finds that the critical line shifts to higher pressures as we reduce the compatibility ξ of the two components. The simulation data of our coarse-grained model agree with the experimental data reasonably well. The experiments, as well as both equations of state, measure a sharp increase of the critical pressure at low temperatures. Unfortunately, the minimum of the critical pressure could not be observed in our simulations, because the liquid—liquid immiscibility occurs at rather large densities making the insertion/deletion of the polymer prohibitively difficult. In view

of these difficulties and the experimental uncertainties, illustrated by the results of two groups, we choose not to fine-tune the mixing parameter to reproduce the critical pressure of the mixture at a specific temperature. The values used in the simulations, however, give a reasonable qualitative description.

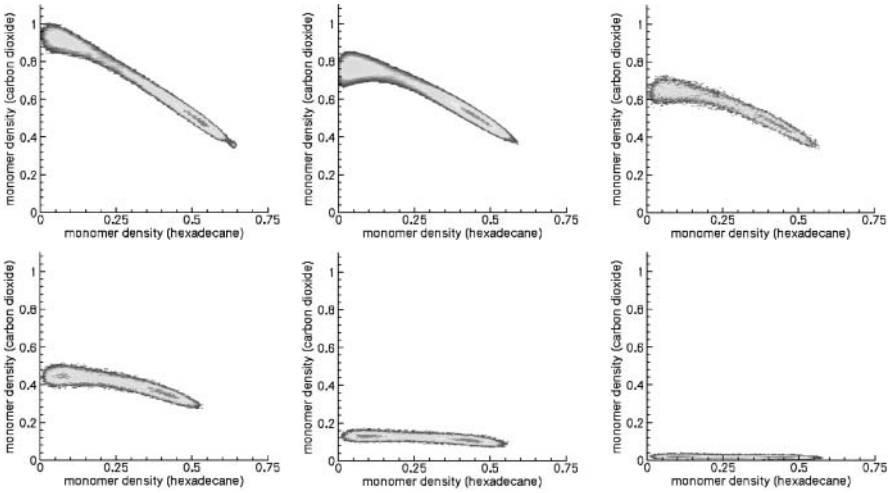

Fig. 33. Joint probability distribution of solvent and polymer density along the critical line in a finite-sized simulation cell for $\xi = 0.886$. The distributions correspond to temperatures $T =$ 314K, 356K, 398K, 486K, 650K, and 713K from *up/left* to *down/bottom*. For temperatures $T = 314$K and 356K the box size is $L = 6.74\sigma_{\mathrm{P}}$ while $L = 9\sigma_{\mathrm{P}}$ was employed for other temperatures

The joint probability distribution for $\xi = 0.866$ is shown in Fig. 33 for various temperatures. While the behavior at high temperatures is quite similar to the case $\xi = 1$ in Fig. 31, the axis defined by the linear combination c does not turn vertical, but connects a liquid solvent with a dense polymer-rich phase. This is the signature of liquid—liquid immiscibility in the MC simulations which is characteristic of the experimental phase diagram of type III. An important feature of the phase behavior is the presence of a triple line, at which a solvent vapor, a solvent at liquid density, and a dense polymer–rich phase coexist. The probability distribution at one point of the triple line (namely at $T_{S\mathrm{crit}} = 304$K) is presented in Fig. 34 for $\xi = 0.9$. One clearly observes the three peaks in the distribution which correspond to the three coexisting phases: a dense polymer—liquid, a solvent—vapor and a solvent—liquid.

This comparison between experiments and the simulation model shows that our coarse-grained model reproduces the qualitative features of hexadecane-carbon dioxide mixture. As seen in the introduction, the phase diagrams of the pure system (cf. Fig. 2) as well as the interfacial tension (cf. Fig. 5) are also in semi-quantitative agreement with the experiment. This makes the model a good starting point for investigating bubble nucleation.

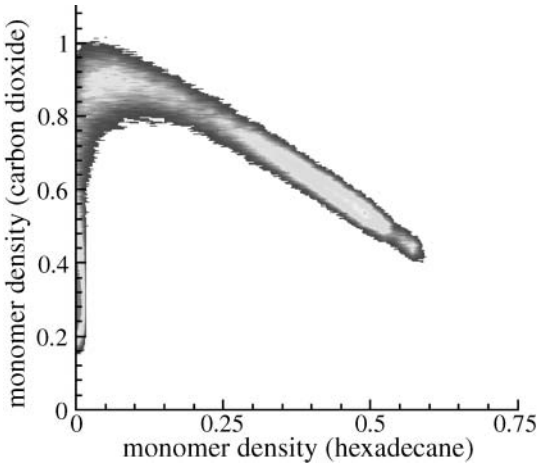

Fig. 34. Joint probability distribution of solvent and polymer density at the critical temperature $T = 304$K of the solvent for $\xi = 0.9$ and $L = 6.74\sigma$

5.3 Bubble Nucleation

In order to observe the kinetics of bubble nucleation in the vicinity of the binodal we control the under-saturation of the system by fixing the chemical potential of both species. As a starting configuration we use a homogeneous state equilibrated at a higher temperature. This situation corresponds to a simulation cell in contact with a much larger reservoir which is held at constant under-saturation. The most natural choice would be to investigate the time evolution via MD simulations (cf. Sect. 2.3). This technique would provide extremely valuable information about the pathway of phase separation without invoking further simplifications than those which define the coarse-grained model. In particular, one could evaluate the basic assumption [16] that the bubble is in equilibrium with the surrounding mother phase. For small bubbles and in the presence of dynamical asymmetries (i.e., volatile solvent and viscous polymer) this approximation might be quite inaccurate [176]. Unfortunately, such simulations face two difficulties: (i) To obtain reliable information many bubble nucleation events would have to be simulated. (ii) Since the number of particles was conserved we would need prohibitively large simulation cells for the under-saturation not to decrease substantially even in the very early stages of nucleation. We recall that the weight fraction of the solvent is only a few percent, but it is much larger inside a small bubble.

In view of these difficulties, we choose to investigate bubble formation in the grandcanonical ensemble. Thereby, we calculate the free energy of a bubble inside of a finite-sized simulation cell. This method does not provide direct information about the time evolution, because the particle numbers are not conserved and particles do not move according to realistic dynamics. Moreover, we also rely on the assumption

of equilibrium between the bubble and its surrounding. Fluctuations, both in the shape and the composition of the bubble are included.

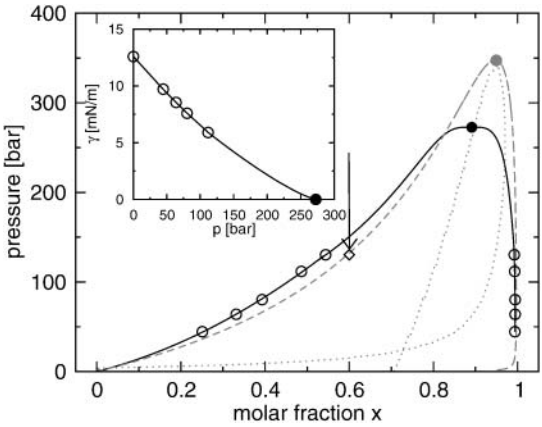

Fig. 35. Isothermal slice of the phase diagram at $T = 486$K as obtained from simulations (*solid line* and *symbols*) and TPT1 (*long-dashed line*). The spinodals obtained from the TPT1 equation of state are indicated as *short-dashed lines*. The *inset* presents the interfacial tension as a function of pressure. From [16]

The kinetics of phase separation in the vicinity of the binodal is chiefly determined by the free energy barrier the system encounters on its path towards the equilibrium state. Hence, we expect the sequence of states that we observe in the simulations to resemble the relaxation path. In the following, we regard a quench to $x = 0.60$ and a final pressure of about $p \approx 130$ bar. In Fig. 35 we present the p-x phase diagram at temperature $T = 486$K. The results for binodals and spinodals obtained from TPT1 are included for comparison, and the quench is schematically indicated by an arrow. For these parameters we are so close to the binodal and so far away from the spinodal, that we expect phase separation to proceed via bubble nucleation.

The sequence of snapshots of a thin slice in Fig. 36 visualizes how phase separation in polymer + solvent mixtures proceeds via nucleation. In the beginning, the system fluctuates around a metastable super-saturated liquid. One observes the "birth and death" of small density fluctuations in the hexadecane matrix (displayed as red/dark grey spheres) which become visible whenever the blue/dark background shines through the slice. These irregular voids are too small, however, to lead to phase separation. Usually the voids also contain a few CO_2 molecules (displayed as small yellow/light grey spheres). Only after a time lag a void grows to the critical size and overcomes the free energy barrier which separates the metastable from the homogeneous equilibrium state. From then on, the bubble grows until it fills the whole simulation box. As expected from the SCF calculations, the critical void contains also CO_2 molecules, thus decreasing the super-saturation of the remaining polymer-rich

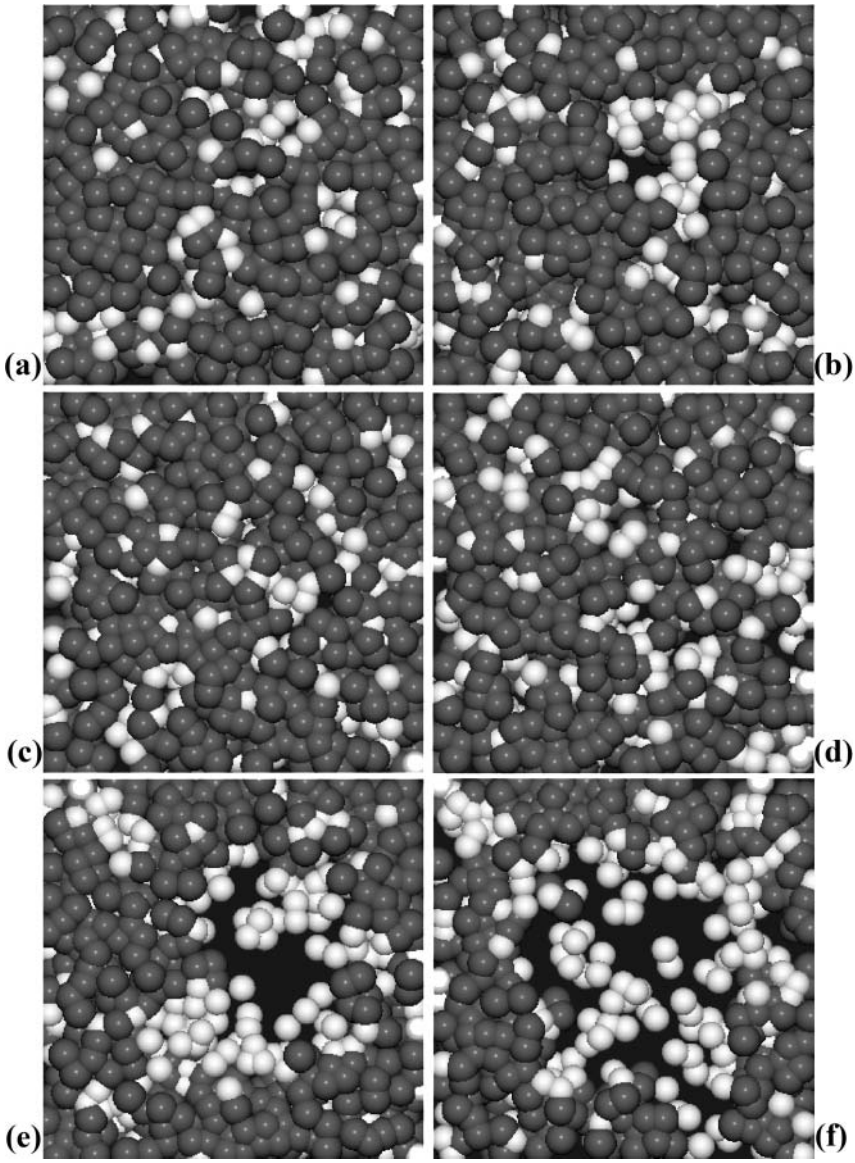

Fig. 36. Time sequence from *top left* (**a**), to *top right* (**b**), . . . , to *bottom right* (**f**) of a quenching experiment in grandcanonical simulations into the metastable region ($T = 486$K, x=0.60 and (final) pressure $p \approx 130$ bar – compare with Fig. 35). Phase separation occurs via nucleation. The linear dimension of the simulation box is 22.5σ. For clarity, not the whole simulation box but only a slice of thickness 2σ is shown. Polymer segments are *red/dark*, while solvent particles are drawn *yellow/grey*. From [16]

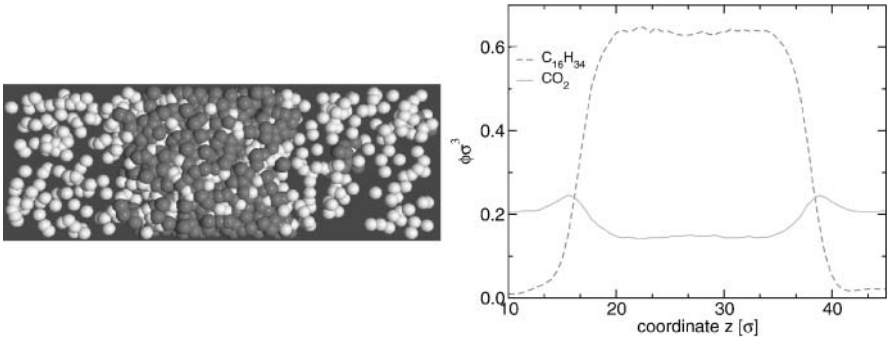

Fig. 37. Simulation snapshot of the interface between polymer-rich liquid and vapor at $T = 486$K and the same parameters as in Fig.36. The *right* panel shows the density profile of the two species

phase. Even at this high temperature, far away from the triple line, the CO_2 molecules are not homogeneously distributed: At the interface between the vapor and the polymer liquid, i.e., at the surface of the bubble, the CO_2 density is clearly higher than in the center of the bubble. This surface enrichment effect is the precursor of the interfacial wetting of the liquid CO_2 predicted by the SCF calculations when one approaches the triple line.

Under the conditions of the simulation, a small enrichment of solvent is even detectable at a planar polymer liquid—vapor interface. This is illustrated qualitatively by the snapshot in Fig. 37, which resembles the interface profiles in Fig. 10 (**b**). Of course, a more quantitative comparison has to consider capillary waves that broaden the interface profiles in the simulations [100] and the density correlations (packing) which are neglected in the SCF calculations.

6 Concluding Remarks

Even more than half a century after the application of Flory-Huggins theory [13, 14, 15] to polymer solutions, the description of inhomogeneous polymer + solvent systems still poses a challenge. The Flory-Huggins approach captures the qualitative phase behavior of polymer solutions if the compressibility of the mixture is very low, where many experimental systems exhibit immiscibility between a solvent–rich and a polymer–rich liquid. A much richer phase behavior is found for compressible mixtures, where one has to explicitly account for the solvent properties. In a compressible mixture, not only liquid—liquid unmixing but also liquid—vapor and three phase coexistences might occur at moderate pressures. By virtue of its simple structure, Flory-Huggins theory has routinely been used in comparison to experiments [5]. In the limit of long chain lengths the unmixing transition belongs to the tricritical universality class with an upper critical dimension $d_u = 3$ [3, 29, 30, 31, 32, 33].

Hence, one expects the predictions of the mean-field theory are not strongly affected by fluctuations (i.e., except for logarithmic corrections) in the limit $N \to \infty$.

For a quantitative prediction of properties in polymer + solvent mixtures one has to improve the Flory-Huggins theory, at least, in the following three aspects: (i) An accurate equation of state that describes the competition between liquid—liquid and liquid—vapor phase coexistence has to be taken into account, (ii) an accurate description of the interface between the coexisting phases, which incorporates some features of the molecular architecture on the length scale of the width of the liquid—vapor interface, and (iii) an approach that takes account of thermal fluctuations has to be considered. Of course, this is a formidable call. At present there has not yet emerged a single, computationally tractable scheme that can address all three issues simultaneously. In this review we have described self-consistent field calculations, thermodynamic perturbation theory (TPT1) and Monte Carlo (MC) simulations. Each of these approaches is targeted to improve some of the deficiencies of the Flory-Huggins theory and we have ordered them in the sequence of increasing accuracy of the description and increasing computational effort.

The first approach – SCF theory – is quite close in sprit to the original Flory-Huggins approach. We have included a third order virial expansion that is flexible enough to describe the qualitative features of the phase behavior of compressible mixtures at low pressure. Polymers are modeled as Gaussian chains. The computational scheme allows us to explore the phase behavior and predict properties of planar and curved interfaces as well as nucleation barriers [164]. In the vicinity of the spinodal, we can make a quantitative connection to Cahn—Hillard [146] theory. Close to the binodal the theory agrees with classical nucleation theory [182] if we use the interfacial tension independently measured. Unfortunately, both analytical approaches are limited to very large or very small nucleation barriers, respectively, while the SCF theory can predict the properties of critical bubbles in the practically important range of nucleation barriers of a few tens of $k_B T$. Hence, the SCF theory is suitable for investigating the qualitative phenomena in polymer + solvent mixtures: for instance, the interfacial wetting of the solvent upon approaching the triple line the condensation of the solvent inside the bubble or the non-monotonous temperature dependence of the nucleation barrier. Apart from being a mean-field theory, the main disadvantage of the SCF theory is the lack of quantitative accuracy when applied to a specific chemical substance: The third order virial expansion is not predictive and even when the parameters are fitted to experiments it is not accurate enough to provide a quantitative description over a wide range of density and temperature. Additionally, the structure and conformations of a molecule on the length scale below a few nanometers cannot be faithfully represented by a Gaussian chain model with strictly local interactions.

The second approach – TPT1 – provides a versatile and accurate method to calculate the equation of state of coarse-grained models [221, 222, 223, 224] of compressible polymer + solvent mixtures. It does capture the local structure (e.g., packing effects) in a homogeneous fluid and can reproduce much of the complex phase behavior. This is an excellent starting point for exploring the phase behavior. While it cannot predict the behavior of spatially inhomogeneous systems, e.g., interfacial ten-

sion, the knowledge of the location of the binodals and mean-field spinodals already tells a great deal about the kinetics of phase separation. Therefore this approach enjoys considerable attention in the engineering community [253, 254, 258, 261]. While the general theoretical approach is quite powerful [221, 226, 227, 228] most applications are limited to first order perturbation theory. In this case, the theory does not capture the consequences of chain connectivity on large length scales. Nevertheless, it does predict the correct asymptotic dependence of the critical point of polymer liquid—vapor coexistence on chain length, and it even qualitatively captures some of the large deviations at intermediate chain lengths [238, 271]. Unfortunately, it fails to reproduce the scaling of higher order virial coefficients with chain length [280] and the power-law dependence of the pressure in semi-dilute polymer solutions Moreover, when applied to a specific substance, the parameters of the TPT approach – the effective segment size, the effective attraction between segments and ratio between the number of segments and the molecular weight – are often obtained from fitting experimental data.

In principle, all three issues mentioned above could be tackled with fully atomistic MD simulations. Apart from the astronomical resources in computer time that an accurate determination of the phase diagram and a study of the kinetics of phase separation in a fully atomistic model would require, the lack of accurate interaction potentials between the constituents of the polymer + solvent mixture might seriously upset the predictive power of such a brute-force approach. This is particularly relevant for the specific system – hexadecane and carbon dioxide – because a small change of the mixing rule for interactions between unlike segments can alter the qualitative type of phase diagram.

Therefore we have used computer simulations of a coarse-grained model [16, 22] in the grandcanonical ensemble to assess the accuracy of the previous approaches and to compare the results of our model to experiments on hexadecane and carbon dioxide for a few selected parameters. The qualitative predictions of the SCFT and TPT1 are confirmed: In the simulations we corroborate a strong dependence of the phase diagram on the mixing parameter ξ, and the simulations show a layer of liquid solvent at the interface between polymer and vapor. The simulation snapshots also indicate that this interfacial excess of solvent occurs in bubbles. Furthermore, the simulations highlight the role of composition fluctuations at the critical line. As expected from a mean-field theory, TPT1 overestimates the critical temperature of the liquid-vapor coexistence of the pure components or the critical pressure along the critical line. The deviations between MC simulations and TPT1 in polymer + solvent systems are qualitatively similar to the behavior in the pure components [244]. The simulations also aid in deciding whether deviations between the predictions of theory and experiment are a consequence of the coarse-grained model (i.e., representing 3.2 hydrocarbon units by an effective Lennard—Jones particle) or the subsequent approximations in the statistical mechanics of this model. For instance, the SCF calculations give a qualitatively reasonable description of the dependence of the interfacial tension on pressure, but the magnitude of the interfacial tension is about a factor of 3.5 too small. Extrapolating the results for the interfacial tension of the pure pentamer into the relevant temperature regime, we find that our coarse-grained model

is able to predict the interfacial tension with a reasonable accuracy. This indicates that the deviations between the SCF calculation and experiment are rooted in the additional simplifications made in SCF theory.

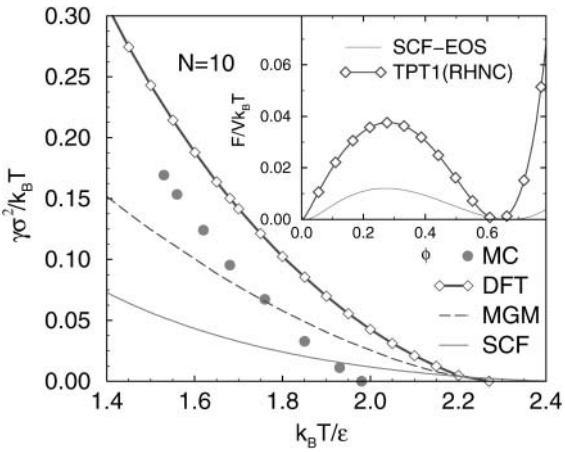

Fig. 38. Temperature dependence of the interfacial tension of the pure polymer for chain length $N = 10$. Circles correspond to MC results and the *solid line* to the SCF calculations. The line with *diamonds* shows the the result of a density functional calculation, which uses the TPT1-equation of state, decomposes the interaction free energy functional into a repulsive short-ranged and an attractive long-ranged contribution, and employs a partial enumeration scheme to take due account of the chain conformations on all length scales [154]. The *dashed line* shows the result of density functional calculations which do not use the decomposition of the free energy functional, but employ the same equation of state and chain model [99]. The *inset* compares the free energy densities $f = F/Vk_BT$ of the SCF calculations and the accurate TPT1 equation of state. Adapted from [99, 154]

The comparison between the three complementary approaches suggest several avenues towards improving the modeling of polymer + solvent systems: (i) A better description of the equation of state is of paramount importance in practical applications. Although deriving equation of states from microscopic interaction potentials is a fundamental problem of statistical mechanics which has has attracted abiding interest over decades, much practical use relies on fitting phenomenological models to a limited set of parameters. (ii) Some of the quantitative inaccuracies of the SCF theory can be alleviated by using a weighted density functional [99, 154, 155, 157, 158, 159] that takes due account of the equation of state and incorporates a decomposition of short-ranged repulsions and longer-ranged attractive interactions. In Fig. 38 we compare the results for longer chains ($N = 10$) with the SCF calculations and MC simulations. The density functional theory is quantitatively more accurate than the SCF calculations. The computational scheme can also be extended to arbitrary-chain architecture by calculating the single-chain properties in an external field by partial enumeration over a large sample of representative molecular conforma-

tions [99, 154, 155, 166, 167, 168, 169]. The latter might be constructed from the Rotational-Isomeric State model [1, 170] or obtained from atomistic modeling. (iii) Computer simulation of coarse-grained model systems might prove valuable to investigate the role of dynamical asymmetries between the species. Typically, the solvent is volatile, while the polymer is viscous. Also the fundamental assumption of nucleation theory of the bubble to be in equilibrium with the mother phase might be less accurate in polymer + solvent systems.

Acknowledgement

It is a great pleasure to thank E. Hädicke, D.W. Heermann, Y.-C. Lin, B. Rathke, R. Strey, C. Vega, L. Yelash, and A. Yethiraj for stimulating discussion and collaboration. Financial support was provided by the DFG under grants Bi314/17, Mu1674/1, and the BASF AG. LGM would like to thank the Ministerio de Ciencia y Tecnología for a Ramón y Cajal fellowship and grant number BFM-2001-1420-C02-01. We gratefully acknowledge a generous grant of computing time at the NIC Jülich and the HLR Stuttgart.

Note added in proof

After this review was submitted, we also have completed a more detailed account of the Monte Carlo simulations of the carbon dioxide–hexadecane mixture [323].

References

1. Flory PJ (1953) Principles of polymer chemistry. Cornell University Press, Ithaca 3, 6, 8, 31, 97
2. Tompa H (1956) Polymer Solutions. Butterworths, London 3, 6, 8
3. deGennes PG (1979) Scaling concepts in polymer physics. Cornell University Press, Ithaca 3, 8, 10, 12, 21, 64, 93
4. Kramer EJ (ed.) (1992) Materials science and technology, Vol 12, Structure and properties of polymers. VCH Verlag, Weinheim 3
5. Binder K (1994) Adv Polym Sci 112:181 3, 7, 8, 9, 10, 11, 12, 93
6. Rowlinson JS, Swinton FL (1982) Liquids and liquid mixtures. Butterworths, London 3, 4, 5, 21, 36, 58, 66
7. Kiran E, Levelt-Sengers JMH (eds) (1994) Supercritical fluids. Kluwer, Dordrecht 3, 4, 21
8. Han JH, Han CD (1990) J Polym Sci, Part B: Polymer Phys 28:711 3, 22
9. Goel SK, Beckman EJ (1994) Polym Eng Sci 34:1137, 1148 3, 22
10. Stafford CM, Russell TP, Mc Carthy TJ (1999) Macromol 32:7610 3, 22
11. Krause B, Sijbesma H-JP, Münüklü P, van der Vegt NFA, Wessburg W (2001) Macromolecules 34:8792 3, 22, 57, 58
12. Hikmet RM, Callister S, Keller A (1988) Polymer 29:1378 3
13. Huggins ML (1941) J Chem Phys 9:440 3, 6, 7, 21, 93
14. Flory PJ (1941) J Chem Phys 9:660 3, 6, 7, 21, 93
15. Staverman AJ, Van Santen JH (1941) Recl Trac Chim 60:76 3, 21, 93

16. Virnau P, Müller M, González MacDowell L, Binder K (2004) New J Phys 6, No 7 [http://stacks.iop.org/1367-2630/6/7] 3, 4, 90, 91, 92, 95
17. Swinney HL, Henry DL (1973) Phys Rev A8:2586 4, 5
18. Moldover MR (1985) Phys Rev A31:1022 4, 5
19. Anselme MJ, Gude M, Teja AS (1990) Fluid Phase Equilibria 57:317 4, 5, 14
20. Ambrose D, Tsnopoulos C,(1995) J Chem Eng Data 531:317 4, 5
21. Span R, Wagner W (1996) J Phys Chem Ref Data 25:1509 4, 5, 21
22. Virnau P, Müller M, González MacDowell L, Binder K (2002) Computer Phys Commun 147:378 4, 5, 17, 18, 95
23. Schneider GM (1970) Adv Chem Phys 27:1 4, 5, 36, 38
24. Van Konynenburg P, Scott RL (1980) Philos Trans Soc London Series A298:495 4, 5, 21, 22
25. Cahn JW, Hilliard JE (1958) J Chem Phys 28:258 8, 10
26. Joanny JF, Leibler L (1978) J Phys (Paris) 39:951 8, 10
27. deGennes PG (1980) J Chem Phys 72:4756 8, 10, 46
28. Binder K (1983) J Chem Phys 79:6387 8, 9, 10, 46
29. Widom B (1988) J Stat Phys 52:1343 10, 93
30. Szleifer I, Widom B (1989) J Chem Phys 90:7524 10, 12, 93
31. Sarbach S, Lawrie ID (1984) in: Phase Transitions and Critical Phenomena, Vol 9, Domb C, Lebowitz JL (eds) Academic Press, London 10, 12, 93
32. deGennes PG (1975) J Phys Lett (Paris) 36:L55 10, 93
33. Daoud M, Jannink G (1976) J Phys (Paris) 37:973 10, 93
34. Fisher ME (1974) Rev Mod Phys 46:587 11
35. LeGuillou JC, Zinn-Justin J (1980) Phys Rev B21:3976 11
36. Binder K, Luijten E (2001) Phys Repts 344:179 11
37. Zinn-Justin J (2001) Phys Repts 344:159
38. Widom B (1972) in: Phase Transitions and Critical Phenomena, Vol 2, eds Domb C, Green MS (Academic Press, London) 11
39. Ginzburg VL (1960) Soviet Phys Solid State 2:1824 11
40. Binder K (1995) in: Cohesion and Structure of Surfaces, Pettifor DG (ed) Elsevier Science, Amsterdam 11
41. Anisimov MA, Kiselev SB, Sengers JV, Tang S (1992), Physica A188:487 11
42. deGennes PG (1977) J Phys Lett (Paris) 38:L44 12
43. Joanny JF (1978) J Phys A 11:L117 12
44. Cavallo A, Müller M, Binder K (2003) Europhys Lett 61:214 12
45. Schwahn D, Meier G, Mortensen K, Janssen S (1994) J Phys II (Paris) 4:837 12
46. Deutsch H-P, Binder K (1993) J Phys II (Paris) 3:1049 12, 15
47. Müller M (1999) Macromol Theory Simul 8:343 12
48. Povodyrev AA, Anisimov MA, Sengers JV (1999) Physica A264:345 12
49. Widom B (1993) Physica A194:532 12
50. Enders S, Wolf BA, Binder K (1995) J Chem Phys 103:3809 12
51. Dobashi T, Nakata M, Kaneko M (1980) J Chem Phys 72:6685 13, 64
52. Shinozaki K, Tan T, Saito Y, Nose T (1982) Polymer 23:727 13
53. Prezynski R, Delsanti M, Adam M (1987) J Phys (Paris) 48:115 13, 64
54. Chu B, Wang Z (1988) Macromolecules 21:2283 13
55. Sanchez IZ (1989) J Phys Chem 93:6983 13, 64
56. Heinrich M, Wolf BA (1992) Polymer 33:1926 13
57. Enders S, Huber A, Wolf, BA (1994) Polymer 35:5743 13, 64
58. Sanchez IC (1985) J Appl Phys 58:2871 13

59. Muthukumar M (1986) J Chem Phys 85:2871 13
60. Stepanow S (1987) J Phys (Paris) Lett 48:2087 13
61. Kholodenko AL, Qian C (1989) Phys Rev B40:2477 13
62. Cherayil BJ (1991) J Chem Phys 95:2135 13
63. Lhuillier D (1992) J Phys II (Paris) Lett 2:1411 13
64. Duplantier B (1982) J Phys (France) 43:991 13, 64
65. Privman V, Aharony A, Hohenberg PC (1991) in: Phase Transition and Critical Phenomena Vol 14, Domb C, Lebowitz JL (eds) Academic Press, London p. 1 14
66. Tsonopoulos C, Tan Z (1993) Fluid phase equilibria 83:127 14
67. Smith BD, Srivastava R (1986) Thermodynamics data for pure compounds: Part A: hydrocarbones and ketones. Elsevier Science Publ., Amsterdam 14
68. Younglove BA, Ely JF (1987) J Phys Chem Ref Data 16:577 14
69. Timmerman J (1965) Physico-Chemical Constants of Pure Organic Compounds. Elsevier Science Publ., Amsterdam 14
70. Binder K (1995) (ed) Monte Carlo and Molecular Dynamics Simulations in Polymer Science. Oxford University Press, New York 14, 15, 19, 84
71. Binder K, Ciccotti G (1996) (ed.) Monte Carlo and Molecular Dynamics of Condensed Matter Systems. Società Italiana di Fisica, Bologna 14, 19, 84
72. Landau DP, Binder K (2000) A Guide to Monte Carlo Simulation in Statistical Physics. Cambridge Univ Press, Cambridge 14, 16, 19, 84
73. Binder K, Heermann DW (2002) Monte Carlo Simulation in Statistical Physics: An Introduction. Springer, Berlin 14, 16, 19, 84
74. Rosenbluth MN, Rosenbluth AW (1955) J Chem Phys 23:356 14
75. Metropolis N, Rosenbluth AW, Rosenbluth MN, Teller AH, Teller E (1953) J Chem Phys 21:1087 14
76. Sariban A, Binder K (1987) J Chem Phys 86:5859 14, 15
77. Müller M, Binder K (1995) Macromolcules 28:1825 14, 19
78. Müller M (1995) Macromolecules 28:6556 14, 19
79. Siepmann I (1990) Mol Phys 70:1145 15
80. Frenkel D, Mooij GCAM, Smit B (1992) J Phys Condens Matter 3:3053 15
81. Frenkel D (1993) in: Computer Simulation in Chemical Physics, Allen MP, Tildesley DJ (eds) Kluwer Acad Publ., Dordrecht 15, 19
82. Wilding NB, Müller M, Binder K (1996) J Chem Phys 105:802 15, 16, 19, 20, 21, 64, 86
83. Carmesin I, Kremer K (1988) Macromolecules 21:2819 15
84. Deutsch H-P, Binder K (1991) J Chem Phys 94:2294 15
85. Frauenkron H, Grassberger P (1997) J Chem Phys 107:9599 15, 16, 19, 20, 21, 64
86. Fisher ME (1971) in: Critical Phenomena, Green MS (ed) Academic Press, London p. 1 15, 16, 85
87. Privman VP (1990) (ed) Finite Size Scaling and the Numerical Simulation of Statistical Systems. World Scientific, Singapore 15, 16, 85
88. Binder K (1992) in: Computational Methods in Field Theory, Gausterer H, Lang CB (eds) Springer, Berlin p. 59 15, 16, 85
89. Wilding NB (1993) Z Phys B93:119 15, 16, 19, 85
90. Ferrenberg AM, Swendsen RH (1988) Phys Rev Lett 61:2635 15, 86
91. Ferrenberg AM, Swendsen RH (1989) Phys Rev Lett 63:1195 15, 19, 86
92. Deutsch H-P (1992) J Stat Phys 67:1039 15
93. Wilding NB, Bruce AD (1992) J Phys Condens Matter 4:3087 15, 16, 19, 86
94. Wilding NB, Müller M (1995) J Chem Phys 102:2562 15, 16, 19

95. Madden WG (1990) J Chem Phys 88:3934 15
96. Madden WG, Pesci AI, Freed KF (1990) Macromolecules 23:1181 15
97. Binder K (2001) in: Multiscale Simulations in Chemistry and Physics, Brandt A, Bernholc J, Binder K (eds) IOS Press, Amsterdam p. 207 15
98. Milchev A, Binder K (2001) J Chem Phys 114:8610 15
99. Müller M, MacDowell LG (2000) Macromolecules 33:3902 15, 17, 19, 23, 26, 31, 34, 70, 84, 96, 97
100. Werner A, Müller M, Schmid F, Binder K (1999) J Chem Phys 110:1221; Werner A, Schmid F, Müller M, Binder K (1999) Phys Rev E59:728 15, 21, 40, 93
101. Panagiotopoulos AZ (1987) Mol Phys 61:813 15
102. Panagiotopoulos AZ (1992) Fluid Phase Equilibria 76:97 15
103. Panagiotopoulos AZ (1992) Mol Simul 9:1 15
104. de Pablo JJ, Laso M, Suter UW (1992) J Chem Phys 97:2817 16, 84
105. de Pablo JJ, Laso M, Suter UW (1993) J Chem Phys 98:6157 16, 84
106. Siepmann JI, Karaborni S, Smit B (1993) Nature (London) 365:330 16, 84
107. Siepmann JI, Karaborni S, Smit B (1993) J Am Chem Soc 115:6454 16, 84
108. de Pablo JJ (1995) Fluid Phase Equilibria 104:196 16, 84
109. Smit B, Siepmann JI, Karaborni S (1995) J Chem Phys 102:2126 16, 76, 84
110. Escobedo FA, de Pablo JJ (1996) J Chem Phys 103:1946 16
111. Escobedo FA, de Pablo JJ (1996) J Chem Phys 105:4391 16
112. Gromov DG, de Pablo JJ, Luna Barcenas G, Sanchez IC, Johnston KP (1998) J Chem Phys 108:4647 16, 23, 32
113. Brennan JK, Madden WG (2002) Macromolecules 35:2827 16, 17
114. Sheng Y-J, Panagiotopoulos AZ, Kumar SK, Szleifer I (1994) Macromolecules 27:400 16
115. Kumar SK, Szleifer I, Panagiotopoulos AZ (1991) Phys Rev Lett 66:2935 16
116. Mackie AD, Panagiotopoulos AZ, Kumar SK (1995) J Chem Phys 102:1014 16, 64
117. Mackie AD, Panagiotopoulos AZ, Frenkel D, Kumar SK (1994) Europhys Lett 27:549 16
118. Vega C, Garzon B, MacDowell LG, Lago S (1995) Mol Phys 85:679 16
119. Wilding NB (1997) J Phys Condens Matter 9:585 16, 19
120. Potoff JJ, Panagiotopolous AZ (2000) J Chem Phys 112:6411 16, 17
121. Singh JK, Kofke DA, Errington JR (2003) J Chem Phys 119:3405 16, 17, 19
122. Kim YC, Fisher ME, Luijten E (2003) Phys Rev Lett 91:065701 16
123. Wilding NB (2003) Phys Rev E67:052503 16
124. Goetz WT (2003) J Chem Phys 119:3309 16
125. Binder K (1982) Phys Rev A25:1699 17
126. Berg BA, Hansmann U, Neuhaus T (1993) Phys Rev B47:497 17
127. Müller M, Binder K, Oed W (1995) J Chem Soc Faraday Trans 28:8639 17
128. Hunter JE, Reinhardt WP (1995) J Chem Phys 103:8627 17
129. Errington JR (2003) Phys Rev E67:012102 17
130. Müller M, Schick M (1996) J Chem Phys 105:8885 17
131. Berg BA, Neuhaus T (1992) Phys Rev Lett 68:9 17, 85
132. Hansmann U, Berg, BA, Neuhaus T (1992) Int J Mod Phys C3:1155 17, 85
133. Fitzgerald M, Picard RR, Silver NN (1999) Europhys Lett 46:282 17
134. Virnau P, Müller M (2004) J Chem Phys 120:10925 6, 17, 85
135. Dee GT, Sauer BB (1992) J Colloid Interface Sci 152:85 18
136. Dee GT, Sauer BB (1998) Adv Phys 47:161 18
137. CRC Handbook of Chemistry and Physics (1985) CRC Press, Boca Raton 18

138. Rao M, Berne BJ (1978) Mol Phys 37:455 18
139. Smit B (1988) Phys Rev A37:3481 18
140. Alejandre J, Tildesley DJ, Chapela GA (1995) J Chem Phys 102:4374 19
141. Alejandre J, Tildesley DJ, Chapela GA (1995) Mol Phys 85:651 19
142. Heermann DW, Wang T, Lee WD (2003) Int J Mod Phys C 14:81 19
143. Hager JS, Anisimov MA, Sengers JV, Gorodelskii EE (2002) J Chem Phys 117:5940 21
144. Anisimov MA, Kostko A, Sengers JV (2002) Phys Rev E65:051805 21
145. Virnau P (2003) *Monte-Carlo-Simulationen zum Phasen- und Keimbildungsverhalten von Polymerlösungen*, Dissertation, Mainz 6
146. Cahn JW, Hilliard JE (1959) J Chem Phys 31:688 21, 45, 46, 94
147. Rowlinson JS, Widom B (1982) *Molecular Theory of Capillarity*, Clarendon, Oxford 21, 40, 43
148. Rathke B (2003) *Blasenbildung in gasgesättigten Flüssigkeiten: Der Nachweis homogener Keimbildung*, Fortschritt-Berichte VDI, Reihe 3:770 22, 37, 42, 43
149. Kremer K, Grest GS (1990)J Chem Phys 92:5057 23
150. Luna-Barcenas G, Meredith JC, Sanchez IC, Johnston KP, Gromov DG, dePablo JJ (1997) J Chem Phys 107:10782 23, 32
151. Wignal GD (1999) J Phys :Condens Matter 11:R157 23
152. Müller M (2002) Phys Rev E65:030802(R) 24
153. Hong KM, Noolandi J (1981) Macromolecules 14:727; Noolandi J, Hong KM (1982) Macromolecules 15:483 25, 27, 29
154. Müller M, MacDowell LG, Yethiraj A (2003) J Chem Phys 118:2929 26, 31, 96, 97
155. Müller M, MacDowell LG (2003) J Phys Condens Matter 15:R609 26, 31, 96, 97
156. vanSwol F, Henderson JR (1991) Phys Rev A43:2932 26
157. Woodward CE, Yethiraj A (1994) J Chem Phys 100:3181 26, 96
158. Patra CN, Yethiraj A (2000) J Chem Phys 112:1570 26, 96
159. Patra CN, Yethiraj A (2003) J Chem Phys 118:4702 26, 96
160. Matsen MW, Schick M (1995) Phys Rev Lett 74:4225 27, 29
161. Matsen MW (1999) J Chem Phys 110:4658 27, 29, 30
162. Helfand E (1975) J Chem Phys 62:999 27, 29
163. Oxtoby DW, Evans R (1988) J Chem Phys 89:7521 27, 45, 48
164. Müller M, MacDowell LG, Virnau P, Binder K (2002) J Chem Phys 117:5480 28, 35, 37, 39, 42, 45, 47, 48, 49, 50, 51, 53, 54, 56, 94
165. Press WH, Flannery PB, Teukolsky SA, Vetterling WT (1987) *Numerical Recipes: The Art of Scientific Computing*, Cambridge University Press, New York 30
166. Szleifer I, Carignano MA (1996) Adv Chem Phys 94:742 31, 97
167. Szleifer I (1997) Curr Opin Colloid Interface Sci 2:416 31, 97
168. Müller M, Schick M (1998) Phys Rev E57:6973 31, 97
169. Müller M, Schick M (1996) Macromolecules 29:8900 31, 97
170. Mattice WL, Suter UW (1994) *Conformational theory of large molecules: The Rotational Isometric State model in macromolecular systems*, Wiley Interscience, New York 31, 97
171. Grayce CJ, Yethiraj A, Schweizer KS (1994) J Chem Phys 100:6857 Grayce CJ, Schweizer KS (1994) J Chem Phys 100:6846 32
172. Müller M (1998) Macromolecules 31:9044 32
173. Weinhold JD, Curro JG, Habenschuss A, Londono JD (1999) Macromolecules 32:7276 32
174. Schick M (1990) *Les Houches lectures on "Liquids at interfaces"*, Elsevier Science Publishers B.V. Dietrich S (1988), in *Phase Transitions and Critical Phenomena*, Vol. 12, Domb C and Lebowitz JL (eds), NY Academic Press 40

175. Binder K, Stauffer D (1976) Adv Phys 25:343 41, 43
176. Tanaka HM (2000) J Phys Condens Mat 12:R207 (2000); (1999) Prog Theo Phys 101:863 41, 90
177. Debregeas G, deGennes PG, Brochard–Wyart F (1998) Science (London) 279:1704 41
178. Klein W, Lookman T, Saxena A, Hatch DM (2002) Phys Rev Lett 88:085701 41
179. Zettlemoyer AC (1977) *Nucleation*, Elsevier, Amsterdam 42
180. Binder K (1984) Phys Rev A29:341 43
181. Heermann DW (1984) Z Phys B55:309 43
182. Volmer M, Weber A (1926) Z Phys Chem 119:227; Becker R, Döring W (1935) Ann Phys (Leipzig) 24:719 43, 94
183. Wood SM, Wang ZG (2002) J Chem Phys 116:2289 45, 48
184. Laaksonen A, Talanquer V, Oxtoby DW (1995) Ann Rev Phys Chem 46:489; Oxtoby DW (1992) J Phys Condens Matt 4:7627 48
185. Talanquer V (1997) J Chem Phys 106:9957 52
186. Shen VK, Debenedetti PG (2001) J Chem Phys 114:4149 48, 52
187. Shen VK, Debenedetti PG (2003) J Chem Phys 118:768 52
188. Kusaka I (2003) J Chem Phys 118:1837 52
189. Kusaka I (2003) J Chem Phys 119:1808 52
190. McGraw R, Laaksonen A (1996) Phys Rev Lett 76:2754 52
191. MacDowell LG (2003) J Chem Phys 119:453 52
192. Granasy L, Oxtoby DW (2000) J Chem Phys 112:2410 51
193. ten Wolde RP, Ruiz–Montero MJ, Frenkel D (1995) Phys Rev Lett 75:2714; (1996) J Chem Phys 104:9932 51
194. Ostwald W (1897) Z Phys Chem 22:289 51
195. Talanquer V, Oxtoby DW (1995) J Chem Phys 102:2156 52
196. Talanquer V, Cunningham C, Oxtoby DW (2001) J Chem Phys 114:6759 52, 53, 102
197. The gas has a large entropy and, hence, is favored at high temperatures[196]. Moreover, the interfacial tension is expected to decrease upon increasing temperature. 52
198. Auer S, Frenkel D (2001) Nature (London) 413:711 54
199. Prigogine I (1957) The Molecular Theory of Solutions (North-Holland, Amsterdam) 58
200. Flory PJ, Orwoll RA, Vrij A (1964) J Am Chem Soc 86:3507 58
201. Flory PJ, Orwoll RA, Vrij A (1964) J Am Chem Soc 86:3515 58
202. Flory PJ (1964) J Am Chem Soc 87:1833 58
203. Orwoll RA, Flory PJ (1967) J Am Chem Soc 89:6814 58
204. Orwoll RA, Flory PJ (1967) J Am Chem Soc 89:6822 58
205. Patterson D (1969) Macromolecules 2:672 58
206. Curro JG, Schweizer KS (1987) J Chem Phys 87:1842 58
207. Curro JG, Schweizer KS, Grest GS, Kremer K (1989) J Chem Phys 91:1357 58
208. Attard P (1995) J Chem Phys 102:5411 58
209. Taylor MP, Lipson JEG (1998) J Chem Phys 102:2118 58
210. Gan HH, Eu BC (1995) J Chem Phys 103:2140 58
211. Gan HH, Eu BC (1996) AIChE J 42:2960 58
212. Yethiraj A, Curro JG, Schweizer KS, McCoy JD (1993) J Chem Phys 98:1635 59
213. Yethiraj A (1995) J Chem Phys 102:6874 59
214. Dickman R, Hall CK (1986) J Chem Phys 85:4108 59
215. Honnell KG, Hall CK (1989) J Chem Phys 90:1841 59
216. Wichert JM, Hall CK (1994) Chem Eng Sci 49:2793 59
217. Gulati H, Wichert J, Hall C (1996) J Chem Phys 104:5220 59
218. Yethiraj A, Hall CK (1991) J Chem Phys 95:8494 59

219. Costa LA, Zhou Y, Hall CK, Carra S (1995) J Chem Phys 102:6212 59
220. Mehta SD, Honnell KG (1996) Mol Phys 96:1285 59
221. Wertheim MS (1984) J Stat Phys 35:19 59, 94, 95
222. Wertheim MS (1984) J Stat Phys 35:35 59, 94
223. Wertheim MS (1986) J Stat Phys 42:459 59, 94
224. Wertheim MS (1986) J Stat Phys 42:477 59, 94
225. Wertheim MS (1986) J Chem Phys 85:2929 59
226. Wertheim MS (1987) J Chem Phys 87:7323 59, 61, 95
227. Phan S, Kierlik E, Rosinberg ML, Yu H, Stell G (1993) J Chem Phys 99:5326 59, 61, 95
228. Blas FJ, Vega LF (2001) J Chem Phys 115:3906 59, 95
229. Jackson G, Chapman WG, Gubbins KE (1988) Mol Phys 65:1 59
230. Chapman WG, Jackson G, Gubbins KE (1988) Mol Phys 65:1057 59, 61, 65
231. Chapman WG (1990) J Chem Phys 93:4299 59
232. Johnson JK, Gubbins KE (1992) Mol Phys 77:1033 59
233. Ghonasgi D, Chapman WG (1993) Mol Phys 79:291 59
234. Johnson JK, Muller EA, Gubbins KE (1994) J Phys Chem 98:6413 59, 67, 78
235. Johnson JK (1996) J Chem Phys 104:1729 59
236. Banaszak M, Chiew YC, O'Lenick R, Radosz M (1994) J Chem Phys 100:3803 59
237. Gil-Villegas A, Galindo A, Whitehead PJ, Mills SJ, Jackson G, Burgess AN (1997) J Chem Phys 106:4168 59, 64, 67
238. MacDowell LG, Müller M, Vega C, Binder K (2000) J Chem Phys 113:419 59, 70, 71, 72, 73, 79, 95
239. Tang Y, Lu BCY (2000) Fluid Phase Equilibria 171:27 59, 75
240. Blas FJ, Vega LF (1997) Mol Phys 92:135 59, 78
241. Amos MD, Jackson G (1991) Mol Phys 74:191 59
242. Amos MD, Jackson G (1992) J Chem Phys 96:4604 59
243. Ghonasgi D, Chapman WG (1994) AIChE J 40:878 59
244. MacDowell LG, Virnau P, Müller M, Binder K (2002) J Chem Phys 117:6360 59, 79, 80, 82, 95
245. P Paricaud SV, Jackson G (2003) J Chem Phys 118:8525 59
246. Vega C, MacDowell LG (2001) J Chem Phys 114:10411 59
247. McBride C, Vega C (2002) J Chem Phys 116:1757 59
248. Vega C, Blas FJ, Galindo A (2002) J Chem Phys 116:7645 59
249. Ghonasgi D, Llano-Restrepo M, Chapman WG (1993) J Chem Phys 98:5662 59
250. Escobedo FA, de Pablo JJ (1996) Mol Phys 87:347 59
251. Banaszak M, Chiew YC, Radosz M (1993) Phys Rev E 48:3760 59
252. Davies LA, Gil-Villegas A, Jackson G (1999) J Chem Phys 111:8659 59
253. Chapman WG, Gubbins K, Jackson G, Radosz M (1989) Fluid Phase Equilibria 52:31 59, 64, 67, 95
254. Chapman WG, Gubbins K, Jackson G, Radosz M (1990) Ind Eng Chem Res 29:1709 59, 60, 67, 95
255. McCabe C, Jackson G (1999) Phys Chem Chem Phys 1:2057 60, 74, 75, 78, 80
256. Tang Y, Wang Z, Lu BCY (2001) Mol Phys 99:65 60, 74
257. Galindo A, Whitehead PJ, Jackson G, Burgess AN (1997) J Phys Chem B 101:2082 60
258. Galindo A, Gil-Villegas A, Whitehead PJ, Jackson G, Burgess AN (1998) J Phys Chem B 102:7632 60, 95
259. McCabe C, Galindo A, Gil-Villegas A, Jackson G (1998) J Phys Chem B 102:4138 60
260. McCabe C, Galindo A, Gil-Villegas A, Jackson G (1998) J Phys Chem B 102:8060 60

261. Blas FJ, Vega LF (1998) Ind Eng Chem Res 37:660 60, 80, 95
262. Blas FJ, Vega LF (1998) J Chem Phys 109:7405 60, 74, 75
263. Chen CK, Banaszak M, Radosz M (1998) J Phys Chem B 102:2427 60, 74, 75
264. Passarello JP, Benzaghou S, Tobaly P (2000) Ind Eng Chem Res 39:2578 60, 82
265. Pamies JC, Vega LF (2001) Ind Eng Chem Res 40:2532 60, 74, 75, 76, 78
266. Galindo A, Blas FJ (2002) J Phys Chem B 106:4503 60, 80, 82
267. Imre AR, Kraska T, Yelash LV (2002) Phys Chem Chem Phys 4:992 60
268. Müller E, Gubbins K (2001) Ind Eng Chem Res 40:2193 60
269. Zhou Y, Stell G (1992) J Chem Phys 96:1507 60
270. Jackson G, Sears R (1994) in M Baus, LF Rull, JP Ryckaert, eds., Observation, Prediction and Simulation of Phase Transitions in Complex Fluids (Kluwer, Dordrecht) 625–640 60
271. Vega C, MacDowell LG (2000) Mol Phys 98:1295 60, 63, 73, 78, 95
272. McQuarrie DA (1976) Statistical Mechanics (Harper & Row, New York) 60
273. Dickman R (1989) J Chem Phys 91:454 61
274. Yethiraj A, Honnell KG, Hall CK (1992) Macromolecules 25:3979 61
275. Dautenhahn J, Hall CK (1994) Macromolecules 27:5399 61
276. Rubio AM, Freire JJ (1996) Macromolecules 29:6946 61
277. Bruns W (1996) Macromolecules 29:2641 61
278. MacDowell LG, Vega C (1998) J Chem Phys 109:5670 61, 74
279. Bruns W (1997) Macromolecules 30:4429 61
280. Vega C, Labaig JM, MacDowell LG, Sanz E (2000) J Chem Phys 113:10398 61, 82, 95
281. Zhou Y, Smith SW, Hall CK (1995) Mol Phys 86:1157 61
282. Lue L, Kiselev B (1999) J Chem Phys 110:2684 61
283. Lue L (2000) J Chem Phys 112:3442 61
284. Boublik T (1989) Mol Phys 66:191 61
285. Boublik T, Vega C, Diaz-Peña M (1990) J Chem Phys 93:730 61
286. Vega C, Lago S, Garzon B (1994) J Chem Phys 100:2182 61, 74
287. Phan S, Kierlik E, Rosinberg ML (1994) J Chem Phys 101:7997 61
288. Vega C, MacDowell LG, Padilla P (1996) J Chem Phys 104:701 61
289. Zhou Y, Hall CK, Stell G (1995) J Chem Phys 103:2688 61
290. MacDowell LG, Vega C, Sanz E (2001) J Chem Phys 115:6220 61, 74
291. Kierlik E, Rosinberg ML (1993) J Chem Phys 99:3950 61
292. Chatterjee AP, Schweizer KS (1998) J Chem Phys 108:3813 64
293. Yan Q, de Pablo JJ (2000) J Chem Phys 113:5954 64
294. Yelash LV, Kraska T, Imre AR, Rzoska SJ (2003) J Chem Phys 118:6110 64, 67, 82
295. Nikitin ED, Pavlov PA, Skripov PV (1996) Int J Thermophys 17:455 67
296. Nikitin ED (2000) High Temp (USSR) 38:337 67
297. Yelash LV, Kraska T (1999) Phys Chem Chem Phys 1:2449 67
298. Yelash LV, Kraska T (1999) Phys Chem Chem Phys 1:4315 67, 83
299. Tang Y, Lu BCY (1997) AIChE J 43:2215 see also reference [317] 67, 70
300. Barker JA, Henderson D (1967) J Chem Phys 47:4714 67, 68
301. Tang Y, Lu BCY (1998) Fluid Phase Equilibria 146:73 68, 69
302. Boublik T (1970) J Chem Phys 53:471 68
303. Tang Y, Lu BCY (1999) Fluid Phase Equilibria 165:183 69
304. Hansen JP, McDonald IR (1986) Theory of Simple Liquids (Academic Press, London) 69
305. Tang Y, Lu BCY (1997) Mol Phys 90:215 see also reference [317] 70
306. MacDowell LG, Vega C (1998) J Chem Phys 109:5681 74, 77

307. Ambrose D, Tsnopoulos C (1995) J Chem Eng Data 40:531 76, 77
308. Nikitin ED, Pavlov PA, Popov AP (1997) Fluid Phase Equilibria 141:155 76, 77
309. Vega C, López Rodríguez A (1996) J Chem Phys 105:4223 76
310. Nath SK, Escobedo FA, de Pablo JJ (1998) J Chem Phys 108:9905 76
311. López Rodríguez A, Vega C, Freire JJ (1999) J Chem Phys 111:438 76
312. Ryckaert JP, Bellemans A (1978) Chem Soc Faraday Discussions 66:95 76
313. Vega C, MacDowell LG (1996) Mol Phys 88:1575 77
314. Pamies JC, Vega LF (2002) Mol Phys 100:2519 77
315. Johnson JK, Zollweg JA, Gubbins KE (1993) Mol Phys 78:591 78
316. Blas FJ, Galindo A (2002) Fluid Phase Equilibria 194–197:501 82
317. Tang Y, Lu BCY (2001) Fluid Phase Equilibria 190:149 67, 104
318. Binder K (2003) Physica A319:99 85
319. MacDowell LG, Virnau P, Müller M, Binder K (2004) J Chem Phys, 120:5292 85
320. Wang F, Landau DP (2001) Phys Rev Lett 86:2050 85
321. Schneider G, Alwani Z, Heim W, Horvath E, Franck EU (1967) Chem Ing Techn 39:649 88
322. Amon CT, Martin RJ, Kobayashi R (1986) Fluid Phase Equilibria 31:89 88
323. Virau P, Müller M, MacDowell LG, Binder K (2004) J Chem Phys 121:2169 97

Index

Adv. Polym. Sci. (2005) 173:105–149
DOI:10.1007/b99427

Thermostat Algorithms for Molecular Dynamics Simulations

Philippe H. Hünenberger

Laboratorium für Physikalische Chemie, ETH Zürich, CH-8093 Zürich, Switzerland
phil@igc.phys.chem.ethz.ch

Abstract Molecular dynamics simulations rely on integrating the classical (Newtonian) equations of motion for a molecular system and thus, sample a microcanonical (constant-energy) ensemble by default. However, for compatibility with experiment, it is often desirable to sample configurations from a canonical (constant-temperature) ensemble instead. A modification of the basic molecular dynamics scheme with the purpose of maintaining the temperature constant (on average) is called a thermostat algorithm. The present article reviews the various thermostat algorithms proposed to date, their physical basis, their advantages and their shortcomings.

Keywords Computer simulation, Molecular dynamics, Canonical ensemble, Thermostat algorithm

List of Abbreviations and Symbols

CM center of mass
MC Monte Carlo

MD	molecular dynamics
NMR	nuclear magnetic resonance
SD	stochastic dynamics
δ	Kronecker delta symbol or Dirac delta function
h	Heaviside step function
k_B	Boltzmann's constant
$\mathcal{U}$	instantaneous potential energy
$\mathcal{K}$	instantaneous kinetic energy
$\mathcal{H}$	Hamiltonian
E	energy (thermodynamical)
H	enthalpy
L	Hill energy
R	Ray enthalpy
$\mathcal{T}$	temperature (instantaneous)
T	temperature (thermodynamical)
T_o	reference temperature (heat bath)
β	$\beta = (k_B T_o)^{-1}$
$\mathcal{V}$	volume (instantaneous)
V	volume (thermodynamical)
$\mathcal{P}$	pressure (instantaneous)
P	pressure (thermodynamical)
$\boldsymbol{\mathcal{N}}$	number of particles (n-species, instantaneous)
$\mathbf{N}$	number of particles (n-species, thermodynamical)
$\boldsymbol{\nu}$	chemical potential (n-species, instantaneous)
$\boldsymbol{\mu}$	chemical potential (n-species, thermodynamical)
$\mathbf{p}_{sys}$	system linear momentum
$\mathbf{L}_{sys}$	system angular momentum
$\mathbf{p}_{box}$	box linear momentum
$\mathbf{L}_{box}$	box angular momentum
N_{df}	number of internal degrees of freedom
N_c	number of geometrical constraints
N_r	number of external degrees of freedom
m_i	mass of atom i
$\dot{\mathbf{r}}_i^o$	real velocity of atom i
$\dot{\mathbf{r}}_i$	peculiar velocity of atom i
$\mathbf{F}_i$	force on atom i
$\mathbf{p}_i$	momentum of atom i
$\mathbf{R}_i$	stochastic force on atom i
γ_i	friction coefficient of atom i
λ	velocity scaling factor
Δt	timestep
ζ_T	temperature relaxation time
α	collision frequency (Andersen thermostat)
τ_B	relaxation time (Berendsen thermostat)
Q	"mass" of the time-scaling coordinate (Nosé-Hoover thermostat)

τ_{NH}	effective relaxation time (Nosé-Hoover thermostat)
$\mathcal{L}_e$	extended-system Lagrangian (Nosé-Hoover thermostat)
$\mathcal{H}_e$	extended-system Hamiltonian (Nosé-Hoover thermostat)
E_e	extended-system energy (Nosé-Hoover thermostat)

1 Introduction

Classical atomistic simulations, and in particular molecular dynamics (MD) simulations, have nowadays become a common tool for investigating the properties of polymer [1] and (bio-)molecular systems [2, 3, 4, 5, 6, 7]. Due to their remarkable resolution in space (single atom), time (femtosecond), and energy, they represent a powerful complement to experimental techniques, providing mechanistic insight into experimentally observed processes. However, direct comparison with experiment requires that the boundary conditions imposed on the simulated system are in adequation with the experimental conditions. The term *boundary condition* is used here to denote any geometrical or thermodynamical constraint enforced within the whole system during the simulation. One may distinguish between hard and soft boundary conditions. A *hard* boundary condition represents a constraint on a given instantaneous observable, i.e. it is satisfied exactly at any timepoint during the simulation. A *soft* boundary condition represents a constraint on the average value of an observable, i.e. the corresponding instantaneous value is allowed to fluctuate around the specified average. The definition of a soft boundary condition generally also requires the specification of a timescale for which the average observable should match the specified value. There exist four main types of boundary conditions in simulations:

1. *Spatial boundary conditions* include the definition of the shape of the simulated system and the nature of its surroundings. In molecular simulations, one typically uses either: (i) vacuum boundary conditions (solute molecule surrounded by vacuum); (ii) fixed boundary conditions (solute-solvent system surrounded by vacuum, e.g. droplet [8, 9, 10, 11, 12, 13, 14, 15]); (iii) periodic boundary conditions (solute-solvent system in a space-filling box, surrounded by an infinite array of periodic copies of itself [16, 17]). In the two former cases, the effect of a surrounding solvent can be reintroduced in an implicit fashion by a modification of the system Hamiltonian. Typical modifications are the inclusion of: (i) solvation forces accounting for the mean effect of the solvent [18, 19, 20, 21]; (ii) stochastic and frictional forces accounting for the effect of collisions with solvent molecules [22, 23, 24, 25, 2]; (iii) forces at the system boundary to mimick a system-solvent interface [8, 9, 10, 11, 12, 13, 14, 15]. Spatial boundary conditions are hard boundary conditions, because they apply strictly to all configurations during a simulation.
2. *Thermodynamical boundary conditions* include the definition of the $n + 2$ thermodynamical quantities characterizing the macroscopic state of a (monoplastic) n-component system (for systems under vacuum boundary conditions, only $n + 1$ quantities are required because the volume is not defined while

the thermodynamical pressure is zero). These quantities can be selected form pairs of extensive and intensive quantities including: (i) the number of particles ($\mathbf{N} \equiv \{N_i \mid i = 1...n\}$) or chemical potential ($\boldsymbol{\mu} \equiv \{\mu_i \mid i = 1...n\}$) of all species; (ii) the volume V or pressure P; (iii) the energy E (or a related extensive thermodynamical potential) or temperature T. The selected set of $n + 2$ quantities, together with their reference (macroscopic) values, define the thermodynamical ensemble that is sampled during a simulation (Table 1). By default, MD simulations sample microstates in the microcanonical ($\mathbf{N}VE$) ensemble. By applying specific modifications to the system Hamiltonian or equations of motion, it is possible to maintain instead a constant temperature, pressure or chemical potential for the different species (or any combination of these changes). The thermodynamical boundary conditions involving extensive quantities should be treated as hard boundary conditions, while those involving intensive quantities should be soft.

3. *Experimentally derived boundary conditions* are used to explicitly enforce agreement between a simulation and some experimental result. These may be applied to enforce, e.g., the reproduction of (average) electron density maps from X-ray crystallography [27, 28, 29, 30], or the agreement with (average) interatomic distances and J-coupling constants from NMR measurements [31, 32, 33, 30]. Since experiments always provide averages over a given time and number of molecules, experimentally derived boundary conditions should be handled as soft boundary conditions.
4. *Geometrical constraints* can also be considered as boundary conditions. A typical example is the use of bond-length constraints in simulations [34, 35, 36, 37, 38, 39], which represent a better approximation to the quantum-mechanical behavior of high-frequency oscillators ($h\nu \gg k_B T$) compared to the classical treatment [40]. Since they are satisfied exactly at every timepoint during a simulation, geometrical constraints represent hard boundary conditions.

The present article is concerned with one specific type of thermodynamical boundary condition, namely the imposition of a constant (average) temperature during MD simulations by means of thermostat algorithms. The simultaneous enforcement of a constant (average) pressure [51, 52, 53, 54, 55, 46, 56, 57, 58, 59, 60, 61, 53, 62, 63, 64, 65, 66, 67, 68, 69, 70] or chemical potential [71, 72, 73, 74] will not be considered here. The discussion is also restricted to systems under either vacuum or periodic boundary conditions, i.e., isolated systems. This implies that the Hamiltonian is time-independent, and invariant upon translation or rotation of the whole system. This Hamiltonian may contain terms accounting for the mean effect of the environment (e.g., implicit-solvation term), as long as it still satisfies the above conditions. The only exception considered here (whenever explicitly stated) is the possible inclusion of stochastic and frictional forces as applied in stochastic dynamics (SD) simulations, or of random collisional forces as applied in the stochastic-coupling (Andersen) thermostat. Finally, it should be stressed that the inclusion of geometrical constraints during a simulation affects the statistical mechanics of the sampled microstates [75]. This is mainly because in the presence of such constraints,

Table 1. The eight thermodynamical ensembles, and the corresponding independent and dependent variables. Intensive variables are the chemical potential for all n species ($\boldsymbol{\mu} \equiv \{\mu_i \mid i = 1...n\}$), the pressure ($P$) and the temperature ($T$). Extensive variables are the number of particles for all species ($\mathbf{N} \equiv \{N_i \mid i = 1...n\}$), the volume ($V$), and the energy ($E$), enthalpy ($H = E + PV$), Hill energy ($L = E - \sum \mu_i N_i$), or Ray enthalpy ($R = E + PV - \sum \mu_i N_i$). Note that grand-ensembles may be open with respect to a subset of species only (e.g., semi-grand-canonical ensemble). The generalized ensemble is not a physical ensemble, because its size is not specified (no independent extensive variable). Isothermal ensembles are discussed in many standard textbooks. Specific references are given for the (less common) adiabatic ensembles

Independent	Dependent	Ensemble
$\mathbf{N}VE$	$\boldsymbol{\mu}PT$	Microcanonical [41, 42, 43, 44, 45]
$\mathbf{N}VT$	$\boldsymbol{\mu}PE$	Canonical
$\mathbf{N}PH$	$\boldsymbol{\mu}VT$	Isoenthalpic-isobaric [46, 47, 48, 45]
$\mathbf{N}PT$	$\boldsymbol{\mu}VH$	Isothermal-isobaric (Gibbs)
$\boldsymbol{\mu}VL$	$\mathbf{N}PT$	Grand-microcanonical [49, 45]
$\boldsymbol{\mu}VT$	$\mathbf{N}PL$	Grand-canonical
$\boldsymbol{\mu}PR$	$\mathbf{N}VT$	Grand-isothermal-isobaric [50, 45]
$\boldsymbol{\mu}PT$	$\mathbf{N}VR$	Generalized

the kinetic energy of the system cannot be written in a configuration-independent way (unless the constraints are exclusively involved in fully-rigid atom groups, e.g., rigid molecules). This restriction limits the validity of a number of equations presented in this article. However, many results are expected to remain approximately valid for systems involving a small proportion of constrainted degrees of freedom, and no attempt is made here to derive forms including explicitly the effect of geometrical constraints.

2 Ensembles

An isolated system is characterized by a time-independent, translationally invariant and rotationally invariant Hamiltonian. Integration of the classical equations of motion for such a system leads, in the limit of infinite sampling, to a trajectory mapping a microcanonical ($\mathbf{N}VE$) ensemble of microstates[1]. Assuming an infinite numerical precision, this is also what a standard MD simulation will deliver.

The laws of classical mechanics also lead to two additional conserved quantities, namely the linear momentum $\mathbf{p}_{sys}$ of the system, and the angular momentum $\mathbf{L}_{sys}$ of

[1] Thermodynamical ensembles are generally defined without the constraint of Hamiltonian translational and rotational invariance, in which case the previous statement is not entirely correct. In the present article, however, the terminology of Table 1 will be (loosely) retained to encompass ensembles where this invariance is enforced. The statistical mechanics of these latter ensembles must be adapted accordingly [76, 77, 78, 79, 80, 81]. This requires in particular the introduction of a modified definition for the instantaneous temperature, relying solely on internal degrees of freedom and kinetic energy (Sect. 3).

the system around its center of mass (CM). In simulations under periodic boundary conditions, the two quantities refer to the infinite periodic system. However, in this case, if the linear momentum $\mathbf{p}_{box}$ of the computational box is also conserved, the corresponding angular momentum $\mathbf{L}_{box}$ is not. This is because correlated rotational motion in two adjacent boxes exert friction on each other, leading to an exchange of kinetic energy with the other (internal) degrees of freedom of the system. Note that the physical properties of a molecular system are independent of $\mathbf{p}_{sys}$. However, they depend on $\mathbf{L}_{sys}$, because the rotation of the system leads to centrifugal forces. For this reason, $\mathbf{L}_{sys}$ should be added to the list of independent variables defining the ensemble sampled. Whenever $\mathbf{L}_{sys}$ is not given, it generally implicitly means that $\mathbf{L}_{sys} = \mathbf{0}$. The use of $\mathbf{L}_{sys} \neq \mathbf{0}$ in simulations under periodic boundary conditions (overall uniform rotation of the infinite periodic system) is actually impossible, because it would lead to non-periodic centrifugal forces. Finally, it should be specified that the total energy E of the system is defined here so as to exclude the kinetic energy contributions corresponding to the overall translation and rotation of the system (so that E is independent of $\mathbf{p}_{sys}$ and $\mathbf{L}_{sys}$).

Because the independent variables of the microcanonical ensemble are all extensive, they should be strictly conserved (i.e., time-independent) during the course of a simulation. The corresponding dependent variables, namely the chemical potential $\boldsymbol{\mu}$, the pressure P, and the temperature T, are not conserved. In a non-equilibrium simulation, these quantities may undergo a systematic drift. In an equilibrium simulation, the corresponding instantaneous observables (denoted by $\boldsymbol{\nu}$, $\mathcal{P}$, and $\mathcal{T}$) will fluctuate around well-defined average values $\boldsymbol{\mu}$, P, and T. Two important comments should be made concerning the previous statement. First, the instantaneous observables $\boldsymbol{\nu}$, $\mathcal{P}$, and $\mathcal{T}$ are not uniquely defined. The instantaneous temperature is generally related to the total kinetic energy of the system (Eq. (8)), and the instantaneous pressure to the total virial and kinetic energy. However, alternative definitions are available (differing from the above by any quantity with a vanishing equilibrium average), leading to identical average values in equilibrium situations, but to different fluctuations. Second, a microcanonical ensemble at equilibrium could equally well be specified by stating that $\mathbf{N}$, V, and E are conserved, and giving the values of $\boldsymbol{\mu}$ instead of $\mathbf{N}$, P instead of V, or T instead of E (as long as at least one extensive variable is specified). However, such a specification would be rather unnatural as well as inapplicable to non-equilibrium situations. Furthermore, only the natural variables for defining a given thermodynamical ensemble (Table 1) are either time-independent or characterized by vanishing fluctuations in the limit of a macroscopic system. Finally, it should be stressed that computer simulations cannot be performed at infinite numerical precision. As a consequence, quantities which are formally time-independent in classical mechanics may still undergo a numerical drift in simulations. In microcanonical simulations, this is typically the case for E, as well as $\mathbf{p}_{sys}$ and $\mathbf{L}_{sys}$ (vacuum boundary conditions), or $\mathbf{p}_{box}$ (periodic boundary conditions).

Unfortunately, the microcanonical ensemble that comes out of a standard MD simulation does not correspond to the conditions under which most experiments are

carried out. For comparison with experiment, the following ensembles are more useful, which involve one or more intensive independent variables (Table 1):

1. In the *canonical ensemble* ($\mathbf{N}VT$), the temperature has a specified average (macroscopic) value, while the instantaneous observable representing the total energy of the system (i.e., the Hamiltonian $\mathcal{H}$) can fluctuate. At equilibrium, the root-mean-square fluctuations σ_E of the Hamiltonian around its average value E are related to the system isochoric heat capacity, c_V, through [16]

$$\sigma_E^2 = \left\langle \mathcal{H}^2 \right\rangle_{\mathbf{N}VT} - \langle \mathcal{H} \rangle_{\mathbf{N}VT}^2 = k_B T^2 c_V \ . \tag{1}$$

   The fluctuations σ_T of the instantaneous temperature $\mathcal{T}$ (defined by Eq. (8)) in a canonical ensemble are given by [16]

$$\sigma_T^2 = \left\langle \mathcal{T}^2 \right\rangle_{\mathbf{N}VT} - \langle \mathcal{T} \rangle_{\mathbf{N}VT}^2 = 2N_{df}^{-1} T^2 \ , \tag{2}$$

   where N_{df} is the number of internal degrees of freedom in the system (Eq. (9)). These fluctuations vanish in the limit of a macroscopic system, but are often non-negligible for the system sizes typically considered in simulations.
2. In the *isothermal-isobaric (Gibbs) ensemble* ($\mathbf{N}PT$), the pressure has (just as the temperature) a specified average value, while the instantaneous volume $\mathcal{V}$ of the system can fluctuate. At equilibrium, the root-mean-square fluctuations σ_V of the instantaneous volume around its average value V are related to the system isothermal compressibility, β_T, through [16]

$$\sigma_V^2 = \langle \mathcal{V}^2 \rangle_{\mathbf{N}PT} - \langle \mathcal{V} \rangle_{\mathbf{N}PT}^2 = V k_B T \beta_T \ . \tag{3}$$

   The root-mean-square fluctuations σ_H of the instantaneous enthalpy $\mathcal{H} + P\mathcal{V}$ around its average value H are related to the system isobaric heat capacity, c_P, through [16]

$$\sigma_H^2 = \langle (\mathcal{H} + P\mathcal{V})^2 \rangle_{\mathbf{N}PT} - \langle \mathcal{H} + P\mathcal{V} \rangle_{\mathbf{N}PT}^2 = k_B T^2 c_P \ . \tag{4}$$

   Both the instantaneous temperature $\mathcal{T}$ and the instantaneous pressure $\mathcal{P}$ will fluctuate around their corresponding macroscopic values, the magnitude of these fluctuations vanishing in the limit of a macroscopic system.
3. The *grand-canonical ensemble* ($\boldsymbol{\mu} VT$) has a constant volume and temperature (as the canonical ensemble), but is open for exchanging particles with a surrounding bath. In this case, the chemical potential of the different species has a specified average, while the instantaneous value $\boldsymbol{\mathcal{N}}$ of the number of particles can fluctuate. For a one-component system at equilibrium, the fluctuations σ_N of the instantaneous number of particles around its average value N are related to the system isothermal compressibility, β_T, through [16]

$$\sigma_N^2 = \left\langle \mathcal{N}^2 \right\rangle_{\mu VT} - \langle \mathcal{N} \rangle_{\mu VT}^2 = N^2 V^{-1} k_B T \beta_T \ . \tag{5}$$

The root-mean-square fluctuations σ_L of the instantaneous Hill energy $\mathcal{H} - \mu\mathcal{N}$ around its average value L are given by [16]

$$\sigma_L^2 = \left\langle (\mathcal{H} - \mu\mathcal{N})^2 \right\rangle_{\mu VT} - \langle \mathcal{H} - \mu\mathcal{N} \rangle_{\mu VT}^2 = k_B T^2 \left(\frac{\partial L(\mu, V, T)}{\partial T} \right)_{\mu V} . \quad (6)$$

Three other combinations of variables are possible (Table 1), but the corresponding ensembles [45] are of more limited practical relevance. The last combination (generalized ensemble) is not physical, because its size is not specified (no independent extensive variable). Note that although MD samples the microcanonical ensemble by default, the basic Monte Carlo (MC; [82, 83, 84]) and stochastic dynamics (SD; [22, 23, 24, 25, 2]) algorithms sample the canonical ensemble.

Performing a MD simulation in an other ensemble than microcanonical requires a means to keep at least one intensive quantity constant (on average) during the simulation. This can be done either in a hard or in a soft manner. Applying a hard boundary condition on an intensive macroscopic variable means constraining a corresponding instantaneous observable to its specified macroscopic value at every timepoint during the simulation (constraint method). Remember, however, that the choice of this instantaneous observable is not unique. In contrast, the use of a soft boundary condition allows for fluctuations in the instantaneous observable, only requiring its average to remain equal to the macroscopic value (on a given timescale). Typical methods for applying soft boundary conditions are the penalty-function, weak-coupling, extended-system and stochastic-coupling methods [85]. These methods will be discussed in the following sections in the context of constant-temperature simulations. Although there are many ways to ensure that the average of an instantaneous quantity takes a specified value, ensuring that the simulation actually samples the correct ensemble (and in particular provides the correct fluctuations for the specific instantaneous observable in the given ensemble) is much more difficult.

3 Thermostat Algorithms

A modification of the Newtonian MD scheme with the purpose of generating a thermodynamical ensemble at constant temperature is called a thermostat algorithm. The use of a thermostat can be motivated by one (or a number) of the following reasons: (i) to match experimental conditions (most condensed-phase experiments are performed on thermostatized rather than isolated systems); (ii) to study temperature-dependent processes (e.g., determination of thermal coefficients, investigation of temperature-dependent conformational or phase transitions); (iii) to evacuate the heat in dissipative non-equilibrium MD simulations (e.g., computation of transport coefficients by viscous-flow or heat-flow simulations); (iv) to enhance the efficiency of a conformational search (e.g., high-temperature dynamics, simulated annealing); (v)

to avoid steady energy drifts caused by the accumulation of numerical errors during MD simulations[2].

The use of a thermostat requires the definition of an instantaneous temperature. This temperature will be compared to the reference temperature T_o of the heat bath to which the system is coupled. Following from the equipartition theorem, the average internal kinetic energy K of a system is related to its macroscopic temperature T through

$$K = \langle \mathcal{K} \rangle = \frac{1}{2} k_B N_{df} T \tag{7}$$

where k_B is Boltzmann's constant, N_{df} the number of internal degrees of freedom of the system, and $\mathcal{K}$ its instantaneous internal kinetic energy. Defining the instantaneous temperature $\mathcal{T}$ at any timepoint as

$$\mathcal{T} = \frac{2}{k_B N_{df}} \mathcal{K} \,, \tag{8}$$

one ensures that the average temperature $\langle \mathcal{T} \rangle$ is identical to the macroscopic temperature T. This definition is commonly adopted, but by no means unique. For example, the instantaneous temperature could be defined based on the equipartition principle for only a subset of the internal degrees of freedom. It may also be defined purely on the basis of configuration, without any reference to the kinetic energy [87, 88].

In the absence of stochastic and frictional forces (see below; Eq. (17)), a few degrees of freedom are not coupled (i.e., do not exchange kinetic energy) with the internal degrees of freedom of the system. These external degrees of freedom correspond to the system rigid-body translation and, under vacuum boundary conditions, rigid-body rotation. Because the kinetic energy associated with these external degrees of freedom can take an arbitrary (constant) value determined by the initial atomic velocities, they must be removed from the definition of the system internal temperature. Consequently, the number of internal degrees of freedom is calculated as three times the total number N of atoms in the system, minus the number N_c of geometrical constraints, i.e.

$$N_{df} = 3N - N_c - N_r \,. \tag{9}$$

The subtraction of constrained degrees of freedom is necessary because geometrical constraints are characterized by a time-independent generalized coordinate associated with a vanishing generalized momentum (i.e., no kinetic energy). A more formal statistical-mechanical justification for the subtraction of the external degrees of

[2] A thermostat algorithm (involving explicit reference to a heat-bath temperature T_o) will avoid systematic energy drifts, because if the instantaneous temperature is forced to fluctuate within a limited range around T_o, the energy will also fluctuate within a limited range around its corresponding equilibrium value. To perform long microcanonical simulations (no thermostat), it is also advisable to employ an algorithm that will constrain the energy to its reference value E^o (ergostat algorithm [86]).

freedom in the case of periodic boundary conditions can be found elsewhere [45]. A corresponding derivation for vacuum boundary conditions has, to our knowledge, never been reported. When stochastic and frictional forces are applied, as in SD, these forces will couple the rigid-body translational and rotational degrees of freedom with the internal ones. In this case all degrees of freedom are considered internal to the system. Thus, Eq. (9) is to be used with $N_r = 0$ in the presence of stochastic and frictional forces, and otherwise with $N_r = 3$ under periodic boundary conditions or $N_r = 6$ under vacuum boundary conditions. Similarly, the instantaneous internal kinetic energy is defined as

$$\mathcal{K} = \frac{1}{2} \sum_{i=1}^{N} m_i \dot{\mathbf{r}}_i^2 \,, \tag{10}$$

where the internal (also called peculiar) velocities $\dot{\mathbf{r}}_i$ are obtained from the real atomic velocities $\dot{\mathbf{r}}_i^o$ by excluding any component along the external degrees of freedom[3]. These corrected velocities are calculated as

$$\dot{\mathbf{r}}_i = \begin{cases} \dot{\mathbf{r}}_i^o & \text{if} \quad N_r = 0 \\ \dot{\mathbf{r}}_i^o - \dot{\mathbf{r}}_{CM}^o & \text{if} \quad N_r = 3 \\ \dot{\mathbf{r}}_i^o - \dot{\mathbf{r}}_{CM}^o - \underline{\mathbf{I}}_{CM}^{-1}(\mathbf{r}^o)\, \mathbf{L}_{CM}^o \times (\mathbf{r}_i^o - \mathbf{r}_{CM}^o) & \text{if} \quad N_r = 6 \end{cases} , \tag{11}$$

where $\mathbf{r}_{CM}^o$ is the coordinate vector of the system center of mass (CM), $\mathbf{L}_{CM}^o$ the system angular momentum about the CM, and $\underline{\mathbf{I}}_{CM}$ is the (configuration-dependent) inertia tensor of the system relative to the CM. The latter quantity is defined as

$$\underline{\mathbf{I}}_{CM}(\mathbf{r}) = \sum_{i=1}^{N} m_i \, (\mathbf{r}_i - \mathbf{r}_{CM}) \otimes (\mathbf{r}_i - \mathbf{r}_{CM}) \,, \tag{12}$$

where $\mathbf{a} \otimes \mathbf{b}$ denotes the tensor with elements μ, ν equal to $a_\mu b_\nu$. Application of Eq. (11) ensures that

$$\sum_{i=1}^{N} m_i \, \dot{\mathbf{r}}_i = \mathbf{0} \quad \text{for} \quad N_r = 3 \text{ or } 6 \tag{13}$$

and (irrespective of the origin of the coordinate system)

$$\sum_{i=1}^{N} m_i \, \mathbf{r}_i \times \dot{\mathbf{r}}_i = \mathbf{0} \quad \text{for} \quad N_r = 6. \tag{14}$$

Equation (13) is a straightforward consequence of the definition of $\mathbf{r}_{CM}^o$. Equation (14) is proved by using $\boldsymbol{\omega}_{CM}^o \times (\mathbf{r}_i^o - \mathbf{r}_{CM}^o) = \dot{\mathbf{r}}_i^o - \dot{\mathbf{r}}_{CM}^o$ where $\boldsymbol{\omega}_{CM}^o = \underline{\mathbf{I}}_{CM}^{-1}(\mathbf{r}^o)\, \mathbf{L}_{CM}^o$ is the angular velocity vector about the CM. Thus, the linear and angular momenta of the internal velocities vanish, as expected.

[3] It is assumed that the velocities $\dot{\mathbf{r}}_i^o$ are already exempt of any component along possible geometrical constraints.

Because the instantaneous temperature is directly related to the atomic internal velocities (Eqs. (8) and (10)), maintaining the temperature constant (on average) in MD simulations requires imposing some control on the rate of change of these velocities. For this reason, thermostat algorithms require a modification of Newton's second law[4]

$$\ddot{\mathbf{r}}_i(t) = m_i^{-1}\mathbf{F}_i(t) \; . \tag{15}$$

In the present context, this equation (and the thermostatized analogs discussed below) should be viewed as providing the time-derivative of the internal velocity $\dot{\mathbf{r}}_i$ defined by Eq. (11). In turn, $\dot{\mathbf{r}}_i$ is related to the real atomic velocity $\dot{\mathbf{r}}_i^o$ through the inverse of Eq. (11), namely

$$\dot{\mathbf{r}}_i^o = \begin{cases} \dot{\mathbf{r}}_i & \text{if} \quad N_r = 0 \\ \dot{\mathbf{r}}_i + \dot{\mathbf{r}}_{CM}^* & \text{if} \quad N_r = 3 \\ \dot{\mathbf{r}}_i + \dot{\mathbf{r}}_{CM}^* + \underline{\mathbf{I}}_{CM}^{-1}(\mathbf{r}^o)\, \mathbf{L}_{CM}^* \times (\mathbf{r}_i^o - \mathbf{r}_{CM}^o) & \text{if} \quad N_r = 6 \end{cases} , \tag{16}$$

where $\mathbf{r}_{CM}^*$ and $\mathbf{L}_{CM}^*$ are constant parameters determined by the initial velocities $\dot{\mathbf{r}}_i^o(0)$. This distinction between real and internal velocities is often ignored in standard simulation programs. Many programs completely disregard the problem, while others only remove the velocity component along the external degrees of freedom for the computation of the temperature (but do not use internal velocities in the equations of motion). However, as discussed in Sect. 4, this can have very unpleasant consequences in practice. In the following discussion, it is assumed that the equation of motion (Eq. (15) or any thermostatized modification) is applied to the internal velocities defined by Eq. (11), while the atomic coordinates are propagated simultaneously in time using the real velocities $\dot{\mathbf{r}}_i^o$ defined by Eq. (16).

The prototype of most isothermal equations of motion is the Langevin equation (as used in SD; see Sect. 3.2), i.e.

$$\ddot{\mathbf{r}}_i(t) = m_i^{-1}\mathbf{F}_i(t) - \gamma_i(t)\dot{\mathbf{r}}_i(t) + m_i^{-1}\mathbf{R}_i(t) \; , \tag{17}$$

where $\mathbf{R}_i$ is a stochastic force and γ_i a (positive) atomic friction coefficient. Many thermostats avoid the stochastic force in Eq. (17) and use a single friction coefficient for all atoms. This leads to the simplified form

$$\ddot{\mathbf{r}}_i(t) = m_i^{-1}\mathbf{F}_i(t) - \gamma\,(t)\dot{\mathbf{r}}_i(t) \; . \tag{18}$$

In this case, γ loses its physical meaning of a friction coefficient and is no longer restricted to positive values. A positive value indicates that heat flows from the system to the heat bath. A negative value indicates a heat flow in the opposite direction. Note that if Eq. (18) was applied to the real velocities $\dot{\mathbf{r}}_i^o$ (as often done in simulation programs) instead of the internal velocities $\dot{\mathbf{r}}_i$, the linear and angular momenta of the system would not be conserved (unless they exactly vanish).

[4] It is assumed that the forces $\mathbf{F}_i$ are exempt of any component along possible geometrical constraints.

Any algorithm relying on the equation of motion given by Eq. (18) is smooth (i.e., generates a continuous velocity trajectory) and deterministic[5]. It is also time-reversible if γ is antisymmetric with respect to time-reversal[6].

Practical implementations of Eq. (18) often rely on the stepwise integration of Newton's second law (Eq. (15)), altered by the scaling of the atomic velocities after each iteration step. In the context of the leap-frog integrator[7] [89], this can be written

$$\begin{aligned}\dot{\mathbf{r}}_i\left(t+\frac{\Delta t}{2}\right) &= \lambda(t;\Delta t)\,\dot{\mathbf{r}}'_i\left(t+\frac{\Delta t}{2}\right)\\ &= \lambda(t;\Delta t)\left[\dot{\mathbf{r}}_i(t-\frac{\Delta t}{2})+m_i^{-1}\mathbf{F}_i(t)\Delta t\right],\end{aligned} \tag{20}$$

where $\lambda(t;\Delta t)$ is a time- and timestep-dependent velocity scaling factor. Imposing the constraint[8] $\lambda(t;0)=1$, one recovers Eq. (18) in the limit of an infinitesimal timestep Δt, with

$$\gamma(t) = -\lim_{\Delta t\to 0}\frac{\lambda(t;\Delta t)-1}{\Delta t} = -\frac{\partial\lambda(t;\Delta t)}{\partial(\Delta t)}\Big|_{\Delta t=0}. \tag{21}$$

Note that for a given equation of motion, i.e., a specified form of $\gamma(t)$, Eq. (21) does not uniquely specify the scaling factor $\lambda(t;\Delta t)$. It can be shown that Eq. (20) retains the original accuracy of the leap-frog algorithm if the velocity-scaling factor applied to atom i is chosen as [90]

$$\lambda_i(t;\Delta t) = 1-\gamma(t)\Delta t+\left[\frac{\gamma^2(t)}{2}+\frac{\gamma(t)F_i(t)}{2m_i\dot{r}_i(t)}\right](\Delta t)^2. \tag{22}$$

From a thermodynamical point of view, some thermostats can be proved to generate (at constant volume and number of atoms) a canonical ensemble in the limit of infinite sampling times (and within the usual statistical-mechanical assumptions of equal *a priori* probabilities and ergodicity). More precisely, some thermostats lead to a canonical ensemble of microstates, i.e., microstates are sampled with a statistical

[5] The advantages of deterministic algorithms are that (i) the results can be exactly reproduced (in the absence of numerical errors), and (ii) there are well-defined conserved quantities (constants of the motion). In the case of Eq. (18), the constant of the motion is

$$C = \mathcal{K}(t)+\mathcal{U}(t)+2\int_0^t dt\,\mathcal{K}(t)\gamma(t). \tag{19}$$

[6] Considering a given microstate, time-reversibility is achieved if the change $dt\to -dt$ (leading in particular to $\mathbf{r}\to\mathbf{r}$, $\dot{\mathbf{r}}\to-\dot{\mathbf{r}}$, and $\ddot{\mathbf{r}}\to\ddot{\mathbf{r}}$) leaves the equation of motion for the coordinates unaltered (while the velocities are reversed). Clearly, this condition is satisfied for Eq. (18) only if the corresponding change for γ is $\gamma\to-\gamma$.

[7] The implementation of thermostats will only be discussed here in the context of the leap-frog integrator. However, implementation with other integrators is generally straightforward.

[8] An algorithm with $\lambda(t;0)\neq 1$ would involve a Dirac delta function in its equation of motion.

weight proportional to $e^{-\beta\mathcal{H}}$ where $\beta = (k_B T_o)^{-1}$. In this case and in the absence of geometrical constraints, expressing the Hamiltonian in Cartesian coordinates as $\mathcal{H}(\mathbf{r}, \mathbf{p}) = \mathcal{U}(\mathbf{r}) + \mathcal{K}(\mathbf{p})$, $\mathcal{U}$ being the potential energy, the probability distribution of microstates may be written

$$\rho(\mathbf{r}, \mathbf{p}) = \frac{e^{-\beta\mathcal{H}(\mathbf{r},\mathbf{p})}}{\int d\mathbf{r} \int d\mathbf{p}\, e^{-\beta\mathcal{H}(\mathbf{r},\mathbf{p})}} = \frac{e^{-\beta\mathcal{U}(\mathbf{r})}}{\int d\mathbf{r}\, e^{-\beta\mathcal{U}(\mathbf{r})}} \frac{e^{-\beta\mathcal{K}(\mathbf{p})}}{\int d\mathbf{p}\, e^{-\beta\mathcal{K}(\mathbf{p})}} \,. \tag{23}$$

Integrating this expression over either momenta or coordinates shows that the distribution is also canonical in both configurations (i.e., configurations are sampled with a statistical weight proportional to $e^{-\beta\mathcal{U}}$) and momenta (i.e., momenta are sampled with a statistical weight proportional to $e^{-\beta\mathcal{K}}$). In Cartesian coordinates, such a canonical distribution of momenta reads

$$\rho_p(\mathbf{p}) = \frac{e^{-\beta\mathcal{K}(\mathbf{p})}}{\int d\mathbf{p}\, e^{-\beta\mathcal{K}(\mathbf{p})}} = \prod_{i\mu}^{3N} \frac{e^{-\beta(2m_i)^{-1}p_{i\mu}^2}}{\int dp_{i\mu}\, e^{-\beta(2m_i)^{-1}p_{i\mu}^2}} = \prod_{i\mu}^{3N} p(p_{i\mu}) \,, \tag{24}$$

where Eq. (10) was used together with $\mathbf{p}_i = m_i \dot{\mathbf{r}}_i$. Noting that $p(\dot{r}_{i\mu}) = m_i\, p(p_{i\mu})$ and evaluating the required Gaussian integral, this result shows that internal velocities obey a Maxwell-Boltzmann distribution, i.e., the velocity components $\dot{r}_{i\mu}$ appear with the probability

$$p(\dot{r}_{i\mu}) = \left(\frac{\beta m_i}{2\pi}\right)^{1/2} e^{-(1/2)\beta m_i \dot{r}_{i\mu}^2} \,. \tag{25}$$

Note that the above statements do not formally hold in the presence of geometrical constraints, but are generally assumed to provide a good approximation in this case. Some other thermostats only generate a canonical ensemble of configurations, but not of microstates and momenta. This is generally not a serious disadvantage for the computation of thermodynamical properties, because the contribution of momenta to thermodynamical quantities can be calculated analytically (ideal-gas contribution). Finally, there also exists thermostats that generate distributions that are canonical neither in configurations nor in momenta.

From a dynamical point of view, assessing the relative merits of different thermostats is somewhat subjective[9]. Clearly, the configurational dynamics of a system will be affected by the timescale of its instantaneous temperature fluctuations, and a good thermostat should reproduce this timescale at least qualitatively. However, the direct comparison between experimental thermostats (e.g., a heat bath surrounding

[9] An objective question, however, is whether the thermostat is able to produce correct time-correlation functions (at least in the limit of a macroscopic system). Since transport coefficients (e.g., the diffusion constant) can be calculated either as ensemble averages (Einstein formulation) or as integrals of a time-correlation function (Green-Kubo formulation), at least such integrals should be correct if the thermostat leads to a canonical ensemble. When this is the case, it has been shown that the correlation functions themselves are also correct at least for some thermostats [91, 86].

a macroscopic system, or the bulk medium around a microscopic sample of matter) and thermostats used in simulations is not straightforward. The reason is that experimental thermostats, because they involve the progressive diffusion of heat from the system surface towards its center (or inversely), lead to inhomogeneities in the spatial temperature distribution within the sample. On the other hand, the thermostats used in simulations generally modify instantaneously and simultaneously the velocities of all atoms irrespective of their locations, and should lead to an essentially homogeneous temperature distribution.

One may nevertheless try to quantify the timescale of the temperature fluctuations to be expected in a thermostatized simulation. This timescale can be estimated based on a semi-macroscopic approach [55]. Consider a system characterized by an average temperature $\overline{\mathcal{T}}$, in contact with a heat bath at a different temperature T_o. By average temperature, it is meant that the quantity $\overline{\mathcal{T}}$ is spacially-averaged over the entire system and time-averaged over an interval that is short compared to the experimental timescale, but long compared to the time separating atomic collisions. The difference between $\overline{\mathcal{T}}$ and T_o may result, e.g., from a natural fluctuation of $\overline{\mathcal{T}}$ within the system. From macroscopic principles, the rate of heat transfer from the heat bath to the the system should be proportional to the temperature difference $T_o - \overline{\mathcal{T}}$ and to the thermal conductivity κ of the system. Thus, the rate of change in the average temperature can be written (at constant volume)

$$\dot{\overline{\mathcal{T}}}(t) = c_v^{-1}\dot{\overline{E}}(t) = \zeta_T^{-1}\,[T_o - \overline{\mathcal{T}}(t)] \tag{26}$$

with the definition

$$\zeta_T = \xi^{-1} V^{-1/3} c_v \kappa^{-1}\,, \tag{27}$$

where c_v is the system isochoric heat capacity, V the system volume, and ξ a dimensionless constant depending on the system shape and on the temperature inhomogeneity within the system. For a given system geometry (e.g., spherical) and initial temperature distribution (i.e., $T(\mathbf{x}, 0)$), a reasonable value for ξ could in principle be estimated by solving simultaneously the flux equation

$$\mathbf{J}(\mathbf{x}, t) = -\kappa \nabla T(\mathbf{x}, t), \tag{28}$$

where $\mathbf{J}(\mathbf{x}, t)$ is the energy flux through a surface element perpendicular to the direction of the vector, and the conservation equation

$$\frac{\partial T(\mathbf{x}, t)}{\partial t} = -V c_v^{-1} \nabla \cdot \mathbf{J}(\mathbf{x}, t)\,. \tag{29}$$

Eq. (26) implies that, at equilibrium, the natural fluctuations of $\overline{\mathcal{T}}$ away from T_o decay exponentially with a temperature relaxation time ζ_T, i.e.

$$\overline{\mathcal{T}}(t) = T_o + [\overline{\mathcal{T}}(0) - T_o]\, e^{-\zeta_T^{-1} t}\,. \tag{30}$$

Note that on a very short timescale (i.e., of the order of the time separating atomic collisions), the instantaneous temperature $\mathcal{T}(t)$ is also affected by important stochastic variations (see Sect. 3.2). Only on an intermediate timescale does the mean effect

of these stochastic fluctuations result in an exponential relaxation for $\overline{\mathcal{T}}(t)$. However, because stochastic variations contribute significantly to the instantaneous temperature fluctuations, a thermostat based solely on an exponential relaxation for $\mathcal{T}(t)$ leads to incorrect (underestimated) temperature fluctuations (see Sect. 3.5).

To summarize, although assessing whether one thermostat leads to a better description of the dynamics compared to another one is largely subjective, it seems reasonable to assume that: (i) thermostats permitting temperature fluctuations are more likely to represent the dynamics correctly compared to thermostats constraining the temperature at a fixed value; (ii) thermostats with temperature fluctuations are more likely to represent the dynamics correctly when these fluctuations occur at a timescale (measured in a simulation, e.g., as the decay time of the temperature autocorrelation function) of the order of ζ_T (Eq. (26)), and when the dynamics is smooth (continuous velocity trajectory). These differences will be more significant for small systems, where the temperature fluctuations are of of larger magnitudes (the corresponding root-mean-square fluctuations scale as $N^{-1/2}$, see Eq. (2)) and higher frequencies (the corresponding relaxation times scale as $N^{-1/3}$, see Eq. (27)).

A summary of the common thermostats used in MD simulations, together with their main properties, is given in Table 2. The various algorithms are detailed in the following sections.

3.1 Temperature in the Monte Carlo Algorithm

Although the present discussion mainly focuses on thermostatized MD, the simplest way to generate a thermodynamical ensemble at constant temperature is to use the MC algorithm [82, 83, 84]. This algorithm does not involve atomic velocities or kinetic energy. Random trial moves are generated, and accepted with a probability

$$p = \min\{e^{-\beta \Delta \mathcal{U}}, 1\} \tag{31}$$

depending on the potential energy change $\Delta \mathcal{U}$ associated with the move and on the reference temperature T_o. Following this criterion, moves involving rigid-body translation and, under vacuum boundary conditions, rigid-body rotation are always accepted because they do not change the potential energy. For this reason, the corresponding degrees of freedom are external to the system. Note also that under vacuum boundary conditions, the centrifugal forces due to the rigid-body rotation of the system, which would be included in a MD simulation, are absent in the MC procedure. Therefore, MC samples by default an ensemble at zero angular momentum. It can be shown that the ensemble generated by the MC procedure represents (at constant volume) a canonical distribution of configurations. The modification of the MC scheme to sample other isothermal ensembles (including the grand-canonical ensemble [92]) is possible. Modifications permitting the sampling of adiabatic ensembles (e.g., the microcanonical ensemble [92, 93, 94]) have also been devised. The MC procedure is non-smooth, non-deterministic, time-irreversible, and does not provide any dynamical information.

Table 2. Characteristics of the main thermostat algorithms used in MD simulations. MD: molecular dynamics (generates a microcanonical ensemble, only shown for comparison); MC: Monte Carlo (Sect. 3.1); SD: stochastic dynamics (with $\gamma_i > 0$ for at least one atom; Sect. 3.2); A: MD with Andersen thermostat (with $\alpha > 0$; Sect. 3.3); HE: MD with Hoover-Evans thermostat (Sect. 3.4); W: MD with Woodcock thermostat (Sect. 3.4); HG: MD with Haile-Gupta thermostat (Sect. 3.4); B: MD with Berendsen thermostat (with $\Delta t < \tau_B < \infty$; Sect. 3.5); NH: MD with Nosé-Hoover thermostat (with $0 < Q < \infty$; Sect. 3.6). MD is a limiting case of SD (with $\gamma_i = 0$ for all atoms), A (with $\alpha = 0$), B (with $\tau_B \to \infty$), and NH (with $Q \to \infty$, $\gamma(0) = 0$). HE/W is a limiting cases of B (with $\tau_B = \Delta t$) and is a constrained form of NH. HG is also a constrained form of NH. Deterministic: trajectory is deterministic; Time-reversible: equation of motion is time-reversible; Smooth: velocity trajectory is available and continuous. Energy drift: possible energy (and temperature) drift due to accumulation of numerical errors; Oscillations: possible oscillatory behavior of the temperature dynamics; External d.o.f.: some external degrees of freedom (rigid-body translation and, under vacuum boundary conditions, rotation) are not coupled with the internal degrees of freedom. Constrained $\mathcal{K}$: no kinetic energy fluctuations; Canonical in $\mathcal{H}$: generates a canonical distribution of microstates; Canonical in $\mathcal{U}$: generates a canonical distribution of configurations. Dynamics: dynamical information on the system is either absent (−−) or likely to be unrealistic (−; constrained temperature or non-smooth trajectory), moderately realistic (+; smooth trajectory, but temperature fluctuations of incorrect magnitude), or realistic (++; smooth trajectory, correct magnitude of the temperature fluctuations). The latter appreciation is rather subjective and depends on an adequate choice of the adjustable parameters of the thermostat

	MD	MC	SD	A	HE	W	HG	B	NH
Deterministic	+	−	−	−	+	+	+	+	+
Time−reversible	+	−	−	−	+	+	+	−	+
Smooth	+	−	+	−	+	+	+	+	+
Energy drift	+	−	−	−	+	−	−	−	−
Oscillations	−	−	−	−	−	−	−	−	+
External d.o.f.	+	+	−	−	+	+	+	+	+
Constrained $\mathcal{K}$	−	−	−	−	+	+	+	−	−
Canonical in $\mathcal{H}$	−	−	+	+	−	−	−	−	+
Canonical in $\mathcal{U}$	−	+	+	+	+	+	−	−	+
Dynamics	++	−−	++	−	−	−	−	+	++
Eqn. of motion	15		17	41	46	51	52	57	78,79

3.2 Temperature Relaxation by Stochastic Dynamics

The SD algorithm relies on the integration of the Langevin equation of motion [22, 23, 95, 96, 97, 98, 99, 100] as given by Eq. (17). The stochastic forces $\mathbf{R}_i(t)$ have the following properties[10]: (i) they are uncorrelated with the velocities $\dot{\mathbf{r}}(t')$ and systematic forces $\mathbf{F}_i(t')$ at previous times $t' < t$; (ii) their time-averages are zero; (iii) their mean-square components evaluate to $2m_i\gamma_i k_B T_o$; (iv) the force component $R_{i\mu}(t)$

[10] More complex SD schemes can be used, which incorporate time or space correlations in the stochastic forces. It is also assumed here that the friction coefficients γ_i are time-independent.

along the Cartesian axis μ is uncorrelated with any component $R_{j\nu}(t')$ along axis ν unless $i = j$, $\mu = \nu$, and $t' = t$. The two last conditions can be combined into the relation

$$\langle R_{i\mu}(t) R_{j\nu}(t') \rangle = 2m_i \gamma_i k_B T_o \delta_{ij} \delta_{\mu\nu} \delta(t' - t) \; . \tag{32}$$

It can be shown that a trajectory generated by integrating the Langevin equation of motion (with at least one non-vanishing atomic friction coefficient γ_i) maps (at constant volume) a canonical distribution of microstates at temperature T_o.

The Langevin equation of motion is smooth, non-deterministic and time-irreversible. Under vacuum boundary conditions and aiming at reproducing bulk properties, it may produce a reasonable picture of the dynamics if the mean effect of the surrounding solvent is incorporated into the systematic forces, and if the friction coefficients are representative of the solvent viscosity (possibly weighted by the solvent accessibility). If SD is merely used as a thermostat in explicit-solvent simulations, as is the case, e.g., when applying stochastic boundary conditions to a simulated system [101, 11, 12], some care must be taken in the choice of the atomic friction coefficients γ_i. On the one hand, too small values (loose coupling) may cause a poor temperature control. Indeed, the limiting case of SD where all friction coefficients (and thus the stochastic forces) are set to zero is MD, which generates a microcanonical ensemble. However, arbitrarily small atomic friction coefficients (or even a non-vanishing coefficient for a single atom) are sufficient to guarantee in principle the generation of a canonical ensemble. But if the friction coefficients are chosen too low, the canonical distribution will only be obtained after very long simulation times. In this case, systematic energy drifts due to accumulation of numerical errors may interfere with the thermostatization. On the other hand, too large values of the friction coefficients (tight coupling) may cause the large stochastic and frictional forces to perturb the dynamics of the system. In principle, the perturbation of the dynamics due to stochastic forces will be minimal when the atomic friction coefficients γ_i are made proportional to m_i. In this case, Eqs. (17) and (32) show that the root-mean-square acceleration due to stochastic forces is identical for all atoms. In practice, however, it is often more convenient to set the friction coefficients to a common value γ. The limiting case of SD for very large friction coefficients (i.e., when the acceleration $\ddot{\mathbf{r}}_i$ can be neglected compared to the other terms in Eq. (17)) is Brownian dynamics (BD), with the equation of motion

$$\dot{\mathbf{r}}_i(t) = \gamma_i^{-1} m_i^{-1} [\mathbf{F}_i(t) + \mathbf{R}_i(t)] \; . \tag{33}$$

Although the magnitude of the temperature fluctuations is in principle not affected by the values of the friction coefficients (unless they are all zero), the timescale of these fluctuations strongly depends on the γ_i coefficients. In fact, it can be shown [54] that there is a close relationship between the friction coefficients in SD (used as a mere thermostat) and the temperature relaxation time ζ_T in Eq. (26). Consider the case where all coefficients γ_i are set to a common value γ. Following from Eqs. (8) and (10), the change $\Delta\mathcal{T}$ of the instantaneous temperature over a time interval from $t = 0$ to $\Delta\tau$ can be written

$$\Delta\mathcal{T} = \frac{2}{k_B N_{df}} \int_0^{\Delta\tau} dt\, \dot{\mathcal{K}}(t) = \frac{2}{k_B N_{df}} \sum_{i=1}^{N} m_i \int_0^{\Delta\tau} dt\, \ddot{\mathbf{r}}_i(t) \cdot \dot{\mathbf{r}}_i(t) \,. \tag{34}$$

Inserting Eq. (17), this can be rewritten

$$\Delta\mathcal{T} = \frac{2}{k_B N_{df}} \sum_{i=1}^{N} \left\{ \int_0^{\Delta\tau} dt\, \left[\mathbf{F}_i(t) - \gamma\, m_i \dot{\mathbf{r}}_i(t)\right] \cdot \dot{\mathbf{r}}_i(t) + \int_0^{\Delta\tau} dt \right. \tag{35}$$
$$\left. \times\, \mathbf{R}_i(t) \cdot \left[\dot{\mathbf{r}}_i(0) + \int_0^t dt' \left[m_i^{-1} \mathbf{F}_i(t') - \gamma\, \dot{\mathbf{r}}_i(t') + m_i^{-1} \mathbf{R}_i(t') \right] \right] \right\} \,.$$

Using Eq. (32) and the fact that the stochastic force is uncorrelated with the velocities and systematic forces at previous times, this simplifies to

$$\begin{aligned} \Delta\mathcal{T} &= \frac{2}{k_B N_{df}} \sum_{i=1}^{N} \left\{ \int_0^{\Delta\tau} dt\, [\mathbf{F}_i(t) \cdot \dot{\mathbf{r}}_i(t) - \gamma\, m_i \dot{\mathbf{r}}_i^2(t)] \right. \\ &\quad \left. + m_i^{-1} \int_0^{\Delta\tau} dt\, \mathbf{R}_i(t) \cdot \int_0^t dt'\, \mathbf{R}_i(t') \right\} \\ &= \frac{2}{k_B N_{df}} \sum_{i=1}^{N} \int_0^{\Delta\tau} dt\, [\mathbf{F}_i(t) \cdot \dot{\mathbf{r}}_i(t) - \gamma\, m_i \dot{\mathbf{r}}_i^2(t)] \\ &\quad + 6 N_{df}^{-1} N \gamma\, T_o\, \Delta\tau \,. \end{aligned} \tag{36}$$

This expression can be rewritten[11]

$$\frac{\Delta\mathcal{T}}{\Delta\tau} = \frac{2}{k_B N_{df}} \sum_{i=1}^{N} \overline{\mathbf{F}_i \cdot \dot{\mathbf{r}}_i} + 2\gamma\, [T_o - \overline{\mathcal{T}}] \,, \tag{37}$$

where $\overline{\mathbf{F}_i \cdot \dot{\mathbf{r}}_i}$ and $\overline{\mathcal{T}}$ stand for averages over the interval $\Delta\tau$. The first term represents the temperature change caused by the effect of the systematic forces, and would be unaltered in the absence of thermostat (Newtonian MD simulation). Thus, the second term can be identified with a temperature change arising from the coupling to a heat bath. This means that on an intermediate timescale (as defined at the end of Sect. 3), the mean effect of thermostatization can be written

$$\dot{\overline{\mathcal{T}}}(t) = 2\gamma\, [T_o - \overline{\mathcal{T}}(t)] \,. \tag{38}$$

Comparing with Eq. (26) allows to identify 2γ with the inverse of the temperature relaxation time ζ_T in Eq. (26), i.e., to suggest $\gamma = (1/2)\zeta_T^{-1}$ as an appropriate value for simulations. This discussion also shows that the semi-macroscopic expression of Eq. (26) is only valid on an intermediate timescale, when the stochastic fluctuations occuring on a shorter timescale (i.e., of the order of the time separating atomic collisions) are averaged out and only their mean effect is retained.

[11] In the absence of constraints $N_{df} = 3N$ due to Eq. (9) with $N_c = 0$ and $N_r = 0$ (as appropriate for SD). In the presence of constraints, the derivation should include constraint forces.

3.3 Temperature Relaxation by Stochastic Coupling

The stochastic-coupling method was proposed by Andersen [55]. In this approach, Newton's equation of motion (Eq. (15)) is integrated in time, with the modification that at each timestep, the velocity of all atoms are conditionally reassigned from a Maxwell-Boltzmann distribution. More precisely, if an atom i is selected for a velocity reassignment, each Cartesian component μ of the new velocity is selected at random according to the Maxwell-Boltzmann probability distribution of Eq. (25). The selection procedure is such that the time intervals τ between two successive velocity reassignments of a given atom are selected at random according to a probability $p(\tau) = \alpha e^{-\alpha\tau}$, where α is a constant reassignment frequency. In principle, one can select at random and for each atom a series of successive τ-values (obeying the specified probability distribution) before starting the simulation. This series is then used to determine when the particle is to undergo a velocity reassignment. In practice, a simpler procedure can be used when $\Delta t \ll \alpha^{-1}$ (infrequent reassignments). At each timestep and for each atom in turn, one generates a random number between 0 and 1. If this number is larger than $\alpha\Delta t$ for a given atom, this atom undergoes a velocity reassignment. This procedure leads to a probability distribution

$$p(\tau)\Delta t = (1 - \alpha\Delta t)^{\tau/\Delta t}\,\alpha\Delta t \tag{39}$$

for the intervals τ without velocity reassignment. This implies

$$\ln \alpha^{-1} p(\tau) = (\tau/\Delta t)\ln(1 - \alpha\Delta t) = -\alpha\tau + O[(\alpha\Delta t)^2]\,. \tag{40}$$

Thus, when $\Delta t \ll \alpha^{-1}$, $p(\tau) = \alpha e^{-\alpha\tau}$, as expected. If the condition is not satisfied, this second method will not work because the probability of multiple reassignments within the same timestep becomes non-negligible.

The equation of motion for the Andersen thermostat can formally be written

$$\ddot{\mathbf{r}}_i(t) = m_i^{-1}\mathbf{F}_i(t) + \sum_{n=1}^{\infty} \delta\left(t - \sum_{m=1}^{n} \tau_{i,m}\right)\left[\dot{\mathbf{r}}^*_{i,n}(t) - \dot{\mathbf{r}}_i(t)\right]\,, \tag{41}$$

where $\{\tau_{i,n} \mid n = 1, 2, \ldots\}$ is the series of intervals without reassignment for particle i, and $\dot{\mathbf{r}}^*_{i,n}$ the randomly-reassigned velocity after the n^{th} interval. This approach mimicks the effect irregularly-occurring stochastic collisions of randomly chosen atoms with a bath of fictitious particles at a temperature T_o. Because, the system evolves at constant energy between the collisions, this method generates a succession of microcanonical simulations, interrupted by small energy jumps corresponding to each collision.

It can be shown [55] that the Andersen thermostat with non-zero collision frequency α leads to a canonical distribution of microstates. The proof [55] involves similar arguments as the derivation of the probability distribution generated by the MC procedure. It is based on the fact that the Andersen algorithm generates a Markov chain of microstates in phase space. The only required assumption is that every microstate is accessible from every other one within a finite time (ergodicity). Note

also that the system total linear and angular momenta are affected by the velocity reassignments, so that these degrees of freedom are internal to the system, as in SD.

The Andersen algorithm is non-deterministic and time-irreversible. Moreover, it has the disadvantage of being non-smooth, i.e., generating a discontinuous velocity trajectory where the randomly-occurring collisions may interfere with the natural dynamics of the system.

Some care must be taken in the choice of the collision frequency α [55, 102]. On the one hand, too small values (loose coupling) may cause a poor temperature control. The same observations apply here as those made for SD. The limiting case of the Andersen thermostat with a vanishing collision frequency is MD, which generates a microcanonical ensemble. Arbitrarily small collision frequencies are sufficient to guarantee in principle the generation of a canonical ensemble. But if the collision frequency is too low, the canonical distribution will only be obtained after very long simulation times. In this case, systematic energy drifts due to accumulation of numerical errors may interfere with the thermostatization. On the other hand, too large values for the collision frequency (tight coupling) may cause the velocity reassignments to perturb heavily the dynamics of the system. Although the magnitude of the temperature fluctuations is in principle not affected by the value of the collision frequency (unless it is zero), the timescale of these fluctuations strongly depends on this parameter. In fact, it can be shown [55] that there is a close relationship between the collision frequency and the temperature relaxation time ζ_T in Eq. (26). Each collision changes the kinetic energy of the system by $(3/2)k_B[T_o - \mathcal{T}(t)]$ on average, and there are $N\alpha$ such collisions per unit of time. Thus, one expects

$$\dot{\overline{\mathcal{T}}}(t) = c_v^{-1}\dot{\overline{E}}(t) = (3/2)c_v^{-1}N\alpha k_B[T_o - \overline{\mathcal{T}}(t)] \,, \tag{42}$$

where $\overline{\mathcal{T}}$ and $\overline{E}$ stand for averages over an intermediate timescale (as defined at the end of Sect. 3). Comparing with Eq. (26) allows to identify $(3/2)c_v^{-1}N\alpha k_B$ with the inverse of the temperature relaxation time ζ_T in Eq. (26), i.e., to suggest $\alpha = (2/3)(Nk_B)^{-1}c_v\zeta_T^{-1}$ as an appropriate value for simulations. Note that because ζ_T scales as $N^{-1/3}$ (Eq. (27)), the collision frequency for any particle scales as $N^{-2/3}$, so that the time each particle spends without reassignment increases with the system size. On the other hand, the collision frequency for the whole system, $N\alpha$, scales as $N^{1/3}$, so that the length of each microcanonical sub-simulation decreases with the system size.

3.4 Temperature Constraining

Temperature constraining aims at fixing the instantaneous temperature $\mathcal{T}$ to the reference heat-bath value T_o without allowing for any fluctuations. In this sense, temperature constraining represents a hard boundary condition, in constrast to the soft boundary conditions employed by all other thermostats mentioned in this article. Note that constraining the temperature, i.e., enforcing the relation $\mathcal{T}(t) = T_o$ (or $\dot{\mathcal{T}}(t) = 0$) represents a non-holonomic constraint. Holonomic constraints are those

which only involve generalized coordinates and time, excluding any dependence on the generalized velocities. Two main temperature-constraining algorithms have been proposed. The first one is due to Woodcock [103], and the second one was simultaneously proposed by Hoover [104] and Evans [105].

In the Hoover-Evans algorithm [104, 52, 51, 105, 106], the quantity $\lambda(t;\,\Delta t)$ in Eq. (20) is found by imposing temperature conservation in the form $\mathcal{T}(t+\frac{\Delta t}{2}) = \mathcal{T}(t-\frac{\Delta t}{2})$. Using Eqs. (8) and (10), this leads to the condition

$$\frac{\lambda^2(t;\,\Delta t)}{k_B N_{df}} \left\{ \sum_{i=1}^{N} m_i \left[\dot{\mathbf{r}}_i \left(t - \frac{\Delta t}{2} \right) + m_i^{-1} \mathbf{F}_i(t) \Delta t \right]^2 \right\}$$
$$= \frac{1}{k_B N_{df}} \sum_{i=1}^{N} m_i \dot{\mathbf{r}}_i^2 \left(t - \frac{\Delta t}{2} \right) . \tag{43}$$

Solving for $\lambda(t;\,\Delta t)$ gives

$$\lambda(t;\,\Delta t) = \left\{ \frac{\sum_{i=1}^{N} m_i \dot{\mathbf{r}}_i^2 (t - \frac{\Delta t}{2})}{\sum_{i=1}^{N} m_i \left[\dot{\mathbf{r}}_i (t - \frac{\Delta t}{2}) + m_i^{-1} \mathbf{F}_i(t) \Delta t \right]^2} \right\}^{1/2}$$
$$= \left[\frac{\mathcal{T}(t - \frac{\Delta t}{2})}{\mathcal{T}'(t + \frac{\Delta t}{2})} \right]^{1/2} , \tag{44}$$

where $\mathcal{T}(t-\frac{\Delta t}{2})$ and $\mathcal{T}'(t+\frac{\Delta t}{2})$ are the instantaneous temperatures computed based on the velocities $\dot{\mathbf{r}}_i(t-\frac{\Delta t}{2})$ and $\dot{\mathbf{r}}'_i(t+\frac{\Delta t}{2})$, see Eq. (20). Because this quantity satisfies $\lambda(t;\,0) = 1$, applying Eq. (21) gives

$$\gamma\,(t) = \left[N_{df} k_B \mathcal{T}(t) \right]^{-1} \sum_{i=1}^{N} \dot{\mathbf{r}}_i(t) \cdot \mathbf{F}_i(t) . \tag{45}$$

Inserting into Eq. (18) shows that the equation of motion corresponding to the Hoover-Evans thermostat is

$$\ddot{\mathbf{r}}_i(t) = m_i^{-1} \mathbf{F}_i(t) - \left[N_{df} k_B \mathcal{T}(t) \right]^{-1} \left[\sum_{i=1}^{N} \dot{\mathbf{r}}_i(t) \cdot \mathbf{F}_i(t) \right] \dot{\mathbf{r}}_i(t) . \tag{46}$$

This equation of motion should sample an isothermal trajectory at a temperature determined by the initial internal velocities. Eq. (46) can also be derived directly from Eq. (18) by imposing $\dot{\mathcal{T}}(t) = 0$. Using Eqs. (8) and (10) this becomes

$$\dot{\mathcal{T}}(t) = \frac{d}{dt} \left[\frac{1}{k_B N_{df}} \sum_{i=1}^{N} m_i \dot{\mathbf{r}}_i^2(t) \right] = \frac{2}{k_B N_{df}} \sum_{i=1}^{N} m_i \dot{\mathbf{r}}_i(t) \cdot \ddot{\mathbf{r}}_i(t) = 0 . \tag{47}$$

Inserting Eq. (18) and solving for $\gamma\,(t)$ leads to Eq. (46).

The Hoover-Evans algorithm should in principle ensure a constant temperature at all time points. However, this condition is only enforced by zeroing the temperature derivative. Because the reference temperature T_o does not appear explicitly in the scaling factor of Eq. (44), numerical inaccuracies will inevitably prevent temperature conservation, and cause the temperature to actually drift in simulations.

In the Woodcock algorithm [103], the quantity $\lambda(t;\,\Delta t)$ in Eq. (20) is found by imposing temperature conservation in the form $\mathcal{T}(t+\frac{\Delta t}{2}) = \frac{g}{N_{df}}T_o$, thereby making explicit use of the reference temperature. Although $g = N_{df}$ seems to be the obvious choice, it turns out that $g = N_{df} - 1$ is the appropriate choice for the algorithm to generate a canonical ensemble of configurations at temperature T_o (see below). Using Eqs. (8) and (10), this leads to the condition

$$\frac{\lambda^2(t;\,\Delta t)}{k_B N_{df}} \left\{ \sum_{i=1}^{N} m_i \left[\dot{\mathbf{r}}_i \left(t - \frac{\Delta t}{2} \right) + m_i^{-1} \mathbf{F}_i(t) \Delta t \right]^2 \right\} = \frac{g}{N_{df}} T_o \,. \tag{48}$$

Solving for $\lambda(t;\,\Delta t)$ gives[12]

$$\begin{aligned} \lambda(t;\,\Delta t) &= \left\{ \frac{g k_B T_o}{\sum_{i=1}^{N} m_i \left[\dot{\mathbf{r}}_i \left(t - \frac{\Delta t}{2} \right) + m_i^{-1} \mathbf{F}_i(t) \Delta t \right]^2} \right\}^{1/2} \\ &= \left[\frac{g}{N_{df}} \frac{T_o}{\mathcal{T}'\left(t + \frac{\Delta t}{2} \right)} \right]^{1/2} . \end{aligned} \tag{49}$$

If $\mathcal{T}(t - \frac{\Delta t}{2}) = \frac{g}{N_{df}}T_o$ (i.e., if the simulation was started with internal velocities corresponding to the reference temperature, or otherwise, after a first equilibration timestep), this quantity satisfies $\lambda(t;\,0) = 1$. In this case, applying Eq. (21) gives

$$\gamma(t) = (g k_B T_o)^{-1} \sum_{i=1}^{N} \dot{\mathbf{r}}_i(t) \cdot \mathbf{F}_i(t) \,. \tag{50}$$

Inserting into Eq. (18) shows that the equation of motion corresponding to the Woodcock thermostat is

$$\ddot{\mathbf{r}}_i(t) = m_i^{-1} \mathbf{F}_i(t) - (g k_B T_o)^{-1} \left[\sum_{i=1}^{N} \dot{\mathbf{r}}_i(t) \cdot \mathbf{F}_i(t) \right] \dot{\mathbf{r}}_i(t) \,. \tag{51}$$

This equation of motion is rigorously equivalent to the Hoover-Evans equation of motion (Eq. (46)), provided that the initial internal velocities are appropriate for

[12] Note that some simulation programs do not apply the scaling of the velocities by $\lambda(t;\,\Delta t)$ at every timestep, but perform the scaling on a periodic basis, or when the difference between the instantaneous and reference temperatures is larger than a given tolerance [107].

the temperature T_o, i.e., that $\mathcal{T}(0) = \frac{g}{N_{df}} T_o$. However, even in this case, the corresponding algorithms differ numerically. Because the Woodcock algorithm explicitly involves the reference temperature T_o in the calculation of the scaling factor of Eq. (49), its application removes the risk of a temperature drift.

Because maintaining the temperature constant represents a single constraint equation involving a total of N_{df} velocity variables, it should not be surprising that numerous other choices of equations of motion lead to an isothermal dynamics (also satisfying the two constraints that the system linear and angular momenta are constants of the motion). For example, Haile and Gupta [108] have shown how to construct two general classes of isothermal equations of motion based on generalized forces or generalized potentials. An example of the former class is the Hoover-Evans thermostat. An example of the second class is a thermostat similar (but, contrary to the claim of the authors [108], not identical) to the Woodcock thermostat. The equations of motion of this Haile-Gupta thermostat are

$$\dot{\mathbf{r}}_i(t) = \left[\frac{g}{N_{df}} \frac{T_o}{\mathcal{T}'(t)}\right]^{1/2} \dot{\mathbf{r}}'_i(t) \quad \text{and} \quad \ddot{\mathbf{r}}'_i(t) = m_i^{-1}\mathbf{F}_i(t)\,. \tag{52}$$

In words, the auxiliary velocities $\dot{\mathbf{r}}'_i$ are propagated independently in time according to Newton's second law, and the true velocities obtained by multiplying these by the appropriate scaling factor at each timestep. In contrast, in the Woodcock thermostat, the auxiliary velocities $\dot{\mathbf{r}}'_i$ are obtained at each timestep by increasing the true velocities $\dot{\mathbf{r}}_i$ by $m_i^{-1}\mathbf{F}_i\,\Delta t$.

It can be shown that the ensemble generated by the (identical) Woodcock and Hoover-Evans equations of motion represents a canonical distribution of configurations (though obviously not of momenta) at temperature T_o, provided that one sets $g = N_{df} - 1$ ([104, 53]; see Appendix). This may seem surprizing at first sight, but canonical sampling of configurations is only achieved with $\langle \mathcal{T}(t) \rangle = \frac{N_{df}-1}{N_{df}} T_o \neq T_o$, i.e., when simulating at a slightly lower internal temperature. The reason is that constraining the temperature effectively removes one degree of freedom from the system. A more consistent approach would be to alter the definition of the instantaneous temperature (Eq. (8)) by changing N_{df} to $N_{df} - 1$ in this case. However, since other thermostats may involve different values for the factor g (see Sect. 3.6), it is more convenient here to stick to a single definition of $\mathcal{T}$. On the other hand (and countrary to the author's initial claim [108]), the Haile-Gupta thermostat does not generate a canonical ensemble of configurations ([53, 109]; see Appendix). The equations of motion of temperature constraining are smooth, deterministic and time-reversible. However, the absence of kinetic energy fluctuations may lead to inaccurate dynamics, especially in the context of the microscopic systems typically considered in simulations.

3.5 Temperature Relaxation by Weak Coupling

The idea of a thermostat based on a first-order relaxation equation is due to Berendsen [54]. As discussed at the end of Sect. 3, when a system at a given average temperature $\overline{\mathcal{T}}$ is in contact with a heat bath at a different temperature T_o, the rate of temperature change is given by Eq. (26). As discussed in Sect. 3.2, this equation is only valid when the average temperature is calculated on an intermediate timescale (short compared to the experimental timescale, but long compared to the time separating atomic collisions). On this timescale, only the mean effect of the stochastic forces acting in SD needs to be considered, leading to the first-order temperature relaxation law of Eq. (26).

The idea behind the Berendsen thermostat is to modify the Langevin equation of motion (Eq. (17)) in the sense of removing the local temperature coupling through stochastic collisions (random noise), while retaining the global coupling (principle of least local perturbation). This prescription is equivalent to assuming that Eq. (26) also applies to the instantaneous temperature $\mathcal{T}$, i.e., that

$$\dot{\mathcal{T}}(t) = \tau_B^{-1}[T_o - \mathcal{T}(t)] \,, \tag{53}$$

where the appropriate value for τ_B should be the temperature relaxation time ζ_T. In this case, the quantity $\lambda(t;\Delta t)$ in Eq. (20) is found by imposing $\mathcal{T}(t+\frac{\Delta t}{2}) = \mathcal{T}(t-\frac{\Delta t}{2}) + \tau_B^{-1}\Delta t\frac{g}{N_{df}}[T_o - \mathcal{T}(t-\frac{\Delta t}{2})]$, where in principle $g = N_{df}$. Using Eqs. (8) and (10), this leads to the condition

$$\lambda^2(t;\Delta t)\mathcal{T}'\left(t+\frac{\Delta t}{2}\right) = \mathcal{T}\left(t-\frac{\Delta t}{2}\right) + \tau_B^{-1}\Delta t\left[\frac{g}{N_{df}}T_o - \mathcal{T}\left(t-\frac{\Delta t}{2}\right)\right] . \tag{54}$$

Solving for $\lambda(t;\Delta t)$ gives

$$\begin{aligned}\lambda(t;\Delta t) &= \left\{\frac{\mathcal{T}\left(t-\frac{\Delta t}{2}\right)}{\mathcal{T}'\left(t+\frac{\Delta t}{2}\right)} + \tau_B^{-1}\Delta t\,\frac{\frac{g}{N_{df}}T_o - \mathcal{T}\left(t-\frac{\Delta t}{2}\right)}{\mathcal{T}'\left(t+\frac{\Delta t}{2}\right)}\right\}^{1/2} \\ &\approx \left\{1 + \tau_B^{-1}\Delta t\left[\frac{\frac{g}{N_{df}}T_o}{\mathcal{T}'\left(t+\frac{\Delta t}{2}\right)} - 1\right]\right\}^{1/2} .\end{aligned} \tag{55}$$

In general, the algorithm is implemented following the second (approximate) expression. For either of the two expressions, Eq. (21) gives

$$\gamma(t) = \frac{1}{2}\tau_B^{-1}\left[\frac{g}{N_{df}}\frac{T_o}{\mathcal{T}(t)} - 1\right] . \tag{56}$$

Inserting into Eq. (18) shows that the equation of motion corresponding to the Berendsen thermostat is

$$\ddot{\mathbf{r}}_i(t) = m_i^{-1}\mathbf{F}_i(t) - \frac{1}{2}\tau_B^{-1}\left[\frac{g}{N_{df}}\frac{T_o}{\mathcal{T}(t)} - 1\right]\dot{\mathbf{r}}_i(t) . \tag{57}$$

In practice, τ_B is used as an empirical parameter to adjust the strength of the coupling. Its value should be chosen in a appropriate range. On the one hand, a too large value (loose coupling) may cause a systematic temperature drift. Indeed, in the limit $\tau_B \to \infty$, the Berendsen thermostat is inactive leading to the MD equation of motion, which samples a microcanonical ensemble. Thus, the temperature fluctuations will increase with τ_B until they reach the appropriate value for a microcanonical ensemble. However, they will never reach the appropriate value for a canonical ensemble, which are larger. For large values of τ_B, a systematic energy (and thus temperature) drift due to numerical errors may also occur, just as in MD. On the other hand, a too small value (tight coupling) will cause unrealistically low temperature fluctuations. Indeed, the special case of the Berendsen algorithm (Eq. (55)) with $\tau_B = \Delta t$ is the Woodcock thermostat (Eq. (49)), which does not allow for temperature fluctuations. This shows that the limiting case of the Berendsen equation of motion for $\tau_B \to 0$ is the Woodcock/Hoover-Evans equation of motion. Values of $\tau_B \approx 0.1$ ps are typically used in MD simulations of condensed-phase systems. Note, however, that this choice generally leads to fluctuations close to those of the microcanonical ensemble. With this choice, the Berendsen thermostat merely removes energy drifts from a MD simulation, without significantly altering the ensemble sampled (and thus rather plays the role of an ergostat algorithm).

The Berendsen equation of motion is smooth and deterministic, but time-irreversible. The ensemble generated by the Berendsen equations of motion is not a canonical ensemble ([109]; see Appendix). Only in the limit $\tau_B \to 0$ (or in practice $\tau_B = \Delta t$), when the Berendsen equation of motion becomes identical to the Woodcock/Hoover-Evans equation of motion, does it generate a canonical distribution of configurations. In the limit $\tau_B \to \infty$, the microcanonical ensemble is recovered. All intermediate situations correspond to the sampling of an unusual "weak-coupling" ensemble[13], which is neither canonical nor microcanonical [109]. The reason why the Berendsen thermostat systematically (for all values of τ_B) underestimates temperature fluctuations (and thus does not give the correct thermodynamical ensemble) resides in the transition from Eq. (26) to Eq. (53), corresponding to the neglect of the stochastic contribution to these fluctuations on the microscopic timescale.

3.6 Temperature Relaxation by the Extended-System Method

The idea of a thermostat based on an extended-system method is due to Nosé [61]. A simpler formulation of the equations of motion was later proposed simultaneously[14]

[13] Assuming a relationship of the form of Eq. (115), it is possible to derive the configurational partition function of the weak-coupling ensemble as a function of α ([109]; see Appendix) The limiting cases $\alpha = 0$ ($\tau_B \to 0$; canonical) and $\alpha = 1$ ($\tau_B \to \infty$; microcanonical) are reproduced. Note that the Haile-Gupta thermostat generates configurations with the same probability distribution as the Berendsen thermostat with $\alpha = 1/2$.

[14] Eqs. (2.24) and (2.25) in [53] are equivalent to Eq. (6) in [63], provided that one identifies $\zeta = \dot{s}'/s'$. These equations are Eqs. (78) and (79) of the present article.

by Nosé [53] and Hoover [63], so that this algorithm is generally referred to as the Nosé-Hoover thermostat.

The idea behind the original Nosé [61] algorithm is to extend the real system by addition of an artificial $(N_{df}+1)^{th}$ dynamical variable $\tilde{s}$ (associated with a "mass" $Q > 0$, with actual units of energy$\times$(time)^2, as well as a velocity $\dot{\tilde{s}}$, and satisfying $\tilde{s} > 0$) that plays the role of a time-scaling parameter[15]. More precisely, the timescale in the extended system is stretched by the factor $\tilde{s}$, i.e., an infinitesimal time interval $d\tilde{t}$ at time $\tilde{t}$ in the extended system corresponds to a time interval $dt = \tilde{s}^{-1}(\tilde{t})\,d\tilde{t}$ in the real system[16]. Consequently, although the atomic coordinates are identical in both systems, the extended-system velocities are amplified by a factor $\tilde{s}^{-1}$ compared to the real-system velocities, i.e.

$$\tilde{\mathbf{r}} = \mathbf{r}\ ,\ \dot{\tilde{\mathbf{r}}} = \tilde{s}^{-1}\dot{\mathbf{r}}\ ,\ \tilde{s} = s\ ,\ \text{ and }\ \dot{\tilde{s}} = \tilde{s}^{-1}\dot{s}\ . \tag{58}$$

The Lagrangian for the extended system is chosen to be

$$\mathcal{L}_e(\tilde{\mathbf{r}},\dot{\tilde{\mathbf{r}}},\tilde{s},\dot{\tilde{s}}) = \frac{1}{2}\sum_{i=1}^{N} m_i\tilde{s}^2\dot{\tilde{\mathbf{r}}}_i^2 - \mathcal{U}(\tilde{\mathbf{r}}) + \frac{1}{2}Q\dot{\tilde{s}}^2 - gk_BT_o\ln\tilde{s}\ , \tag{59}$$

where g is equal to the number of degrees of freedom N_{df} in the real system, possibly increased by one (see below). The first two terms of the Lagrangian represent the kinetic energy minus the potential energy of the real system (the extended-system velocities are multiplied by $\tilde{s}$ to recover the real-system ones). The third and fourth terms represent the kinetic energy minus the potential energy associated with the $\tilde{s}$-variable. The form of the last term is chosen to ensure that the algorithm produces a canonical ensemble of microstates (see below). The Lagrangian equations of motion derived from Eq. (59) read

$$\ddot{\tilde{\mathbf{r}}}_i = m_i^{-1}\tilde{s}^{-2}\tilde{\mathbf{F}}_i - 2\tilde{s}^{-1}\dot{\tilde{s}}\,\dot{\tilde{\mathbf{r}}}_i \tag{60}$$

for the physical variables, and[17]

[15] All extended-system variables will be noted with a tilde overscript, to distinguish them from the real-system variables (the real-system variable corresponding to $\tilde{s}$ is noted s).

[16] To simplify the notation, explicit dependence of the different functions on time is generally omitted in this section. The time-dependent functions are $\tilde{\mathbf{F}}(\tilde{t})$, $\tilde{\mathbf{r}}(\tilde{t})$, $\tilde{\mathbf{p}}(\tilde{t})$, $\tilde{s}(\tilde{t})$ and $\tilde{p}_s(\tilde{t})$ (together with their first and second time derivatives) for the extended system, and $\mathbf{F}(t)$, $\mathbf{r}(t)$, $\mathbf{p}(t)$, $s(t)$, $p_s(t)$, $\gamma(t)$ and $\mathcal{T}(t)$ (together with their first and second time derivatives) for the real system. The dot overscripts indicate differentiation with respect to the extended-system time $\tilde{t}$ for the extended-system variables, and with respect to the real-system time t for the real-system variables.

[17] Because the time-average of the time-derivative of a bounded quantity (for example, $\dot{\tilde{s}}$) vanishes, this equation implies

$$\left\langle \tilde{s}^{-1}\sum_{i=1}^{N} m_i\tilde{s}^2\dot{\tilde{\mathbf{r}}}_i^2 \right\rangle_{e,v} = \left\langle \tilde{s}^{-1}\sum_{i=1}^{N} m_i\dot{\mathbf{r}}_i^2 \right\rangle_{e,v} = \left\langle \tilde{s}^{-1}\right\rangle_{e,v} gk_BT_o\ , \tag{61}$$

$$\ddot{\tilde{s}} = Q^{-1}\tilde{s}^{-1}\left(\sum_{i=1}^{N} m_i \tilde{s}^2 \dot{\tilde{\mathbf{r}}}_i^2 - g k_B T_o\right) \tag{63}$$

for the $\tilde{s}$-variable. These two second-order differential equations can be discretized (based on a timestep $\Delta\tilde{t}$ in the extended system) and integrated simultaneously during the simulation. The successive values of $\mathbf{r} = \tilde{\mathbf{r}}$ and $\dot{\mathbf{r}} = \tilde{s}\dot{\tilde{\mathbf{r}}}$ describe the evolution of the atomic coordinates and velocities in the real system at successive time points separated by $\Delta t = \tilde{s}^{-1}(\tilde{t})\,\Delta\tilde{t}$. This means that the algorithm implemented in this form (referred to as virtual-time sampling) leads to sampling of the real-system trajectory at uneven time intervals. A trajectory with real-time sampling can be achieved either by interpolation at evenly spaced real-time points of the coordinates and velocities issued from virtual-time sampling, or by rewriting the equations of motion in terms of the real-system variables (Nosé-Hoover formulation [53, 63]; see below).

As an alternative to Eqs. (60) and (63), the Nosé equations of motion can be equivalently formulated using a Hamiltonian formalism. In this case, the extended-system conjugate momenta $\tilde{\mathbf{p}}_i$ and $\tilde{p}_s$ associated with the physical degrees of freedom and with the $\tilde{s}$-variable are defined as

$$\tilde{\mathbf{p}}_i = \frac{\partial \mathcal{L}_e(\tilde{\mathbf{r}}, \dot{\tilde{\mathbf{r}}}, \tilde{s}, \dot{\tilde{s}})}{\partial \dot{\tilde{\mathbf{r}}}} = m_i \tilde{s}^2 \dot{\tilde{\mathbf{r}}}_i \quad \text{and} \quad \tilde{p}_s = \frac{\partial \mathcal{L}_e(\tilde{\mathbf{r}}, \dot{\tilde{\mathbf{r}}}, s, \dot{\tilde{s}})}{\partial \dot{\tilde{s}}} = Q\dot{\tilde{s}}\,. \tag{64}$$

Comparison with the corresponding real-system momenta[18], defined as

$$\mathbf{p}_i = m_i \dot{\mathbf{r}}_i \quad \text{and} \quad p_s = Q s^{-2} \dot{s}\,, \tag{66}$$

shows that the extended-system momenta are amplified by a factor $\tilde{s}$ compared to the real-system momenta. The extended-system Hamiltonian corresponding to the Lagrangian of Eq. (59) can now be written

where $\langle ... \rangle_{e,v}$ denotes ensemble averaging over the extended system (with virtual-time sampling). Considering Eqs. (8) and (10), this result already suggests that the average temperature of the real system coincides with T_o. Using Eq. (101) and $\mathbf{p}_i = m_i \dot{\mathbf{r}}_i$, the above equation can indeed be rewritten

$$\langle \mathcal{T} \rangle_{e,r} = \left\langle \frac{1}{k_B N_{df}} \sum_{i=1}^{N} m_i \dot{\mathbf{r}}_i{}^2 \right\rangle_{e,r} = \frac{g}{N_{df}} T_o\,, \tag{62}$$

where $\langle ... \rangle_{e,r}$ denotes ensemble averaging over the extended system (with real-time sampling). From Eq. (102), this latter ensemble average can be identified with a canonical one when $g = N_{df}$.

[18] In the absence of thermostat (i.e., when the variable s is uncoupled from the system), the real-system Lagrangian may be written

$$\mathcal{L}(\mathbf{r}, \dot{\mathbf{r}}, s, \dot{s}) = \frac{1}{2}\sum_{i=1}^{N} m_i \dot{\mathbf{r}}_i^2 - \mathcal{U}(\mathbf{r}) + \frac{1}{2} Q s^{-2} \dot{s}^2\,. \tag{65}$$

The momenta of Eq. (66) are derived from this Lagrangian.

$$\mathcal{H}_e(\tilde{\mathbf{r}},\tilde{\mathbf{p}},\tilde{s},\tilde{p}_s)=\frac{1}{2}\sum_{i=1}^{N}m_i^{-1}\tilde{s}^{-2}\tilde{\mathbf{p}}_i^2+\mathcal{U}(\tilde{\mathbf{r}})+\frac{1}{2}Q^{-1}\tilde{p}_s^2+gk_BT_o\ln\tilde{s}\;. \tag{67}$$

This function is a constant of the motion and evaluates to E_e, the total energy of the extended system. The corresponding Hamiltonian equations of motion read

$$\dot{\tilde{\mathbf{p}}}_i=\tilde{\mathbf{F}}_i \quad\text{and}\quad \dot{\tilde{\mathbf{r}}}_i=m_i^{-1}\tilde{s}^{-2}\tilde{\mathbf{p}}_i \tag{68}$$

for the physical variables, and

$$\dot{\tilde{p}}_s=\tilde{s}^{-1}\left(\sum_{i=1}^{N}m_i^{-1}\tilde{s}^{-2}\tilde{\mathbf{p}}_i^2-gk_BT_o\right)\quad\text{and}\quad\dot{\tilde{s}}=Q^{-1}\tilde{p}_s \tag{69}$$

for the $\tilde{s}$-variable.

The Nosé equations of motion sample a microcanonical ensemble in the extended system $(\tilde{\mathbf{r}},\tilde{\mathbf{p}},\tilde{t})$, with a constant total energy E_e. However, the energy of the real system ($\mathbf{r}=\tilde{\mathbf{r}}$, $\mathbf{p}=\tilde{s}^{-1}\tilde{\mathbf{p}}$, $t=\int\tilde{s}^{-1}d\tilde{t}$) is not constant. Accompanying the fluctuations of $\tilde{s}$, heat transfers occur between the system and a heat bath, which regulate the system temperature. As will be seen below (Eq. (78) where $\gamma=\tilde{\gamma}$ can be identified with $\dot{\tilde{s}}$), the sign of $\dot{\tilde{s}}$ determines the direction of the heat flow. When $\dot{\tilde{s}}<0$, heat flows into the real system. When $\dot{\tilde{s}}>0$, heat flows out of the real system. It can be proved ([61]; see Appendix) that the Nosé equations of motion sample a canonical ensemble of microstates in the real system, provided that $g=N_{df}+1$ (virtual-time sampling) or $g=N_{df}$ (real-time sampling), and that Q is finite, this irrespective of the actual values of Q and E_e. If the potential energy $\mathcal{U}(\tilde{\mathbf{r}})$ does not involve terms giving rise to external forces, the total linear and angular momenta associated with the physical degrees of freedom in the extended system, namely

$$\sum_{i=1}^{N}\tilde{\mathbf{p}}_i=\sum_{i=1}^{N}m_i\tilde{s}^2\dot{\tilde{\mathbf{r}}}_i\quad\text{and}\quad\sum_{i=1}^{N}\tilde{\mathbf{r}}_i\times\tilde{\mathbf{p}}_i=\sum_{i=1}^{N}m_i\tilde{s}^2\tilde{\mathbf{r}}_i\times\dot{\tilde{\mathbf{r}}}_i\;, \tag{70}$$

are also conserved. Because $\dot{\tilde{\mathbf{r}}}_i=\tilde{s}^{-1}\dot{\mathbf{r}}_i$ (Eq. (58)), this implies that the total linear and angular momenta of the real system are linearly related to $\tilde{s}^{-1}$ and thus not conserved, unless they vanish. This should be the case if the components of the real velocities $\dot{\mathbf{r}}_i^o$ along the external degrees of freedom have been removed by application of Eq. (11).

The Nosé equations of motion are smooth, deterministic and time-reversible. However, because the time-evolution of the variable $\tilde{s}$ is described by a second-order equation (Eq. (63)), heat may flow in and out of the system in an oscillatory fashion [110], leading to nearly-periodic temperature fluctuations. However, from the discussion of Sects. 3 and 3.2, the dynamics of the temperature evolution should not be oscillatory, but rather result from a combination of stochastic fluctuations and exponential relaxation. At equilibrium, the approximate frequency of these oscillations can be estimated in the following way [61]. Consider small deviations $\delta\tilde{s}$ of $\tilde{s}$ away from the equilibrium value $\langle\tilde{s}\rangle_{e,r}$, where $\langle\ldots\rangle_{e,r}$ denotes ensemble averaging over the

extended system with real-time sampling. Assuming that the interatomic forces have a weak effect on the temperature dynamics (as, e.g., in a perfect gas), the quantity $\sum_{i=1}^{N} m_i^{-1}\tilde{\mathbf{p}}_i^2$, which is solely altered by the action of the forces (Eq. (68)), can be assumed nearly constant. In this case, one may write (with $g = N_{df}$)

$$\frac{1}{2}\sum_{i=1}^{N} m_i \tilde{s}^2 \dot{\tilde{\mathbf{r}}}_i^2 = \frac{1}{2}\sum_{i=1}^{N} m_i^{-1}\tilde{s}^{-2}\tilde{\mathbf{p}}_i^2 \approx \frac{1}{2}\langle\tilde{s}\rangle_{e,r}^2 \tilde{s}^{-2} N_{df} k_B T_o \,. \tag{71}$$

Using this result, Eq. (63) may be written (for small $\delta\tilde{s}$)

$$\delta\ddot{\tilde{s}} = N_{df} k_B T_o Q^{-1}\tilde{s}^{-1}\left(\langle\tilde{s}\rangle_{e,r}^2 \tilde{s}^{-2} - 1\right) \approx -2N_{df} k_B T_o Q^{-1}\langle\tilde{s}\rangle_{e,r}^{-2}\delta\tilde{s} \,. \tag{72}$$

This corresponds to a harmonic oscillator with frequency

$$\nu = (2\pi)^{-1}(2N_{df} k_B T_o)^{1/2} Q^{-1/2}\langle\tilde{s}\rangle_{e,r}^{-1} \,, \tag{73}$$

where[19]

$$\langle\tilde{s}\rangle_{e,r} = \left(\frac{N_{df}}{N_{df}+1}\right)^{1/2} \left\langle \exp\left\{\left(N_{df} k_B T_o\right)^{-1}\left[E_e - \mathcal{H}\left(\mathbf{r},\mathbf{p}\right)\right]\right\}\right\rangle \,, \tag{75}$$

$\langle ... \rangle$ denoting a canonical ensemble average. Comparison of the approximate oscillation frequency ν with the inverse of the temperature relaxation time ζ_T (Eq. (26)) may guide the choice of parameters Q and E_e leading to a realistic timescale of temperature fluctuations. If the number of degrees of freedom is large and E_e is close to $\langle\mathcal{H}(\mathbf{r},\mathbf{p})\rangle$, the average canonical energy corresponding to the real system, Eq. (75) becomes $\langle\tilde{s}\rangle_{e,r} = 1$. The latter condition will be satisfied if the algorithm is initiated using real-system velocities taken from a Maxwell-Boltzmann distribution (Eq. (25)), together with $\tilde{s}(0) = 1$ and $\dot{\tilde{s}}(0) = 0$. In this case, comparing Eq. (73) with Eq. (26) allows to identify[20] $1.2(2N_{df} k_B T_o)^{-1/2} Q^{1/2}$ with the temperature relaxation time ζ_T, i.e., to suggest $Q \approx 1.4 N_{df} k_B T_o \zeta_T^2$ as an appropriate value for simulations. In fact, it may make sense to use an effective relaxation time

$$\tau_{NH} = (N_{df} k_B T_o)^{-1/2} Q^{1/2} \tag{76}$$

instead of the (less intuitive) effective mass Q to characterize the strength of the coupling to the heat bath.

[19] Considering Eqs. (98) and (101), one has

$$\langle\tilde{s}\rangle_{e,r} = \frac{\int d\mathbf{p}\int d\mathbf{r}\int d\tilde{p}_s \int d\tilde{s}\,\tilde{s}^{N_{df}+1}\delta[\tilde{s}-\tilde{s}_o]}{\int d\mathbf{p}\int d\mathbf{r}\int d\tilde{p}_s \int d\tilde{s}\,\tilde{s}^{N_{df}}\delta[\tilde{s}-\tilde{s}_o]} \,. \tag{74}$$

Inserting Eq. (94), integrating over $\tilde{p}_s$ for the numerator and denominator, and setting $g = N_{df}$ leads to Eq. (75).

[20] Because $\cos(1.2) \approx \exp(-1)$, it is assumed here that the exponential relaxation time is approximately given by $1.2/(2\pi)\nu^{-1}$.

The use of an extended system with a stretched timescale is not very intuitive, and the sampling of a trajectory at uneven time intervals is rather impractical for the investigation of the dynamical properties of a system. However, as shown by Nosé [53] and Hoover [63], the Nosé equations of motion can be reformulated in terms of real-system variables (together with real-time sampling) so as to avoid these problems. The transformation from extended-system to real-system variables is achieved through

$$\begin{aligned}
&s = \tilde{s}\ ,\ \dot{s} = \tilde{s}\dot{\tilde{s}}\ ,\ \ddot{s} = \tilde{s}^2\ddot{\tilde{s}} + \tilde{s}\dot{\tilde{s}}^2\ ,\\
&\mathbf{r} = \tilde{\mathbf{r}}\ ,\ \dot{\mathbf{r}} = \tilde{s}\dot{\tilde{\mathbf{r}}}\ ,\ \ddot{\mathbf{r}} = \tilde{s}^2\ddot{\tilde{\mathbf{r}}} + \tilde{s}\dot{\tilde{s}}\dot{\tilde{\mathbf{r}}}\ ,\\
&p_s = \tilde{s}^{-1}\tilde{p}_s\ ,\ \dot{p}_s = \dot{\tilde{p}}_s - Q^{-1}\tilde{s}^{-1}\tilde{p}_s^2\ ,\\
&\mathbf{p} = \tilde{s}^{-1}\tilde{\mathbf{p}}\ ,\ \dot{\mathbf{p}} = \dot{\tilde{\mathbf{p}}} - Q^{-1}\tilde{s}^{-1}\tilde{p}_s\tilde{\mathbf{p}}\ ,\\
&\text{and}\quad \mathbf{F} = \tilde{\mathbf{F}}\ .
\end{aligned} \tag{77}$$

Because $dt = \tilde{s}^{-1}\,d\tilde{t}$, these equations are derived using $d/dt = \tilde{s}\,d/d\tilde{t}$, together with the definition of the real-system (Eq. (66)) and extended-system (Eq. (64)) momenta. Based on these expressions, and defining the quantity $\gamma = s^{-1}\dot{s} = Q^{-1}sp_s$, the Lagrangian equations of motion (Eqs. (60) and (63)) can be rewritten

$$\ddot{\mathbf{r}}_i = m_i^{-1}\mathbf{F}_i - \gamma\,\dot{\mathbf{r}}_i \tag{78}$$

and

$$\dot{\gamma} = -k_B N_{df} Q^{-1}\mathcal{T}\left(\frac{g}{N_{df}}\frac{T_o}{\mathcal{T}} - 1\right)\ . \tag{79}$$

Note that the variable γ is a real-system variable (i.e., a function of the real-system time t). The equivalent extended-system variable is $\tilde{\gamma} = \gamma = \dot{\tilde{s}}$. If the effective coupling time τ_{NH} (Eq. (76)) is used instead of Q, Eq. (79) becomes

$$\dot{\gamma} = -\tau_{NH}^{-2}\frac{\mathcal{T}}{T_o}\left(\frac{g}{N_{df}}\frac{T_o}{\mathcal{T}} - 1\right)\ . \tag{80}$$

In a similar way, the Hamiltonian equations of motion (Eqs. (68) and (69)) can be rewritten

$$\dot{\mathbf{p}}_i = \mathbf{F}_i - \gamma\,\mathbf{p}_i \quad\text{and}\quad \dot{\mathbf{r}}_i = m_i^{-1}\mathbf{p}_i \tag{81}$$

and

$$\dot{p}_s = -k_B N_{df}\mathcal{T}s^{-1}\left(\frac{g}{N_{df}}\frac{T_o}{\mathcal{T}} - 1\right) - \gamma\,p_s \quad\text{and}\quad \dot{s} = \gamma\,s\ . \tag{82}$$

Equation (81) is easily identified with Eq. (78), and Eq. (82) with Eq. (79). The variable s is absent from the first set of equations, i.e., its dynamics has been decoupled. In the second set of equations, the evolution of the real-system variables is independent of the actual value of s, i.e., any choice of the initial value s(0) will lead to the

same dynamics. Finally, it should be stressed that these equations of motion are no longer Hamiltonian, although the quantity (Eq. (67))

$$H(\mathbf{r}, \mathbf{p}, s, p_s) = \frac{1}{2}\sum_{i=1}^{N} m_i^{-1}\mathbf{p}_i^2 + \mathcal{U}(\mathbf{r}) + \frac{1}{2}Q^{-1}s^2 p_s^2 + gk_B T_o \ln s \tag{83}$$

is still a constant of the motion (evaluating to E_e). On the other hand, Eqs. (78) and (79) are still Lagrangian, the corresponding Lagrangian being

$$\mathcal{L}(\mathbf{r}, \dot{\mathbf{r}}, s, \dot{s}) = s\,[\,\mathcal{L}_e(\mathbf{r}, s^{-1}\dot{\mathbf{r}}, s, s^{-1}\dot{s}) + E_e\,]\,. \tag{84}$$

To obtain the corresponding Lagrangian equations of motion, E_e is initially treated as a constant and later expanded using Eq. (83). It appears that Eq. (78) has exactly the form of Eq. (18), i.e., the Nosé-Hoover thermostat has one equation of motion in common with both the Woodcock/Hoover-Evans and the Berendsen thermostats. However, in contrast to these other thermostats where the value of γ was uniquely determined by the instantaneous microstate of the system (compare Eq. (79) with Eqs. (45), (50), and (56)), γ is here a dynamical variable which derivative (Eq. (79)) is determined by this instantaneous microstate. Accompanying the fluctuations of γ, heat transfers occur between the system and a heat bath, which regulate the system temperature. Because $\gamma = s^{-1}\dot{s} = \tilde{\gamma} = \dot{\tilde{s}}$ (Eq. (77)), the variable γ in the Nosé-Hoover formulation plays the same role as $\dot{\tilde{s}}$ in the Nosé formulation. When γ (or $\dot{\tilde{s}}$) is negative, heat flows from the heat bath into the system due to Eq. (78) (or Eq. (60)). When the system temperature increases above T_o, the time derivative of γ (or $\dot{\tilde{s}}$) becomes positive due to Eq. (79) (or Eq. (63)) and the heat flow is progressively reduced (feedback mechanism). Conversely, when γ (or $\dot{\tilde{s}}$) is positive, heat is removed from the system until the system temperature decreases below T_o and the heat transfer is slowed down.

The second- and first-order Eqs. (78) and (79) can be discretized (based on a timestep Δt in the real system) and integrated simultaneously during the simulation. Note that the Nosé thermostat with $g = N_{df} + 1$ and virtual-time sampling and the Nosé-Hoover thermostat with $g = N_{df}$ formally sample the same trajectory. In practice, however, the trajectories are sampled at different real-system time points and will numerically diverge for finite timestep sizes. It can be proved ([63]; see Appendix) that the Nosé-Hoover equations of motion sample a canonical ensemble. in the real system provided that $g = N_{df}$ and that Q is finite, this irrespective of the actual values of Q and E_e. Though interesting, such a proof is not really necessary since the Nosé and Nosé-Hoover formalisms are equivalent. As a by-product of this proof, it is shown that the probability distribution of the γ variable is a Gaussian of width determined by the parameter Q (Eq. (112)). The Nosé-Hoover equations of motion are smooth, deterministic and time-reversible. However, just as the Nosé algorithm, Nosé-Hoover dynamics may lead to temperature oscillations.

In both algorithms, Some care must be taken in the choice of the fictitious mass Q and extended-system energy E_e. On the one hand, too large values of Q (loose coupling) may cause a poor temperature control. Indeed, the limiting case of the

Nosé-Hoover thermostat with $Q \to \infty$ and $\gamma(0) = 0$ is MD, which generates a microcanonical ensemble. Although any finite (positive) mass is sufficient to guarantee in principle the generation of a canonical ensemble, if Q is too large, the canonical distribution will only be obtained after very long simulation times. In this case, systematic energy drifts due to accumulation of numerical errors may interfere with the thermostatization. On the other hand, too small values (tight coupling) may cause high-frequency temperature oscillations (Eq. (73)) leading to the same effect. This is because if the $\tilde{s}$ variable oscillates at a very high frequency, it will tend to be off-resonance with the characteristic frequencies of the real system, and effectively decouple from the physical degrees of freedom (slow exchange of kinetic energy). The choice of the parameters Q and E_e can be guided by comparison of the frequency ν (Eq. (73)) with the inverse of the temperature relaxation time ζ_T (Eq. (26)). Note that if a simulation is initiated with $s(0) = 1$ and $\gamma(0) = 0$, which seems the most reasonable choice, the value of E_e will match the initial energy of the real system. The numerical integration of the Nosé and Nosé-Hoover equations will not be discussed here. A number of alternative schemes have been proposed in the literature [111, 112, 113, 114, 90].

The constant-temperature Woodcock/Hoover-Evans equation of motion can be retrieved from the the Nosé-Hoover formalism by a slight modification of the extended-system Hamiltonian. This is done by introducing the constraints

$$\tilde{s} = (g k_B T_o)^{-1/2} \left(\sum_{i=1}^{N} m_i^{-1} \tilde{\mathbf{p}}_i^2 \right)^{1/2} \quad \text{and} \quad \tilde{p}_s = 0 \tag{85}$$

into Eq. (67), leading to the modified Hamiltonian

$$\mathcal{H}_c(\tilde{\mathbf{r}}, \tilde{\mathbf{p}}) = \frac{1}{2} g k_B T_o + \mathcal{U}(\tilde{\mathbf{r}}) + \frac{1}{2} g k_B T_o \ln \left[(g k_B T_o)^{-1} \sum_{i=1}^{N} m_i^{-1} \tilde{\mathbf{p}}_i^2 \right] . \tag{86}$$

The corresponding Hamiltonian equations of motion for the physical variables in the extended system are still given by Eq. (68). It can be proved ([61]; see Appendix) that these equations of motion sample a canonical ensemble of configurations in the real system ($\mathbf{r} = \tilde{\mathbf{r}}, \dot{\mathbf{r}} = \tilde{s}^{-1} \tilde{\mathbf{p}}, t = \int \tilde{s}^{-1} d\tilde{t}$) with $\tilde{s}$ given by Eq. (85), provided that $g = N_{df}$ (virtual-time sampling) or $g = N_{df} - 1$ (real-time sampling), irrespective of the constant value E_e of $\mathcal{H}_c$. To show that this situation matches the Woodcock/Hoover-Evans equation of motion, the equation of motion must be rewritten in terms of real-system variables. Evaluating $\dot{\tilde{s}}$ based on Eq. (85) gives

$$\dot{\tilde{s}} = (g k_B T_o)^{-1} \tilde{s}^{-1} \sum_{i=1}^{N} m_i^{-1} \tilde{\mathbf{p}}_i \cdot \dot{\tilde{\mathbf{p}}}_i \, . \tag{87}$$

Applying the transformations of Eq. (77), setting $\gamma = s^{-1} \dot{s}$, and inserting Eq. (68) for $\dot{\tilde{\mathbf{p}}}$, it is easily seen that the equation of motion in terms of the real-system variables is Eq. (78) together with

$$\gamma = (gk_BT_o)^{-1} \sum_{i=1}^{N} \dot{\mathbf{r}}_i \cdot \mathbf{F}_i \ , \tag{88}$$

which is identical to the corresponding factor for the Woodcock (Eq. (50)) and Hoover-Evans (Eq. (45), when $\mathcal{T}(0) = \frac{g}{N_{df}} T_o$) equations of motion. This also shows that the appropriate choice for g so as to generate a canonical ensemble of configurations using either of these two thermostats is $g = N_{df} - 1$.

If, in addition to incorporating the constraint of Eq. (85), the Hamiltonian is changed to

$$\mathcal{H}_h(\tilde{\mathbf{r}}, \tilde{\mathbf{p}}) = \left(gk_BT_o \sum_{i=1}^{N} m_i^{-1} \tilde{\mathbf{p}}_i^2 \right)^{1/2} + \mathcal{U}(\tilde{\mathbf{r}}) \ , \tag{89}$$

the corresponding Hamiltonian equations of motion for the physical variables in the extended system become

$$\dot{\tilde{\mathbf{p}}}_i = \tilde{\mathbf{F}}_i \quad \text{and} \quad \dot{\tilde{\mathbf{r}}}_i = m_i^{-1} \tilde{s}^{-1} \tilde{\mathbf{p}}_i \ . \tag{90}$$

Setting $\dot{\mathbf{r}}_i = \dot{\tilde{\mathbf{r}}}_i$ and $\mathbf{p}_i = m_i \dot{\mathbf{r}}_i$, one recovers (using Eq. (85) and identifying $\dot{\mathbf{r}}_i' = m_i^{-1} \tilde{\mathbf{p}}_i$) the Haile-Gupta equations of motion (Eq. (52)). Note that $\tilde{s}$ no longer acts as a scaling parameter and the extended-system Lagragian has been changed, so that Eqs. (58) and (64) no longer apply. It can be proved ([53]; see Appendix) that this equation of motion does not sample a canonical ensemble of configurations in the real system, irrespective of the choice of g.

3.7 Generalizations of the Previous Methods

An interesting extension of the SD thermostat (Sect. 3.2) is the so-called dissipative-particle-dynamics (DPD) thermostat [115, 116, 117, 118]. This scheme retains a key advantage of the SD thermostat (shared with the Andersen thermostat), namely that it couples atomic velocities to the heat bath on a local basis (as opposed to the global coupling applied by all other thermostats discussed in this article). Local coupling leads to an intrinsically more efficient thermostatization and in turn, permits the use of longer timesteps to integrate the equations of motion (in applications where this timestep is not further limited by the curvature of the interaction function, i.e., when using soft intermolecular potentials). On the other hand, the DPD scheme alleviates two drawbacks of the SD scheme, namely (i) the non-conservation of the system linear and angular momentum, and (ii) the loss of local hydronamic correlations between particles. In practice, this is achieved by replacing the frictional and stochastic forces acting on individual atoms in SD (Eq. (17)), by corresponding central pairwise forces acting on atom pairs within a given cutoff distance.

A number of extensions or generalizations of the Nosé or Nosé-Hoover approaches (Sect. 3.6) have also been reported in the literature, following three main directions.

First, more general extended Hamiltonians (including the Nosé Hamiltonian as a particular case) have been shown to also produce canonical phase-space sampling [119, 120, 121, 122, 123, 124, 125, 126, 127]. The additional flexibility offered by these new schemes may be used to overcome the non-ergodic behaviour of the Nosé-Hoover thermostat in the context of small or stiff systems (e.g., single harmonic oscillator) or systems at low temperatures [63, 128, 129, 121, 130, 131, 132]. A number of these variants can indeed produce the correct canonical distribution for a single harmonic oscillator [121, 122, 123, 125, 126]. The most popuar of these schemes is probably the Nosé-Hoover chain thermostat [123], where the single thermostatting variable γ of the Nosé-Hoover scheme is replaced by a series of variables thermostatting each other in sequence.

Second, alternatives have been proposed for the Nosé-Hoover scheme, which are phase-space conserving [133] or even symplectic [127]. One of the latter schemes, referred to as the Nosé-Poincaré thermostat, leads to the same phase-space trajectory as the Nosé-Hoover thermostat with real time sampling, but has the advantage of being Hamiltonian.

Third, generalized equations of motion have been proposed to sample arbitrary (i.e., not necessarily canonical) probability distributions [134, 135, 136, 137]. Such methods can be used, e.g., to optimize the efficiency of conformational searches [134, 135, 137] or for generating Tsallis distributions of microstates [136].

4 Practical Considerations

This section briefly mentions two practical aspects related to the use of thermostats in MD simulations of (bio-)molecular systems.

The first problem is encountered when simulating molecular systems involving distinct sets of degrees of freedom with either (i) very different characteristic frequencies or (ii) very different heating rates caused by algorithmic noise. In this case, the joint coupling of all degrees of freedom to a thermostat may lead to different effective temperatures for the distinct subsets of degrees of freedom, due to a too slow exchange of kinetic energy between them. A typical example is the so-called "hot solvent – cold solute problem" in simulations of macromolecules. Because the solvent is more significantly affected by algorithmic noise (e.g., due to the use of an electrostatic cutoff), the coupling of the whole system to a single thermostat may cause the average solute temperature to be significantly lower than the average solvent temperature. A solution to this problem is to couple separately the solute and solvent degrees of freedom to two different thermostats.

The second problem is encountered when using a simulation program that (incorrectly) applies the thermostatization directly to the atomic velocities rather than to the internal (peculiar) velocities (Sect. 3). In this case, the system linear and (under vacuum boundary conditions) angular momenta are not conserved, unless they exactly vanish. However, even if these quantities are set to zero at the beginning of a simulation, numerical errors will unavoidably alter these initial values, permitting a flow

of kinetic energy between internal and external degrees of freedom. Unfortunately, it appears that at least some thermostats tend to pump kinetic energy from high-frequency to low-frequency degrees of freedom (thereby violating equipartition). In this case, uniform translational and (under vacuum boundary conditions) rotational motion will tend to build up. For simulations started with vanishing overall momenta, one generally observes a very slow initial rise (often taking nanoseconds) followed by a very sudden burst of translational and rotational kinetic energy. The accumulation of kinetic energy in these degrees of freedom will effectively cool down the internal ones, giving rise to the so-called "flying ice cube effect" [138, 139]. The most obvious remedy to this problem is to remove the overall center of mass motion from the atomic velocities at regular interval during the simulation. However, the application of thermostatization on the basis of internal velocities (Sect. 3) should probably be preferred, because it is more consistent and avoids the indrotuction of discontinuities in the generated velocity trajectory.

5 Appendix: Phase-Space Probability Distributions

Here, the phase-space probability distributions are derived that correspond to the Woodcock/Hoover-Evans (Sect. 3.4), Haile-Gupta (Sect. 3.4), Berendsen (Sect. 3.5), Nosé (Sect. 3.6) and Nosé-Hoover (Sect. 3.6) thermostats. The derivations are given for all but the Berendsen thermostat, for which the result is merely quoted.

The proof that the Nosé thermostat samples a canonical ensemble of microstates, provided that $g = N_{df} + 1$ (virtual-time sampling) or $g = N_{df}$ (real-time sampling), is as follows [53]. The partition function of the microcanonical ensemble generated for the extended system using virtual-time sampling (i.e., using the natural time evolution of the extended system) reads

$$Z_{e,v} = C \int d\tilde{\mathbf{p}} \int d\tilde{\mathbf{r}} \int d\tilde{p}_s \int d\tilde{s}\, \delta[\mathcal{H}_e(\tilde{\mathbf{r}}, \tilde{\mathbf{p}}, \tilde{s}, \tilde{p}_s) - E_e] \,, \tag{91}$$

where C is a normalization constant, E_e the (constant) extended-system energy, δ the Dirac delta function, and $\mathcal{H}_e$ the extended-system Hamiltonian (Eq. (67)). Recasting this expression in terms of the real-system momenta $\mathbf{p}_i = \tilde{s}^{-1}\tilde{\mathbf{p}}_i$ and substituting $\mathbf{r} = \tilde{\mathbf{r}}$ leads to

$$\begin{aligned} Z_{e,v} = C \int d\mathbf{p} \int d\mathbf{r} \int d\tilde{p}_s \int d\tilde{s}\, \tilde{s}^{N_{df}} \\ \times \delta\left[\mathcal{H}(\mathbf{r}, \mathbf{p}) + \frac{1}{2} Q^{-1} \tilde{p}_s^2 + g\beta^{-1} \ln \tilde{s} - E_e\right] , \end{aligned} \tag{92}$$

where $\mathcal{H}$ is the real-system Hamiltonian, i.e.

$$\mathcal{H}(\mathbf{r}, \mathbf{p}) = \frac{1}{2} \sum_{i=1}^{N} m_i^{-1} \mathbf{p}_i^2 + \mathcal{U}(\mathbf{r}) \,. \tag{93}$$

The argument of the delta function in Eq. (92) has a single zero with respect to the $\tilde{s}$ variable, namely

$$\tilde{s}_o = \exp\left\{-g^{-1}\beta\left[\mathcal{H}(\mathbf{r},\mathbf{p}) + \frac{1}{2}Q^{-1}\tilde{p}_s^2 - E_e\right]\right\} . \tag{94}$$

Using the relationship $\delta[f(\tilde{s})] = \mid f'(\tilde{s}_o) \mid^{-1} \delta(\tilde{s} - \tilde{s}_o)$, one obtains

$$\begin{aligned} Z_{e,v} &= Cg^{-1}\beta \int d\mathbf{p} \int d\mathbf{r} \int d\tilde{p}_s \int d\tilde{s}\, \tilde{s}^{N_{df}+1}\delta[\tilde{s} - \tilde{s}_o] \\ &= Cg^{-1}\beta \int d\mathbf{p} \int d\mathbf{r} \int d\tilde{p}_s \\ &\quad \times \exp\left\{-(N_{df}+1)g^{-1}\beta\left[\mathcal{H}(\mathbf{r},\mathbf{p}) + \frac{1}{2}Q^{-1}\tilde{p}_s^2 - E_e\right]\right\} . \end{aligned} \tag{95}$$

Integrating with respect to the variable $\tilde{p}_s$ and using the appropriate Gaussian integral gives

$$Z_{e,v} = C' \int d\mathbf{p} \int d\mathbf{r}\, \exp[-(N_{df}+1)g^{-1}\beta\mathcal{H}(\mathbf{r},\mathbf{p})] \tag{96}$$

with

$$C' = C[(N_{df}+1)\beta]^{-1/2}(2\pi g Q)^{1/2}\exp[(N_{df}+1)g^{-1}\beta E_e] . \tag{97}$$

Equation (96) shows that the virtual-time extended-system ensemble average of any quantity A depending on the real-system coordinates $\mathbf{r} = \tilde{\mathbf{r}}$ and momenta $\mathbf{p} = \tilde{s}^{-1}\tilde{\mathbf{p}}$ (and also possibly on $\tilde{s}$), defined as

$$\langle A(\mathbf{r},\mathbf{p})\rangle_{e,v} = \frac{\int d\mathbf{p} \int d\mathbf{r} \int d\tilde{p}_s \int d\tilde{s}\, \tilde{s}^{N_{df}+1} A(\mathbf{r},\mathbf{p})\delta[\tilde{s} - \tilde{s}_o]}{\int d\mathbf{p} \int d\mathbf{r} \int d\tilde{p}_s \int d\tilde{s}\, \tilde{s}^{N_{df}+1}\delta[\tilde{s} - \tilde{s}_o]} , \tag{98}$$

is equivalent to a canonical ensemble average, i.e.

$$\langle A(\mathbf{r},\mathbf{p})\rangle_{e,v} = \langle A(\mathbf{r},\mathbf{p})\rangle \quad \text{when} \quad g = N_{df} + 1. \tag{99}$$

If real-time sampling is used instead, the probability of any microstate in the ensemble is amplified by a factor $\tilde{s}^{-1}$ due to the contraction of the timescale. For example, ten microstates at 1 ps interval in the extended system represent 10 ps of real-system time if $\tilde{s} = 1$ but only 5 ps if $\tilde{s} = 2$. Thus, the larger $\tilde{s}$, the lower the real-system weight. Consequently, the real-time ensemble average of the quantity A, defined from Eqs. (98) and (101) as

$$\langle A(\mathbf{r},\mathbf{p})\rangle_{e,r} = \frac{\int d\mathbf{p} \int d\mathbf{r} \int d\tilde{p}_s \int d\tilde{s}\, \tilde{s}^{N_{df}} A(\mathbf{r},\mathbf{p})\delta[\tilde{s} - \tilde{s}_o]}{\int d\mathbf{p} \int d\mathbf{r} \int d\tilde{p}_s \int d\tilde{s}\, \tilde{s}^{N_{df}}\delta[\tilde{s} - \tilde{s}_o]} , \tag{100}$$

satisfies

$$\langle A(\mathbf{r},\mathbf{p})\rangle_{e,r} = \langle \tilde{s}^{-1}\rangle_{e,v}^{-1}\langle \tilde{s}^{-1} A(\mathbf{r},\mathbf{p})\rangle_{e,v} , \tag{101}$$

irrespective of the value of g. A straightforward consequence of Eqs. (98) and (101) is that the real-time extended-system ensemble average of any quantity A is equivalent to a canonical ensemble average, i.e.

$$\langle A(\mathbf{r},\mathbf{p})\rangle_{e,r} = \langle A(\mathbf{r},\mathbf{p})\rangle \quad \text{when} \quad g = N_{df}. \tag{102}$$

From Eq. (96), the real-system phase-space probability density for the Nosé thermostat (virtual-time sampling) can be written

$$\rho_v(\mathbf{r},\mathbf{p}) = \frac{\exp[-(N_{df}+1)g^{-1}\beta\mathcal{H}(\mathbf{r},\mathbf{p})]}{\int d\mathbf{p}\int d\mathbf{r}\,\exp[-(N_{df}+1)g^{-1}\beta\mathcal{H}(\mathbf{r},\mathbf{p})]}\,. \tag{103}$$

The proof that the Woodcock/Hoover-Evans thermostat samples a canonical ensemble of configurations provided that $g = N_{df}-1$ follows similar lines [53]. It has been seen that this thermostat is identical to the Nosé thermostat with the constraints of Eq. (85) and the Hamiltonian of Eq. (86). In this case, the analog of Eq. (92) reads

$$\begin{aligned}
Z_{e,v} &= C\int d\mathbf{p}\int d\mathbf{r}\int d\tilde{s}\,\tilde{s}^{N_{df}}\,\delta\left[g^{-1/2}\beta^{1/2}\tilde{s}\left(\sum_{i=1}^{N} m_i^{-1}\mathbf{p}_i^2\right)^{1/2} - \tilde{s}\right] \\
&\quad\times\delta\left[\mathcal{H}_c\left(\mathbf{r},\tilde{\mathbf{s}}\mathbf{p}\right) - E_e\right]\,, \\
&= Cg\beta^{-1}\int d\mathbf{p}\,\delta\left[\frac{1}{2}\sum_{i=1}^{N} m_i^{-1}\mathbf{p}_i^2 - \frac{1}{2}g\beta^{-1}\right] \\
&\quad\times\int d\mathbf{r}\int d\tilde{s}\,\tilde{s}^{N_{df}-1}\,\delta\left[\frac{1}{2}g\beta^{-1} + \mathcal{U}(\mathbf{r}) + g\beta^{-1}\ln\tilde{s} - E_e\right] \\
&= C\int d\mathbf{p}\,\delta\left[\frac{1}{2}\sum_{i=1}^{N} m_i^{-1}\mathbf{p}_i^2 - \frac{1}{2}g\beta^{-1}\right] \\
&\quad\times\int d\mathbf{r}\int d\tilde{s}\,\tilde{s}^{N_{df}}\,\delta\left[\tilde{s} - \exp\left\{-g^{-1}\beta\left[\frac{1}{2}g\beta^{-1} + \mathcal{U}(\mathbf{r}) - E_e\right]\right\}\right] \\
&= C'\int d\mathbf{p}\delta\left[\frac{1}{2}\sum_{i=1}^{N} m_i^{-1}\mathbf{p}_i^2 - \frac{1}{2}g\beta^{-1}\right]\int d\mathbf{r}\exp\left\{-N_{df}g^{-1}\beta\mathcal{U}(\mathbf{r})\right\}
\end{aligned} \tag{104}$$

The second equality follows from the relationship $\delta[f(x)] = \mid f'(x_o)\mid^{-1}\delta(x-x_o)$, with $x = \frac{1}{2}\sum_{i=1}^{N} m_i^{-1}\mathbf{p}_i^2$ and $x^o = \frac{1}{2}g\beta^{-1}$ and inserting Eqs. (85) and (86). The third equality follows from the relationship $\delta[f(\tilde{s})] = \mid f'(\tilde{s}_o)\mid^{-1}\delta(\tilde{s}-\tilde{s}_o)$. This partition function is canonical in the configurations if $g = N_{df}$ (virtual-time sampling). Considering Eq. (101), Eq. (104) shows that the real-time extended-system ensemble average of any quantity A depending solely on the coordinates is equivalent to a canonical ensemble average if $g = N_{df}-1$. From Eq. (104), the real-system phase-space probability density for the Woodcock/Hoover-Evans thermostat can be written (real-time sampling)

$$\rho_r(\mathbf{r},\mathbf{p}) = \frac{\delta(\frac{1}{2}\sum_{i=1}^{N} m_i^{-1}\mathbf{p}_i^2 - \frac{1}{2}g\beta^{-1})\exp[-(N_{df}-1)g^{-1}\beta\mathcal{U}(\mathbf{r})]}{\int d\mathbf{r}\,\exp[-(N_{df}-1)g^{-1}\beta\mathcal{U}(\mathbf{r})]}\,. \tag{105}$$

The derivation of the phase-space probability distribution for the Haile-Gupta thermostat follows similar lines [53]. It has been seen that this thermostat is identical to the Nosé thermostat with the constraints of Eq. (85) and the Hamiltonian of Eq. (89). In this case, the analog of Eq. (104) reads

$$\begin{aligned} Z_{e,\upsilon} &= C \int d\mathbf{p} \int d\mathbf{r} \int d\tilde{s}\, \tilde{s}^{N_{df}}\, \delta\left[g^{-1/2}\beta^{1/2}\tilde{s}\left(\sum_{i=1}^{N} m_i^{-1}\mathbf{p}_i^2\right)^{1/2} - \tilde{s}\right] \\ &\quad \times \delta[\mathcal{H}_h(\mathbf{r},\tilde{\mathbf{s}}\mathbf{p}) - E_e] \\ &= C g\beta^{-1} \int d\mathbf{p}\, \delta\left(\frac{1}{2}\sum_{i=1}^{N} m_i^{-1}\mathbf{p}_i^2 - \frac{1}{2}g\beta^{-1}\right) \\ &\quad \times \int d\mathbf{r} \int d\tilde{s}\, \tilde{s}^{N_{df}-1}\, \delta\left[g\beta^{-1}\tilde{s} + \mathcal{U}(\mathbf{r}) - E_e\right] \\ &= C' \int d\mathbf{p}\, \delta\left(\frac{1}{2}\sum_{i=1}^{N} m_i^{-1}\mathbf{p}_i^2 - \frac{1}{2}g\beta^{-1}\right) \\ &\quad \times \int d\mathbf{r} \{g^{-1}\beta[E_e - \mathcal{U}(\mathbf{r})]\}^{N_{df}-1} h[E_e - \mathcal{U}(\mathbf{r})]\,, \end{aligned} \tag{106}$$

where h is the Heaviside function. This function arises because $\tilde{s} \geq 0$, so that $E_e < \mathcal{U}(\mathbf{r})$ leads to no solution for $\tilde{s}$. Thus, the real-system phase-space probability density corresponding to the Haile-Gupta thermostat (virtual-time sampling) is

$$\rho_\upsilon(\mathbf{r},\mathbf{p}) = \frac{\delta(\frac{1}{2}\sum_{i=1}^{N} m_i^{-1}\mathbf{p}_i^2 - \frac{1}{2}g\beta^{-1})\{g^{-1}\beta[E_e - \mathcal{U}(\mathbf{r})]\}^{N_{df}-1} h[E_e - \mathcal{U}(\mathbf{r})]}{\int d\mathbf{r}\, \{g^{-1}\beta[E_e - \mathcal{U}(\mathbf{r})]\}^{N_{df}-1} h[E_e - \mathcal{U}(\mathbf{r})]}\,. \tag{107}$$

Using Eq. (106), it is easily seen that

$$\langle \tilde{s} \rangle_{e,\upsilon} = \langle g^{-1}\beta[E_e - \mathcal{U}(\mathbf{r})] \rangle_{e,\upsilon}\,. \tag{108}$$

Thus, E_e in Eq. (107) can be evaluated as

$$E_e = g\beta^{-1}\langle s \rangle_{e,\upsilon} + \langle \mathcal{U}(\mathbf{r}) \rangle_{e,\upsilon}\,. \tag{109}$$

This distribution function is not canonical, irrespective of the value of g (an alternative derivation of this result can be found in [109]).

The proof that the Nosé-Hoover thermostat samples a canonical ensemble of microstates provided that $g = N_{df}$ is as follows [63]. Consider the Nosé-Hoover equations of motion, Eqs. (79) and Eq. (81). Because the variables $\mathbf{r}$, $\mathbf{p}$, and γ are independent, the flow of the $(2N_{df}+1)$-dimensional probability density $\rho(\mathbf{r},\mathbf{p},\gamma)$ is given by the generalized (non-Hamiltonian) analog of the Liouville equation[21]

$$\frac{\partial\rho}{\partial t} = -\frac{\partial\rho}{\partial\mathbf{r}}\cdot\dot{\mathbf{r}} - \frac{\partial\rho}{\partial\mathbf{p}}\cdot\dot{\mathbf{p}} - \frac{\partial\rho}{\partial\gamma}\cdot\dot{\gamma} - \rho\left[\frac{\partial}{\partial\mathbf{r}}\cdot\dot{\mathbf{r}} + \frac{\partial}{\partial\mathbf{p}}\cdot\dot{\mathbf{p}} + \frac{\partial}{\partial\gamma}\cdot\dot{\gamma}\right]. \tag{111}$$

[21] The generalized Liouville equation states the conservation of the total number of systems in an ensmble. If $\Gamma = (\mathbf{q},\mathbf{p})$, this conservation law can be written

One can postulate the following extended-system phase-space distribution function

$$\rho_{e,r}(\mathbf{r}, \mathbf{p}, \gamma) = C \exp\left\{-\beta\left[\mathcal{U}(\mathbf{r}) + \frac{1}{2}\sum_{i=1}^{N} m_i^{-1}\mathbf{p}_i^2 + \frac{1}{2}Q\gamma^2\right]\right\}, \tag{112}$$

where C is a normalization factor. Using Eqs. (58), (79), and (81) the derivatives involved in Eq. (111) are

$$\begin{aligned}
-\frac{\partial\rho}{\partial\mathbf{r}}\cdot\dot{\mathbf{r}} &= \beta\rho\sum_{i=1}^{N} m_i^{-1}\mathbf{F}_i\cdot\mathbf{p}_i \\
-\frac{\partial\rho}{\partial\mathbf{p}}\cdot\dot{\mathbf{p}} &= -\beta\rho\sum_{i=1}^{N} m_i^{-1}\mathbf{p}_i\cdot(\mathbf{F}_i - \gamma\,\mathbf{p}_i) \\
-\frac{\partial\rho}{\partial\gamma}\cdot\gamma &= \beta\rho\gamma\, k_B N_{df}\mathcal{T}\left(\frac{g}{N_{df}}\frac{T_o}{\mathcal{T}} - 1\right) \\
\rho\frac{\partial}{\partial\mathbf{r}}\cdot\dot{\mathbf{r}} &= 0 \\
\rho\frac{\partial}{\partial\mathbf{p}}\cdot\dot{\mathbf{p}} &= -\rho N_{df}\gamma \\
\rho\frac{\partial}{\partial\gamma}\cdot\dot{\gamma} &= 0\,.
\end{aligned} \tag{113}$$

Using these results and the definition of $\mathcal{T}$, it is easily shown that $\partial\rho/\partial t = 0$ in Eq. (111) provided that $g = N_{df}$. This shows that the extended-system phase-space density $\rho_{e,r}(\mathbf{r}, \mathbf{p}, \gamma)$ is a stationary (equilibrium) solution of Eq. (111) corresponding to the Nosé-Hoover equations of motion. Integrating out the γ variable leads to the real-system phase-space probability density for the Nosé-Hoover thermostat (real-time sampling)

$$\rho_r(\mathbf{r}, \mathbf{p}) = \frac{\exp[-N_{df}\, g^{-1}\beta\mathcal{H}(\mathbf{r}, \mathbf{p})]}{\int d\mathbf{p}\int d\mathbf{r}\, \exp[-N_{df}\, g^{-1}\beta\mathcal{H}(\mathbf{r}, \mathbf{p})]}\,. \tag{114}$$

which is the canonical probability density if $g = N_{df}$. The Nosé-Hoover equations of motion are unique in leading to the stationary extended-system phase-space density of Eq. (112). However, they are not unique in leading to the real-system phase-space density, because the γ distribution (Gaussian in Eq. (112)) is irrelevant here. Finally, it should be mentionned that because the Nosé-Hoover thermostat can be derived from the Nosé thermostat with real-time sampling, the above proof is not really necessary. It is given anyway as a nice illustration of the use of the generalized Liouville equation to derive probability distribution functions for thermodynamical ensembles.

$$\frac{\partial\rho}{\partial t} = -\frac{\partial}{\partial\boldsymbol{\Gamma}}\cdot(\rho\dot{\boldsymbol{\Gamma}}) \quad \text{or} \quad \frac{d\rho}{dt} = -\rho\frac{\partial}{\partial\boldsymbol{\Gamma}}\cdot\dot{\boldsymbol{\Gamma}}\,. \tag{110}$$

The two forms can be interconverted by expressing $d\rho/dt$ as a total derivative. If the equations of motion are Hamiltonian, one shows easily that $d\rho/dt = 0$. If $\rho(\boldsymbol{\Gamma})$ is a stationary (equilibrium) solution, one has $\partial\rho/\partial t = 0$.

The derivation of the phase-space probability distribution for the Berendsen thermostat follows again similar lines [109]. The final expression relies on the assumption of a relationship

$$[\langle \mathcal{K}^2 \rangle - \langle \mathcal{K} \rangle^2]^{1/2} = \alpha(\tau_B)[\langle \mathcal{U}^2 \rangle - \langle \mathcal{U} \rangle^2]^{1/2} \,, \tag{115}$$

between the fluctuations in the kinetic and potential energies in simulations with the Berendsen thermostat. Clearly, such a relationship exists for any system. However, it is unclear is whether a common $\alpha(\tau_B)$ applies to all systems, irrespective of their composition and size. The derivation is then based on finding a stationary solution for the generalized Liouville equation (Eq. (111)). The final (approximate) result is (with $g = N_{df}$)

$$\rho_b(\mathbf{r},\mathbf{p}) = \frac{\rho_p(\mathbf{p}) \exp\{-\beta[\mathcal{U}(\mathbf{r}) - N_{df}^{-1}\alpha\beta^2[\mathcal{U}(\mathbf{r})^2 - \langle \mathcal{U}(\mathbf{r})\rangle_b^2]]\}}{\int d\mathbf{p}\, \rho_p(\mathbf{p}) \int d\mathbf{r} \exp\{-\beta[\mathcal{U}(\mathbf{r}) - N_{df}^{-1}\alpha\beta^2[\mathcal{U}(\mathbf{r})^2 - \langle \mathcal{U}(\mathbf{r})\rangle_b^2]]\}} \,, \tag{116}$$

where $\rho_p(\mathbf{p})$ is the (unknown) momentum probability distribution. Note that the Haile-Gupta thermostat generates configurations with the same probability distribution as the Berendsen thermostat with $\alpha = 1/2$ [109].

References

1. Baschnagel J, Binder K, Doruker P, Gusev AA, Hahn O, Kremer K, Mattice WL, Müller-Plathe F, Murat M, Paul W, Santos S, Suter UW, Tries W (2000) Adv Polymer Sci 152:41–156 106
2. van Gunsteren WF, Berendsen HJC (1990) Angew Chem Int Ed Engl 29:992–1023 106, 107, 111
3. Karplus M, McCammon JA (2002) Nature Struct Biol 9:646–652 106
4. Daura X, Glättli A, Gee P, Peter C, van Gunsteren WF (2002) Adv Prot Chem 62:341–360 106
5. Cheatham III TE, Kollman PA (2000) Annu Rev Phys Chem 51:435–471 106
6. Saiz L, Bandyopadhyay S, Klein ML (2002) Bioscience Reports 22:151–173 106
7. Engelsen SB, Monteiro C, Hervé de Penhoat C, Pérez S (2001) Biophys Chem 93:103–127 106
8. Warshel A, King G (1985) Chem Phys Lett 121:124–129 107
9. King G, Warshel A (1989) J Chem Phys 91:3647–3661 107
10. Juffer AH, Berendsen HJC (1993) Mol Phys 79:623–644 107
11. Brooks III CL, Karplus M (1983) J Chem Phys 79:6312–6325 107, 120
12. Brünger A, Brooks III CL, Karplus M (1984) Chem Phys Lett 105:495–500 107, 120
13. Beutler TC, Mark AE, van Schaik R, Gerber PR, van Gunsteren WF (1994) Chem Phys Lett 222:529–539 107
14. Essex JW, Jorgensen WL (1995) J Comput Chem 16:951–972 107
15. Im W, Berbèche S, Roux B (2001) J Chem Phys 117:2924–2937 107
16. Allen MP, Tildesley DJ (1987) Computer simulation of liquids. Oxford University Press, New York 107, 110, 111

17. Bekker H (1997) J Comput Chem 18:1930–1942 107
18. Tomasi J, Persico M (1994) Chem Rev 94:2027–2094 107
19. Smith PE, Pettitt BM (1994) J Phys Chem 98:9700–9711 107
20. Roux B, Simonson T (1999) Biophys Chem 78:1–20 107
21. Orozco M, Luque FJ (2000) Chem Rev 100:4187–4225 107
22. Schneider T, Stoll E (1978) Phys Rev B 17:1302–1322 107, 111, 120
23. Schneider T, Stoll E (1978) Phys Rev B 18:6468–6482 107, 111, 120
24. van Gunsteren WF, Berendsen HJC, Rullmann JAC (1981) Mol Phys 44:69–95 107, 111
25. Åkesson T, Jönsson B (1985) Mol Phys 54:369–381 107, 111
26. Börjesson U, Hünenberger PH (2001) J Chem Phys 114:9706–9719
27. Gros P, van Gunsteren WF, Hol WGJ (1990) Science 249:1149–1152 108
28. Gros P, van Gunsteren WF (1993) Mol Simul 10:377–395 108
29. Schiffer CA, Gros P, van Gunsteren WF (1995) Acta Crystallogr D D51:85–92 108
30. van Gunsteren WF, Brunne RM, Gros P, van Schaik RC, Schiffer CA, Torda AE (1994) Accounting for molecular mobility in structure determination based on nuclear magnetic resonance spectroscopic and X-ray diffraction data. In: James TL, Oppenheimer NJ (eds) Methods in enzymology: nuclear magnetic resonance, Vol. 239, Academic Press, New York, pp 619–654 108
31. Torda AE, Scheek RM, van Gunsteren WF (1989) Chem Phys Lett 157:289–294 108
32. Torda AE, Scheek RM, van Gunsteren WF (1990) J Mol Biol 214:223–235 108
33. Torda AE, Brunne RM, Huber T, Kessler H, van Gunsteren WF (1993) J Biomol NMR 3:55–66 108
34. van Gunsteren WF, Berendsen HJC (1977) Mol Phys 34:1311–1327 108
35. Ryckaert JP, Ciccotti G, Berendsen HJC (1977) J Comput Phys 23:327–341 108
36. Andersen HC (1983) J Comput Phys 52:24–34 108
37. Miyamoto S, Kollman PA (1992) J Comput Chem 13:952–962 108
38. Hess B, Bekker H, Berendsen HJC, Fraaije JGEM (1997) J Comput Chem 18:1463–1472 108
39. Kräutler V, van Gunsteren WF, Hünenberger PH (2001) J Comput Chem 22:501–508 108
40. Tironi IG, Brunne RM, van Gunsteren WF (1996) Chem Phys Lett 250:19–24 108
41. Lebowitz JL, Percus JK, Verlet L (1967) Phys Rev 153:250–254 108
42. Cheung PSY (1977) Mol Phys 33:519–526 108
43. Ray JR, Graben HW (1981) Mol Phys 43:1293–1297 108
44. Ray JR, Graben HW (1991) Phys Rev A 44:6905–6908 108
45. Graben HW, Ray JR (1991) Phys Rev A 43:4100–4103 108, 111, 113
46. Haile JM, Graben HW (1980) J Chem Phys 73:2412–2419 108
47. Haile JM, Graben HW (1980) Mol Phys 40:1433–1439 108
48. Ray JR, Graben HW (1986) Phys Rev A 34:2517–2519 108
49. Ray JR, Graben HW, Haile JM (1981) J Chem Phys 75:4077–4079 108
50. Ray JR, Graben HW (1990) J Chem Phys 93:4296–4298 108
51. Evans DJ, Morriss GP (1983) Chem Phys 77:63–66 108, 124
52. Evans DJ, Morriss GP (1983) Phys Lett 98A 98A:433–436 108, 124
53. Nosé S (1984) J Chem Phys 81:511–519 108, 127, 129, 131, 133, 136, 138, 140, 141
54. Berendsen HJC, Postma JPM, van Gunsteren WF, DiNola A, Haak JR (1984) J Chem Phys 81:3684–3690 108, 121, 127
55. Andersen HC (1980) J Chem Phys 72:2384–2393 108, 117, 122, 123
56. Parrinello M, Rahman A (1980) Phys Rev Lett 45:1196–1199 108
57. Parrinello M, Rahman A (1982) J Phys Chem 76:2662–2666 108

58. Ryckaert JP, Ciccotti G (1983) J Chem Phys 78:7368–7374 108
59. Nosé S, Klein ML (1983) Mol Phys 50:1055–1076 108
60. Heyes DM (1983) Chem Phys 82:285–301 108
61. Nosé S (1984) Mol Phys 52:255–268 108, 129, 132, 136
62. Brown D, Clarke JHR (1984) Mol Phys 51:1243–1252 108
63. Hoover WG (1985) Phys Rev A 31:1695–1697 108, 129, 131, 133, 135, 137, 142
64. Hoover WG (1986) Phys Rev A 34:2499–2500 108
65. Ferrario M, Ryckaert JP (1985) Mol Phys 54:587–603 108
66. Ray JR, Rahman A (1985) J Chem Phys 82:4243–4247 108
67. Melchionna S, Ciccotti G, Holian BL (1993) Mol Phys 78:533–544 108
68. Martyna GJ, Tobias DJ, Klein ML (1994) J Chem Phys 101:4177–4189 108
69. Melchionna S, Ciccotti G (1997) J Chem Phys 106:195–199 108
70. Hünenberger PH (2002) J Chem Phys 116:6880–6897 108
71. Çağin T, Pettitt BM (1991) Mol Phys 72:169–175 108
72. Ji J, Çağin T, Pettitt BM (1992) J Chem Phys 96:1333–1342 108
73. Lo C, Palmer B (1995) J Chem Phys 102:925–931 108
74. Lynch GC, Pettitt BM (1997) J Chem Phys 107:8594–8610 108
75. Fixman M (1974) Proc Natl Acad Sci USA 71:3050–3053 109
76. Lado F (1981) J Chem Phys 75:5461–5463 109
77. Wallace DC, Straub GK (1983) Phys Rev A 27:2201–2205 109
78. Çağin T, Ray JR (1988) Phys Rev A 37:247–251 109
79. Çağin T, Ray JR (1988) Phys Rev A 37:4510–4513 109
80. Lustig R (1994) J Chem Phys 100:3048–3059 109
81. Ray JR, Zhang H (1999) Phys Rev E 59:4781–4785 109
82. Metropolis N, Rosenbluth AW, Rosenbluth MN, Teller AH, Teller E (1953) J Chem Phys 21:1087–1092 111, 119
83. Valleau JP, Whittington SG (1977) A guide to Monde Carlo for statistical mechanics: 2. Byways. In: Berne BJ (ed) Modern theoretical chemistry, Vol. 5, Plenum Press, New York, pp 137–168 111, 119
84. Frenkel D (1993) Monte Carlo simulations: A primer. In: van Gunsteren, WF, Weiner PK, Wilkinson AJ (eds) Computer simulation of biomolecular systems, theoretical and experimental applications, Vol. 2, ESCOM Science Publishers, B.V., Leiden, The Netherlands, pp 37–66 111, 119
85. van Gunsteren WF, Nanzer AP, Torda AE (1995) Molecular simulation methods for generating ensembles or trajectories consistent with experimental data. In: Binder K, Ciccotti G (eds) Monte Carlo and molecular dynamics of condensed matter systems, Proceedings of the Euroconference, Vol. 49, SIF, Bologna, Italy, pp 777–788 112
86. Evans DJ, Sarman S (1993) Phys Rev E 48:65–70 112, 117
87. Rugh HH (1997) Phys Rev Lett 78:772–774 113
88. Butler BD, Ayton G, Jepps OG, Evans DJ (1998) J Chem Phys 109:6519–6522 113
89. Hockney RW (1970) Methods Comput Phys 9:136–211 115
90. Morishita T (2003) Mol Simul 29:63–69 116, 135
91. Holian BL, Evans DJ (1983) J Chem Phys 78:5147–5150 117
92. Adams DJ (1975) Mol Phys 29:307–311 120
93. Creutz M (1983) Phys Rev Lett 50:1411–1414 120
94. Ray JR (1991) Phys Rev A 44:4061–4064 120
95. Ciccotti G, Ferrario M, Ryckaert JP (1982) Mol Phys 46:875–889 120
96. Berkowitz M, Morgan JD, McCammon JA (1983) J Chem Phys 78:3256–3261 120
97. Vesely FJ (1984) Mol Phys 53:505–524 120

98. Guàrdia E, Padró JA (1985) J Chem Phys 83:1917–1920 120
99. van Gunsteren WF, Berendsen HJC (1988) Mol Simul 1:173–185 120
100. Wang W, Skeel RD (2003) Mol Phys 101:2149–2156 120
101. Berkowitz M, McCammon JA (1982) Chem Phys Lett 90:215–217 120
102. Tanaka H, Nakanishi K, Watanabe N (1983) J Chem Phys 78:2626–2634 123
103. Woodcock LV (1971) Chem Phys Lett 10:257–261 124, 125
104. Hoover WG, Ladd AJC, Moran B (1982) Phys Rev Lett 48:1818–1820 124, 127
105. Evans DJ (1983) J Chem Phys 78:3297–3302 124
106. Evans DJ, Hoover WG, Failor BH, Moran B, Ladd AJC (1983) Phys Rev A 28:1016–1020 124
107. Broughton JQ, Gilmer GH, Weeks JD (1981) J Chem Phys 75:5128–5132 126
108. Haile JM, Gupta S (1983) J Chem Phys 79:3067–3076 126, 127
109. Morishita T (2000) J Chem Phys 113:2976–2982 127, 129, 142, 143, 144
110. Nosé S (1993) Phys Rev E 47:164–177 132
111. Holian BL, De Groot AJ, Hoover WG, Hoover CG (1990) Phys Rev A 41:4552–4553 135
112. Toxvaerd S (1991) Mol Phys 72:159–168 135
113. Martyna GJ, Tuckerman ME, Tobias DJ, Klein ML (1996) Mol Phys 87:1117–1157 135
114. Jang S, Voth GA (1997) J Chem Phys 107:9514–9526 135
115. Hoogerbrugge PJ, Koelman JMVA (1992) Europhys Lett 19:155–160 137
116. Español P, Warren P (1995) Europhys Lett 30:191–196 137
117. Groot RD, Warren PB (1997) J Chem Phys 107:4423–4435 137
118. Soddemann T, Dünweg B, Kremer K (2003) Phys Rev E 68:046702(1)–046702(8) 137
119. Jellinek J, Berry SR (1988) Phys Rev A 38:3069–3072 137
120. Hoover WG (1989) Phys Rev A 40:2814–2815 137
121. Hamilton IP (1990) Phys Rev A 42:7467–7470 137
122. Winkler RG (1992) Phys Rev A 45:2250–2255 137
123. Martyna GJ, Klein ML, Tuckerman M (1992) J Chem Phys 97:2635–2643 137
124. Holian BL, Posch HA, Hoover WG (1993) Phys Rev E 47:3852–3861 137
125. Brańka AC, Wojciechowski KW (2000) Phys Rev E 62:3281–3292 137
126. Brańka AC, Kowalik M, Wojciechowski KW (2003) J Chem Phys 119:1929–1936 137
127. Laird BB, Leimkuhler BJ (2003) Phys Rev E 68:016704(1)–016704(6) 137
128. Posch HA, Hoover WG, Vesely FJ (1986) Phys Rev A 33:4253–4265 137
129. Jellinek J, Berry SR (1989) Phys Rev A 40:2816–2818 137
130. Toxvaerd S (1990) Ber Bunsenges Phys Chem 94:274–278 137
131. Calvo F, Galindez J, Gadéa FX (2002) J Phys Chem A 106:4145–4152 137
132. D'Alessandro M, Tenenbaum A, Amadei A (2002) J Phys Chem B 106:5050–5057 137
133. Winkler RG, Kraus V, Reineker P (1995) J Chem Phys 102:9018–9025 137
134. Pak Y, Wang S (1999) J Chem Phys 111:4359–4361 137
135. Fukuda I (2001) Phys Rev E 64:016203(1)–016203(8) 137
136. Fukuda I, Nakamura H (2002) Phys Rev E 65:026105(1)–026105(5) 137
137. Barth EJ, Laird BB, Leimkuhler BJ (2003) J Chem Phys 118:5759–5768 137
138. Harvey SC, Tan RKZ, Cheatham III TE (1998) J Comput Chem 19:726–740 138
139. Chiu SW, Clark M, Subramaniam S, Jakobsson E (2000) J Comput Chem 21:121–131 138

Index

Adv. Polym. Sci. (2005) 173:149–207
DOI:10.1007/b99429

Numerical Simulation of Crystal Nucleation in Colloids

Stefan Auer[1] and Daan Frenkel[2]

[1] Department of Chemistry, Cambridge University, Lensfield Road, Cambridge, CB2 1EW, United Kingdom, *sa372@cam.ac.uk*
[2] FOM Institute for Atomic and Molecular Physics, Kruislaan 407, 1098 SJ Amsterdam, The Netherlands, *frenkel@amolf.nl*

Abstract This article reviews the recent progress that has been made in the application of computer simulations to study crystal nucleation in colloidal systems. We discuss the concept and the numerical methods that allow for a quantitative prediction of crystal nucleation rates. The computed nucleation rates are predicted from first principles and can be directly compared to experiments. These techniques have been applied to study crystal nucleation in hard-sphere colloids, polydisperse hard-sphere colloids, weakly charged or slightly soft colloids and hard-sphere colloids that are confined between two plane hard walls.

Keywords Crystal nucleation, Colloids, Monte Carlo simulation, Nucleation barrier, Kinetic prefactor, Crystal nucleation rate

1 Introduction

Heating a block of ice will result in melting. Cooling the resulting water will freeze it again. At a given pressure, water and ice can coexist at only one temperature. The water-ice coexistence temperature at ambient pressure is of such importance for every-day life, that it has been chosen as the zero-point of the widely used temperature scale invented by the Swedish physicist Celsius. Closer inspection of the melting and freezing transition shows that this transition is not quite symmetric. Ice heated above 0° C always melts, whereas cooling it below 0° C does not always result in immediate freezing. In fact water, and most other liquids, can be cooled significantly below their freezing temperature and kept there without crystallizing [1, 2]. This phenomena is known as supercooling. A supercooled liquid can be triggered into freezing by adding a little bit of the corresponding solid. A single snowflake in a glass of supercooled water will induce freezing of water that touches it and grow rapidly into a big chunk of ice. Other disturbances, such as dust or even shocks, can trigger the freezing of supercooled liquids as well. It thus seems that the freezing process has great difficulty to start spontaneously, but becomes very easy once it is initiated. The spontaneous formation of a piece of solid is an example of nucleation.

The fact that a liquid can be supercooled is best understood qualitatively in the framework of classical nucleation theory (CNT) (see e.g. Ref. [3]). According to CNT the free energy of a spherical nucleus that forms in a supersaturated solution contains two terms. The first term accounts for the fact that the solid phase is more stable than the liquid. This term is negative and proportional to the volume of the nucleus. The second term is a surface term. It describes the free energy needed to create a solid/liquid interface. This term is positive and proportional to the surface area of the nucleus. The (Gibbs) free energy of a spherical nucleus of radius R has the following form:

$$\Delta G = \frac{4}{3}\pi R^3 \rho_s \Delta\mu + 4\pi R^2 \gamma, \tag{1}$$

where ρ_s is the number density of the bulk solid, $\Delta\mu$ the difference in chemical potential between the solid and the liquid, and γ is the solid/liquid surface free energy density. The function ΔG has a maximum at $R = 2\gamma/(\rho_s|\Delta\mu|)$ and the corresponding height of the nucleation barrier is given by

$$\Delta G^* = \frac{16\pi}{3}\frac{\gamma^3}{(\rho_s|\Delta\mu|)^2}. \tag{2}$$

For small nuclei the surface term dominates and the free energy increases. Only if this nucleus exceeds a critical size does its free energy decrease and the crystallite can grow spontaneously (see Fig. 1). The probability for the formation of a critical nucleus depends exponentially on its free energy of formation:

$$P_c \propto \exp(-\Delta G^*/k_B T). \tag{3}$$

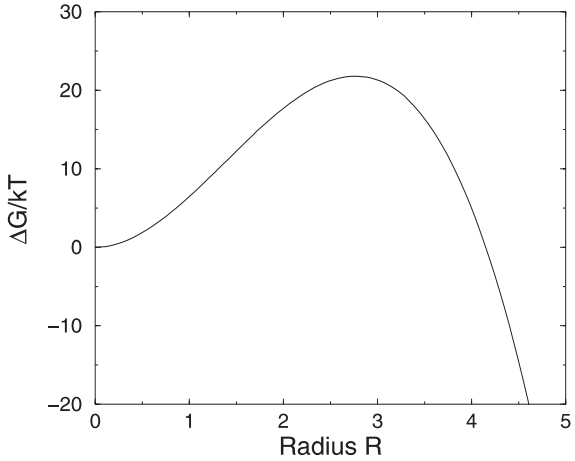

Fig. 1. Free energy barrier of a spherical nucleus described by classical nucleation theory Eq. (1). For small radii the surface term dominates and the free energy increases. When the radius exceeds a critical size the bulk term dominates and the free energy decreases

The crystal nucleation rate is given by the product of P_c and a kinetic factor Γ that describes the rate with which a critical nucleus grows. The CNT expression for the nucleation rate per unit volume is:

$$I = \Gamma \exp\left[-\frac{16\pi}{3k_BT}\frac{\gamma^3}{(\rho_s|\Delta\mu|)^2}\right], \tag{4}$$

with $\Gamma = Z\rho_l f_c^+$. Here ρ_l is the number density of the liquid, $Z = \sqrt{|\Delta\mu|/6\pi k_BTn_c}$ is the Zeldovich factor and f_c^+ is the attachment rate of particles to the critical cluster. The Zeldovich factor arises from the fact that not all particles that are at the top of the nucleation barrier crystallize: some will recross the barrier and melt again. The attachment rate of particles to the critical nucleus can be estimated by multiplying the number of monomers available at the surface of the nucleus – which is proportional to ${n_c}^{2/3}$ – with a typical transition rate of these particles to become part of the nucleus. This transition rate is proportional to D_S/λ^2, where D_S is a self diffusion coefficient and λ is a typical distance over which diffusion takes place:

$$f_c^+ = \frac{24D_S{n_c}^{2/3}}{\lambda^2}. \tag{5}$$

The above expression for the nucleation rate is the one most commonly used to analyze crystal nucleation rate experiments. The problem with the CNT approach is however that, in most cases, neither λ nor γ are accurately known. More often than not, both parameters are obtained by fitting the CNT expression to experimental nucleation data.

To illustrate the problems associated with the fitting of CNT to experimental data, we give two examples. Let us start with Turnbull's first quantitative measurement of

a nucleation rate in liquid mercury [2] (see Fig. 2). For the interpretation of his data he used Eq. (4), where he estimated the difference in chemical potential between the two phases by $\Delta\mu \approx \Delta h(T_m - T)/T_m$. Here Δh is the enthalpy change per particle on freezing at coexistence, T_m is the coexistence temperature and T is the temperature of the liquid mercury. A plot of $\log(I)$ vs. $1/T\,\Delta T^2$ should give a straight line with the slope proportional to γ^3 and the intercept equal to $\log(\kappa)$. From this two

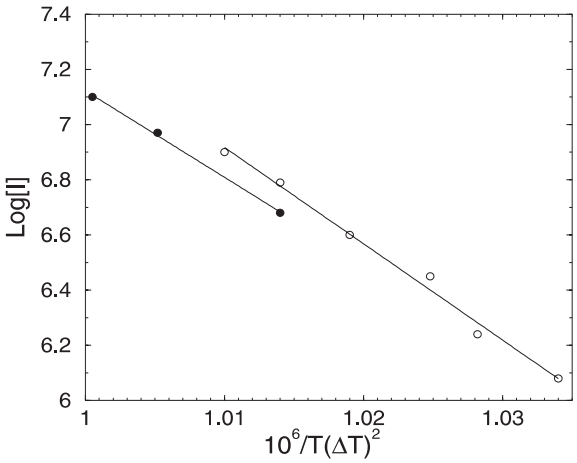

Fig. 2. The steady state nucleation rate, I in units of $1/(m^3 s)$, as a function of undercooling in Kelvin for liquid mercury from Ref. [2]. The *open* and the *filled circles* correspond to two different samples. The *solid lines* result from a two parameter fit of Eq. (4) to the experimental data

parameter fit we see that the functional form given by CNT for the nucleation rate reproduces the experimental data. However, the resulting value of κ is a factor 10^7 larger than predicted from CNT. The corresponding estimate for the typical diffusion distance λ is many orders of magnitude too small. To explain this Turnbull noted is his paper: *"...suppose that γ depends upon temperature according to the equation:* $\gamma = \gamma_0 + bT$, [where γ_0 is the value at coexistence and b is a constant], ... *a value of b=0.0008/K is sufficient to change the apparent value of the kinetic factor by six orders of magnitude."* A remarkable statement which might be correct, but at the time direct corroboration was not possible because of the absence of a priori knowledge of both fit parameters. The major problem of experimental investigations of crystallization kinetics in atomic systems is the high speed of nucleus formation and subsequent crystal growth, as well as the difficulty of preventing heterogeneous nucleation. The second example we take from more recent experiments on the crystallization kinetics in a suspension of hard-sphere colloids. Crystallization in colloidal suspensions is interesting because it can be studied in considerable detail, since colloidal particles are much larger than atoms. Colloids therefore crystallize on a timescale which is about ten orders of magnitude longer than that for an atomic liquid. Moreover because of

their size, colloids can be probed by powerful optical methods such as time-resolved static laser light scattering and confocal microscopy. In these systems it is also somewhat easier to control heterogeneous nucleation. In Fig. 3 we show the results from crystallization rate measurements in hard-sphere colloids, performed by two different groups [5, 6]. For this system the difference in chemical potential between the two phases can be calculated accurately from existing analytical expressions for the equation of state. The curves in the figure result from a two parameter fit of Eq. (4) to the experimental data. Palberg [4] fitted the data from Harland and van Megen [5]

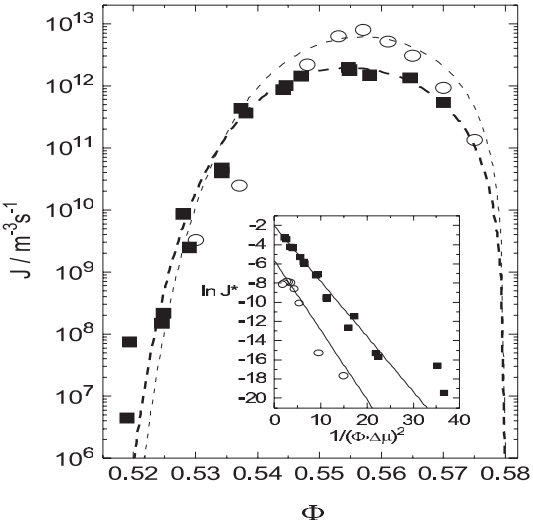

Fig. 3. Measured crystal nucleation rates I as of function of volume fraction ϕ in a system of hard-sphere colloids. The data are taken from Ref. [5] (*open circles*) and Ref. [6] (*filled cubes*). The lines result from a two parameter fit of Eq. (4) to the experimental data. The *inset* shows the dimensionless nucleation rate densities plotted logarithmically versus $1/(\phi\Delta\mu)^2$. The figure is taken from Ref. [4]

and obtained $\gamma = 0.5k_BT/\sigma^2$ and $\lambda = 17d_{NN}$, while for the data from Heymann et al. [6] he found $\gamma = 0.54k_BT/\sigma^2$ and $\lambda = 2.8d_{NN}$, where σ is the particle diameter and d_{NN} is the nearest neighbor distance. The estimates for the surface free energy are rather low when compared to numerical estimates [7] and the values of the effective jump length λ seem rather large (a factor 10 to 100 larger than the mean free path in the liquid). However, as the experimental results could be fitted with Eq. (4), there was little reason to doubt the values of the fit parameters thus obtained from experiment.

As experiments to determine absolute crystal nucleation rates are notoriously difficult, there is a clear need for a first principle prediction of a crystal nucleation rate.

In this review we discuss some of the recent progress that has been made in the application of computer simulation to gain a better understanding of the kinetics of colloidal crystallization.

2 Method

Simulating the crystallization process is a computational challenge, precisely because crystal nucleation is an activated process. This implies that the formation of small crystal nuclei in a supersaturated liquid is infrequent but, when it happens, the process is quite fast, i.e. it proceeds on a time scale that can be followed in a molecular simulation. For instance, experimentally measured nucleation rates are typically on the order of $O(10^1)$ to $O(10^6)$ nuclei per cm^3 per sec. We can estimate the number of time steps needed in a molecular dynamics (MD) simulation to observe one nucleation event. In a large-scale computer simulation, it is feasible to study the dynamics of $O(10^6)$ particles, but the number of particles in a typical simulation is some two to three order of magnitude less. For an atomic liquid, the volume of a simulation box containing one million particles is of order $O(10^{-15})\,cm^3$. If a million nuclei form per second in one cubic centimeter, then it will take, on average, 10^9 seconds for a nucleus to form in a system of a million particles. As the typical time step in a molecular simulation (MD) is on the order of femto seconds, this implies that it would take some 10^{24} MD time-steps to observe a single nucleation event under experimental conditions.

This example illustrates why it will be difficult to compute nucleation rates using conventional MD simulations. One way around this problem is to simulate a system at a much higher supersaturation, where the free energy barrier for the formation of crystal nuclei is sufficiently low to allow the system to crystallize spontaneously on a time scale that is accessible in a MD simulation. The problem with this approach is that, at such extreme supersaturations, crystallization may proceed differently than at moderate supersaturations. For example at high supersaturations, many crystal nuclei may form simultaneously and may interact in an early stage of their development. It then becomes difficult to compare the computed crystallization rates with predictions based on CNT.

In order to study crystal nucleation at moderate supersaturation, we exploit the fact that the crystallization rate is determined by the product of a static term, namely the probability for the formation of a critical nucleus P_c, and a kinetic factor Γ that describes the rate at which such nuclei grow. We use umbrella sampling to compute P_c and kinetic Monte Carlo simulations to compute Γ. The computed nucleation rates can be directly compared to experimental data.

In the following we describe the numerical techniques needed to compute a nucleation rate based on Ref. [8]. First we discuss the calculation of the cluster size distribution. After that we turn to the calculation of the kinetic prefactor.

2.1 Calculation of the Cluster Size Distribution

The probability to form a crystal nucleus of size n can be approximated by $P(n) = N_n/N$, where N_n is the number of crystal nuclei of size n in a system containing N particles [8, 9, 10], see also Appendix A. The approximation becomes better as N_n/N becomes smaller, i.e. when the spontaneous formation of clusters is rare. Knowledge of the ratio N_n/N allows us to define the Gibbs free energy $\Delta G(n)$ for the formation of a nucleus of size n:

$$\frac{N_n}{N} = \exp[-\Delta G(n)/k_B T]. \tag{6}$$

Before we can calculate N_n in a Monte Carlo simulation we need to have a numerical technique that enables us to distinguish between particles in a liquid and solid environment. To this end, we use local bond-order analysis introduced by Steinhardt et al. [11] and applied to study nucleation by Frenkel and coworkers [8, 12, 13]. The advantage of this analysis is that it is only sensitive to the overall degree of crystallinity in the system, but independent of any specific crystal structure. This requirement is important as otherwise we would apply an external biasing potential, that could force the system to crystallize in a specific structure. A second advantage is that these bond-order parameters can be constructed so as to be independent of the reference frame.

The local bond-order parameters are a measure of the local structure around a particle and are constructed as follows. First we define a $(2l + 1)$ dimensional complex vector with the components

$$q_{lm}(i) = \frac{1}{N_b(i)} \sum_{j=1}^{N_b(i)} Y_{lm}(\hat{\mathbf{r}}_{ij}),$$

where the sum goes over all neighboring particles $N_b(i)$ of particle i. Neighbors are usually defined as all particles that are within a given radius r_q around a particle. $Y_{lm}(\hat{\mathbf{r}}_{ij})$ are the spherical harmonics evaluated for the normalized direction vector $\hat{\mathbf{r}}_{ij}$ between the neighbors.

The orientation of the unit vector $\hat{\mathbf{r}}_{ij}$ is determined by the polar and azimuthal angles θ_{ij} and ϕ_{ij}. The rotationally invariant local bond-order parameters are then defined as follows:

$$q_l(i) = \left(\frac{4\pi}{2l+1} \sum_{m=-l}^{l} |q_{lm}(i)|^2 \right)^{1/2}$$

and

$$\hat{w}_l(i) = \frac{w_l(i)}{(\sum_{m=-l}^{l} |q_{lm}(i)|^2)^{3/2}}$$

with

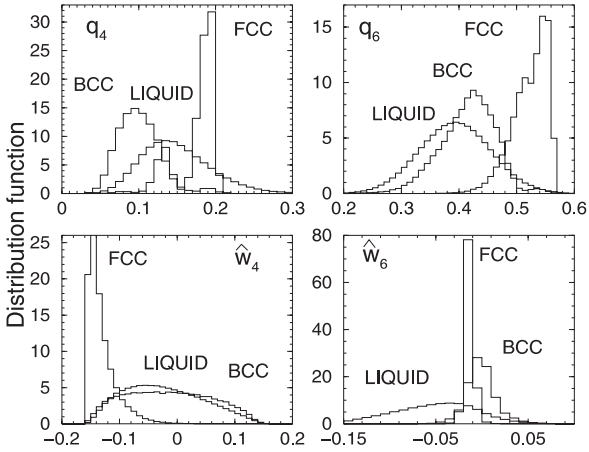

Fig. 4. Distribution functions of the local bond-order parameters: q_4, q_6, $\hat{w}_4$ and $\hat{w}_6$ from Monte Carlo simulations in a hard-sphere system. Here the cutoff radius r_q for the local environment of a particle is chosen to be 1.4σ, where σ is the hard-core diameter. This means that we included the first, and in some cases also the second nearest neighbors

$$w_l(i) = \sum_{\substack{m_1,m_2,m_3 \\ m_1+m_2+m_3=0}} \begin{pmatrix} l & l & l \\ m_1 & m_2 & m_3 \end{pmatrix} q_{lm_1}(i) q_{lm_2}(i) q_{lm_3}(i).$$

The term in brackets in the last equation is the Wigner-3j symbol. In Fig. 4 we show typical distribution functions of the local bond-order parameters q_4, q_6, $\hat{w}_4$, $\hat{w}_6$ calculated in a Monte Carlo simulation of hard-spheres under conditions close to the coexistence point, where the liquid and the solid phase are equally stable. The figure illustrates that there is some separation between the distribution functions obtained from the liquid and those obtained from the solid. Sometimes, there is even a separation between the solid structures themselves, a property that we will use later to distinguish between different solid structures. For the identification of solid-like particles we have to choose an order parameter that is able to distinguish between the liquid on the one hand, and all possible solid structures, on the other. From Fig. 4 we see that q_6 has some of the desired properties, as the values of the solid phases are all shifted to higher values compared to the liquid. These order parameters are sensitive to the degree of orientational correlations of the vectors that join neighboring particles. In simple liquids we expect that there are no preferred orientations around a particle and therefore the correlations decay rapidly. In contrast, for a particle with a solid-like environment the vectors are correlated and as result there should be a clear separation between distribution functions for the bond-order parameter. For this reason we can enhance the selectivity of the method by calculating the correlation function of the vectors $\mathbf{q}_6$ of neighboring particles i and j

$$\mathbf{q}_6(i) \cdot \mathbf{q}_6(j) = \sum_{m=-6}^{6} q_{6m}(i) \cdot q_{6m}^*(j),$$

where the $*$ indicates the complex conjugate. In Fig. 5 we show the corresponding distribution functions for a hard-sphere system. Note that we did not attempt to normalize the dot-product. The relevant solid structures, which for the hard sphere system are fcc, hcp and bcc, yield much higher values for the dot-product than the liquid. We now define two neighboring particles i and j to be connected, if the dot-product described above exceeds a certain threshold. In the case of hard spheres this threshold is set to 20. By using this definition we can correctly identify effectively all particles in a solid to be solid-like, however also in the liquid it happens quite frequently that a particle has more than one connection. To illustrate this, we show in Fig. 6 the distribution functions for the number of connections per particle. Note, that the peak for the solid structures is at 12 for fcc, hcp and around 13 for bcc. These numbers correspond to the first, or first and second nearest neighbors, which were included in the local environment. For the bcc structure the peak is slightly shifted to lower values, which is due to the fact that the bcc structure is relatively disordered. The bcc lattice of monodisperse hard-spheres melts spontaneously. We found, however, that a slightly polydisperse (3%) bcc crystal is mechanically stable. We used such a crystal to study the bcc bond-order properties. Thus far, we have no clear separation between solid-like and liquid-like particles, because the order-parameter distributions overlap. We therefore apply a more stringent criterion to distinguish between solid and liquid. To this end, we impose a threshold on the number of connections a particle has with its neighbors. All particles with less connections than this threshold are considered to be liquid-like. We should bear in mind that, in a small nucleus, most particles are at the surface. These should be recognized as solid-like. We found this is achieved if we choose threshold value between 6 and 8. The present analysis provides us with an unambiguous local criterion to identify solid-like particles. Finally, we need a criterion to identify which solid particles belong to a single cluster. For this purpose, we used a simple distance criterion: if two solid-like particles are closer than a certain threshold distance, then they belong to the same cluster. The values that we chose for this were between 1.5σ and 2σ, where σ is the hard-core diameter. We note that, whereas the absolute number of particles in the cluster depends somewhat on the choice of the threshold values, the height of the computed free-energy barriers is fairly insensitive to the precise criterion that is used.

Using this local bond-order analysis we can sample the equilibrium distribution function for the probability $P(n)$ in a Monte Carlo simulation. In all cases we performed Monte Carlo simulations in the isobaric-isothermal (NPT) ensemble. In this ensemble the average of a microscopic quantity A is given by

$$\langle A \rangle_{NPT} = \frac{\int dV \int d\mathbf{r}^N A(\mathbf{r}^N) \exp[-\beta(U(\mathbf{r}^N) + PV)]}{\int dV \int d\mathbf{r}^N \exp[-\beta(U(\mathbf{r}^N) + PV)]}, \tag{7}$$

where $U(\mathbf{r}^N)$ is the potential energy of the system with particle positions $\mathbf{r}^N$. $\beta = 1/k_B T$ is the reciprocal of the thermal energy, N the number of particles and P the applied pressure. In a Metropolis Monte Carlo simulation the above ensemble average is approximated by

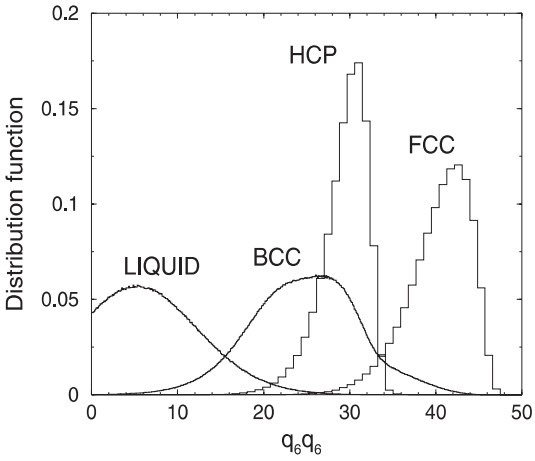

Fig. 5. Distribution functions of the dot product $\mathbf{q}_6(i) \cdot \mathbf{q}_6(j)$ from Monte Carlo simulations in a hard-sphere system

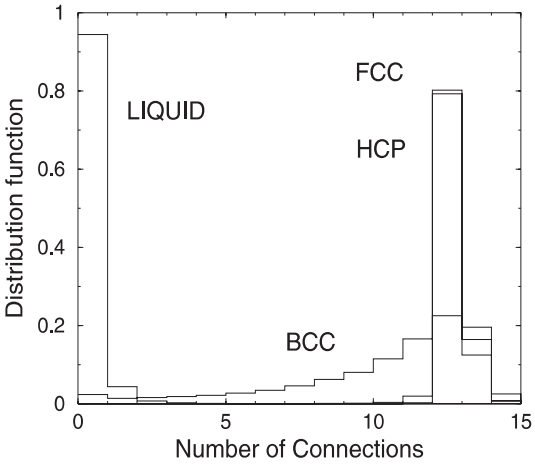

Fig. 6. Distribution functions of the number of connections per particle from Monte Carlo simulations in a hard-sphere system

$$\langle A \rangle_{NPT} \approx \frac{1}{M} \sum_{i=1}^{M} A(\mathbf{r}_i{}^N), \tag{8}$$

where M is the total number of measurements and $A(\mathbf{r}_i{}^N)$ the value of our property A associated with configuration $\mathbf{r}_i{}^N$. In the case of crystal nucleation we need to calculate the average number of clusters of size n and Eq. (8) becomes

$$\langle N_n \rangle_{NPT} \approx \frac{1}{M} \sum_{i=1}^{M} N_n(\mathbf{r}_i{}^N).$$

As an example we show the results from Monte Carlo simulations in a system of hard-spheres. In the simulations we used $N = 3375$ particles and applied a pressure $\beta P\sigma^3 = 16$. At this pressure, the liquid phase is meta stable with respect to the solid, but does not crystallize spontaneously as the Gibbs free energy barrier between the two states is too high. The temperature T does not play a role in that system. After equilibrating the system, one could in principle measure the cluster size distribution after every Monte Carlo move, however this would be computationally expensive and statistics would still be poor, as the measurements are strongly correlated. Instead we measure the cluster size distribution after one trajectory, which consists of 20 moves per particle plus about 10 volume moves. The total length of the simulation was 100000 trajectories. In this simulation we could measure the probability distribution $P(n)$ up to cluster sizes of $n = 15$ particles. The corresponding Gibbs free energy for the formation of such a cluster is shown in the inset of Fig. 8. The formation of larger cluster was so rare that the statistical accuracy was too poor.

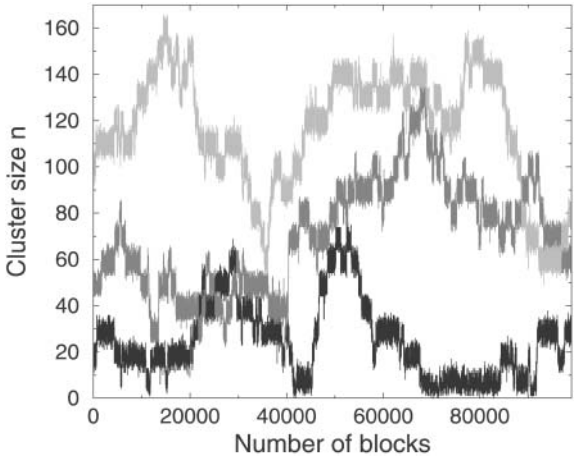

Fig. 7. Examples of the cluster size sampled during one simulation. The different configurations started with clusters of sizes $n = 20$, 50 and 110. Due to the parallel tempering technique, swapping between different windows is possible and the configurations could sample almost all possible cluster sizes

In order to sample larger cluster sizes we needed to apply the umbrella sampling technique of Torrie and Valleau [14]. The method is based on the idea that the ensemble average can be rewritten as follows

$$\langle A\rangle_{NPT} = \frac{\langle A/W(\mathbf{r}^N)\rangle_W}{\langle W(\mathbf{r}^N)^{-1}\rangle_W}, \tag{9}$$

where we have introduced an, as yet unspecified, weighting function $W(\mathbf{r}^N) = \exp[-\beta\omega(\mathbf{r}^N)]$, where $\omega(\mathbf{r}^N)$ is the biasing potential. The subscript $\langle ...\rangle_W$ indicates

an ensemble average according to the biased distribution function $\exp[-\beta(U(\mathbf{r}^N) + PV)]W(\mathbf{r}^N)$. By specifying the weighting function W we can force the system to sample in the relevant regions of phase space. In the case of crystal nucleation we can calculate the ensemble average according to the weighted ensemble, Eq. (9), as follows

$$\langle N_n \rangle_{NPT} \approx \frac{\sum_i^M [N_n(\mathbf{r}_i{}^N)/W(\mathbf{r}_i{}^N)]}{\sum_i^M [W(\mathbf{r}_i{}^N)^{-1}]},$$

where the sum goes over all measurements M. We now need to consider the choice of the weighting function. As the formation of large nuclei is rare, the probability to have two large clusters simultaneously in the system, is vanishingly small. As a consequence, we can choose a bias potential that just controls the size of the largest cluster in the system. Somewhat arbitrarily, we chose the bias potential to be a harmonic function of the size of the largest cluster:

$$\omega[n(\mathbf{r}^N)] = \frac{1}{2} k_n [n(\mathbf{r}^N) - n_0]^2. \tag{10}$$

The constant k_n determines the range of cluster-sizes sampled in one simulation. The parameter n_0 determines the center of the "window". In principle, it should be possible to design a biasing function that makes it possible to sample all cluster sizes in a single simulation. However, such a "smart" simulation would take much longer to equilibrate [15]. This is why we split the simulation into a number of smaller simulations that are restricted to narrow, but overlapping windows of different cluster sizes. The implementation of the biasing potential in the Monte Carlo simulation is straightforward. As the computation of cluster sizes is relatively time-consuming, we do not compute the size of the largest cluster after every Monte Carlo move. Rather, we carry out a fixed number of Monte Carlo moves per particle without bias. We then calculate the final cluster size and accept or reject the whole sequence of trial moves on basis of the change in the biasing potential: $\exp[-\beta \Delta\omega]$, where $\Delta\omega$ is the difference in the biasing potential after and before the trajectory. To facilitate the (very slow) stacking rearrangements of the clusters, we implemented the parallel tempering scheme of Geyer and Thompson [16]. The idea is to run all the simulations in the different windows in parallel and allow them to exchange clusters between adjacent windows. The actual change between windows i, j is accepted according to $\exp[-\beta(w_n - w_o)]$, where $w_o = k_i/2(n_i - n_{0,i})^2 + k_j/2(n_j - n_{0,j})^2$ is the energy of the biasing potential before and $w_n = k_i/2(n_j - n_{0,i})^2 + k_j/2(n_i - n_{0,j})^2$ after the change. In practise, what is exchanged between processors, are the minima of the bias potential rather than configurations. This requires virtually no communication between different computer nodes. In Fig. 7 we show an example of the cluster sizes sampled in the course of a simulation of hard spheres.

In the inset of Fig. 8 we show the results for the Gibbs free energy of a nucleus obtained from the simulations in each window (unbiased+biased runs). The Gibbs free energies in the different windows are determined up to a constant $\Delta G_i(n)/k_B T + b_i$, where the subscript i indicates the number of the window. In order to determine the

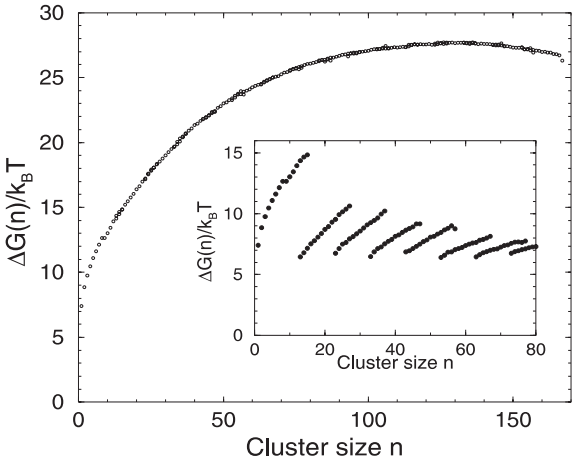

Fig. 8. Gibbs free energy for the formation of a cluster of n hard-spheres at $\beta P\sigma^3 = 16$, after fitting the results for the free energy in the different windows to one polynomial. The *inset* shows the sequence (unbiased + biased) of measured Gibbs free energies $\Delta G_i(n)/k_BT + b_i$ before the fit

constants b_i we fitted all the free energy estimates in the different windows to one polynomial in n. This can be done by a linear least-square fit, where we minimize

$$\chi = \sum_{n=1}^{n_{max}} \left\{ \sum_{i=1}^{n_w} w_i(n)[\Delta G_i(n) - \sum_{k=1}^{k_{max}} a_k n^k - b_i]^2 \right\}.$$

Here $w_i(n) = 1/\sigma^2_{\Delta G_i(n)}$ is the statistical weight determined by the variance $\sigma^2_{\Delta G_i(n)}$ of the free energy measurement and n_w the total number of windows used in the simulation. The maximum order of the polynomial used was $k_{max} = 10$. Note that by using a high-order polynomial, we do not assume a functional form of the nucleation barrier (the barrier might or might not be correctly described by CNT). From the unbiased simulation we get the absolute Gibbs free energy for the formation of a cluster of size n with respect to the liquid state. Therefore the constant b_1 is known. In Fig. 8 we show the final result for the calculation of a nucleation barrier for hard-spheres at pressure $\beta P\sigma^3 = 16$.

2.2 Kinetic Prefactor

In atomistic simulations, the kinetic prefactor is usually calculated using the Bennett-Chandler scheme [17]. In the case where the barrier crossing is relatively diffusive, it is attractive to use a modification proposed by Ruiz-Montero et al. [18]. The principle of both methods is to generate a large number of independent configurations at the top of the barrier. These configurations are then used as the starting point for an unbiased trajectory in which one determines if the nucleus grows and the system

crystallizes, or if it shrinks. From the number of nuclei that grow and shrink one can extract the kinetic factor. However, in order to get a reasonable estimate one has to simulate a rather large number of trajectories, on the order of one hundred. In the present work, we consider barrier crossing phenomena that are, effectively, purely diffusive. In that case, we can compute the kinetic prefactor directly using the expression: $\Gamma = Z\rho_l f_{n_c}^+$. After a barrier calculation at number density ρ_l the only unknown quantity is $f_{n_c}^+$. In order to compute $f_{n_c}^+$, we assume that the critical cluster grows and shrinks via the diffusive attachment of single particles. We can then define an effective diffusion constant for the change in critical cluster size:

$$D_{n_c}^{att} = \frac{1}{2}\frac{\langle \Delta n_c^2(t)\rangle}{t}. \tag{11}$$

Here $\Delta n_{n_c}^2(t) = [n_c(t) - n_c(t=0)]^2$ is the mean square change in the number of particles in the critical cluster. As the slope of this change is related to the corresponding attachment rates via $\langle \Delta n_c^2(t)\rangle/t = (f_{n_c}^+ + f_{n_c}^-)/2$, and as we know that, at the top of the barrier, the forward and backward rates are equal ($f_{n_c}^+ = f_{n_c}^-$), we get

$$f_{n_c}^+ = \frac{1}{2}\frac{\langle \Delta n_c^2(t)\rangle}{t}. \tag{12}$$

This is a general expression for the calculation of the kinetic factor for diffusive barrier crossing. Using a Molecular Dynamics simulation one only needs to measure the change in size of the critical cluster as a function of time. The only restriction is that, during the measurement, the critical nucleus needs to fluctuate around its critical value.

To apply this method for the calculation of the attachment rate in a colloidal suspension, we need to have a simulation technique that generates trajectories following Brownian dynamics and hydrodynamic interaction also needs to be considered. Trajectories following Brownian dynamics could be generated using a kinetic Monte Carlo scheme proposed by Hinson and Cichocki [19]. These authors show that, in the limit of very small maximum particle displacement, $\Delta x_{max} \to 0$, the trajectories generated by the kinetic Monte Carlo simulation are stochastically equivalent to the process described by the Smoluchowski equation. The limit $\Delta x_{max} \to 0$ means that simulation time would become infinitely long. However, Hinson and Cichocki also propose an extrapolation procedure with which this limit can be approached systematically by repeating simulations with a smaller maximum displacement. In experiments nucleation rates are usually presented in dimensionless form $I^* = Ik\sigma^5/D_0$, where σ is the diameter of a monomer and D_0 the free diffusion coefficient. Therefore we only need to compute the ratio $f_{n_c}^+/D_0$. From the previous calculation of the nucleation barrier in a hard-sphere system we could determine the critical cluster size and had generated independent configurations in which such a cluster was stabilized. We used these configurations, to perform an unbiased kinetic NVE Monte Carlo simulation, measuring the size of the critical cluster as a function of Monte Carlo blocks. Here one block is 100 trial moves per particle. In the inset of Fig. 9 we show such a measurement at $\phi = 0.5277 (P = 16)$. From these data we then extracted the

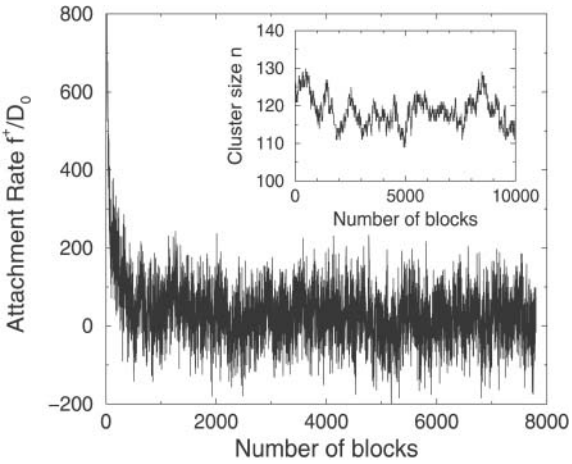

Fig. 9. Reduced attachment rate $f_{n_c}^{+}/D_0$ of particles to the critical cluster at volume fraction $\phi = 0.5277$. Here one block is 100 moves per particle in an NVE Monte Carlo simulation. The *inset* shows the development of the size n of the critical cluster during one trajectory

attachment rate using Eq. (12) which is shown in the same figure. Surprisingly, we see that the attachment rate has a different short time and long time behavior. This implies that, at short times, the diffusion in cluster size is not a Markov process. As the diffusion of the critical cluster over the nucleation barrier is on the time scale of the long time behavior of the attachment rate, this is the value we have to use. To test the dependence of our results on the maximum particle displacement we performed simulations for two different values $\Delta x_{max} = 0.12\sigma$ and 0.012σ. The corresponding values for the free diffusion coefficients are $D_0 = \langle \Delta x_{max}^2 \rangle / 6$. The ratio of the results for $f_{n_c}^{+}/D_0$ in both simulations is equal to 4.79. Computing the long time self diffusion coefficient $D_S^L/D_0 = \langle (r(0) - r(t))^2 \rangle / 6tD_0$ we get a ratio in both simulations of 5.07. Therefore the difference in the results for the attachment rate is mainly due to diffusion. In our simulations we did not follow the extrapolation procedure for $\Delta x_{max} \to 0$ described in [19], as for $\Delta x_{max} = 0.012\sigma$ we are already in a limit where the attachment rate has effectively reached its limiting value. We justify this by testing our approach on the calculation of the long time self diffusion coefficient, which will be discussed later.

To correct for the effect of hydrodynamic interactions that are known to be important at high volume fractions, we used an approach proposed by Medina-Noyola [20]. To this end, we replace the free diffusion coefficient D_0 by the short-time self diffusion coefficient D_S^S. We therefore have to multiply our result by a factor $\alpha = D_S^S/D_0$. In the case of hard spheres, several (rather similar) functional forms for this factor have been proposed in the literature [21, 22, 23, 24]. Here we used the phenomenological expression $(1-\phi/0.64)^{1.17}$ [25] at high volume fraction ϕ. As a test of our approach we computed the long-time self diffusion coefficient of a dense colloidal suspension of hard spheres. Our results, $D_S^L/D_0 = 2.9 \times 10^{-3}, 2.5 \times 10^{-3}, 2.1 \times 10^{-3},$

calculated at volume fractions $\phi = 0.5207, 0.5277, 0.5342$, are within statistical error of experimental data, see e.g. [26, 39].

For the calculation of the kinetic factor we usually performed about 5 trajectories. The length of the trajectory depends on whether the cluster size fluctuates around the critical size or not; if not the simulation is stopped. From these simulations we calculated the attachment rate. The error estimates vary between a factor of one for the larger critical cluster sizes and a factor of two to three for the smaller cluster sizes. In the regime of smaller critical cluster sizes, the fluctuations in cluster size are almost on the order of the critical cluster size and it becomes therefore more difficult to get a good estimate.

3 Hard-Sphere Colloids

A collection of hard, identical spheres is the simplest possible model system that undergoes a first order phase transition. For low packing fractions the particles are in a liquid state, but when the packing fractions exceeds a value of 49.4% a ordered solid state becomes more stable. This was first shown in computer simulations by Hoover and Ree [27] in 1968. The experimental realization of a colloidal suspension that closely mimics the phase behavior of hard spheres followed about 20 years later and was a milestone in soft matter physics [28, 29]. More recently the phase transition kinetics of hard sphere colloids has been studied extensively in experiments [5, 30, 31]. However as mentioned in the introduction the interpretation of the data with CNT was rather indirect.

Using the simulation techniques described before, we can compute the rate of crystal nucleation for hard sphere colloids by a direct calculation of the nucleation barrier and the kinetic prefactor [8, 32]. We first performed Monte Carlo simulations in the isobaric-isothermal ensemble NPT to compute the crystal nucleation barrier at three different pressures $\beta P\sigma^3 = 15, 16, 17$. The corresponding bulk volume fractions of the liquid are $\phi = 0.5207, 0.5277, 0.5343$. The resulting nucleation barriers are shown in Fig. 10. As expected, with increasing volume fraction the crystal nucleation barrier decreases. Our simulation results for the crystal nucleation barrier can be compared directly to the predictions from CNT for the nucleation barrier Eq. (1). For the hard-sphere system the chemical potential difference can be calculated accurately using phenomenological equations of state for the liquid and the solid [33], see Appendix B. As the solid-liquid interfacial free energy γ of a small crystal nucleus in a supersaturated liquid is not known a priory we use its corresponding value for a flat interface at coexistence. This value has been calculated in a recent simulation [7] for three different crystal planes. Here we use $\gamma_{av} = 0.61 k_B T/\sigma^2$ which is the average of the three crystal planes. The results for the barrier height based on CNT in order of increasing density are $\Delta G^*/k_B T = 27, 15.7, 10.2$. These values are about 30–50% lower than our numerical estimate. This discrepancy might be due to the fact that for a small nucleus in a supersaturated liquid the interfacial free energy is different from that of a flat interface at coexistence. For this reason we also used γ

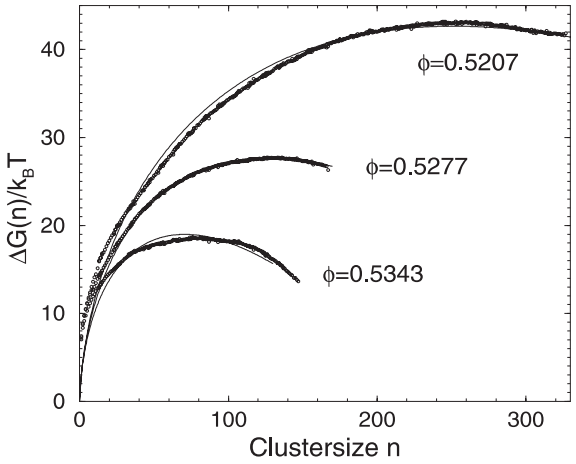

Fig. 10. Calculated free energy barrier for homogeneous crystal nucleation of hard-sphere colloids. The results are shown for three values of the volume fraction. The drawn curves are fits to the CNT-expression Eq. (1). For the identification of solid like particles we used the techniques described before. The cutoff for the local environment was set to $r_q = 1.4\sigma$, the threshold for the dot product $q_6 q_6 = 20$ and the threshold for the number of connections was set to 6. If two solidlike particles are less than 2σ apart, where σ is the diameter of a particle, then they are counted as belonging to the same cluster. The total simulation was split up into a number of smaller simulations that were restricted to a sequence of narrow, but overlapping, windows of n values. The minimum of the bias potential was placed in steps of tens, i.e $n_0 = 10, 20, 30, \ldots$ In addition we applied the parallel tempering scheme of Geyer and Thompson [16] to exchange clusters between adjacent windows. All simulations were carried out at constant pressure and with the total number of particles (solid plus liquid) fixed. For every window, the simulations took at least 1×10^6 MC moves per particle, excluding equilibration. To eliminate noticeable finite-size effects, we simulated systems containing 3375 hard spheres. We also used a combined Verlet and Cell list to speed up the simulations

as a fit parameter to our results. Using $R = (3n/(4\pi\rho_S)^{1/3}$ we fitted Eq. (1) to our data. The result can be seen as the solid line in Fig. 10. As can be seen, the functional form of the nucleation barrier seems to be described well by CNT, but the values for the fit parameter $\gamma_{eff}(P = 15) = 0.71 k_B T/\sigma^2$, $\gamma_{eff}(P = 16) = 0.737 k_B T/\sigma^2$ and $\gamma_{eff}(P = 17) = 0.751 k_B T/\sigma^2$ are higher than the coexistence value and they increase with volume fraction. If we assume that this dependence is linear, than our simulation results extrapolate to a value of $\gamma_{eff}(P = 11.7) = 0.64 k_B T/\sigma^2$ at coexistence – a value that is very close to γ_{av}. For a discussion of the dependence of the surface free-energy density on supersaturation, see Ref. [34]. In Appendix C we discuss an alternative, thermodynamic route to compute the surface free-energy density for the critical nucleus.

Our results for the surface free-energy density can also be compared to the values extracted from experiments. Palberg [4] fitted the data from Harland and van Megen [5] and obtained $\gamma = 0.5 k_B T/\sigma^2$ and for the data from Heymann et al. [6]

he found $\gamma = 0.54 k_B T/\sigma^2$. Note that these values are significantly lower than the numerical estimates.

In the crystal-nucleation experiments, the colloids had a size polydispersity of about 5%. We therefore repeated our simulations for a suspension with 5% polydispersity. We find that both systems have the same nucleation barrier at the same $\Delta\mu$ [35]. For a caculation of $\Delta\mu$ see Appendix C. Therefore polydispersity alone cannot account for the difference between the barrier heights derived from experiment and simulation.

Table 1. Summary of the simulation results for the calculation of the nucleation rate for monodisperse hard sphere colloids. Here ϕ is the volume fraction of the liquid phase. ΔG^* is the measured free energy to form a cluster of critical size n_c. f_c^+/D_0 is the attachment rate of particles to the critical cluster divided by the free diffusion coefficient. $I^* = I\sigma^5/D_0$ is the reduced nucleation rate, and λ is the estimated typical jump distance from the calculation of the attachment rate. $\Delta\mu$ is the difference in chemical potential between the two phases

ϕ	ΔG^*	n_c	f_c^+/D_0	$\log_{10}[I^*]$	λ	$\Delta\mu$
0.5207	43.0	260	189	−19.3	0.31	0.34
0.5277	27.8	130	43	−13.5	0.46	0.44
0.5342	18.5	75	66	−9.14	0.27	0.54

Subsequently, we performed kinetic Monte Carlo simulations to compute the kinetic prefactor and, thereby, the absolute crystal nucleation rate. The results of our calculations of the attachment rate for the monodisperse hard-sphere system are summarized in Table 1. As experimentally determined values for the kinetic factor often differ by orders of magnitude from those predicted by CNT, it is also important to compare our computed kinetic prefactor with the one predicted by CNT. We find that the Zeldovich factor that follows from our numerical calculations is almost identical to the CNT prediction. This is not surprising, as CNT provides a good fit to the numerical data for the shape of the barrier. The remaining quantity to compare is the reduced attachment rate f_c^+/D_0. If we assume that in Eq. (5), $D_S = D_S^L$, where D_S^L is the long-time self-diffusion constant, and if we treat λ as a fit parameter to reproduce our calculated attachment rates, then we get values for λ in the range $0.27 - 0.46\sigma$ (see Table 1). This jump distance – in the case of colloids it might be better to call it a diffusion distance – is comparable to the inter-particle spacing in a dense suspension, which seems reasonable. In contrast, experimental estimates for λ tend to be rather large: $\lambda = 2.8 - 17\sigma$ [4]. The identification $D_S = D_S^L$ is justified by the fact that the time λ^2/D_S^L corresponds to long-time diffusion.

Using our simulation results we can compute steady-state nucleation rates that can be compared directly (i.e. without any adjustable parameters) to experiment. In Fig. 11 we show our numerical predictions for the nucleation rate of a monodisperse suspension and a suspension with 5% polydispersity. These results can be compared directly to the experiments on suspensions with the same polydispersity. Note that

the polydispersity in Ref. [31] is about 2.5%. As can be seen from the figure, the simulations predict a much stronger dependence of the nucleation rates on density than is observed in the experiments. This discrepancy between the simulations and experiment is unexpected and significant because hard-sphere colloids are among the best studied experimental realizations of a simple liquid. We know the structural and thermodynamic properties of hard-sphere suspensions quite accurately and, more significantly, these properties tend to be well reproduced by the ideal, hard-sphere model. Hence, large discrepancies between experiment and simulation cannot be easily dismissed as being due to uncertainties in the parameters that characterize the colloidal suspension. Rather, we must envision the possibility that either our theoretical description of crystallization is inadequate or that what is measured is not really the steady-state, homogeneous nucleation rate. In fact, the latter suggestion is not altogether unreasonable, as light-scattering cannot be used to see the very early stages of crystal nucleation. Secondly, the experiments are extremely sensitive to any residual ordering in the solution that may have survived the preparation of the experimental system. Thirdly, at high supersaturations, the concentration of crystal nuclei rapidly becomes sufficiently large that the interaction between different crystal nuclei may no longer be ignored [36]. In that case, the steady-state nucleation expressions that we employ are no longer applicable. We note that Dixit and Zukoski [37] developed a purely kinetic model to predict nucleation rates which yields good quantitative agreement with the experimental data. Volkov et al. [38] recently reported molecular dynamic simulations of hard-sphere crystallization at large supersaturations. In this regime, the simulations are in good agreement with experiment. In fact, in the simulations of Volkov et al., the simulation data could be analyzed in the same way as the experiments (namely, by studying the time evolution of the first Bragg peak of the static structure).

One unique feature of the simulations is that they allows us to study, in detail, the structure of small crystal nuclei. This is interesting as already in 1897 Ostwald [40] pointed out the role of meta-stable phases in crystal nucleation when he formulated his famous step rule. This rule states that the phase that nucleates does not need to be the one that is thermodaynamically most stable. In the recent years there have been several attempts to provide a microscopic explanation [41, 42, 43, 44] for Ostwald's observation. Alexander and McTague [41] argue, on the basis of Landau theory, that if the differences in the liquid and solid densities were not too great, then the phase that would be nucleated from the liquid would be bcc regardless of the structure of the stable (lowest free energy) phase. Leyvraz and Klein [42, 43], showed that for deeply quenched systems with long-range interactions, the critical droplet can have a bcc symmetry, though not a bcc crystalline structure. Simulations by ten Wolde et al. [13] showed that the situation can even be more subtle, at least for a Lennard-Jones system: The core of a stable Lennard-Jones cluster formed a stable fcc structure while the surface of the nucleus showed indications of a bcc structure. Thermodynamically the formation of metastable phases might be explained by differences in interfacial free energies. The formation of a bcc-liquid interface might cost less energy than that of a fcc-liquid interface. In the case of hard-spheres it is known that the fcc phase is the stable structure, but the free energy difference between the fcc

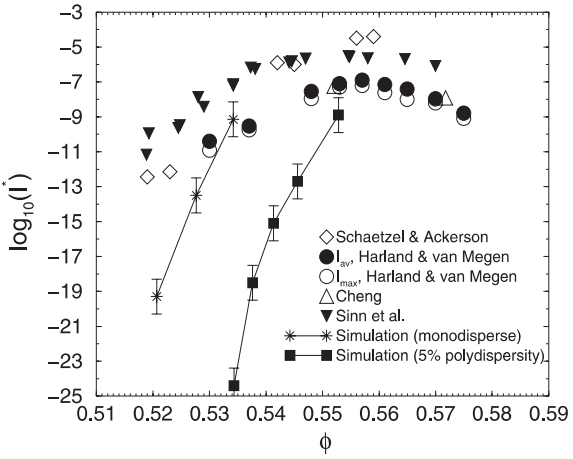

Fig. 11. Reduced nucleation rates ($I^* = I\sigma^5/D_0$) as a function of the volume fraction of the meta-stable liquid. The simulation data for monodisperse colloids are indicated by the $*$-the drawn curve joining the simulation points is meant as a guide to the eye. In the same figure we show the experimental results of Ref. [30] ($\diamond$), Ref. [5] ($\circ$ and $\bullet$), Ref. [39] ($\triangle$) and Ref. [31] ($\blacktriangledown$). We also performed simulations on model systems that have the same polydispersity (5%) as the experimental systems. These simulation results are denoted by the *filled squares*

and the hcp structure is very small ($< 10^{-3}k_BT$) [45, 46]. This means that thermal fluctuations of the order of k_BT could transform a cluster of 1000 particles from fcc to hcp or just cause stacking faults. Note that the fcc and the hcp structure differ only in the stacking of close-packed hexagonal crystal planes. For the fcc structure the stacking is ABC, whereas for the hcp structure the stacking is AB. If the interfacial free energies of a crystal fcc-liquid, hcp-liquid or a rhcp-liquid interface are different, than this could also completely change this picture. Here rhcp refers to a random stacking of the close-packed hexagonal crystal planes. The question if small crystal nuclei are more fcc or hcp like is not clear. Experiments by Pusey et al. [47] and Elliot et al. [48] indicate that the fcc structure is favored. However, microgravity experiments by Zhu et al. [49] showed that, initially, small crystal nuclei have a rhcp structure. A snapshot of the cross-section of a simulated critical nucleus is shown in Fig. 3. From a direct inspection of the nuclei we found that the structure of the nuclei is rhcp. In order to be able to carry out the stacking analysis the nuclei needed to have a size of at least 150 particles, otherwise the number of layers is too small to distinguish in a meaningful way between different stackings. To study the structure of even smaller nuclei we performed a local bond-order analysis. We set up a set of vectors, $\mathbf{v}_{\mathrm{rhcp}}$, $\mathbf{v}_{\mathrm{bcc}}$, $\mathbf{v}_{\mathrm{ico}}\mathbf{v}_{\mathrm{liq}}$, which contain the characteristic distribution functions of the bond-order parameters, q_4, q_6, $\hat{w}_4$, $\hat{w}_6$, of the relevant lattice structures, i.e. rhcp, bcc, ico and the liquid structure, see also Fig 4. In our simulation the distribution functions for the cluster were also calculated. The corresponding vector is $\mathbf{v}_{cl}$. The vector $\mathbf{v}_{cl}$ was then decomposed by minimizing the difference Δ:

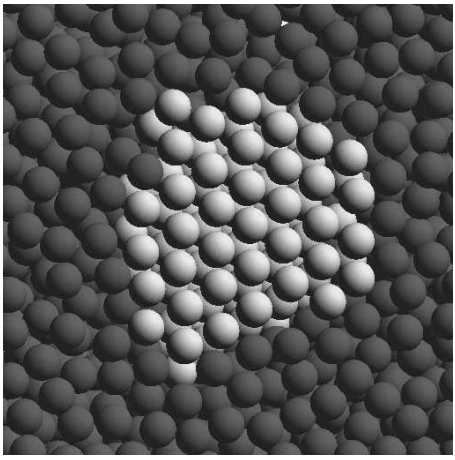

Fig. 12. Snapshot of a cross-section of a critical nucleus of a hard-sphere crystal at a liquid volume fraction $\phi = 0.5207$. The figure shows a three-layer thick slice through the center of the crystallite. Solid-like particles are shown in *yellow* and liquid-like particles in *blue*. The layers shown in the figure are close-packed hexagonal crystal planes. The stacking shown in this figure happens to be fcc-like, i.e. ABC-stacking — however, analysis of many such snapshots showed that fcc and hcp stackings were equally likely

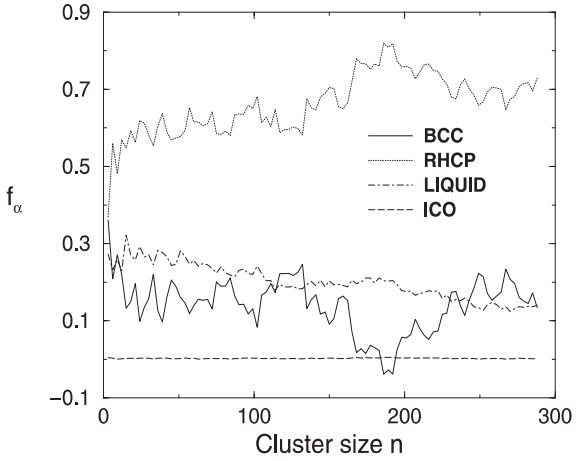

Fig. 13. Structure analysis of (pre) critical crystal nuclei. The figure shows the relative weight of the structural signatures for rhcp, bcc, icosahedral and liquidlike ordering in hard-sphere crystal nuclei of size n

$$\Delta = \{\mathbf{v}_{\rm cl} - (f_{\rm rhcp}\mathbf{v}_{\rm rhcp} + f_{\rm bcc}\mathbf{v}_{\rm bcc} + f_{\rm ico}\mathbf{v}_{\rm ico} + f_{\rm liq}\mathbf{v}_{\rm liq})\}^2.$$

The coefficients $f_{\rm rhcp}$, $f_{\rm bcc}$, $f_{\rm ico}$, $f_{\rm liq}$ are a measure for the type of order in the system. If we apply this analysis to an equilibrated bcc crystal, we would get $f_{\rm bcc} = 1$ and zero for the others. In Fig. 13 we show the results for $f_{\rm rhcp}$, $f_{\rm bcc}$, $f_{\rm ico}$ and $f_{\rm liq}$ as a function of the size of the largest cluster in the system at $P = 15$. The results for $P = 16$ are qualitatively similar. The figure shows that *bcc* and icosahedral structures play no role in the nucleation process. Small clusters are fairly disordered and have an appreciable liquidlike signature. The figure shows that the rhcp signature is dominant for all cluster sizes. This was also found in more recent simulations by O'Malley and Snook [50]. Surprisingly, these simulations also found evidence for multiply twinned nuclei with a decahedral morphology.

4 Effect of Polydispersity

In practice, the colloidal particles used in the experiments have a distribution of particle radii (referred to as polydispersity) that is rarely less than 2–3% of the average radius. In order to compare our measured nucleation rates with experiments we already needed to study the effect of a small polydispersity (up to 5%) in the preceding section. For polydispersities up to 5%, we found no effect of polydispersity on the height of the nucleation barrier. However, experiments on hard-sphere colloids indicate that crystallization is suppressed if the polydispersity exceeds 12% [51]. This suppression of crystallization is usually attributed to the fact that in poly-disperse suspensions the freezing point is shifted to higher densities where the system tend to become glassy. In a glass, the kinetic pre-factor Γ is expected to be very small, but the nucleation barrier itself should continue to decrease with increasing supersaturation. To test this, we studied the behavior of the crystal-nucleation barrier for polydispersities up to 10% [35].

We performed Monte Carlo in the constant-pressure, semi-grand-canonical ensemble of the type described in [52]. In such a simulation it is not possible to impose the size distribution of the particles directly, but the size distribution can be controlled through variation of the imposed activity-ratio distribution function. In our simulations we imposed a Gaussian activity distribution and a typical particle size distribution function is shown in Fig. 14.

In these simulations, we computed the crystal-nucleation barrier and the structure of the critical nucleus, as a function of both polydispersity and supersaturation. As in the case of monodisperse suspensions [32], we find that all critical nuclei have a randomly-stacked close-packed structure. During crystallization, size-fractionation occurs [52, 53]: the particles that make up the critical nucleus are on average larger, and the polydispersity is lower, than those in the metastable liquid, as is shown in Figs. 14 and 15.

We find that ΔG^*, the height of the nucleation barrier, at fixed $|\Delta\mu|$, does not depend on the polydispersity for polydispersities $\leq 5\%$ (see Fig. 16). However, as

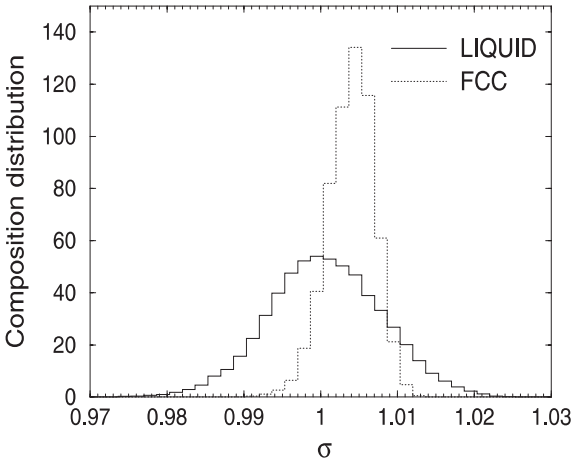

Fig. 14. Typical particle size distribution functions from Monte Carlo simulations in the constant-pressure, semi-grand-canonical ensemble in a bulk liquid and solid. At that pressure the volume fraction of the liquid is $\phi = 0.5775$ at a polydispersity of 10%. The volume fraction of the solid in coexistence with the liquid is $\phi = 0.6196$ and has a polydispersity of 4.2%

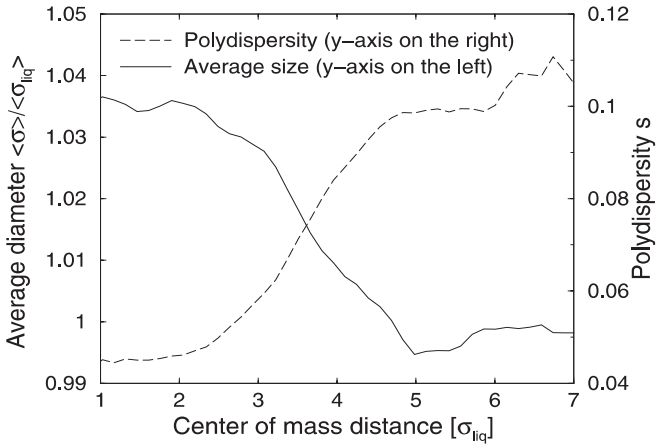

Fig. 15. Average size and polydispersity of particles as a function of the center of mass of the cluster in units of the average diameter of particles in the bulk liquid. Here the average size is scaled to the diameter of the particles in the liquid $\langle\sigma\rangle / \langle\sigma_{liq}\rangle$. The polydispersity is defined as $s^2 = \langle\sigma^2\rangle / \langle\sigma\rangle - 1$. Fractionation in particle size and polydispersity occurs. The particles in the crystal nucleus are in average larger as the particles in the bulk liquid, while they are less polydisperse

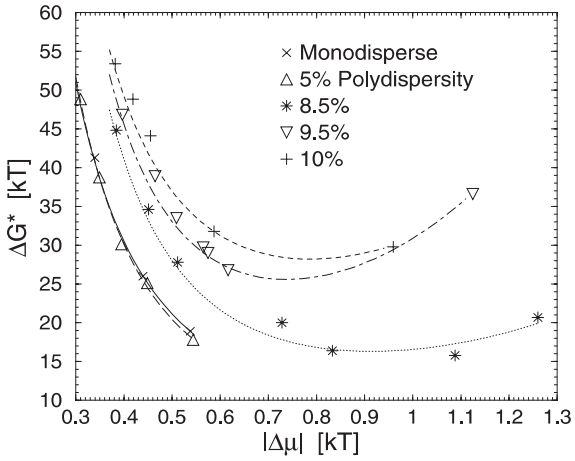

Fig. 16. Computed dependence of the free-energy barrier ΔG^* for crystal nucleation of polydisperse suspensions of hard, colloidal spheres. The free energy is expressed in terms of $k_B T$, where k_B is Boltzmann's constant and T is the absolute temperature. $|\Delta\mu|$ (also in units of $k_B T$) is the absolute difference between the chemical potential of the liquid and the solid. It is a measure for the degree of supersaturation. The curves are fits that have been drawn as a guide to the eye. To facilitate comparison with experiment, we have collected in Table 2, the relation between $|\Delta\mu|$ and the volume fraction ϕ of the liquid, for the different systems that we studied

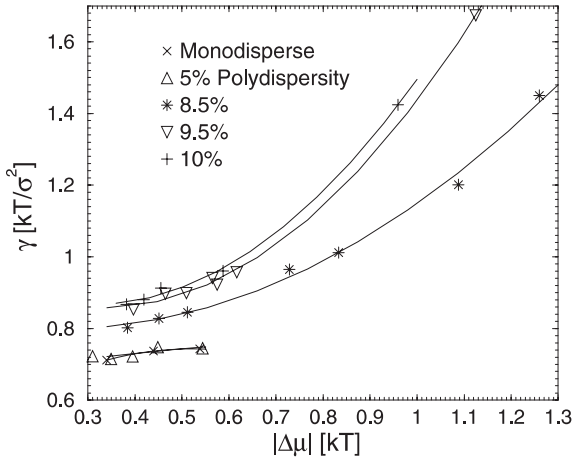

Fig. 17. Dependence of the interfacial free energy γ of crystal nuclei in polydisperse suspensions of hard, colloidal spheres. The interfacial free energy is expressed in terms of $k_B T/\sigma^2$, where σ is the average hard-sphere diameter. The curves are fits that have been drawn as a guide to the eye

the polydispersity is increased beyond 5%, ΔG^* increases rapidly. This implies that the probability to form a critical nucleus, is suppressed in polydisperse suspensions.

It follows from Eq. (2) (or actually from its polydisperse equivalent, see Appendix C), that at constant $|\Delta\mu|$, the variation of ΔG^* with polydispersity is due to an increase of the interfacial free energy γ, see Fig. 17.

Table 2. Supersaturation and volume fraction of polydisperse colloids. $\Delta\mu$ is the supersaturation and ϕ is the volume fraction of the colloidal fluid. For a calculation of $\Delta\mu$ in polydisperse systems see Ref. [8]. The polydispersity ranges from 0% (left) to 10% (right). The polydispersities quoted in this table and in the figures, are those of the metastable liquid

0%		5%		8.5%		9.5%		10%	
$\Delta\mu$	ϕ	$\Delta\mu$	ϕ	$\Delta\mu$	ϕ	$\Delta\mu$	ϕ	$\Delta\mu$	ϕ
0.339	0.5207	0.310	0.5344	0.385	0.5614	0.397	0.5697	0.382	0.5717
0.439	0.5277	0.349	0.5377	0.451	0.5673	0.465	0.5746	0.419	0.5738
0.538	0.5342	0.395	0.5414	0.512	0.5726	0.509	0.5782	0.455	0.5775
		0.448	0.5456	0.728	0.5864	0.565	0.5808	0.587	0.5878
		0.544	0.5528	0.833	0.5948	0.575	0.5828	0.959	0.6239
				1.088	0.6145	0.616	0.5859		
				1.260	0.6212	1.125	0.6239		

The increase of γ with polydispersity runs counter to Turnbull's suggestion that the interfacial free energy should be proportional to ΔH, the latent heat of fusion [3]. For the systems that we studied, ΔH crosses zero at a polydispersity of 9% [54], where the liquid becomes denser than the coexisting solid [52]. Yet, γ clearly remains non-zero, see Fig. 18.

Surprisingly, the variation of ΔG^* with $|\Delta\mu|$ is non-monotonic. As $|\Delta\mu|$ is increased, the nucleation barrier goes through a minimum (Fig. 16). This non-monotonic behavior of ΔG^* is due to the increase of γ with $|\Delta\mu|$. To illustrate this, let us approximate the $|\Delta\mu|$-dependence of γ by $\gamma \approx \gamma_0(1 + a|\Delta\mu|)$. Ignoring the slight $|\Delta\mu|$-dependence of the solid density, it then follows from Eq. (2) that ΔG^* must go through a minimum when $|\Delta\mu| = 2/a$. The nucleation theorem [55, 56, 57] suggests that the minimum in ΔG^* is due to the inversion of the densities of the polydisperse fluid and the crystal nucleus. In CNT it is usually assumed that γ is constant. A linear variation of γ with $|\Delta\mu|$ has been observed in inorganic glasses [3], but there the constant a is negative and hence there is no minimum in ΔG^*. In other systems [58, 59], non-monotonic behavior of ΔG^* is induced by a hidden phase transition in the meta-stable phase.

The minimum value of ΔG^* increases rapidly with polydispersity. Using kinetic Monte Carlo simulations, we can estimate the value of the attachment rate [19]. We find that, over the range of supersaturations studied, the attachment rates vary by at most an order of magnitude (Table 3). This means that the variation in the rate of nucleation is dominated by the behavior of ΔG^*. We estimate that, for colloidal particles with a radius $\geq$ 500 nm, homogeneous nucleation will be effectively sup-

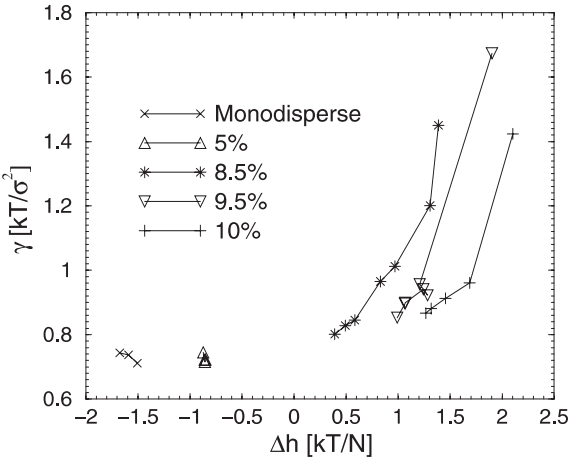

Fig. 18. Surface free energy γ as a function of the enthalpy difference Δh (per particle) between the liquid and the crystal phase shown for the different polydispersities

pressed (less than one nucleus per cm^3 per day) when the polydispersity exceeds 10%. This finding has important implications for the morphology of polycrystalline colloidal materials. Using a simplified version of the analysis proposed by Shi et al.

Table 3. Reduced attachment rate $f_{n_c}^+/D_0$ as a function of the volume fraction ϕ

8.5%		9.5%		10%	
$f_{n_c}^+/D_0$	ϕ	$f_{n_c}^+/D_0$	ϕ	$f_{n_c}^+/D_0$	ϕ
40	0.5614	12	0.5697	20	0.5717
75	0.5673	60	0.5746	55	0.5738
21	0.5726	15	0.5782	40	0.5775
30	0.5864	50	0.5808	10	0.5878
15	0.5948	10	0.5828	8	0.6239
35	0.6145	20	0.5859		
10	0.6212	5	0.6239		

[58] we can estimate the size of crystallites in a polycrystalline sample at the end of a crystallization experiment. We assume that I, the rate of steady-state nucleation, is given by Eq. (4), and that v_g, the rate at which the crystallite radius grows, is given by the Wilson-Frenkel law:

$$v_g = \frac{D_S}{\lambda}[1 - \exp(-|\Delta\mu|/k_BT)],$$

where λ is a typical atomic jump distance and D_S a self-diffusion constant. Note that both I and v_g are proportional to D_S. The total volume fraction occupied by crystallites as a function of time t is approximately given by the Avrami growth law

$$\phi \approx I\pi v_g t^4/3.$$

Crystallization stops when ϕ is of order 1. This happens after a time $t_{max} \sim (Iv_g^3)^{-1/4}$. The average crystallite radius at this time is equal to $R_c \approx v_g t_{max}$. Using the expression for t_{max} above, it follows that $R_c \sim (v_g/I)^{1/4}$. The crucial point to note is that the average crystallite size depends only on the ratio v_g/I. As the strongly density dependent diffusion constant D_S drops out of this ratio, its $|\Delta\mu|$-dependence is mainly determined by the variation of $\exp(\Delta G^*/k_BT)$, except for small supersaturations. We therefore expect that the typical crystallite size at the end of a nucleation experiment should scale as $R_c \sim \exp(\Delta G^*/4k_BT)$. This should be experimentally observable.

We could only compute ΔG^* if spontaneous nucleation did not occur in the course of a simulation. In practise, this implied that we could not study barriers lower than $15k_BT$. As a result, we could not test whether ΔG^* in systems with a low polydispersity (less than 8.5%) also has a minimum. If we assume that, also at lower polydispersities, we can extrapolate the increase of γ with $|\Delta\mu|$ to large supersaturations, then we predict that a minimum in ΔG^* should occur even in nearly monodisperse systems. Again, this should be experimentally observable, because we should expect to see the formation of larger crystallites if the solution can be compressed rapidly through the region where ΔG^* is small.

There are two ways to interpret the experimental finding that crystallization is not observed in suspensions with a polydispersity $> 12\%$: either crystals do not form, or they are too small to be observed. Our simulations support the first interpretation. Using Shi's approach, we can estimate the maximum number of crystallites per unit volume [58]. For a suspension of colloids with a 500-nm radius, we expect to see less than one crystallite per cubic centimeter, once $\Delta G^* > 32k_BT$. In other words, under those conditions the colloidal glass is truly amorphous.

Our predictions concerning the structure and free energy of colloidal crystal nuclei can be tested experimentally. Recently, the technique of confocal scanning laser microscopy has been applied by Gasser et al. [60] to study the structure and size of critical crystal nuclei in dense colloidal suspensions. This technique would be perfectly suited to test our predictions. Our prediction concerning the minimum in ΔG^* is even easier to verify. By visual inspection, one could verify whether the crystallites that nucleate in strongly supersaturated solutions are larger than those that form at lower supersaturations. Over a decade ago, Pusey and van Megen published beautiful images of the morphology of poly-crystalline hard-sphere colloids [29] (similar morphologies have recently been observed in a study of colloidal crystallization in micro-gravity – Z.D. Cheng, W.B. Russel and P.M. Chaikin, unpublished data). Pusey and van Megen observed an increase of the crystallite size at large supersaturations. However, they attributed this effect to heterogeneous nucleation. Hence, a direct test of our prediction is still lacking.

5
Weakly Charged Colloids

Experiments on colloidal crystallization consistently show that it is much easier to crystallize charged colloids than uncharged ("hard-sphere") colloids. Clearly, long-ranged repulsion has a large effect on the crystal-nucleation rate. This may even be true for colloidal suspensions of particles that are only weakly charged. Using simulations, it is possible to study in detail how repulsive inter-particle forces affect the crystal-nucleation process [61]. The aim of this section is to elucidate the factors that affect the rate of crystal nucleation in a system of weakly charged colloids.

In suspension, the charged colloids are surrounded by a cloud of counterions. This counterion double layer screens the pure Coulomb interaction between the colloids. If we use the linearized Poisson-Boltzmann equation to describe the charge distribution around a charged colloid with hard-core diameter σ, then we obtain the following expression for the pair interaction between two charged macro-ions:

$$\beta U(r) = \begin{cases} \infty & \text{for } r < \sigma \\ \beta\epsilon \frac{\exp(-\kappa(r/\sigma - 1))}{r/\sigma} & \text{for } r > \sigma. \end{cases} \tag{13}$$

$U(r)$ is usually referred to as the "hard-core Yukawa potential". Here κ is the inverse screening length in units of the hard-sphere diameter σ and $\beta\epsilon$ is the value of the Yukawa repulsion at contact. β is a measure for the inverse temperature ($\beta = 1/k_B T$), where k_B is the Boltzmann constant. In the linearized Poisson-Boltzmann theory, we have explicit expressions for both κ and ϵ in terms of the size and surface charge of the colloid, and of the concentration of counterions and added salt. However, the linearized Poisson-Boltzmann description provides only an approximation to the real colloid-colloid interaction. For instance, it is expected to break down at short distances and for low added salt concentrations. A way to treat the interaction between charged colloids at short distances was already proposed by Derjaguin, Landau, Verweij and Overbeek (DLVO) in the 1940s [62]. Since then, several modifications of the form of the pair potential between charged colloids have been proposed [63, 64] but, except at very short distances, most expression are very similar to the hard-core Yukawa model. The main difference between the theories is the values that they yield for κ and ϵ. In the original DLVO theory, these parameters depend only on the ionic strength of the solution and on the bare charge of the colloids. In the more recent theories, κ and ϵ may themselves depend on the concentration of charged colloids. In the present work, we simply assume that the interaction between charged colloids is adequately described by a hard-core Yukawa potential. However, we shall return later to the question whether this is allowed. A special case of the hard-core Yukawa model, is the hard-sphere model. The latter model applies in the limit of high salt concentrations $\kappa \to \infty$ and in the limit that the strength of the repulsion is much less than the thermal energy, i.e. $\beta\epsilon \to 0$. This is typically the case for weakly charged colloids. We note that, whilst the hard-core Yukawa model is commonly used to describe slightly charged colloids, it can also be used as a crude model for sterically stabilized colloids. Hence, many of the con-

clusions that we obtain below, in particular those for systems with a high value of κ, should equally apply to sterically stabilized, uncharged colloids.

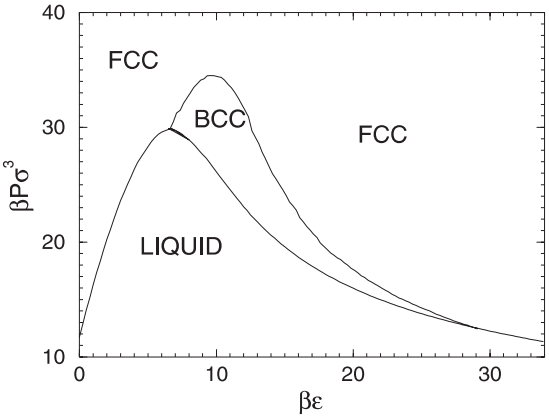

Fig. 19. Calculated coexistence pressure from Ref. [67] for $\kappa = 5$ as function of the Yukawa repulsion $\beta\epsilon$

The phase behavior of the hard-core Yukawa potential has been studied experimentally and by numerical simulation, see e.g. Ref. [65, 66, 67]. The computed phase diagram of Ref. [67] shows a fluid-solid (bcc/fcc) and a solid-solid (bcc-fcc) coexistence line and it exhibits two fluid-bcc-fcc triple points, (see Fig.19). The main difference between the phase diagram of the hard-core Yukawa model and that of the pure (i.e. point-particle) Yukawa potential [68] is the presence of the second triple point. This triple point sets a lower limit for the strength of the Yukawa interaction for which a bcc phase exists.

Only few nucleation experiments on charged colloidal suspensions have been reported. Some of these were based on light-scattering studies [69, 70]. More recently, Gasser et al. [60] reported a confocal microscopy study of homogeneous crystal nucleation in slightly charged hard-sphere colloids. Recent light-scattering experiments of crystallization in more highly charged colloids has been reported by Schöpe et al. [71] and Wette [72].

We performed a computer-simulation study of crystal nucleation in a hard-core Yukawa system varying both parameters, the amplitude of the Yukawa repulsion and the magnitude of screening length. First we computed the nucleation barrier at fixed $\kappa = 5$ for four different values of the amplitude of the Yukawa repulsion $\beta\epsilon = 2, 6, 8$ and 20. Increasing the contact value $\beta\epsilon$ of the Yukawa repulsion shifts the volume fraction of the liquid phase at freezing to lower values than the hard-sphere value $\phi = 0.494$. In order to be able to interpret our numerical data on the free-energy barrier for crystal nucleation, we need an accurate estimate of the density, pressure and chemical potential of the liquid at freezing. The data of Ref. [67] were obtained using a (modified) Gibbs-Duhem integration method. While this tech-

Table 4. Excess free energy per particle for the different bulk structures and the liquid state calculated via a thermodynamic intergration in the limit of infinite number of particles [102]. The reference state for the free energy calculation of the liquid was the hard-sphere fluid, and for the bulk solid structures we used an Einstein-crystal. In some cases we also used the hard-sphere system as a reference state for the solid structures. We found that the solid free energies obtained via these two distinct routes agreed to within $\pm 0.005 k_B T$, which corresponds to our estimate of the statistical error in this calculation. The statistical accuracy of the computed free energy of the liquid is estimated to be $\pm 0.01 k_B T$. In the table, the values in brackets indicate the volume fraction at which the excess free energy was calculated. The calculated excess free energies for the fcc and the hcp structures can be compared directly, as they were calculated at the same pressure, whereas the others are not. The fcc-hcp free energy difference is always smaller than $(1 \times 10^{-2} k_B T)$

	f_{fcc}	f_{hcp}	f_{bcc}	f_{liquid}
$\beta\epsilon = 2$	12.894	12.892	–	11.38
$\kappa = 5$	(0.5425)	(0.5425)	–	(0.5032)
$\beta\epsilon = 6$	23.258	23.256	21.49	19.11
$\kappa = 5$	(0.5027)	(0.5027)	(0.4808)	(0.4503)
$\beta\epsilon = 8$	24.344	24.35	24.32	22.23
$\kappa = 5$	(0.4563)	(0.4563)	(0.4558)	(0.4329)
$\beta\epsilon = 20$	20.872	20.873	20.986	16.16
$\kappa = 5$	(0.2888)	(0.2888)	(0.2895)	(0.2529)
$\beta\epsilon = 8$	11.144	11.147	11.067	10.02
$\kappa = 10$	(0.4084)	(0.4084)	(0.4054)	(0.3853)
$\beta\epsilon = 8$	39.107	39.110	–	38.08
$\kappa = 3.33333$	(0.5168)	(0.5168)	–	(0.5055)

nique is useful to estimate the location of solid-liquid coexistence curves, the computed coexistence data were not sufficiently accurate for the present purpose. We therefore computed the location of all coexistence points by direct free-energy calculation of the solid and liquid phases [15]. The results for the excess free energy per particle are summarized in Table 4. From the computed free energies, we obtain estimates for the chemical potential at freezing that have an error of $\pm 0.01 k_B T$. We found the following values for the volume fraction of the liquid phase at freezing: $\phi = 0.48212, 0.43823, 0.4049$ and 0.26171 for $\beta\epsilon = 2, 6, 8$ and 20, respectively (see Table 5). In Fig. 20 we show the results for the barrier height as a function of supersaturation with respect to the stable solid phase (fcc). As the figure shows, the main effect of increasing the strength of the Yukawa repulsion is to lower the nucleation barrier at constant supersaturation $\Delta\mu$.

Note that the decrease of the height of the nucleation barrier is particularly strong when only a weak repulsion is added to the hard-core potential. In particular, switching on a repulsive Yukawa potential with a contact value of only $2 k_B T$ decreases the nucleation barrier by some $10 k_B T$. This implies that for real hard-sphere colloids,

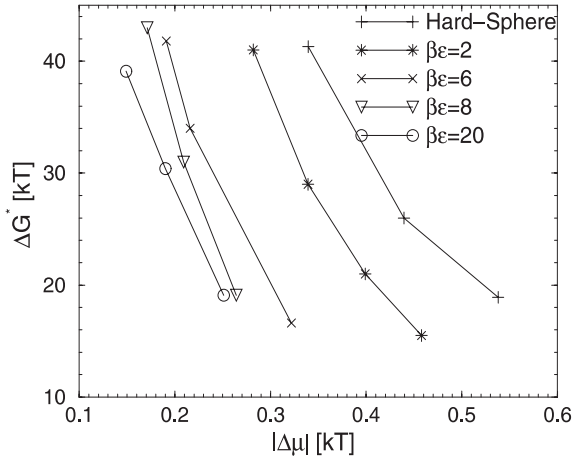

Fig. 20. Calculated barrier heights ΔG^* of the hard-core Yukawa system with $\kappa = 5$ and $\beta\epsilon = 2, 6, 8, 20$ plotted as a function of supersaturation $\Delta\mu$ of the liquid phase to the stable fcc phase

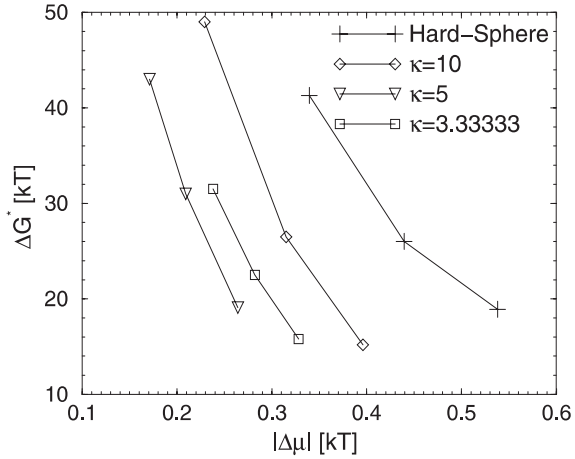

Fig. 21. Calculated barrier heights ΔG^* of the hard-core Yukawa system with $\beta\epsilon = 8$ and $\kappa = 10, 5, 3.33333$ plotted as a function of supersaturation $\Delta\mu$ of the liquid phase to the stable fcc phase

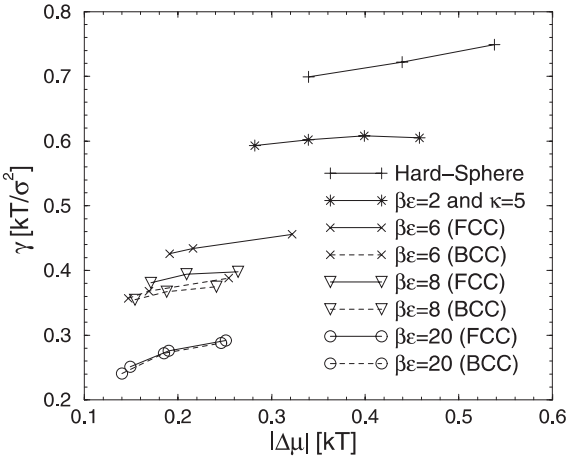

Fig. 22. Interfacial free energy γ calculated from the barrier heights Eq. 2 for $\kappa = 5$ and $\beta\epsilon = 2, 6, 8, 20$. The *solid lines* are the results assuming that the nuclei have a fcc structure, and the *dashed lines* are the results if the nuclei are bcc

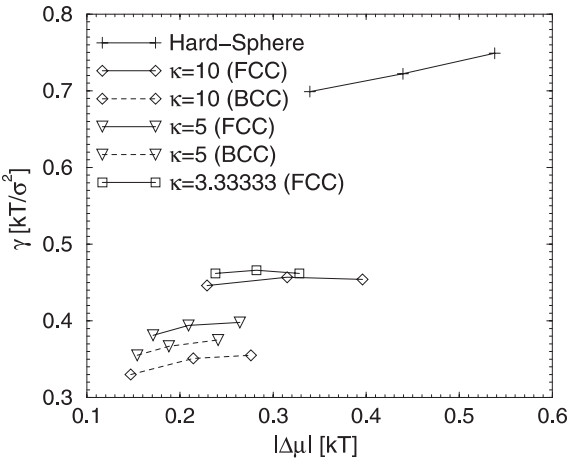

Fig. 23. Interfacial free energy γ calculated from the barrier heights Eq. 2 for $\beta\epsilon = 8$ and $\kappa = 10, 5, 3.33333$. The *solid lines* are the results assuming that the nuclei have a fcc structure, and the *dashed lines* are the results if the nuclei are bcc

the presence of only a small amount of charge can enhance the nucleation rate at constant volume fraction by many orders of magnitude through two mechanisms: first of all, the charge increases the supersaturation at constant density. This effect would shift the nucleation curve to lower densities. But, in addition, the charge lowers the nucleation barrier at constant supersaturation. Further increase of the strength of the Yukawa repulsion leads to some additional decrease of the nucleation barrier, but the effect seems to saturate for values of $\beta\epsilon$ between 8–20.

Table 5. Summary of the data for the calculations with the repulsive hard-core Yukawa potential. Here P is the Pressure and $\phi_{\rm liq}, \phi_{\rm fcc}, \phi_{\rm bcc}$ the corresponding volume fraction of the liquid, fcc and bcc phase. $\Delta\mu_{\rm fcc}$ and $\Delta\mu_{\rm bcc}$ is the difference in chemical potential between the liquid and the fcc/bcc phases. ΔG^* are the measured crystallization barriers. $f_{n_c}^+/D_0$ is the reduced attachment rate of particles to the critical cluster. I is the calculated reduced nucleation rate

	P	$\phi_{\rm liq}$	$\phi_{\rm fcc}$	$\phi_{\rm bcc}$	$\Delta\mu_{\rm fcc}$	$\Delta\mu_{\rm bcc}$	ΔG^*	$f_{n_c}^+/D_0$	$\log_{10}(I)$
$\kappa = 5$	25	0.5103	0.5420	–	0.28	–	41	46	-19.1
and	26	0.5159	0.5484	–	0.34	–	29	84	-13.5
$\beta\epsilon = 2$	27	0.5218	0.5551	–	0.40	–	21	6	-11.1
	28	0.5257	0.5599	–	0.46	–	15.5	19	-8.1
$\kappa = 5$	37	0.4714	0.4827	0.4808	0.19	0.15	48.1	202	-19
and	38	0.4755	0.4864	0.4848	0.22	0.17	34	57	-16.1
$\beta\epsilon = 6$	42	0.4903	0.5031	0.5004	0.32	0.25	16.6	52	-8.3
$\kappa = 5$	38	0.4415	0.4487	0.4481	0.17	0.15	43	218	-19.5
and	40	0.4491	0.4563	0.4558	0.21	0.19	31	200	-14.3
$\beta\epsilon = 8$	43	0.4596	0.4671	0.4668	0.26	0.24	19.1	300	-8.8
$\kappa = 5$	23	0.2859	0.2888	0.2895	0.15	0.14	39.1	167	-18.2
and	25	0.2938	0.2973	0.2974	0.19	0.19	30.4	58	-14.8
$\beta\epsilon = 20$	28	0.3048	0.3084	0.3083	0.25	0.25	19.1	53	-9.7
$\kappa = 10$	18	0.3848	0.3978	0.3949	0.23	0.15	49	80	-22.6
and	20	0.3955	0.4084	0.4054	0.32	0.21	26.5	44	-13
$\beta\epsilon = 8$	22	0.4054	0.4180	0.4150	0.40	0.28	15.2	11	-8.5
$\kappa = 3.33333$	57	0.4937	0.5042	–	0.24	–	31.5	205	-14.4
and	59	0.4996	0.5106	–	0.28	–	22.5	81	-10.8
$\beta\epsilon = 8$	61	0.5055	0.5168	–	0.33	–	15.8	80	-7.7

Let us next consider the effect of the range of the repulsive potential on the nucleation barrier. We computed the height of the crystallization barrier for $\kappa = 10$, 5 and 3.333 at a fixed contact value $\beta\epsilon = 8$. In addition, we know the behavior of the system in the hard-sphere limit ($\kappa = \infty$). As κ is decreased, the range of the potential grows. Initially, (as κ is decreased from ∞ to 10, the density at which the liquid freezes shifts from $\phi = 0.494$ to $\phi = 0.354$. Subsequently, the freezing density increases again. For $\kappa = 5$, the volume fraction at freezing is $\phi = 0.405$ and for $\kappa = 3.333$, the liquid freezes at $\phi = 0.456$. The variation of the crystallization barrier with κ and $\Delta\mu$ is shown in Fig. 21. The figure shows that increasing the range of the repulsive interaction, at constant supersaturation, initially has the effect to lower the nucleation barrier. However, as κ is decreased below 5, the nucleation barrier starts to increase again.

From the CNT expression for the height of the nucleation barrier Eq. (2), we can estimate the corresponding values for the liquid/fcc interfacial free energy $\gamma_{\rm fcc}$. In Fig. 22 we show the variation of the interfacial free energy with $\beta\epsilon$ at fixed κ. Fig-

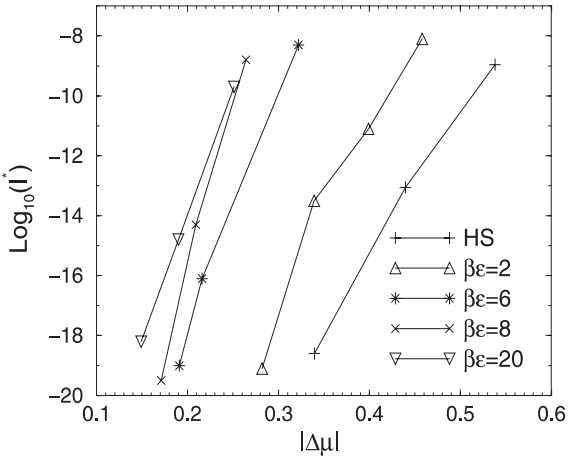

Fig. 24. Dependence of the reduced crystallization rates I^* on the amplitude of the Yukawa repulsion $\beta\epsilon = 2, 6, 8, 20$ for $\kappa = 5$ plotted as a function of supersaturation $\Delta\mu$ of the liquid to the stable fcc phase

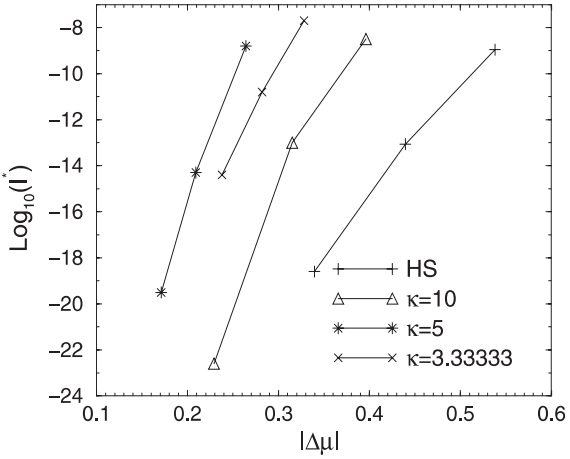

Fig. 25. Dependence of the reduced crystallization rates I^* on the inverse screening length $\kappa a = 10, 5, 3.33333$ for $\beta\epsilon = 8$ plotted as a function of supersaturation $\Delta\mu$ of the liquid to the stable fcc phase

ure 23 shows the variation of the interfacial free energy with κ at fixed $\beta\epsilon$ for various values of the supersaturation $\Delta\mu$. The dependence of the interfacial free energy on the range of repulsion mirrors that of the nucleation barrier and is therefore non-monotonic. Coming from the hard-sphere limit, the interfacial free energy initially goes down, but for κ less than 5, it increases again.

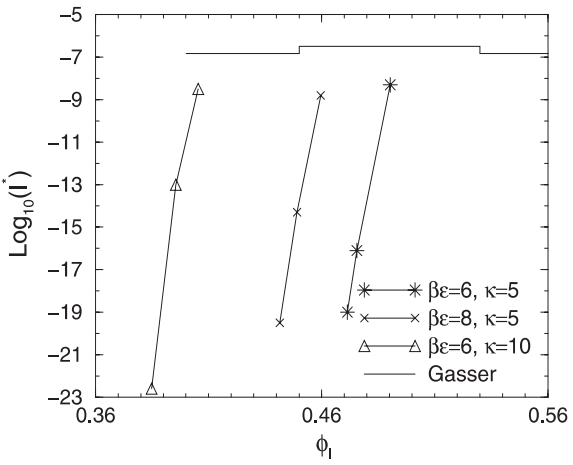

Fig. 26. Comparison between the experimentally measured nucleation rates [60] and the simulation data. The nucleation rates are expressed in reduced units $I^* = I\sigma^5/D_0$ where σ is the hard core diameter and D_0 is the self-diffusion coefficient at infinite dilution. ϕ_l is the volume fraction of the liquid. In the plot we added only the data sets that match the freezing volume fraction of the experimental system

In Refs. [32, 35] we found that, for hard spheres, the interfacial free energy γ increases with supersaturation $\Delta\mu$. As can be seen in Fig. 23, such behavior is also observed in a system of charged colloids. In polydisperse hard-sphere systems [35], the increase of γ with supersaturation could even result in a non-monotonic dependence of the nucleation barrier on supersaturation. In the present system, the interfacial free energy also increases with supersaturation, but the effect is not strong enough to result in a minimum in the nucleation barrier.

Using the techniques described before we computed the kinetic prefactors. Note that for the correction of the hydrodynamic interaction we used the expression $D_S^S/D_0 = (1-\phi/0.64)^{1.17}$ for the short time self diffusion coefficient from the hard sphere system. We therefore defined an effective packing fraction of the Yukawa system such that the packing fraction at freezing of the two systems are equal. We find that the kinetic prefactors do not vary strongly with either supersaturation or interaction potential and therefore the behavior of the nucleation rate is reflected by that of the barrier height. Our results for the computed nucleation rates are shown in Figs. 24 and 25, where we plot the nucleation rate as a function of supersaturation.

It is interesting to compare the computed crystallization rates with the results of the confocal microscopy experiments of Ref. [60]. In order to do this we need to know the potential parameters that best characterize the experimental system used in Ref. [60]. From the fact that the suspensions studied by Gasser et al. freeze at a volume fraction $\phi = 0.38$, it is clear that the colloidal particles used in these experiments are slightly charged. It is therefore natural to describe them by a Yukawa model that also has its freezing point at $\phi = 0.38$. This condition is, however, not sufficient to fix the values of both κ and ϵ. For instance, if $\kappa = 5$, then the observed freezing density can be reproduce by choosing $\beta\epsilon \sim 7$. Conversely, if we choose $\beta\epsilon = 8$, then there are in fact, two values of κ that will reproduce the observed freezing density ($\kappa \sim 20$ and $\kappa \sim 6$) [67]. In Fig. 26, we show a comparison of the reduced nucleation rates reported in Ref. [60] with the simulation results for those κ-$\beta\epsilon$ combinations that yield a freezing point near $\phi = 0.38$. As can be seen from the figure, different κ-$\beta\epsilon$ combinations yield very different nucleation rates. However, the main effect of the variation of κ and ϵ is to shift the nucleation curves horizontally: the slopes of the different curves are all rather similar. When we compare the computed nucleation rates with the experimental data, we note two things: first of all, the experimental rates tend to be (much) higher than the computed rates (Gasser et al. find $-6.9 \leq \log[I^*] \leq -6.5$ for ϕ between 0.45 and 0.53). But, more importantly, the experiments suggest that the nucleation rate barely varies with volume fraction. We were unable to reproduce this behavior with any of the Yukawa models that we studied. This discrepancy between experiment and simulation suggests that the experimental system is not well described by a Yukawa model with density-independent κ and ϵ. On the contrary, it is likely that the effective potential parameters of weakly charged colloids in the absence of added salt depend strongly on concentration. In fact, recent experiments by Schöpe et al. [73] clearly illustrate this effect: with increasing concentration, the effective potential of charged polystyrene spheres in dilute aqueous solution, becomes increasingly hard-sphere like. If we assume that the same phenomenon occurs in the more concentrated suspensions of Ref. [60], then experimental results for the nucleation rates at different densities should be compared with the numerical predictions that correspond to different effective Yukawa potentials. As can be seen from Fig. 26, the variation of the nucleation rate with density can be strongly reduced (and can possibly even become non-monotonic) if, as we expect, ϵ and κ decrease with density. It is, however, not obvious that this effect is large enough to account for the apparent discrepancy between experiment and simulation. Clearly, a truly quantitative comparison between simulation and experiment requires better knowledge of the density dependence of the effective interaction between slightly charged colloidal spheres.

The repulsive Yukawa system offers a unique opportunity to study the effect of meta-stable crystal phases on the pathway for crystal nucleation. To study the effect of meta-stable intermediates on crystallization, we analyzed the structure of the (pre)critical nucleus in different regions of the phase diagram. Note that the pressure range region where the bcc phase is stable is rather narrow. For these pressures, the supersaturation of the fluid phase is small, and hence the nucleation barrier is very high. As a consequence, we could only study the formation of pre-critical nuclei in

the fcc regime. In order to study the structure of the (pre)critical nuclei, we used the local bond-order analysis proposed by ten Wolde et. al. [13]. In this analysis the local bond-order signature of a nucleus is decomposed into the signatures of the different bulk structures (liquid, fcc and bcc) using a linear least square fit. The value of the resulting coefficients $\{f_{\mathrm{liq}}, f_{\mathrm{fcc}}, f_{\mathrm{bcc}}\}$ are a measure of the structure of the nucleus. Our simulations show that the pre-critical nuclei always have a strong bcc signature. Only for larger (post)critical nuclei well inside the fcc regime, do we find a mixture of bcc and fcc signatures. In this sense, our simulations unambiguously support the prediction that nucleation into bcc nuclei is always uniquely favored, even when the fcc phase is closer in free energy to the fluid phase.

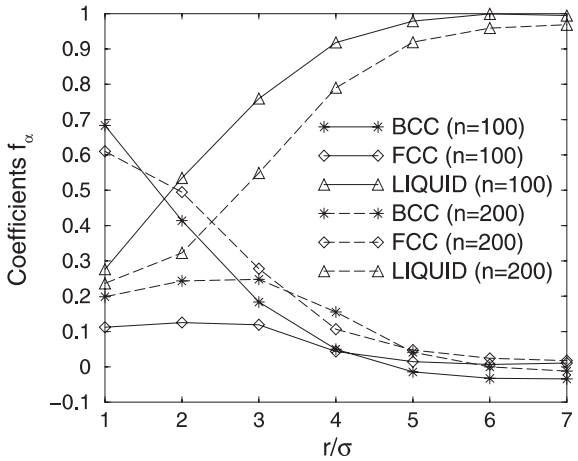

Fig. 27. Structure analysis of two independent crystal nuclei of size $n = 100$ and 200 from the simulations with parameters $\beta\epsilon = 8$ and $\kappa = 10$. The figure shows the results for the fit parameters for the local bond-order analysis as a function of the distance from the center of mass of the nuclei. The core of the cluster of size $n = 100$ has a clear bcc signature, where the cluster of size $n = 200$ shows a clear fcc structure

Figure 27 shows the results of our cluster analysis for two distinct nuclei of size $n = 100$ and $n = 200$. The picture shows the variation of the structural signature with the distance from the center of mass of the nucleus. The results shown in this figure apply to the case $\kappa = 10$ and $\beta\epsilon = 8$. This corresponds to the points in the phase diagram where the preference for the fcc structure is strongest. The core of the cluster of size $n = 100$ has a clear bcc signature while the fcc phase does not seem to play a role. However, for the larger nuclei ($n = 200$) the core of the nuclei becomes fcc like while the bcc phase seem to disappear. In this case the cluster transformation happened before it could reach critical size. This phase transition in the pre-critical nucleus allows us to quantify what value of the bcc-fluid interfacial free energy is needed in order to compensate for the difference in chemical potential of the two bulk structures. From our free-energy calculations, we deduce

$\mu_{\rm bcc} - \mu_{\rm fcc} = 0.082(\pm 0.01) k_B T$. We used the CNT expression for the barrier height to estimate the fcc-liquid interfacial free energy: $\gamma_{\rm fcc} = 0.45 k_B T/\sigma^2$. The transformation from bcc to fcc nuclei occurred for $n \approx 100$. At that point, the gain in bulk free energy is $100 * 0.082 = 8.2 k_B T$. This free-energy gain must be compensated by the increase in surface free energy as the crystallite transforms from bcc to fcc. To estimate this surface free energy, we need to know the radius of the crystal nucleus for $n = 100$. If we assume that the nucleus is spherical and that the solid is effectively incompressible, we arrive at the estimate $\gamma_{bcc} = 0.38 k_B T/\sigma^2$. We find such a pre-critical transformation from bcc to fcc for $\beta\epsilon = 2$ with $\kappa = 5$, and for $\beta\epsilon = 8$ with $\kappa = 10$ and 3.33333. In all the other cases ($\beta\epsilon = 6, 8, 20$ with $\kappa = 5$) even the critical nuclei had a strong bcc signature. This observation has implications for the interfacial free energies shown in Figs. 22 and 23. In these figures, we show interfacial free energies that were computed from the CNT expression for the barrier height, assuming that the nucleus had the same structure as the stable crystal phase. We now see that, in some cases, the critical nucleus has a meta-stable bcc structure. This affects the value for $\Delta\mu$ in the CNT expression, and hence our estimate for γ . In the cases where the critical nucleus has a bcc structure, we therefore also estimated the value of $\gamma_{\rm bcc}$ from the height of the nucleation barrier. The results are also shown in Figs. 22 and 23.

Thus far we did not mention the possibility that the structure of the crystal nuclei could also be hexagonal closed packed (hcp) or a random stacking of the fcc and hcp domains (rhcp). In the case of hard-spheres it is known that the free-energy difference between the stable fcc and hcp solid structure is very small ($\approx 10^{-3} k_B T$) and therefore stacking faults are expected. Such stacking faults have been observed in experiments and computer simulations. In the case of charged spheres the situation is less clear. Some experiments indicate that the situation changes and there seems to be tendency that crystal nuclei become more fcc-like [74]. Other experiments suggest that the structure of the cluster is still rhcp [60]. To resolve this question for the present model system, we first calculated the free energy difference between the fcc and hcp solid, for all the different parameters of the model potential for which we performed the rate calculations. It turns out that the free energy difference per particle between the fcc and hcp structure was always smaller than $1 \times 10^{-2} k_B T$ (see Table 4), which is about the limit of the accuracy that we had in our calculations. This means that thermal fluctuations on the order of a few $k_B T$ could easily transform clusters containing hundreds of particles from fcc to hcp, or generate intermediate stackings. To find out if this really happens we, analysed the stacking of the (111)-planes of 10 nuclei with parameters $\beta\epsilon = 8, \kappa = 10$ and $\beta\epsilon = 8, \kappa = 3.33333$. In both cases, we do find stacking faults, but they seem to be less frequent than in the pure hard-sphere case. We stress, however, that these preliminary conclusions are based on the analysis of only a small number of crystallites.

6
Poly-12-hydroxystearic Coated Polymethylmethacrylate Particles

Our findings for the weakly charged colloids suggest that even a slight "softness" of the intermolecular potential, has important consequences for the crystallization behavior. This effect could be relevant for experimental "hard-sphere" colloids, as these particles are, in fact, slightly soft. A particularly popular experimental hard-sphere colloid consists of a polymethylmethacrylate (PMMA) core coated with a thin layer of poly-12-hydroxystearic (PHSA). Due to the coating, the particles are slightly soft. We studied the effect that such a softness has on the phase behavior and the crystallization kinetics [75].

The potential that we used to model the interaction between two PHSA-coated PMMA spheres was deduced from surface-force measurements. Costello et al. [76, 77] measured the force between two mica surfaces coated with a PMMA (backbone)-PHSA (sidechain) comb copolymer, with the PMMA backbone directly adsorbed on the mica and the PHSA side chains protruding into the solvent. The interaction thus mimics that between the surfaces of two PHSA-stabilized PMMA colloids. Costello et al. analyzed their measurements according to a model proposed by Alexander and de Gennes [78]. In this model, expected to be valid for high grafting densities, each chain is assumed to consist of connected semi-dilute blobs. The chains are stretched by osmotic repulsion between the blobs. This tendency is opposed by the increase in elastic free energy of the chain upon stretching. The resulting expression for the force per unit area between two parallel plates at a distance r is

$$F(r) = \frac{\alpha k_B T}{s^3}\left[\left(\frac{2L}{r}\right)^{9/4} - \left(\frac{r}{2L}\right)^{3/4}\right], \tag{14}$$

where s is the mean spacing between between grafting points and L is the thickness of the polymer layer; α is a numerical prefactor and $k_B T$ the thermal energy. The expression is supposed to hold for $0 < r < 2L$. Integration yields the corresponding energy density. From the distance of onset of the interaction, Costello et al. estimated that their layer thickness was $L = 12.5$ nm. A fit of the Alexander-de Gennes model to experimental measurements yielded $\alpha = 0.025$ and $s = 2.8$ nm. By using the Derjaguin approximation (see e.g. Ref. [79]) we can estimate the interaction potential between two spheres. Different methods have been used to measure the thickness of the PHSA layer on PMMA colloids synthesized according to the method of Antl et al. [80], giving values of $L = 7$–13 nm [81] and a maximum distance between grafting points of $s = 2.0$ nm [82]. As a starting point in our calculations, we used $L = 13.5$ nm and $s = 2.0$ nm to yield the strongest repulsion compatible with these experimental data. Denoting the radius of a particle's PMMA core (without the PHSA hair) as R, we plot the interaction potentials for two cases, $R = 305$ nm and 201 nm, in Fig. 28. These two radii are chosen to enable us to compare our calculations with the equilibrium phase behavior data of Pusey and van Megen [29, 83] and the crystallization kinetics data of Harland and van Megen [5] respectively.

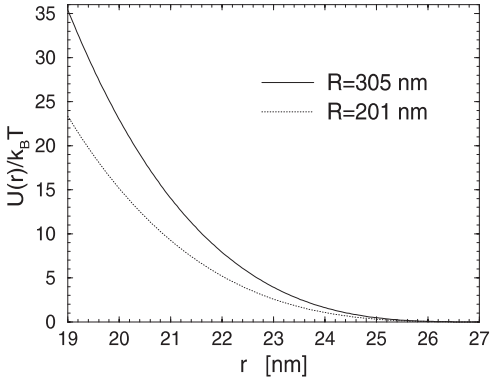

Fig. 28. Estimated interaction potential between two PMMA spheres coated with a layer of PHSA. Results are shown for particles with core radii of $R = 201$ nm and 305 nm with the following values for the parameters: $s = 2.0$ nm, $L = 13.5$ nm, $\alpha = 0.025$

We see that in both cases the interparticle interaction increases steeply to $10k_BT$ within 6–7 nm from the point of first contact.

We used the potential obtained in the previous section to calculate the freezing and melting densities of the colloidal suspensions from simulations using thermodynamic integration [15]. The resulting freezing and melting core volume fractions for our model potential were estimated to be $\phi_f = 0.4137$ and $\phi_m = 0.4579$ (for $R = 201$ nm) and $\phi_f = 0.4380$ and $\phi_m = 0.4850$ (for $R = 305$ nm). By scaling the freezing volume fractions to that of hard-spheres $\phi_f^{HS} = 0.494$ [27] we obtain the effective hard-sphere diameter $\sigma_{\text{eff}} = 1.061\sigma$ and $\sigma_{\text{eff}} = 1.041\sigma$ of the two systems. We can compare these diameters to the effective hard-sphere diameter predicted by first order perturbation theory: $\sigma_{\text{eff}} = \int_0^\infty dr\{1 - exp[-U(r)/k_BT]\}$. The results $\sigma_{\text{eff}} = 1.061\sigma$ (for $R = 201$ nm) and $\sigma_{\text{eff}} = 1.041\sigma$ (for $R = 305$ nm) are identical to the estimate above. The values for the interaction potential at this distance are $U(r = \sigma_{\text{eff}})/k_BT = 0.7056$ and 0.7065. If we use the effective hard-sphere diameter to rescale the melting volume fractions of the soft systems to that of the hard spheres we find $\phi_m = 0.5469$ and $\phi_m = 0.5463$ (to be compared with $\phi_m^{\text{HS}} = 0.545$ [27]).

Our results can be compared directly with the observations of Pusey and van Megen [29, 83]. These authors measured the core radius of their PMMA particles by static light scattering and electron microscopy, and found $R = 305$ nm. Knowing the core radius R, Pusey and van Megen dried down their suspensions and converted the measured mass fraction to core volume fractions using literature values of the densities of PMMA and the suspending liquid. They found core volume fractions at freezing and melting $\phi_{\text{f}} = 0.407$ and $\phi_{\text{m}} = 0.441$ [47]. The corresponding effective hard sphere diameter is $\sigma_{\text{eff}} = 1.067$. The experimental volume fractions are some 3.1% lower than the freezing volume fraction determined in our simulations. If we consider the fact that the particles are polydisperse (5%) the discrepancy increases to 4.1% [52]. One may seek to obtain a better fit to experiments by varying the parameters s and L. The value of s used gives the minimum surface coverage (at

areal density s^{-2}) necessary for steric stabilization to function [82]. In any case, we find that the effective hard sphere diameter is somewhat insensitive to variations in s. Instead, agreement with the hard-core freezing volume fraction of Pusey and van Megen can be obtained by using a value of $L \approx 22$ nm. While there was no

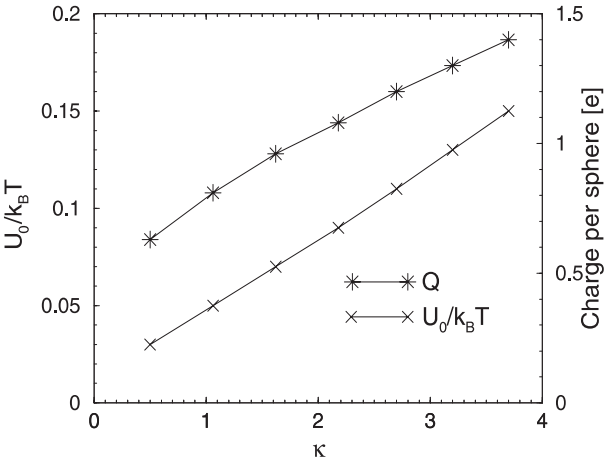

Fig. 29. Calculated parameter set (U_0/k_BT,κ) of a hard-core Yukawa potential that accounts for the observed shift in the freezing density. The same curve but in units of charge per sphere is also shown

direct determination of the PHSA chain length for the batch of PMMA particles used by these authors, this value of L is twice to three times as long as values obtained from a variety of experiments on PHSA-coated PMMA particles [81]. Pusey and van Megen, who estimated the effective hard sphere diameter of their particles to be $\sigma_{\text{eff}} = 2R \times (0.494/0.407)^{1/3}$, also concluded [83] that the implied PHSA layer thickness of $L \sim 20$ nm was rather larger than expected. It is therefore possible that there is an additional source of weak repulsion, such as a slight charge on the colloids. If we assume that the interaction between charged colloids is described by a repulsive hard core Yukawa potential: $U_0/k_BT \exp[-\kappa(r/\sigma - 1)]/(r/\sigma)$ for $r > \sigma$, we can use the previous equation for the effective hard-sphere diameter from first order perturbation theory to estimate the values of the parameter U_0/k_BT and κ needed to account for the observed shift in freezing volume fraction. Here U_0/k_BT is the value of the Yukawa repulsion at contact and κ is the inverse screening lenght in units of the hard-sphere diameter σ. We find that the added repulsion is indeed quite weak, and very soft (see Fig. 29). Note that such a weak, soft repulsion can hardly be detected in the surface-force measurement. We can estimate the charge on a particle from the contact value of the interaction potential: $U_0/k_BT = Q^2/4\pi\epsilon_0\epsilon\sigma$, where Q is the charge, ϵ_0 and ϵ are the permittivity of the vacuum and the solvent. A value $U_0/k_BT = 0.1$ corresponds to an average colloidal charge of about one electron per sphere. More recent experiments by Bryant et al. [84] indicate that the polymer layer

thickness is even smaller, which suggests that the charge might even be higher. In more polar solvents, long range repulsions have been observed for the same kind of particles [85].

We turn now to study how the softness of the potential affects the crystallization kinetics. For the system with $R = 201$ nm we computed the crystal nucleation barrier at four different pressures $P\sigma^3/k_BT = 12.5, 13, 13.5$ and 14, corresponding to volume fractions of the liquid $\phi_l = 0.43441, 0.43803, 0.44144$ and 0.44480. In Fig. 30 we show the results for the crystal nucleation barrier as a function of $\Delta\mu$. In the figure we also show the results for the hard-sphere system. As can be seen, despite the only slight softness, the crystal nucleation barrier is reduced by about 2–$4\,k_BT$ at constant $\Delta\mu$. This is largely the result of a lowering of the surface tension compared to the case of hard spheres. If we assume that the nuclei are spherical we can use Eq. (2) to calculate the surface free energy density of the critical nuclei. The results are $\gamma = 0.592, 0.608, 0.629, 0.636 k_BT/\sigma^2$ (in order of increasing density).

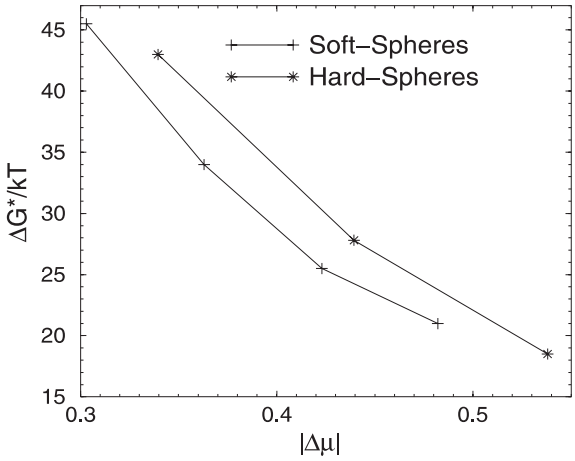

Fig. 30. Computed crystal nucleation barrier heights ΔG^* for the slightly soft-spheres plotted as a function of supersaturation $\Delta\mu$. In addition we also show results from previous simulation on the hard-sphere system

To estimate the crystal nucleation rate we computed the kinetic prefactor Γ as described before. The result for the crystal nucleation rates as a function of $\Delta\mu$ is that the decrease in the nucleation barrier transforms into an increase of the crystal nucleation rate of about two orders of magnitudes. Our simulations can be compared directly with the experimental results of Harland and van Megen [5], who measured nucleation rates by time-resolved static light scattering for PMMA spheres of radius 201 nm[1]. To make this comparison, we show in Fig. 31 the crystal nucleation rate as a function of the rescaled volume fraction of the metastable fluid. Comparing

[1] Essentially, this radius was determined by assuming the hard-sphere freezing and melting volume fractions of 0.494 and 0.545 respectively. Thus 201 nm is *not* the core radius (but

first the results for monodisperse hard spheres [32] and monodisperse soft spheres (this work), we see that there is again an increase of the nucleation rate of more than one order of magnitude. However, the particles used in Harland and van Megen were 5% polydisperse. Previous simulation results for 5% polydisperse hard spheres [32] are reproduced in Fig. 31: these disagree with Harland and van Megen's data by up to 10 orders of magnitude. If we assume that the effect of softness on the nucleation rate is also an upward shift of a little over an order of magnitude, then results for polydisperse soft spheres would agree somewhat better with the data, but substantial disagreement remains. We also show the results of experiments by Sinn et al. [31]. The particles they used are larger (435 nm, and therefore less soft) and have a polydispersity of 2.5% (i.e. more monodisperse than the particles used by Harland and van Megen). The simulation results for monodisperse hard spheres can therefore be expected to be more comparable. Even here, however, there remains many orders of magnitude disagreement.

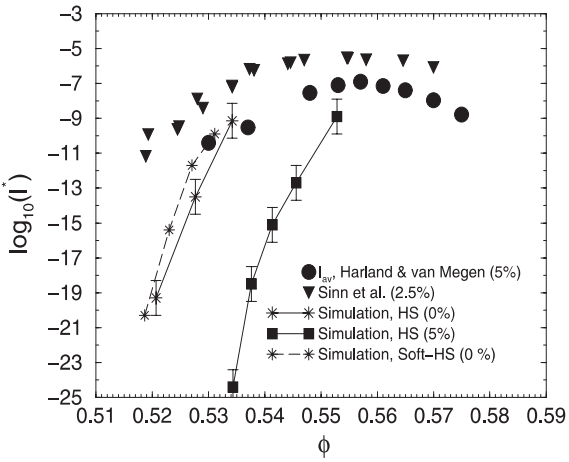

Fig. 31. Reduced nucleation rates I^* as a function of the rescaled volume fraction of the meta-stable fluid. We show the experimental results of Ref. [5] (•) and Ref. [31] (▼). The simulation data for the monodisperse colloids are indicated by (∗), where the *solid* and the *dotted lines* correspond to the hard sphere system and the slightly soft system. The results of the hard sphere system that has a polydispersity of 5% are shown as (■)

The fact that the particles may be weakly charged and the system has a large Debye screening length might have two additional effects on the crystallization kinetics. First of all, the charge further lowers the surface free energy which increases the nucleation rates. Secondly, as both the surface charge and the Debye screening

more like $R + L$). We nevertheless have estimated the interparticle potential in this case using $R = 201$ nm, because the accuracy of our nucleation barrier simulations and the uncertainties associated with estimating the absolute nucleation rates do not warrant any attempt at estimating R to an accuracy of 5%.

length may depend on density this can qualitatively change the dependence of the nucleation rate on supersaturation [61]. A better agreement with experimental nucleation rates would be obtained if we make the (not unreasonable) assumption that the colloids become more hard-sphere like at higher densities.

7 Wall Induced Crystallization

Thus far, we have focused on the homogeneous nucleation in colloidal suspensions. However, in the real world, crystallization is usually initiated by heterogeneous nucleation. If ice could only form through homogeneous nucleation, the freezing of water would be a rare phenomenon in countries with moderate climates.

To study the effect of an external surface on the crystallization process, we studied the behavior of monodisperse hard-sphere colloids near a hard wall [86]. Depending on the nature of the surface, it may have different effects on the freezing transition. One possibility is that the crystal phase “wets" the surface: in that case, one or more crystalline layers form at the surface, before the bulk freezing transition. Alternatively, the crystal may partially wet the wall, in which case crystal nucleation from a supersaturated solution takes place at the wall, rather than in the bulk.

The effect of a structured surface on the crystallization of hard-sphere colloids has been extensively studied in experiments [87, 88, 89, 90]. These experiments indicate that crystallization on a template is induced at densities below freezing. This finding is supported by computer simulations of hard spheres in contact with a patterned substrate, by Heni and Löwen [91]. These simulations indicate that surface freezing already sets in 29% below the coexistence pressure. Furthermore the effect of a surface on crystallization has also been studied in mixtures of binary hard-spheres [92, 93] and colloid-polymer mixtures [94, 95, 96]. In both systems surface crystallization was found to take place before bulk fluid-solid coexistence. In the systems studied in Refs. [92, 93, 94, 95, 96], depletion forces favor the accumulation of the larger component on the wall, and this should facilitate surface crystallization [97].

For the important case of pure hard-sphere systems confined by flat walls, it is not *a priori* clear if bulk freezing will be preceded by surface crystallization. Yet, we are not aware of any systematic, experimental studies of surface crystallization in pure hard-sphere systems. Courtemanche and Swol [98] reported a numerical study of a (rather small) one-component hard sphere system, confined between two plane hard walls. These simulations suggested that surface crystallization occurred at a pressure some 3% below the coexistence value.

Before we present the simulation results, we briefly discuss the effect of a wall on crystal nucleation in the context of Classical Nucleation Theory (CNT). Turnbull [99] extended CNT to the case of heterogeneous nucleation of a crystal that forms on a plane substrate. The difference with the homogeneous case is that there are now two interfaces present. The Gibbs free energy of a crystal containing n particles is given by:

$$\Delta G(n) = n\Delta\mu + A_{ws}(\gamma_{ws} - \gamma_{wl}) + A_{ls}\gamma_{ls}, \tag{15}$$

where the subscripts w, l, s refer, respectively, to the wall, the liquid and the solid. Note that in this formulation the contribution to $\Delta G(n)$ due to the line tension is neglected. More seriously, the dependence of the interfacial free energy on the surface orientation is ignored. With those assumptions, the shape that minimizes $\Delta G(n)$ at fixed n, is a sphere sector, with a contact angle θ of the two phases with the wall given by: $\cos(\theta) = (\gamma_{wl} - \gamma_{ws})/\gamma_{ls}$. The resulting height of the nucleation barrier is

$$\Delta G^* = \frac{16\pi}{3}\frac{\gamma_{ls}^3 f(\theta)}{(\rho_s \Delta\mu)^2}, \tag{16}$$

where ρ_s is the number density of the bulk solid and the factor $f(\theta) = (2 + \cos(\theta))(1 - \cos(\theta))^2/4$. The only difference with the expression for the homogeneous case is the factor $f(\theta)$. Depending on the values for the interfacial free energy densities, we distinguish three different cases. The first case corresponds to the situation where $\gamma_{ws} > \gamma_{wl} + \gamma_{sl}$. Under these conditions the crystal will not form on the substrate, because this would increase its free energy, and nucleation will take place in the bulk. A second scenario applies when $-\gamma_{ls} < \gamma_{wl} - \gamma_{ws} < \gamma_{ls}$. Then $-1 < \cos(\theta) < 1$. This means that a crystal can lower its free energy by attaching to the wall (partial wetting). The final case is when $\cos(\theta) = 1 (\theta = 0^\circ)$ or $\gamma_{wl} > \gamma_{ws} + \gamma_{ls}$. In that case, the solid phase prefers to form a thin layer on the wall (complete wetting) and the barrier to nucleation disappears.

For the hard-sphere system, we can speculate what scenario should apply, as all relevant surface free energies have been estimated numerically [100, 7], at least at coexistence. The estimated value for the wall/liquid interfacial free energy density at the freezing volume fraction $\phi = 0.494$ is $\gamma_{wl} = 1.99 k_B T/\sigma^2$ [100], where σ is the hard-sphere diameter and $k_B T$ the thermal energy. The values for the wall/solid interfacial free energies for different orientations (111), (110), (100) are estimated to be $\gamma_{ws} = 1.42, 3.08, 2.01 k_B T/\sigma^2$ [100]. The values for the liquid/solid interfacial free energy for the same three orientations are $\gamma_{ls} = 0.58, 0.64, 0.62 k_B T/\sigma^2$ [7]. These numbers suggest that the (110) plane will not attach to the wall as $\gamma_{wl} + \gamma_{ls} < \gamma_{ws}$. In contrast, the (100) planes is expect to partially wet the wall. For the (111)-plane, the difference between $\gamma_{ls} + \gamma_{ws}$ and γ_{wl} is estimated to be 0.01 ± 0.18, which is not significantly different from zero. Hence, the (111) plane is expected to be at, or very close to, complete wetting.

To explore the pathway for wall-induced crystallization, we performed Monte Carlo simulations in the constant normal-pressure ($NP_\perp T$) ensemble. Here N refers to the number of hard-spheres in the system. The simulation box was rectangular with periodic boundary conditions in the x and y directions. In the z-direction, the system is confined by two flat, hard walls at a distance L_z. $P_\perp$ is the component of the pressure tensor perpendicular to the plane wall, and T is the temperature. As our unit of length we used the hard-sphere diameter σ. T only sets the energy scale. In the following we always use reduced units. The state of the bulk hard-sphere system is completely specified by its volume fraction ϕ. The coexistence volume fractions for the bulk fluid and solid phase are known [27]: $\phi_f = 0.494$ and $\phi_m = 0.545$. The

corresponding coexistence pressure is $P_c = 11.57$. To suppress finite-size effects, we simulated a system containing $N = 13824$ particles. The wall area was fixed at $L_x L_y = 600.25\sigma^2$, the distance between the two walls in the z-direction fluctuated but was close to 24σ, which is much larger than any correlation length in the fluid. During the simulations, we performed on average one volume move per two cycles (trial moves per particle).

The simplest way to detect if a crystal phase wets the surface is to measure the density profile of the particles between the two walls. In Fig. 32a we show the ob-

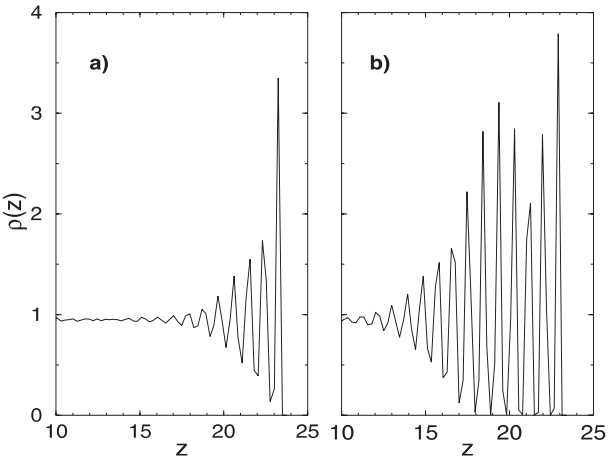

Fig. 32. (**a**) Density profile along the z-direction for a hard-sphere system between the two plane walls at an excess pressure $\Delta P = 0.53$. The corresponding bulk volume fraction is $\phi = 0.4966$. Simulation length: $2 \cdot 10^6$ cycles. (**b**) as in **(a)** but at an excess pressure $\Delta P = 0.63$

served density profile at the end of a simulation performed at a pressure just above bulk freezing (excess pressure $\Delta P \equiv P_\perp - P_c = 0.53$). If crystallization at the wall had taken place, this would cause a pronounced dip between the first and the second peak in Fig. 32a. No such behavior was observed, even at pressures well above P_c.

The situation changes when the excess pressure is increased to $\Delta P = 0.63$. The liquid starts to crystallize, as can be seen from the density profile shown in Fig. 32b. These results indicate that supersaturation is needed to induce crystallization. Yet, the degree of supersaturation needed to induce nucleation is very small compared to that typical for bulk systems. In fact, in simulations of homogeneous systems of comparable size, the rate of crystal nucleation during a simulation of similar length, is negligible up to excess pressures that are an order of magnitude larger ($\Delta P \approx 5.4$ ($\phi \approx 0.53$)). In order to identify the early stages of crystal nucleation, we used a local bond-order analysis [32] to distinguish between particles with a liquid-like and solid-like local environment. The result of this analysis is shown in Fig. 33, which shows a snapshot of the particles closest to the wall at $\Delta P = 0.53$. The dark particles have a liquid-like environment and the light particles have a solid-like environment.

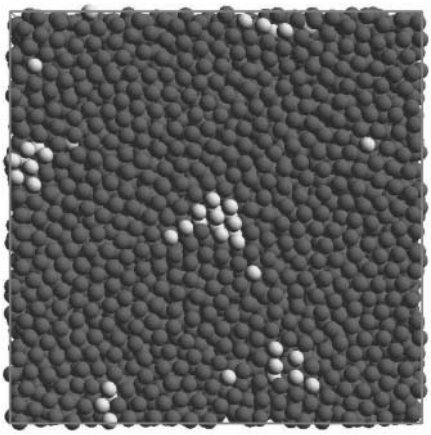

Fig. 33. Snapshot of a configuration which shows the particles at the wall. A local bond-order analysis was used to distinguish between particles with a liquid-like (*dark particles*) and solid-like (*light particles*) environment. The snapshot is taken from a simulation at pressure $P_\perp = 12.1$

Only a few small crystalline clusters can be identified. These clusters form and break up spontaneously. Under the same conditions, not a single solid-like cluster formed in the bulk of the fluid.

A more quantitative measure of the effect of the surface on crystal nucleation we obtained from a direct calculation of the crystal-nucleation barrier. We performed Monte Carlo simulations in the constant normal-pressure ($NP_\perp T$) ensemble where we used $N = 13824$ particles and simulated $2 \cdot 10^6$ cycles for every window. The result for the free energy barrier calculated at a pressure $\Delta P = 0.63$ is shown in Fig. 34 (dots). At this pressure, the estimated barrier height is $\Delta G^* = 17 k_B T$ at a critical cluster size $n_c = 150$.

We can compare this estimate with a prediction for the barrier height in a homogeneous system. For the hard-sphere colloids we showed before that, given the correct value for the interfacial free energy, CNT describes the barrier height quite well [32]. But we also found that the interfacial free energy depends on density. As the present system is close to coexistence we use its average coexistence value $\gamma_{av} = 0.61 k_B T/\sigma^2$ [7]. We then obtain $\Delta G^*_{CNT} = 1334 k_B T$ at a critical cluster size of $n_c = 52\,000$. The overall reduction of the nucleation barrier due to the plane wall is about two orders of magnitudes, resulting in a huge ($O(10^{570})$) increase in the nucleation rate. The computed nucleation rate per unit area is $\sim 10^{-9}$ (in units D_0/σ^4).

The implication for experiments is clearly that crystallization of suspensions of hard-sphere colloids should proceed heterogeneously, whenever a sufficiently flat surface is available. Yet, somewhat surprisingly, there are, to our knowledge, no systematic experimental observations of surface-induced freezing in hard sphere colloids, even though most bulk crystallization studies are performed in contain-

ers with, effectively flat walls. When we compare the computed nucleation barrier

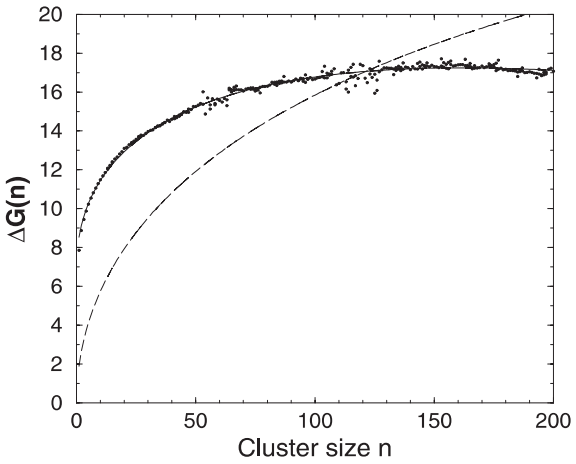

Fig. 34. Calculated nucleation barrier $\Delta G(n)$ of a crystal nucleus formed at the wall as a function of its size n (*filled dots*). In the figure, we show two fits to the nucleation barrier: the *dashed curve* assumes the published values for the surface free energies and uses a curvature-independent line tension. To obtain the drawn curve, we used γ_{wl} as a fit parameter and we assumed that the line-tension was curvature dependent. If we had used the CNT expression (Eq. 15), there would not be a nucleation barrier at this supersaturation

with the predictions of CNT (Eq. (15)), we find that this expression seriously underestimates the height of the nucleation barrier. In fact, CNT would predict that, at an excess pressure $\Delta P = 0.53$), (where $\Delta\mu = -0.05 k_B T$ [33]), the barrier to nucleation is negligible compared to $k_B T$. In order to resolve this discrepancy, we are forced to take into account the line tension, τ_{Line}, of the crystal nuclei on the wall. If we attempt to fit our numerical data to Eq. (15) plus a term due to line tension, we can indeed reproduce a nucleation barrier with the same height as found in the simulations, but the shape of the simulated barrier is reproduced rather poorly (see Fig. 34). A much better fit can be obtained by allowing γ_{wl} to vary within the bounds set by the (large) estimated error in the computed value: $1.99(\pm 0.18) k_B T/\sigma^2$. In addition, it turns out that we have to allow for a curvature correction of the line tension: $\tau_{Line} = \tau_\infty + c/R$. This fit yields $\tau_\infty = 0.43 k_B T/\sigma$, $c = 1.1 k_B T$ and $\gamma_{wl} = 2.016 k_B T/\sigma^2$. Note that with this value of γ_{wl}, the condition for complete wetting would be satisfied $\gamma_{ws} + \gamma_{sl} - \gamma_{wl} = -0.02 k_B T/\sigma^2$. This would agree with the conclusion of Ref. [98]. However, the statistical inaccuracy in this estimate is appreciable. We can compare our fitted value for τ_∞ with a naive estimate by assuming that the contribution to the free energy due to line tension is really nothing else than the surface free energy of the lateral surface of a cylinder of height 1σ. Assuming that the lateral surface free-energy density is approximately equal to $\gamma_{ls}^{(110)}$, our estimate for τ_∞ would be $\tau_\infty \approx 0.64 k_B T/\sigma$, which is within 50% of the numerical

result. An estimate of the curvature correction to τ_{Line} would necessarily be even cruder. From the simulations, we can also determine the orientation and shape of the

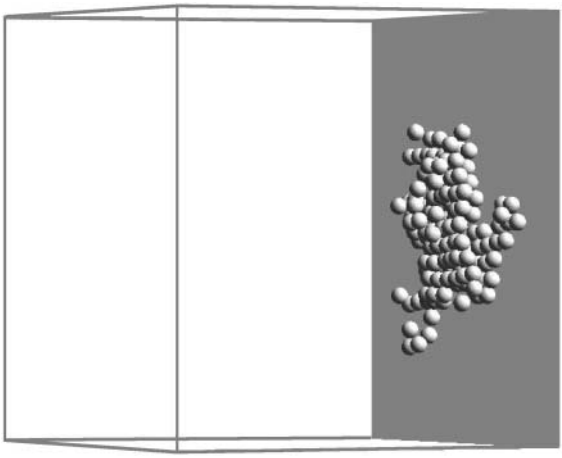

Fig. 35. Sideview of the snapshot of a crystal nucleus of size $n = 150$

incipient crystal nucleus. Figure 35 shows a snapshot of a critical nucleus containing 150 particles. From the figure, it is clear that the (111) plane attaches to the wall. Note that the critical nucleus is quite flat. Clearly, small nuclei prefer to spread on the surface rather to grow into the bulk. This is in agreement with the CNT predictions in the case where the (111) face wets the wall, either completely or very nearly so.

The fact that the range of metastability becomes very narrow might provide a powerful tool for the determination of the freezing density in experiments. Using confocal microscopy it should be possible to detect the formation of crystallites on a flat surface. Provided the interaction of the particles with the wall is the same as the interparticle potential, such crystallites will be first observed under conditions where the bulk density differs less than 1% from its value at coexistence. Our simulations suggest that pre-freezing first occurs at a pressure that is some 2% below the coexistence pressure, but, as explained above, this estimate is subject to a large statistical uncertainty.

8 Concluding Remarks

Computer simulations of crystal nucleation play a dual role. On the one hand, they can be used as a direct test of existing nucleation theories and, on the other, they can be compared directly with experiments (provided we have a good model for the experimental system). The fact that both types of comparisons lead to discrepancies, is

interesting. It suggests that the existing nucleation theories may need to be improved, and it indicates that there is something wrong with our interpretation of nucleation experiments. There may be a problem with our model, or with our assumption about the experimental conditions ("steady-state, homogeneous nucleation"). Of course, there may also be problems with our numerical approach. It is appropriate to consider the latter possibility in this paragraph. As we discussed in the text, there is a certain degree of arbitrariness in the choice of the order parameter that measures crystallinity. Hence, the reported size of the crystal nuclei should be taken with a grain of salt. However, as long as the real size of the nucleus is related linearly to the computed size, the height of the nucleation barrier is not affected by a different choice of order parameter. Any estimate of the surface free energy that is based on this height, is therefore also insensitive to the choice of order parameter. However, if we use the complete *shape* of the nucleation barrier to compute the surface free energy, then we may expect to find that the results depend on the choice of order parameter. In fact, this is not surprising, as the surface free energy of a spherical object necessarily depends on our choice for the location of the surface (e.g. surface of tension or equimolar surface). Finally, the nucleation *rate* should not depend at all on our choice of order parameter: this is a true, physical observable that cannot depend on the scheme that we use to compute it.

We should always bear in mind that the Classical Theory of Nucleation is, in essence, a macroscopic theory. But, at the microscopic level, such a level of description is not adequate. In the end, all observable quantities should be expressed as functions of material properties that are, themselves, unambiguously observable.

Acknowledgements

We gratefully acknowledge Alfons van Blaaderen and Thomas Palberg for helpful discussions. Thomas Palberg we thank for permission to show Fig. 3 and Evert Jan Meijer for permission to show Fig. 19. The work of the FOM Institute is part of the research program of FOM and is made possible by financial support from the Netherlands Organization for Scientific Research (NWO).

A
Distribution of Cluster Sizes in Equilibrium

The distribution of cluster sizes can be derived microscopically from statistical mechanics. The derivation is based on Refs. [10, 101, 9]. The partition function of a system containing N particles in a volume V at temperature T is given by

$$Q(N,V,T) = \frac{1}{\Lambda^{3N} N!} \int d\mathbf{r}^N \exp[-\beta U(\mathbf{r}^N)].$$

Here $U(\mathbf{r}^N)$ is the potential energy of the configuration with coordinates $\mathbf{r}^N$ and $\Lambda = h/\sqrt{2\pi mkT}$ is the thermal de Broglie wavelength. Now we assume that we

have a criterion, that enables us to identify a cluster in our system. We then define a function $w_n(\mathbf{r}^n)$ such that

$$w_n(\mathbf{r}^n) = \begin{cases} 1 & \text{if all } n \text{ particles belong to the cluster} \\ 0 & \text{otherwise} \end{cases}$$

In addition, we define a function $w_r(\mathbf{r}^N) = \prod_{i=n+1}^{N}[1 - w_{n+1}(\mathbf{r}^n, \mathbf{r}_i)]$, which ensures that all other particles do not belong to the cluster

$$w_r(\mathbf{r}^N) = \begin{cases} 1 & \text{if no other particle belongs to the cluster} \\ 0 & \text{if any other particle belongs to the cluster} \end{cases}$$

We can then define a partition function for a system that contains at least one n-particle cluster

$$Q_n(N, V, T) = \frac{1}{\Lambda^{3n} n!} \frac{1}{\Lambda^{3(N-n)}(N-n)!} \times \int d\mathbf{r}^n \int d\mathbf{r}^{N-n} w_n(\mathbf{r}^n) w_r(\mathbf{r}^N) \exp[-\beta U(\mathbf{r}^n, \mathbf{r}^{N-n})],$$

where we have used the fact that there are $N!/(n!(N-n)!)$ ways to select an n-particle cluster. Note that the remaining particles may still form additional clusters of size n. The product $w_n(\mathbf{r}^n)w_r(\mathbf{r}^{N-n}) = 1$, only if all $\mathbf{r}^n$ particles belong to the specified cluster and all the other $\mathbf{r}^{N-n}$ do not. We now rewrite the potential energy of the system as the sum of contributions from the particles in the cluster $U_n(\mathbf{r}^n)$ and the contribution from all other particles $U_{N-n}(\mathbf{r}^{N-n})$, plus the contribution from the interactions between particles in the cluster and the others $U_{n,N-n}(\mathbf{r}^n, \mathbf{r}^{N-n})$. The partition function then becomes

$$Q_n(N, V, T) = \frac{1}{\Lambda^{3n} n!} \frac{1}{\Lambda^{3(N-n)}(N-n)!} \int d\mathbf{r}^{N-n} \exp[-\beta U_{N-n}(\mathbf{r}^{N-n})] \times \int d\mathbf{r}^n w_n w_r \exp[-\beta U_n(\mathbf{r}^n)] \exp[-\beta U_{n,N-n}(\mathbf{r}^n, \mathbf{r}^{N-n})].$$

We can now define effective potentials for all the particles in the cluster

$$U_n' = U_n - kT \ln[w_n],$$

and the interaction between cluster particles and the others

$$U_{n,N-n}' = U_{n,N-n} - kT \ln[w_r],$$

yielding

$$Q_n(N, V, T) = \frac{1}{\Lambda^{3(N-n)}(N-n)!} \frac{1}{\Lambda^{3n} n!} \int d\mathbf{r}^{N-n} \exp[-\beta U_{N-n}(\mathbf{r}^{N-n})] \int d\mathbf{r}^n \exp[-\beta U_n'] \exp[-\beta U_{n,N-n}'].$$

Multiplication of the right side by $Q(N-n,V,T)/Q(N-n,V,T)$ gives

$$Q_n(N,V,T) = \frac{1}{n!\Lambda^{3n}} Q(N-n,V,T) \int d\mathbf{r}^n \langle \exp[-\beta U'_{n,N-n}] \rangle \exp[-\beta U'_n], \tag{17}$$

where we have defined a potential of mean force

$$\langle \exp[-\beta U'_{n,N-n}] \rangle = \frac{\int d\mathbf{r}^{N-n} \exp[-\beta U'_{n,N-n}] \exp[-\beta U_{N-n}(\mathbf{r}^{N-n})]}{(N-n)!\Lambda^{3(N-n)} Q(N-n,V,T)}.$$

It is the average potential the particles in the cluster feel due to the interactions with all other particles. We define now the partition function of an n-mer as

$$q_n(V,T) = \frac{1}{n!\Lambda^{3n}} \int d\mathbf{r}^n \langle \exp[-\beta U'_{n,N-n}] \rangle \exp[-\beta U'_n]. \tag{18}$$

Note that $q_n(V,T,\mu)$ is the partition function of a cluster in which the interaction with the remaining $(N-n)$ molecules is included in the factor $\langle \exp[-\beta U'_{n,N-n}] \rangle$. The interaction with possible other clusters is also included as such clusters can still exist in the remaining $(N-n)$ particles. The partition function Eq. (18) can then be written as

$$Q_n(N,V,T) = Q(N-n,V,T) q_n(V,T).$$

The probability to find at least one cluster of size n is then given by

$$P_n = \frac{Q_n(N,V,T)}{Q(N,V,T)} = \frac{Q(N-n,V,T)}{Q(N,V,T)} q_n(V,T).$$

As the free energy of the system is given by $F = -kT \ln[Q]$, the above equation becomes

$$P_n = q_n(V,T) \exp[-\beta(F(N-n,V,T) - F(N,V,T))].$$

Using

$$F(N-n,V,T) \approx F(N,V,T) - \left(\frac{\partial F}{\partial N}\right)_{V,T} n$$

it follows that

$$P_n = q_n(V,T) \exp[+\beta\mu n].$$

The problem with this definition of the probability is that it depends on the volume V. To see this we rewrite Eq. (18)

$$q_n(V,T) = \frac{1}{n!\Lambda^{3n}} \int d\mathbf{r}^n \exp[-\beta U_{eff}],$$

where we defined an effective potential $U_{eff} = \langle U'_{n,N-n} \rangle + U'_n$. Rewriting the partition function in terms of the center of mass of the cluster yields

$$q_n(V,T) = \frac{n^3}{n!\Lambda^{3n}} \int dR_{CM} \int d\mathbf{r}'^{n-1} \exp[-\beta U_{eff}].$$

Performing the integral over the center of mass and defining a partition function of the cluster in terms of the internal coordinates we get

$$q_n = \frac{V}{\Lambda_n^3} \times q_n^{internal},$$

where $\Lambda_n = h/\sqrt{2\pi nmkT}$ is the de Broglie wavelength of the cluster and

$$q_n^{internal} = \frac{n^{3/2}}{\Lambda^{3(n-1)}n!} \int d\mathbf{r}'^{n-1} \exp[-\beta U_{eff}].$$

It is better to define an intensive probability distribution

$$\frac{P_n}{N} = \frac{1}{\rho \Lambda_n^3} q_n^{internal} \exp[-\beta \mu n],$$

where ρ is the number density of the system. For rare clusters we can write the probability as

$$P_n = p_n(1) + p_n(2) + \cdots \approx p_n(1), \tag{19}$$

where $p_n(i)$ is the probability that there are exactly i clusters of size n. If we assume that the formation of different clusters is uncorrelated $p_n(i) = [p_n(1)]^i$, then we can neglect higher order terms provided the probabilities are small, $p_n(1) \ll 1$. As the average number of clusters of size n is equal to

$$N_n = 1p_n(1) + 2p_n(2) + 3p_n(3) + \cdots \tag{20}$$

we can write in the case of rare clusters

$$\frac{P_n}{N} \approx \frac{N_n}{N} = \frac{1}{\rho \Lambda_n^3} q_n^{internal} \exp[-\beta \mu n] \tag{21}$$

We note that this is a classical result and should not depend on Planck's constant h, and, in fact it does not, as the ideal gas part of the chemical potential

$$\mu = \mu^{ex} + kT \ln[\Lambda]$$

cancels the h in Λ_n.

The main point of Eq. (21) is that we can write down a microscopic expression for the equilibrium number of n-clusters if this number, which is equal to the probability of finding one cluster of size n, is much less than one. Using Eq. (6) this in turn defines an intensive Gibbs free-energy of the cluster where the reference state is the homogeneous phase:

$$\frac{N_n}{N} = \exp[-\Delta G(n)/k_B T]. \tag{22}$$

This is the key relation which enables us to compute a nucleation barrier in a Monte Carlo simulation.

B
Calculation of the Chemical Potential

Here we describe the calculation of the chemical potential for the monodisperse hard-sphere system. For the calculation of the chemical potential of the two phases, we performed a thermodynamic integration. The Helmholtz free energy F, per particle and in units of the thermal energy k_BT, of a liquid is determined by integrating the equation of state, starting from low densities, where the fluid behaves like an ideal gas [15]:

$$\frac{F(\rho)}{Nk_BT} = \frac{F^{id}(\rho)}{Nk_BT} + \frac{1}{k_BT}\int_0^\rho d\rho' \left(\frac{P(\rho') - \rho' k_BT}{\rho'^2}\right),$$

where $P(\rho)$ is the pressure and $F^{id}(\rho)/Nk_BT = \ln(\rho) - 1$ the free energy of an ideal gas at density ρ. The corresponding chemical potential is given by:

$$\frac{\mu(\rho)}{k_BT} = \frac{F(\rho)}{Nk_BT} + \frac{P(\rho)}{\rho k_BT}.$$

The calculation of the chemical potential of the solid is slightly more complicated. The reason is that it is not possible to perform the integration from the ideal gas limit, as the solid melts at lower densities. One has to calculate the excess free energy of a solid at a reference density where the solid is stable, which requires a different thermodynamic integration technique, the so-called Einstein integration. The idea is to transform the solid reversibly into an Einstein crystal, where the atoms are coupled harmonically to their lattice sites. The free energy can be calculated very precisely and we use the results from Polson et al. [102] for the excess free energy of a (defect free) hard sphere solid at coexistence: $F^{ex}(\rho_{coex} = 1.0409)/Nk_BT = 5.91889$. From the above equation we can then calculate the chemical potential of the solid at any other density according to:

$$\frac{\mu(\rho)}{k_BT} = \frac{F^{id}(\rho)}{Nk_BT} + 5.91889 + \frac{1}{k_BT}\int_{\rho_{coex}}^\rho d\rho' \left(\frac{P(\rho') - \rho' k_BT}{\rho'^2}\right) + \frac{P(\rho)}{\rho k_BT}.$$

For the equation of state $P(\rho)$ we used the analytical expressions by Hall [33] for the liquid and the solid. The integration was performed numerically.

C
Surface Free Energies of Critical Nuclei

In general, the value of the surface tension (or, more generally, surface free-energy density) depends on the criterion used to define the surface of a cluster. However, in the special case that we consider a critical nucleus, there exists a thermodynamic

relation between the height of the nucleation barrier and the surface free-energy density associated with the thermodynamic surface of tension. Below, we derive this relation.

Consider two systems. System I contains the homogeneous, metastable phase β. System II contains the parent phase (β) in unstable equilibrium with a critical nucleus of phase α. We consider the general case that the parent phase is an n-component mixture. The height of the nucleation barrier can be computed in several ways (depending on the thermodynamic variables that we keep fixed). For instance, for a system at constant pressure and temperature, the nucleation barrier is given by the difference in Gibbs free energy between states II and I. To compute this barrier, we first evaluate the difference in the internal energy

$$\Delta U = U^{\mathrm{II}} - U^{\mathrm{I}}. \tag{23}$$

The internal energy of system I is given by

$$U^{\mathrm{I}} = T^{\mathrm{I}} S^{\mathrm{I}} - p^{\mathrm{I}} V^{\mathrm{I}} + \sum_{i=1}^{n} \mu_i^{\mathrm{I}} N_i, \tag{24}$$

where μ_i^{I} is the chemical potential of component i in state I. As state II is also in equilibrium (be it an unstable one), the chemical potentials of all species are also constant throughout the system – even though the system itself is inhomogeneous. The internal energy of system II is given by

$$\begin{aligned} U^{\mathrm{II}} &= T^{\mathrm{II}} S^{\mathrm{II}} - p_\alpha^{\mathrm{II}} V_\alpha^{\mathrm{II}} - p_\beta^{\mathrm{II}} V_\beta^{\mathrm{II}} + \gamma A + \sum_{i=1}^{n} \mu_i^{\mathrm{II}} N_i \\ &= T^{\mathrm{II}} S^{\mathrm{II}} + (p_\beta^{\mathrm{II}} - p_\alpha^{\mathrm{II}}) V_\alpha^{\mathrm{II}} - p_\beta^{\mathrm{II}} V^{\mathrm{II}} + \gamma A + \sum_{i=1}^{n} \mu_i^{\mathrm{II}} N_i \end{aligned} \tag{25}$$

We consider the situation that the nucleus is formed at constant pressure and temperature. In that case, $p^{\mathrm{I}} = p_\beta^{\mathrm{II}} = p$, $T^{\mathrm{I}} = T^{\mathrm{II}} = T$ and $\mu_i^{\mathrm{I}} = \mu_i^{\mathrm{II}} = \mu_i$. The last equality follows because the chemical potential in the parent phase is a function of P and T only. The difference between the internal energies of systems I and II is then given by

$$\Delta U = T \Delta S + (p - p_\alpha^{\mathrm{II}}) V_\alpha^{\mathrm{II}} + \gamma A - p \Delta V, \tag{26}$$

where $\Delta S = S^{\mathrm{II}} - S^{\mathrm{I}}$ and $\Delta V = V^{\mathrm{II}} - V^{\mathrm{I}}$. Note that the terms involving the chemical potentials drop out of the expression for ΔU. The expression for the nucleation barrier then becomes

$$\Delta G = \Delta U + p \Delta V - T \Delta S = (p - p_\alpha^{\mathrm{II}}) V_\alpha^{\mathrm{II}} + \gamma A. \tag{27}$$

This equation holds for every dividing surface. Moreover, we have not made any approximations concerning the compressibility of either phase, nor concerning the

interfacial free energy. If we choose the surface of tension as the dividing surface, then we can use the Laplace equation ($\Delta p = 2\gamma_s/R_s$) to express the height of the barrier as

$$\Delta G = \frac{4}{3}\pi R_s^2 \gamma_s = \frac{2\pi}{3}\Delta p R_s^3. \tag{28}$$

In what follows, it will turn out to be convenient to express the surface tension γ_s in terms of the barrier height ΔG and the Laplace pressure Δp

$$\gamma_s = \left(\frac{3}{16\pi}\right)^{1/3} \Delta G^{1/3} \Delta p^{2/3}. \tag{29}$$

We stress that, for every component, the chemical potentials in the parent phase and in the critical nucleus are the same. In the absence of the Laplace pressure, the chemical potentials in phase α would be lower than those in phase β. The effect of the Laplace pressure is to compensate this difference for every component i. At first sight, it would seem that the computation of Δp is an intractable problem for a multicomponent system – to satisfy the condition that $\mu_i^\alpha = \mu_i^\beta$ for all i, it is not enough to compress phase α; we should also change its composition. The problem is greatly simplified if we make use of the semi-grand canonical ensemble. In the semi-grand ensemble, the independent variables that describe the state of an n-component system are: the temperature T, the pressure P, the total number of particles N and the set of $n-1$ differences in the chemical potential ($\Delta\mu_i$) between a reference species (say, species 1) and all other species $i \neq 1$. The number of components n can be infinite.

At coexistence, the chemical potentials of all species i in the two phases, are equal: $\mu_i^\alpha = \mu_i^\beta$. In the notation of the semi-grand ensemble, this means that, at coexistence, the temperature and pressure of the two phases are equal, as are all $\Delta\mu_i$, and finally also the chemical potential μ_1 of the reference compound. Now consider what happens if we supersaturate the parent phase, for instance by compression (the analysis for the case of supercooling follows by analogy). In the semi-grand ensemble we perform this supersaturation by increasing P, while keeping T and all $\Delta\mu_i$ constant. Note that this route need not correspond to the physical route for supersaturation. The reason is the physical route is (usually) to supersaturate *at constant composition*. But in that case, all $\Delta\mu_i$ change by different amounts, and this is precisely the factor that complicates the analysis of nucleation in multicomponent systems.

Suppose that we have compressed the system up to a pressure P_β where μ_1 (and thereby all μ_i) in the parent phase have increased by an amount $\Delta\mu^\beta$. An equal compression of the phase α leads to an increase $\Delta\mu^\alpha$ in the chemical potential of all species in that phase. Obviously, $\Delta\mu^\alpha$ is less than $\Delta\mu^\beta$, because beyond coexistence, phase β is metastable. However, we can compress phase α to a higher pressure P_α such that

$$\Delta\mu^\alpha(P_\alpha) = \Delta\mu^\beta(P_\beta) \tag{30}$$

Note that, as we are working in the semi-grand ensemble where we keep all $\Delta\mu_i$ constant, we have thus achieved equality of the chemical potentials in the two phases

for *all* species in the multicomponent mixture. In homogeneous nucleation, it is the Laplace pressure Δp that ensures that the chemical potential of every individual species is equal inside and outside the critical nucleus. We can therefore make the immediate identification:

$$\Delta p = P_\alpha - P_\beta \tag{31}$$

Of course, once we have determined the pressure P_a, then the density and composition of phase α follow.

In a simulation, we can solve Eq. 30 by making use of the fact that, for a semi-grand ensemble we have the following relation:

$$\frac{\partial \mu_1}{\partial P} = \frac{V}{N}. \tag{32}$$

We can compute the average volume V in a semi-grand simulation, and hence we can obtain $\Delta\mu$ by integration. Our expression for the Laplace pressure then becomes

$$\int_{P_{coex}}^{P_\beta+\Delta p} \langle V(P)\rangle_\alpha \, dP = \int_{P_{coex}}^{P_\beta} \langle V(P)\rangle_\beta \, dP. \tag{33}$$

This can also be written as

$$\int_{P_\beta}^{P_\beta+\Delta p} \langle V(P)\rangle_\alpha \, dP = \Delta\mu^\beta(P_\beta). \tag{34}$$

For an incompressible system, we can simplify this expression further, but we will not do this here. Once we have computed Δp, we can estimate the interfacial free-energy γ_s by using our numerical information about the nucleation barrier ΔG, using Eq. (29):

$$\gamma_s = \left(\frac{3}{16\pi}\right)^{1/3} \Delta G^{1/3} \Delta p^{2/3}.$$

References

1. Fahrenheit DB (1724) Phil. Trans. Roy. Soc. 39:78 149
2. Turnbull D, Fischer JC (1949) J. Chem. Phys. 17:71 149, 151, 152
3. Kelton KF (1991) Solid State Physics 45:75 149, 173
4. Palberg T, (1999) J. Phys.: Condens. Matter 11:323 152, 153, 165, 166
5. Harland JL, van Megen W (1997) Phys. Rev. E 55:3054 152, 153, 164, 165, 167, 187, 189, 191
6. Heymann A, Stipp C, Sinn C, Palberg T (1998) J. Coll. Interf. Sci. 206:119 152, 153, 165
7. Davidchack RL, Laird BB (2000) Phys. Rev. Lett. 85:4751 152, 165, 192, 195
8. Auer S, Frenkel D (2003) submitted to J. Chem. Phys. 154, 164, 172
9. Reiss H, Bowles RK (1999) J. Chem. Phys. 111:7501 154, 198

10. ten Wolde PR (1998), Numerical Study of Pathways for Homogeneous Nucleation (available from: http://www.amolf.nl) Ph.D. thesis, University of Amsterdam, Amsterdam, The Netherlands. 154, 198
11. Steinhardt PL, Nelson DR, Ronchetti M (1983) Phys. Rev. B 28:784 154
12. van Duijneveldt JS, Frenkel D (1992) J. Chem. Phys. 96:4655 154
13. ten Wolde PR, Ruiz-Montero MJ, Frenkel D (1995) Phys. Rev. Lett. 75:2714 154, 167, 184
14. Torrie GM, Valleau JP (1974) Chem. Phys. Lett. 28:578 158
15. Frenkel D, Smit B (2002) Understanding Molecular Simulations: from Algorithms to Applications, Academic Press San Diego 160, 178, 187, 201
16. Geyer CJ, Thompson EA (1995) J. Am. Stat. Assoc. 90:909 160, 164
17. Chandler D (1978) J. Chem. Phys. 68:2959 161
18. Ruiz-Montero MJ, Frenkel D,Brey JJ (1997) Mol. Phys. 90:925 161
19. Cichocki B, Hinson K (1990) Physica A 166:473 162, 163, 173
20. Medina-Noyola M (1988) Phys. Rev. Lett. 60:2705 163
21. Batchelor GK (1976) J. Fluid. Mech. 74:1 163
22. Cichocki B, Felderhof BU (1988) J. Chem. Phys. 89:1049 163
23. Beenakker CWJ, Mazur P (1983) Physica A 120:388 163
24. Tokuyama M, Oppenheim I (1994) Phys. Rev. E 50:R16 163
25. van Duijneveldt JS, Lekkerkerker HNW (1995) Science and Technology of Crystal Growth, edited van der Eerden JP and O. S. L. Bruinsma OSL, Kluwer-Academic Dordrecht 163
26. van Megen W, Underwood SM (1994) Phys. Rev. E 49:4206 163
27. Hoover WG, Ree FH (1968) J. Chem. Phys. 49:3609 164, 187, 188, 193
28. Vrij A. et al. (1983) Faraday Discuss. chem. Soc. 76:19 164
29. Pusey PN, van Megen W (1986) Nature 320:340 164, 175, 187, 188
30. Schätzel K, Ackerson BJ (1993) Phys. Rev. E 48:3766 164, 167
31. Sinn C, Heymann A, Stipp A, Palberg T (2001) Progr Coloid Polym Sci 118:266 164, 166, 167, 190, 191
32. Auer S, Frenkel D (2001) Nature 409:1020 164, 170, 180, 189, 190, 194, 195
33. Hall KR (1970) J. Chem. Phys. 57:2252 165, 195, 202
34. Cacciuto A, Auer S, Frenkel D (2003) accepted J. Chem. Phys. 165
35. Auer S, Frenkel D (2001) Nature 413:711 165, 170, 180
36. Cheng Z. et al. (2002) Phys. Rev. Lett. 88:015501 166
37. Dixit NM, Zukoski CF (2001) Phys. Rev. E 64:041604 166
38. Volkov I, Cieplak M, Koplik J, Banavar R (2002) Phys. Rev. E 66:061401 167
39. Cheng Z (1998) Colloidal Hard Sphere Crystallization and Glass Transition, Ph.D. thesis, Pinceton University, Princeton, US 163, 167
40. Ostwald W (1897) Z. Phys. Chem. 22:289 167
41. Alexander S, McTague JP (1978) Phys. Rev. Lett. 41:702 167
42. Klein W, Leyvraz F (1986) Phys. Rev. Lett. 57:2845 167
43. Klein W (2001) Phys. Rev. E 64:056110 167
44. Groh B, Mulder B (1999) Phys. Rev. E 59:5613 167
45. Pronk S, Frenkel D (1999) J. Chem. Phys. 110:4589 168
46. Mau SC, Huse DA (1999) Phys. Rev. E 59:4396 168
47. Pusey PN et al. (1989) Phys. Rev. Lett. 63:2753 168, 188
48. Haddon MS, Haddon SB, Poon WCK (2001) J. Phys.: Condensed Matter 13:553 168
49. Zhu J et al. (1997) Nature 387:883 168
50. O'Malley B, Snook I (2003) Phys. Rev. Lett. 90:085702 169

51. Pusey PN (1991) Les Houches; Liquids, Freezing and Glass Transition (edited by Hansen JP, Levesque D, Zinn-Justin J), North-Holland Amsterdam 170
52. Kofke DA, Bolhuis PG (1999) Phys. Rev. E 59:618 170, 173, 188
53. Fasolo M, Sollich P (2003) Phys. Rev. Lett. 91:068301 170
54. Auer S (2002) Quantitative prediction of crystal nucleation rates for spherical colloids: A computational study, Ph.D. thesis, University of Amsterdam, Amsterdam, The Netherlands (available from: http://www.amolf.nl) 173
55. Viisanen Y, Strey R, Reiss H (1993) J. Chem. Phys. 99:4680 173
56. Oxtoby DW, Kashchiev D (1994) J. Chem. Phys. 100:7665 173
57. Oxtoby D (2001) Nature 413:694 173
58. Shi FG, Tong HY, Ayers JD (1995) Appl. Phys. Lett. 67:350 173, 174, 175
59. ten Wolde PR, Frenkel D (1997) Science 277:1975 173
60. Gasser U, Weeks ER, Schofield A, Pusey PN, Weitz DA (2001) Science 292:258 175, 177, 182, 183, 184, 185
61. Auer S, Frenkel D (2002) J. Phys.:Condens. Matter 14:7667 175, 190
62. Verweij EJW, Overbeek JTHG (1948) Theory of the Stability of Lyopholic Colloids, Elsevier New York 176
63. Alexander S et al. (1984) J. Chem. Phys. 80:5776 176
64. Bitzer F, Palberg T, Löwen H, Simon R, Leiderer P (1994) Phy. Rev. E 50:2821 176
65. Sirota EB, Ou-Yang HD, Sinha SK, Chaikin PM (1989) Phys. Rev. Lett. 62:1524 177
66. Robbins MO, Kremer K, Grest GS (1988) J. Chem. Phys. 88:3286 177
67. Azhar F El, Baus M, Ryckaert JP,Meijer EJ (2000) J. Chem. Phys. 112:5121 176, 177, 178, 183
68. Meijer EJ, Frenkel D (1991) J. Chem. Phys. 94;2269 177
69. Dhont JKG, Smits C, Lekkerkerker HNW (1992) J. Coll. Interf. Sci. 152:386 177
70. Okubo T (1994) Macro-ion characterization: from dilute solutionto complex fluids, ACS Symposium Series 548:364 Dordrecht 177
71. Schöpe HJ, Palberg T (2002) J.Phys.Condens.Matter 14:11573 177
72. Wette P, Schöpe HJ, Liu J, Palberg T (2003) Europhys. Lett. in press 177
73. Schöpe HJ (2000) Physikalische Eigenschaften kolloidaler Festkörper Ph.D. thesis, Johannes Gutenberg Universität Mainz, Mainz, Germany 183
74. Hoogenboom JP, Derks D, Vergeer P, van Blaaderen A (2002) J. Chem. Phys. 117:11320 185
75. Auer S, Poon WCK, Frenkel D (2003) Phys. Rev. E 67:020401 186
76. de L. Costello BA, Luckham PF (1993) J.Colloid Interface Sci. 156:72 186
77. de L. Costello BA et al. (1992) Langmuir 8:464 186
78. Alexander S (1977) J. Phys. (Paris) 38:983, de Gennes PG (1988) Adv. Colloid Interface Sci. 27:189 186
79. Russel WB, Saville DA, Schowalter WR (1989) Colloidal Dispersions, Cambridge University Press, Cambridge 187
80. Antl L et al. (1986) Colloids Surf. 17:67 187
81. Mewis J et al. (1989) A.I.Ch.E.J. 35:415, Cairns RJR et al. (1976) J. Colloid Interface Sci. 54:51 Doroszkowski A, Lambourne R (1971) J. Polym. Sci. Part C:Polym. Symp. 34:253 van Megen W, Underwood SM (1990) Langmuir 6:35 Markovic I et al. (1986) Langmuir 2:625 187, 188
82. Cebula DJ et al. (1983) Colloid Polymer Sci. 261:555 187, 188
83. Pusey PN, van Megen W (1987) Physics of Complex and Supermolecular Fluids (ed. S.A. Safran and N.A. Clark, Wiley, New York) 187, 188
84. Bryant G et al. (2002) Phys. Rev. E 66:060501(R). 189

85. Yethiraj A, van Blaaderen A (2003) Nature 421:513 189
86. Auer S, Frenkel D (2003) Phys. Rev. Lett. 91:015703 191
87. van Blaaderen A, Ruel R, Wiltzuis P (1997) Nature 385:321 191
88. Hoogenboom JP, van Langen-Suurling AK, Romijn J, van Blaaderen A (2003) Phys. Rev. Lett. 90:138301 191
89. Hoogenboom JP, Derks D, Vergeer P, van Blaaderen A (2002) J. Chem. Phys. 117:11320. 191
90. Hoogenboom JP, Vergeer P, van Blaaderen A (2003) J. Chem. Phys. 119:3371 191
91. Heni M, Löwen H (2000) Phys. Rev. Lett. 85:3668 191
92. Kose A, Hachisu S (1976) J. Coll. Interf. Sci. 55:487 191
93. Gast AP, Russel WB, Hall CK (1986) J. Coll. Interf. Sci. 55:161 191
94. Kaplan PD, Rouke JL, Yodh AG, Pine DJ (1994) Phys. Rev. Lett. 72:582 191
95. Dinsmore AD, Warren PB, Poon WCK, Yodh AG (1997) Europhys. Lett. 40:337 191
96. Martellozzo VC (2001) Crystallization and Phase Separationin Colloidal Systems, Ph.D. thesis, University of Edinburgh, Edinburgh, Scotland 191
97. Poon WCK, Warren PB (1994) Europhys. Lett. 28:513 191
98. Courtemanche DJ, van Swol F (1992) Phys. Rev. Lett. 69:2078 191, 196
99. Turnbull D (1950) J. Chem. Phys. 18:198 192
100. Heni M, Löwen H (1999) Phys. Rev. E 60:7057 192
101. ten Wolde PR, Ruiz-Montero M, Frenkel D (1996) Faraday Discuss. 114:9932 198
102. Polson J.M. et al. (2000) J. Chem. Phys. 112:5339 177, 202

Adv. Polym. Sci. (2005) 173:209–252
DOI:10.1007/b99431

Structure of Polymer Melts and Blends: Comparison of Integral Equation Theory and Computer Simulations

David R. Heine[1,2], Gary S. Grest[1,3], and John G. Curro[1,4]

[1] Sandia National Laboratories, Albuquerque, New Mexico 87185, USA
[2] *drheine@sandia.gov*
[3] *gsgrest@sandia.gov*
[4] *jgcurro@sandia.gov*

Abstract This review covers the most recent developments using the Polymer Reference Interaction Site Model (PRISM) integral equation theory to study polymer melts and blends. Comparisons to computer simulations are presented that have isolated the deficiencies in the theory and led to improvements including the self-consistent approach where the theory is coupled with single chain Monte Carlo simulations. Using recent simulation results, we outline the strengths and weaknesses of the theory at different levels of detail, from coarse grained bead-spring models to explicit atom models. We conclude with an overview of future directions that are beginning to be undertaken.

1 Introduction

The versatility of polymers as plastics, gels, rubbers, and adhesives has created an industry that has undergone enormous growth over the past several decades. The presence of polymers in nearly every aspect of our daily life is a testament to their versatility. Studying the nature of polymer molecules has revealed that this versatility is due to their extremely rich and varied molecular structure. Our ability to engineer materials on the molecular level provides us the means to exploit this range of structures to create materials with a wide range of properties. However, beyond the technological limitations of producing these materials, we are limited by our understanding of precisely how changes in the molecular structure and the interplay between different types of polymers vary the bulk behavior.

The problem of calculating the physical properties of polymer systems from information about the polymer structure was pioneered by Flory [1] and others starting in the 1950s. Many of these original contributions are still useful today. Although the limitations of the classic Flory-Huggins theory (random mixing, incompressibility, lattice model, etc.) are well recognized, this theory is still invaluable in understanding the phase behavior of polymer solutions, blends, and copolymers. More recently, field theoretic methods [2] as well as scaling [3] and renormalization group approaches [4] have led to a deeper understanding of polymers on a global length scale. Many important properties of polymer systems are not “universal" but rather depend on the details of the local packing which, in turn, depends on the specific architecture of the polymer. Field theoretic methods are generally not useful for such problems. The integral equation approach for describing the packing of atomic liquids was first addressed by Kirkwood and others many years ago. For a review of early work see [5, 6]. This led in the 1960s to the Percus-Yevick theory [7, 8] which has been shown to be quite accurate for the packing of atomic liquids [6]. In the 1970s, Chandler and Andersen [9, 10] extended these integral equation methods to molecular fluids. Their theory, the Reference Interaction Site Model (RISM theory) was applied by Chandler and Lowden [10, 11, 12, 13] to many rigid, small molecule liquids. Comparisons with x-ray scattering experiments and computer simulations showed that the RISM theory was accurate for predicting the structure of small molecule liquids at liquid-like densities. In 1987 Curro and Schweizer [14, 15, 16] extended the RISM theory of Chandler and Andersen to polymer liquids. This approach, called the Polymer Reference Interaction Site Model (PRISM theory), was applied to calculate the packing in homopolymer liquids, blends, and copolymers. PRISM theory was first reviewed in 1994 [17] and then again in 1997 [18]. Since

that time additional work on self-consistent PRISM theory has been carried out on atomistic polymer models and detailed comparisons have been made with computer simulations. In this review we focus on these recent developments and, in particular, the comparison between PRISM theory and MD simulations. It should be emphasized that other approaches have been developed to describe polymer liquids including the lattice cluster theory of Freed *et al.* [19, 20, 21] and the associating fluid model of Wertheim [22, 23, 24, 25, 26]. Other extensions of integral equation theories to polymers have been developed by Gan and Eu [27, 28, 29, 30, 31], Taylor and Lipson [32], and Attard [33]. These other approaches are beyond the scope of the present review and will not be discussed here.

The purpose of this chapter is to review some recent developments using PRISM theory to study polymer melts and blends and compare the results to MD simulations. We focus on the self-consistent PRISM (SC/PRISM) approach mentioned briefly in the most recent review [18]. Unlike comparisons to experiments, simulations can be performed using identical interaction potentials. This means that any discrepancies between theory and simulation are due to limitations of the theory and not due to the inaccuracy of the interaction potentials used. We present both the strengths and weaknesses of PRISM theory at three different levels of detail: coarse-grained bead-spring models, united atom models, and explicit atom models.

We begin by presenting an overview of the models used in this review in Sect. 2. PRISM theory is presented in Sect. 3 starting with the Ornstein-Zernike equation and ending with self-consistent PRISM theory. Sections 4 and 5 review recent results for polymer melts and blends, respectively. Section 6 outlines some of the newest applications of PRISM theory and a closing discussion is given in Sect. 7.

2 Models

The dispersion forces between all pairs of atoms are most commonly modeled using the Lennard-Jones (LJ) pair potential,

$$V(r) = 4\epsilon \left[\left(\frac{\sigma}{r}\right)^{12} - \left(\frac{\sigma}{r}\right)^{6} \right]. \tag{1}$$

Here ϵ and σ are, respectively, parameters fixing the energy and length scale. In most computer simulations, this potential is truncated at a distance $r = r_c$ and shifted so that $V(r_c) = 0$ for $r \geq r_c$. The structure of high density liquids is dominated by packing constraints and thus by the repulsive component of the LJ potential. The attractive component has little influence on the structure and is often treated using thermodynamic perturbation theory [6]. Barker and Henderson [34] showed that accurate results can be obtained by separating the LJ potential into an attractive component ($r > \sigma$) and a repulsive component, ($r < \sigma$). The repulsive component provides a convenient short-ranged potential that accurately reproduces the structure of simple

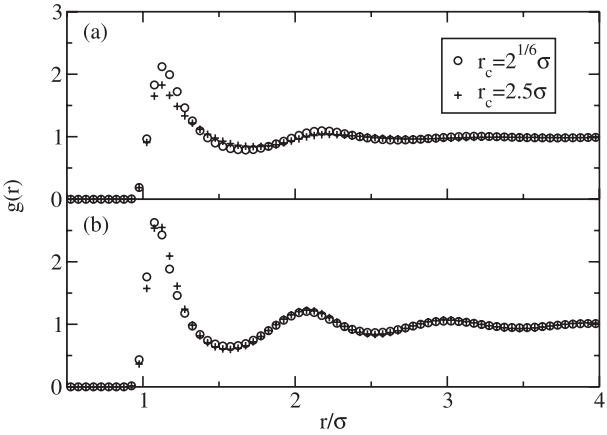

Fig. 1. Effect of attractive potentials on the intermolecular radial distribution function for an atomic Lennard-Jones system at (a) $\rho\sigma^3 = 0.55$ and (b) $\rho\sigma^3 = 0.85$ obtained from MD simulations

liquids. The attractive component is then treated as the perturbation to the repulsive reference system in order to determine the thermodynamic properties of the system. Weeks, Chandler, and Anderson [35, 36] divide the potential according to

$$V_a(r) = \begin{cases} -\epsilon & r \le 2^{1/6}\sigma \\ 4\epsilon\left[\left(\frac{\sigma}{r}\right)^{12} - \left(\frac{\sigma}{r}\right)^{6}\right] & r > 2^{1/6}\sigma, \end{cases} \tag{2}$$

$$V_r(r) = \begin{cases} 4\epsilon\left[\left(\frac{\sigma}{r}\right)^{12} - \left(\frac{\sigma}{r}\right)^{6} + \frac{1}{4}\right] & r \le 2^{1/6}\sigma \\ 0 & r > 2^{1/6}\sigma. \end{cases} \tag{3}$$

This approach is frequently used because the perturbation series is more rapidly convergent and may be truncated after the first-order term. The effect of neglecting the attractive part of the nonbond potential on the intermolecular pair correlation function is shown in Fig. 1 for a system of Lennard-Jones atoms. At lower densities (Fig. 1a), the attractions lead to an overall decrease in the structure. This effect becomes negligible at melt-like densities (Fig. 1b).

Polymeric systems have traditionally been modeled at one of three levels of detail: coarse grained, united atom or explicit atom. Coarse grained models are the simplest and have been widely used to study the long time, large-scale behavior of long, entangled polymers. Bead-spring continuum [37] and bond-fluctuation lattice models [38, 39, 40] are two widely used models in this category. United [41, 42, 43, 44, 45] and explicit atom models [46, 47, 48] are applicable when one is interested in examining the local properties of the polymer, including the local packing and dynamics. The specific versions of these three models used in the present study referred in order of increasing complexity are as follows:

2.1 Bead-Spring Model

Coarse-grained bead-spring models presented here are similar to those used in earlier studies of polymer melts and networks [49, 50] and tethered chains [51]. In this model, each chain consists of N beads, which are referred to as monomers, connected to form a linear chain. The interaction potential $V(r)$ between two monomers separated by a distance r is taken as a Lennard Jones 6 : 12 potential, Eq. 1. In most cases presented here, the cutoff, r_c, is chosen to give a purely repulsive interaction potential, $r_c = 2^{\frac{1}{6}}\sigma$.

Adjacent monomers along the chains are coupled through an anharmonic potential, $V_{ch}(r)$ given by

$$V_{ch}(r) = \begin{cases} -\frac{1}{2}kR_0^2 \ln\left[1 - (\frac{r}{R_0})^2\right] & r \le R_0 \\ \infty & r > R_0. \end{cases} \tag{4}$$

The parameters $k = 30\epsilon/\sigma^2$ and $R_0 = 1.5\sigma$ are chosen so that unphysical bond crossings and chain breaking are eliminated [49, 50, 51]. Because all of the interactions are short ranged, the model is very efficient computationally. To test the effect of stiffness on the local ordering and pair correlation functions, a bending term was added in some simulations [52, 53, 54].

$$V_{bend}(\theta) = k_{bend}\,(1 + \cos\theta) \tag{5}$$

The angle θ is defined as the angle in radians between **a**, **b**, **c**

$$\cos(\theta) := \frac{(\mathbf{b} - \mathbf{a}) \cdot (\mathbf{c} - \mathbf{a})}{\|\mathbf{b} - \mathbf{a}\|\,\|\mathbf{c} - \mathbf{a}\|}, \tag{6}$$

where **a**, **b**, **c** denote the position vectors for three neighboring sites.

Most of the results presented will be for $T = \epsilon/k_B$ and density $\rho\sigma^3 = 0.85$. Chain lengths varied from N=1 to 100. Systems consisted of 25,000 monomers, 50,000 dimers, 1,000 chains of length 10, and 500 chains of length 20, 50, and 100. All MD simulations, both for this model as well as for the united and explicit atom models, were run long enough that the chains moved their own size several times.

2.2 United Atom Model

The united atom model combines each carbon and its bonded hydrogen atoms, CH_x, into a single interaction site. This reduces the number of interaction sites compared to explicit atom models where all H atoms are included. Most of the polyolefin results presented here are for the united atom model known as TraPPE developed by Martin and Siepmann [55, 56]. This model has been optimized to give correct results for

the phase coexistence curve near the liquid-gas critical point for small molecules consisting of up to 12 carbon atoms. Each carbon with its associated hydrogen atoms is represented by a spherical site. Results for methyl terminated PDMS molecules use the united atom model developed by Sok et al. [57], though an improved model has recently been developed by Frischknecht and Curro [58].

Polyethylene has three characteristics that distinguish it from the bead-spring model: (1) The effective diameter of the sites ($\sim$3.9 Å) is considerably larger than the 1.54 Å bond distance. Hence adjacent sites are strongly overlapped. (2) The bond angle is harmonic about a fixed value, θ_0. (3) Torsional angles, ϕ, favor Gauche and anti conformations over eclipsed conformations. In the united atom model, inter- and intra-molecular pairs of sites interact with a Lennard-Jones (LJ) potential, Eq. (4), where the parameters for the various sites of the TraPPE model are given in Table 1. For some earlier work on polyethylene melts, slightly different values, $\epsilon = 0.092$ kcal mol^{-1} and $\sigma = 3.93$ Å, were used for the nonbonded LJ potential [59]. In the MD simulations the full potential is cut off at a distance of 12 Å (which includes most of the attractive tail). A few simulation results will be presented in which r_c is chosen so the interaction is purely repulsive as in the PRISM calculations. For the LJ parameters for sites of different type, the standard Berthelot scaling rules are applied,

$$\begin{aligned} \sigma_{\alpha\gamma} &= \tfrac{1}{2}\left(\sigma_\alpha + \sigma_\gamma\right) \\ \epsilon_{\alpha\gamma} &= \sqrt{\epsilon_\alpha \cdot \epsilon_\gamma}. \end{aligned} \tag{7}$$

For intra-molecular pairs the LJ potential is only applied if they are further than three covalent bonds apart.

Covalent bonds between nearest neighbor carbons are modeled by a simple harmonic potential around a finite average distance l_0,

$$V_{bond}(r) = \frac{1}{2} k_{bond} \left(r - l_0\right)^2 . \tag{8}$$

The constant k_{bond} is set to the experimental value 900 kcal mol^{-1} and the bond length $l_0 = 1.54$ Å regardless of the number of hydrogens bound to a particular carbon.

To respect the angular geometry of nearest- and next-to-nearest neighbor carbons a harmonic bending potential between three neighboring sites is introduced:

$$V_{bend}(\theta) = \frac{1}{2} k_{bend} \left(\theta - \theta_0\right)^2 . \tag{9}$$

The elasticity parameters k_{bend} and the equilibrium angles θ_0 for the various neighbor triplets are listed in Table 1.

Furthermore to incorporate the effect of transitional potential barriers between anti and Gauche conformations and different population densities of these states, a rotational potential for the dihedral angle Φ between nearest neighbor chain-like quadruplets **a**, **b**, **c**, **d** is introduced,

$$V_{rot}(\Phi) = \sum_{i=0}^{3} a_i \cos^i(\Phi), \tag{10}$$

where Φ is defined as

$$\cos(\Phi) := \left(\frac{(\mathbf{c}-\mathbf{b})\times(\mathbf{b}-\mathbf{a})}{\|(\mathbf{c}-\mathbf{b})\times(\mathbf{b}-\mathbf{a})\|}\right)\cdot\left(\frac{(\mathbf{d}-\mathbf{c})\times(\mathbf{c}-\mathbf{b})}{\|(\mathbf{d}-\mathbf{c})\times(\mathbf{c}-\mathbf{b})\|}\right). \tag{11}$$

Table 1 contains the parameters a_i for the various quadruplet combinations of sites. Note that with our definition of Φ, the angle $\Phi = 0^\circ$ corresponds to the *anti* state whereas in [56] (and many other works) *anti* corresponds to $\Phi = 180^\circ$.

For vinyl polyolefins with CH_3 side-groups, such as polypropylene (PP), these side groups are not constrained enough by the angle potentials with the backbone chain to remain on one side of the backbone chain in the course of a simulation. In nature such flips of tacticity cannot occur as the H-atom of the CH-group to which the CH_3-group is attached prevents this. Since in the united atom models the H-atom is not explicitly simulated, a symmetry-breaking potential is introduced to incorporate conservation of tacticity into the model. For this purpose the so-called improper harmonic torsional potential for the star-like CH_2-CH, CH_3-CH_2 quadruplets in PP is used,

$$V_{impr} = \frac{1}{2}k_{impr}\,(\Psi - \Psi_0)^2\,, \tag{12}$$

where Ψ is defined as

$$\cos(\Psi) = \left(\frac{(\mathbf{c}-\mathbf{b})\times(\mathbf{d}-\mathbf{b})}{\|(\mathbf{c}-\mathbf{b})\times(\mathbf{d}-\mathbf{b})\|}\right)\cdot\left(\frac{(\mathbf{c}-\mathbf{a})\times(\mathbf{d}-\mathbf{a})}{\|(\mathbf{c}-\mathbf{a})\times(\mathbf{d}-\mathbf{a})\|}\right) \tag{13}$$

and $\mathbf{a}$, $\mathbf{b}$, $\mathbf{c}$, $\mathbf{d}$ are the position vectors of the CH and CH_3 and the two backbone CH_2 groups (in the same order). Since ref. [56] does not include these parameters, some reasonable *ad hoc* assumptions were made by Pütz et al. [60]: k_{impr} was chosen to be identical to k_{bend} and $\Psi_0 = \pm 30.25^\circ$ depending on the intended tacticity of the chain.

For most of the results presented here, the MD simulations used a multiple time step second-order symplectic integrator (RESPA) [61] to solve the equations of motion. In some earlier simulations [59], the bond length was kept constant using the RATTLE algorithm [62]. For the polyolefins, the simulations were run using a 1.00 or 1.25 fs timestep while for PDMS [63], the timestep was 0.4 fs. Bonded interactions were updated every time step while angle, torsion, and improper forces were updated every two time steps and non-bonded Lennard-Jones and Coulomb forces every four time steps. For the polyolefins, N is the number of CH_x sites per chain. Details of system size and equilibration time can be found in the original papers [59, 60, 63, 64].

2.3 Explicit Atom Model

The explicit atom simulations have been applied to study linear PE and a number of models have been developed [46, 47, 48]. Here we present results for the model of Sorensen et al. [46] for the bond stretching, bond bending, torsional, and non-bonded potentials. In this case, the explicit atom nonbonded potential V(r) differs from the LJ form used for the coarse grained and united atom models and instead uses an exp-6 form[65],

$$V(r) = \epsilon \left[\left(\frac{6}{\zeta - 6} \right) \exp\left[\zeta (1 - r/R_0) \right] - \left(\frac{\zeta}{\zeta - 6} \right) (r/R_0)^{-6} \right]. \tag{14}$$

The model parameters used for the non-bonded interaction are given in Table 2. In the standard form of this potential, the exp-6 potential is non-monotonic in the repulsive regime and has a maximum at a separation r^*. In the MD simulations, separations $r < r^*$ are never accessed, and this cutoff plays no role since $V(r^*)/k_B T > 40$. However in the PRISM calculations, single-chain Monte Carlo simulations using the pivot algorithm are employed, and it is necessary to modify the standard potential at short distance in Eq. (14) so that $V(r) = V(r^*)$ for $r < r^*$ [64]. Some of the MD calculations and all of the PRISM calculations were done for a purely repulsive cut and shifted version of Eq. (14). Additional MD simulations were also carried out for the interaction potential truncated at either 6 or 12 Å [64].

Table 1. Interaction parameters for all CH_x groups [55, 56]

van der Waals	ϵ(kcal mol^{-1})		σ (Å)	
C	0.00099		6.40	
CH	0.0198		4.68	
CH_2	0.0912		3.95	
CH_3	0.1944		3.73	
Angle triplet	Θ_0		k_{bend} (kcal mol^{-1})	
$CH_x - C - CH_y$	109.47		123.75	
$CH_x - CH - CH_y$	112.00		123.75	
$CH_x - CH_2 - CH_y$	114.00		123.75	
Dihedral quadruplet	a_0	a_1	a_2	a_3
$CH_x - C - CH_2 - CH_y$	0.914913	2.74474	0	-3.65965
$CH_x - CH - CH_2 - CH_y$	0.783911	1.77528	0.443682	-3.50082
$CH_x - CH_2 - CH_2 - CH_y$	2.007	4.012	0.271	-6.290

Table 2. Non-bonded potential parameters for the explicit atom model [46]

pair	ϵ(kcal mol^{-1})	R_0(Å)	ζ
CC	0.094813	3.8719	11.964
CH	0.052021	3.2739	11.180
HH	0.009777	3.3706	12.606

3 PRISM Theory

3.1 Origins

3.1.1 *Ornstein-Zernike Equation*

The total correlation function, $h(r)$, is defined as $g(r) - 1$ where $g(r)$ is the radial distribution function describing the probability of finding a second particle a distance r from the center of a particle. For homogeneous fluids,

$$\rho^2 g(r) = \left\langle \sum_{i \neq j}^{N} \delta(\mathbf{r_i})\delta(\mathbf{r} - \mathbf{r_j}) \right\rangle \tag{15}$$

where ρ is the number density of molecules, $\delta(\mathbf{r_i})$ is the Dirac delta function for particle i and the sum is over all pairs of particles in the system.

The direct correlation function was first introduced by Ornstein and Zernike (OZ) [66]. They divide the total correlation function into a direct component and a combination of indirect components according to

$$h(r) = c(r) + \rho \int c(|r - r'|)h(r')dr' \tag{16}$$

where ρ is the density and $c(r)$ is the direct correlation function between two particles. The physical significance of the direct correlation function can be seen by iterating Eq. (16). This can be written as

$$\begin{aligned} h(r) = c(r) &+ \rho \int c(|r - r'|)c(r')dr' \\ &+ \rho^2 \int\int c(|r - r'|)c(|r' - r''|)c(r'')dr''dr' + \ldots \end{aligned} \tag{17}$$

The total correlation between particles at a distance r is an infinite sum of chains of direct correlations between these particles and intermediate particles [14, 6].

3.1.2 *RISM Theory*

The reference interaction site model (RISM) theory of Chandler and Andersen [9, 11, 10] is an extension of the theory of monatomic liquids. In RISM theory, each molecule is envisioned as a collection of spherically symmetric interaction sites. In most applications of RISM theory to small molecule liquids, Chandler and coworkers [9, 11, 12, 13, 10] modeled interaction sites as overlapping hard spheres. The primary difference between RISM theory and monatomic liquid theory is that the correlations can be propagated intramolecularly as well as intermolecularly. Chandler and Andersen generalized the OZ equation as follows for a single component fluid in Fourier space

$$\hat{h}(k) = \hat{\omega}(k)\hat{C}(k)[\hat{\omega}(k) + \rho\hat{h}(k)] \tag{18}$$

where $\hat{h}(k) = \rho \int d\mathbf{r} h(r) \exp(-i\mathbf{k}\cdot\mathbf{r})$ is the Fourier transform of $h(r)$ and ρ is the number density of interaction sites. The intramolecular correlation function in real space, $\omega(r)$, is the probability distribution between sites on the same molecule separated by a distance r.

The RISM equation can be considered to be a definition of the direct correlation function, $\hat{C}(k)$, but cannot be solved without specifying an approximate closure condition, which relates the total correlation function to the intermolecular pair correlation functions. For a fluid composed of fused hard spheres, the closure condition is satisfied in RISM theory by acknowledging that the pair correlation function is zero inside the hard core diameter (molecules do not occupy the same space) and assuming that the direct correlation function is zero outside of the hard core diameter (because "direct" interactions at distances greater than the hard core diameter for hard sphere particles are weak). This is a generalization of the Percus-Yevick approximation [7] and is based on the fact that the direct correlation function is short range for high density liquids. RISM theory has been successful at describing the structure of rigid diatomic and polyatomic molecular liquids [10, 11, 12, 13]. In general, RISM theory can reproduce all of the main features in the structure of simple molecular liquids at high density, but it has been shown to give incorrect results for quantities related to angular correlations in the fluid [67, 68].

3.1.3 *PRISM Equation*

The PRISM theory of Curro and Schweizer extends RISM theory to polymers by considering the intramolecular structure of flexible polymers [14, 15, 16, 69, 70, 17, 18]. The theory assumes that the Flory ideality concept is valid and polymers exhibit ideal behavior in the melt phase. This is justified by the fact that the intramolecular excluded volume is nearly balanced by intermolecular excluded volume when a chain is surrounded by identical chains, so excluded volume forces can be neglected [3, 71]. They also developed a perturbative scheme to account for chain end effects [15].

Since PRISM theory accounts for density fluctuations, it can be used to calculate of local structure and physical properties of polymer liquids. This is not possible, for example, in self-consistent field theory [2] where density fluctuations are neglected due to the incompressibility assumption.

For multi-component systems, the generalized OZ equation is conveniently written in Fourier space as

$$\hat{\mathbf{H}}(k) = \hat{\mathbf{\Omega}}(k) \cdot \hat{\mathbf{C}}(k) \cdot \left[\hat{\mathbf{\Omega}}(k) + \hat{\mathbf{H}}(k)\right] \tag{19}$$

where $\hat{\mathbf{H}}(k)$ and $\hat{\mathbf{C}}(k)$ have matrix elements $\hat{H}_{\alpha\gamma}(k) = \rho_\alpha \rho_\gamma \hat{h}_{\alpha\gamma}(k)$ and $\hat{C}_{\alpha\gamma}(k)$. Here, ρ_α is the site density of species α, $\hat{h}_{\alpha\gamma}(k)$ is the total correlation function between species α on one molecule and γ on another, and $\hat{C}_{\alpha\gamma}(k)$ is the direct intermolecular correlation function. The first term on the right side of Eq. (19) accounts for all pairwise interactions between two tagged molecules. The second term on the right side accounts for all pairwise interactions between two molecules mediated by one or more molecules.

Solution of the PRISM equation for a particular system requires determining the intramolecular correlation functions, $\hat{\Omega}_{\alpha\gamma}(k)$, and specifying a closure approximation. For rigid molecules, $\hat{\Omega}_{\alpha\gamma}(k)$ can be determined analytically. For example, the intramolecular correlation function for a rigid rod is written as

$$\hat{\Omega}(k) = \rho + \frac{2\rho}{N} \sum_{i=1}^{N} (N - i) \frac{\sin(kbi)}{kbi} \tag{20}$$

where b is the bond length. For flexible molecules, $\hat{\Omega}_{\alpha\gamma}(k)$ can be obtained using conformational preaveraging where the instantaneous intramolecular structure is replaced by its ensemble-averaged pair correlation function description [16, 14, 15]. Using this approach, $\Omega_{\alpha\gamma}(r)$ is defined as

$$\Omega_{\alpha\gamma}(r) = \tilde{\rho} \sum_{i\in\alpha, j\in\gamma} \omega_{ij}(r) \tag{21}$$

where $\tilde{\rho}$ is the chain density and $\omega_{ij}(r)$ is the normalized probability density between sites i and j on the same molecule. Analytical expressions for $\hat{\omega}_{ij}(k)$ exist for some flexible polymers, including the freely jointed homopolymer [72], diblock copolymer [73, 74] , or alternating copolymer [75].

These models provide a simple means of determining the intramolecular correlation function even for multicomponent systems, but the assumption of a freely jointed chain severely limits their predictive capabilities. Although they perform adequately over long length scales, MD simulations have shown that these models are incapable of capturing structural details on a monomeric length scale [76]. A more accurate

approach is to use the intramolecular correlation functions obtained from MD simulations of polymer melts and blends [77, 78]. Although this approach eliminates the computational efficiency of PRISM theory, it provides a way to eliminate the error in the intramolecular correlation function to test the accuracy of the remaining components of the theory.

The strength of PRISM theory is its ability to accurately capture the local structural detail of polymer melts, blends, and solutions. This is most readily demonstrated by comparing the structure factor obtained from PRISM theory and scattering experiments. The partial structure factors, defined as

$$\hat{S}_{\alpha\gamma}(k) = \hat{\Omega}_{\alpha\gamma}(k) + \hat{H}_{\alpha\gamma}(k), \tag{22}$$

compose the structure factor matrix. This can be directly compared to the scattering intensity of x-ray scattering experiments, $\hat{I}(k)$, via

$$\hat{I}(k) = \sum_{\alpha\gamma} b_\alpha b_\gamma \hat{S}_{\alpha\gamma}(k) \tag{23}$$

where b_α is the scattering cross section of species α.

3.2 Closures

3.2.1 *Atomic*

The closure approximation is the fundamental statistical mechanical approximation in PRISM theory. Determining the appropriate closure depends on the form of the potentials as well as the system parameters such as temperature and pressure [6]. The standard Percus-Yevick (PY) closure has been found to work well for repulsive force potentials in small molecule and macromolecular systems. The PY closure for atomic liquids can be derived using Percus' method [79, 80] of a perturbative expansion of the density functional or by Stell's [8] graph summation method. The pair and direct correlation functions in PY theory are given by

$$\begin{aligned} g(r) &= 0 & r < d \\ C(r) &= \left(1 - e^{\beta v(r)}\right) g(r) & r > d \end{aligned} \tag{24}$$

where $v(r)$ is the site-site interaction potential, $\beta = 1/k_B T$, and d is the hard core diameter. It should be mentioned that the analogous PY closure for RISM theory cannot be deduced from a diagrammatic expansion, but is based on the intuitive idea that $C(r)$ is short-ranged. A more complex, diagrammatically based RISM theory has been derived by Chandler et al. [81, 82].

A similar closure approximation is the mean spherical approximation (MSA). The MSA was proposed by Lebowitz and Percus [83] for systems with hard core plus tail potentials. The MSA is expressed as

$$\begin{aligned} g(r) &= 0 \qquad r < d \\ C(r) &= -\beta v(r) \; r > d \end{aligned} \tag{25}$$

which coincides with Eq. (24) when $v(r) = 0$. The MSA approximation has been heavily studied because it can be solved analytically for a number of pair potentials [6]. The critical exponents and temperature scaling of the effective χ parameter predicted by PRISM with the MSA closure disagree with Flory-Huggins theory, neutron scattering experiments [84], and Monte Carlo simulations [85, 86].

Using the diagrammatic approach, the atomic hypernetted chain (HNC) closure is obtained by neglecting all diagrams which are free of nodal circles (bridge diagrams) in the cluster expansion of the pair correlation function [6]. The closure based on HNC theory is shown in Eq. (26).

$$\begin{aligned} g(r) &= 0 \qquad\qquad\qquad r < d \\ C(r) &= -\beta v(r) + h(r) - \log\left[h(r) + 1\right] \; r > d \end{aligned} \tag{26}$$

A diagrammatic analysis shows that the PY closure results from the summation of fewer classes of diagrams than the HNC closure [8]. However, HNC exhibits a large increase in bulk density fluctuations that get worse at low density and high chain length. Ultimately, these errors result in quantitative failure on long length scales and prevent a solution from being obtained [87].

3.2.2 *Molecular*

Based on the thermodynamic quantities calculated from atomic closures with the full LJ potential, none of these closures agree with the classical Flory-Huggins scaling [1] of the critical temperature with N. Improvement can be made by incorporating attractive force potentials via thermodynamic perturbation theory. Here, the pair potential is divided into a short-range repulsion and a smoothly varying long-range attraction similar to liquid state theories of Coulombic systems [6]. For dense polymer systems, the structure is assumed to be predominantly controlled by short-ranged repulsive forces. Attractive forces, although important thermodynamically, only weakly influence the structure due to screening by the repulsive forces [34, 35, 88]. The reduced Helmholtz free energy of a blend can be approximated as

$$\frac{\beta F}{V} \approx \frac{\beta F_0}{V} + \frac{1}{2} \sum_{\alpha\gamma} \rho_\alpha \rho_\gamma \int \beta v_{\alpha\gamma}(r) g^0_{\alpha\gamma}(r) d\mathbf{r} \tag{27}$$

where F_0 is the free energy of the repulsive force reference system and the liquid structure is approximated by the structure of the reference system, $g_{\alpha\gamma}(r) \approx g^0_{\alpha\gamma}(r)$. Using Eq. (27), the phase behavior of polymer blends can be determined [89].

This same idea is used in the development of molecular closure approximations by Schweizer and Yethiraj [90]. The hard core reference system is treated with the PY closure. The closure for the attractive tail part of the potential is formulated to exactly describe the weak coupling limit. The simplest molecular closure that correctly treats the longer ranged potentials (i.e., gives Flory-Huggins scaling) is given by

$$\begin{aligned} g_{\alpha\gamma}(r) &= 0 && r \le d_{\alpha\gamma} \\ \omega_\alpha \star C_{\alpha\gamma} \star \omega_\gamma(r) &\cong \omega_\alpha \star C^{(0)}_{\alpha\gamma} \star \omega_\gamma(r) - \omega_\alpha \star \beta v_{\alpha\gamma} \star \omega_\gamma(r) && r > d_{\alpha\gamma} \end{aligned} \tag{28}$$

where the stars indicate convolution integrals and $C^{(0)}(r)$ is the direct correlation function for the hard core reference system. This closure is referred to as the "reference molecular mean spherical approximation" (R-MMSA) [90]. The convolution integration couples direct correlation functions between different pairs on two different molecules. It also couples the direct correlations inside the hard core to their behavior outside the hard core.

The R-MMSA closure avoids the massive fluctuation stabilization present in the HNC closure and to a lesser extent in the PY and MSA closures due to their failure to account for strong interactions between sites near in space but widely separated in chemical sequence [90]. It exhibits the proper $T_c \propto N$ scaling of the critical temperature. A more accurate formulation multiplies the closure for the tail part of the potential by the radial distribution function:

$$\omega_\alpha \star C_{\alpha\gamma} \star \omega_\gamma(r) \cong \omega_\alpha \star C^{(0)}_{\alpha\gamma} \star \omega_\gamma(r) - \omega_\alpha \star \Delta C_{\alpha\gamma} \star \omega_\gamma \quad r > d_{\alpha\gamma} \tag{29}$$

In Eq. (29), $\Delta C_{\alpha\gamma}(r) \cong \left\{1 - \exp\left[\beta v_{\alpha\gamma}(r)\right]\right\} g_{\alpha\gamma}(r)$ for $r > d_{\alpha\gamma}$. This is known as the reference molecular Percus-Yevick (R-MPY) closure [90]. This form allows the influence of density and concentration fluctuations to be determined self-consistently in the PRISM scheme.

3.3 Self-Consistent PRISM

The computational expense of a polymer simulation can be greatly reduced by extracting the intramolecular correlation functions from a simulation of a single chain, usually performed with fixed bond lengths. There are some disadvantages to using a single chain simulation in this manner. First, if all segments interact with Lennard-Jones potentials, then the repulsions between segments result in a radius of gyration typical of a chain in a good solvent instead of a melt. According to the Flory ideality hypothesis [1], interactions between segments separated by more than a few bonds are neglected due to screening and $\langle R^2 \rangle \propto N$ scaling is observed. Unfortunately,

using a strict Gaussian model allows sites to overlap, causing the polymer to occupy less volume than the true melt conformation. The density must then be corrected to compare with experimental data and the uncertainty in the density limits the predictive capabilities of this approach [91]. Also, this strict Gaussian model neglects conformational changes with composition, and hence cannot capture the intramolecular components of the mixing energy. A more accurate approach is to calculate the intramolecular correlation function in a solvation potential that corresponds to the specific polymer melt or blend being studied. This can be accomplished by using the self-consistent PRISM approach developed by Schweizer, Honnell and Curro [92]. In this approach, the effective single molecule potential surface contains a solvation free energy term that accounts for the intermolecular potentials. Assuming pairwise additivity, two forms of the solvation potential have been proposed. The Gaussian fluctuation potential [93, 94, 95] is a HNC-style potential given by

$$\beta\hat{\mathbf{W}}(k) = -\kappa_{HNC}\hat{\mathbf{C}}(k)\cdot\hat{\mathbf{S}}(k)\cdot\hat{\mathbf{C}}(k) \tag{30}$$

where $\hat{\mathbf{S}}(k)$ is the structure factor matrix with matrix elements defined in Eq. (22). This solvation potential is particularly useful for longer-range, slowly varying potentials such as Coulombic and Lennard-Jones potentials [18]. Melenkevitz, Schweizer and Curro showed that at high melt densities use of the HNC-style potential, Eq. (30), can cause the collapse of the polymer [96]. A simple solution to this problem is to add a prefactor κ_{HNC} that is varied to achieve the correct scaling for the mean square end-to-end distance at these high melt densities or to match the end-to-end distance obtained from MD simulations [97]. Empirically it is found that κ_{HNC} deviates only slightly from unity: $0.9 \leq \kappa_{HNC} \leq 1.1$ [97]. An alternative method is to recognize that an HNC solvation potential is too strong at high densities as it is for atomic liquids. Given that, others have suggested weaker solvation potentials based upon analogies with the Percus-Yevick [98, 143] closure,

$$\begin{aligned}&\beta W_{\alpha\gamma}(r) = \\ &-\ln\left[1+\textstyle\sum_{\lambda,\delta}\int d\mathbf{r}'\int d\mathbf{r}'' C_{\alpha\lambda}(|\mathbf{r}-\mathbf{r}'|)S_{\lambda\delta}(|\mathbf{r}'-\mathbf{r}''|)C_{\delta\gamma}(\mathbf{r}'')\right]\end{aligned} \tag{31}$$

or based upon the Martinov-Sarkisov [143] closure of atomic liquid theory. However, we generally find good agreement with the MD end-to-end distance using Eq. (30) with $\kappa_{HNC} = 1$, so all of the results presented in this review are for that form of the solvation potential.

The integrated strength of the HNC solvation potential is attractive and can be shown to have the form [18]

$$\hat{W}(0) = \frac{-\kappa_{HNC}}{\rho^2\kappa_T}. \tag{32}$$

Since the closure approximation generally predicts a compressibility κ_T that is too high, use of the HNC solvation potential generally gives good results because of compensatory effects.

Since the solvation potential requires knowledge of $C_{\alpha\gamma}(r)$ and $h_{\alpha\gamma}(r)$ obtained from PRISM theory and $\hat{\omega}_{\alpha\gamma}(k)$ is used as input to the PRISM equation, a self-consistent approach must be utilized. Initially, a guess is made for the matrix elements of the solvation potential, $W_{\alpha\gamma}(r)$, and single chain simulations are performed to obtain $\hat{\omega}_{\alpha\gamma}(k)$ for each $\alpha\gamma$ pair. The PRISM equation and closure are solved for $C_{\alpha\gamma}(r)$ and $h_{\alpha\gamma}(r)$ and a new estimate of the solvation potential is obtained. This sequence is repeated until $W_{\alpha\gamma}(r)$ converges onto a solution.

Obtaining sufficient accuracy to distinguish the subtle energy changes that occur upon blending polymers can require a large number of iterations with a single chain simulation performed at each iteration. In order to reduce computation time, a Monte Carlo reweighting scheme [60, 99] can be employed to reuse the conformations generated from previous simulations. In this approach, the new chain conformations, $\langle\omega\rangle$, are calculated from the old ones, $\omega^{(j)}$ using

$$\langle\omega\rangle\{W_{new}\} = \frac{1}{Z}\sum_{j=1}^{M}\omega^{(j)}\{W_{old}\}\,e^{\beta[W_{new}(j)-W_{old}(j)]} \tag{33}$$

where

$$Z = \sum_{j=1}^{M} e^{\beta[W_{new}(j)-W_{old}(j)]} \tag{34}$$

and W_{new} and W_{old} refer to the new and old solvation potentials, respectively. The applicability of the reweighting scheme is determined by applying the criterion

$$\min\{Z, 1/Z\} < \frac{M}{4} \tag{35}$$

where M is the number of configurations used in the sample averaging. If the difference between the new and old solvation potentials is large enough to fail the criterion, a new set of conformations is generated. Typically, one or two full simulations need to be performed for each chain before reaching the threshold for allowable error in the convergence of the self-consistent loop of the calculation.

4 Polymer Melts

Because of the closure approximation, together with the pairwise form of the solvation potential, we do not expect PRISM theory to yield quantitative results for the pair correlation functions and thermodynamic properties of polymer melts. However, depending on the degree of polymerization, PRISM theory is orders of magnitude faster than corresponding MD or Monte Carlo simulations and typically can be used for longer chain lengths. In the following sections, we compare the results

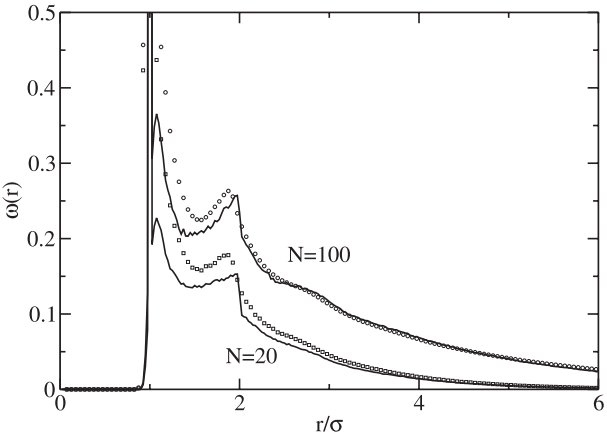

Fig. 2. Intramolecular radial distribution functions from SC/PRISM (*lines*) and MD simulations (*symbols*) for melts of freely jointed ($k_{bend} = 0$)polymers with 20 and 100 monomers per chain for density $\rho\sigma^3 = 0.85$ and $T = \epsilon/k_B$

of SC/PRISM theory using the Percus-Yevick atomic closure with MD simulations using the soft repulsive potential of Weeks, Chandler and Andersen [35, 88] defined in Eq. (3).

4.1 Bead-Spring Model Melts

The predictions of regular (not self-consistent) PRISM theory with the PY closure have been compared to molecular dynamics [76, 100] and Monte Carlo [101, 102, 87, 103] simulations of dense homopolymer melts using the bead-spring model. For these comparisons, either analytical functions or simulation results for the intramolecular correlation functions were used as input to PRISM theory. Good agreement was found on all length scales for hard core potentials. For the bead-spring model, neglecting end effects, there is only a single independent site. Hence the generalized Ornstein-Zernike equation (Eq. (19)) and the solvation potential in Eq. (30) reduce to scalar equations.

The intramolecular radial distribution functions from SC/PRISM for melts of N=20 and N=100 freely jointed ($k_{bend} = 0$) chains (FJC) are shown in Fig. 2. Unlike analytical expressions for the intramolecular structure, the self-consistent approach captures all of the details of the intrachain structure and can be used for molecules of arbitrary complexity. The remaining differences are due to the approximate form of the solvation potential used in the self-consistent calculation.

Figure 3 shows the intermolecular radial distribution functions obtained from SC/PRISM theory and MD simulations for freely jointed, bead-spring chain liquids in which the bond distance is comparable to the site diameter. As the chain length is increased, there is less structure for the first solvation shell due to increased screening

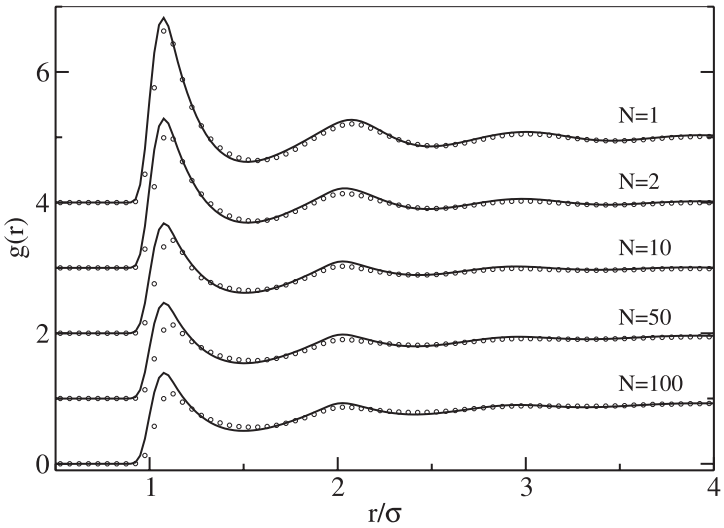

Fig. 3. Intermolecular radial distribution functions from theory (*lines*) and MD simulations (*symbols*) for melts of freely jointed polymers of varying chain length. The lines correspond to PY theory ($N = 1$), RISM theory ($N = 2$), and SC/PRISM theory ($N > 2$)

of intermolecular sites by the greater number of intramolecular sites. This effect saturates quite rapidly as seen by the similarity of results for the N=50 and N=100 melts. The error between SC/PRISM and MD in this region is $\sim 20\%$, but becomes much smaller at larger r for each chain length. Similar conclusions have been reached after comparing Monte Carlo simulations to PRISM theory [104, 102] with the Yukawa closure [105, 106] and to SC/PRISM theory [87] using several different closures.

The intermolecular radial distribution function of polymers in the condensed phase consists of short – range and long – range parts. On monomeric length scales we see that the local packing is similar to packing in atomic liquids as can be seen in the $g(r)$'s in Fig. 3. This short range structure is superimposed on a long range "correlation hole" [3] which approaches one on the length scale of the radius of gyration. The approximate form of g(r) on long length scales was obtained analytically by Schweizer and Curro [18] by solving the PRISM equations for the "thread model",

$$g(r) = 1 + \frac{3}{\pi\rho\sigma^2 r}\left[\exp\left(-r/\xi\right) - \exp\left(-\sqrt{2}r/R_g\right)\right] \tag{36}$$

where the polymer screening length is $\frac{1}{\xi} = \frac{\pi\rho\sigma^3}{3} + \frac{\sqrt{2}}{R_g}$. Since $R_g \sim \sqrt{N}$ in the melt, we expect the correlation hole to become progressively longer range as the chain length increases.

The radial distribution functions from SC/PRISM calculations and MD simulations are shown in Fig. 4 for the semiflexible chain model with N=50 repeat units per chain for different bending potentials, Eq. (5). The fully flexible chain shows

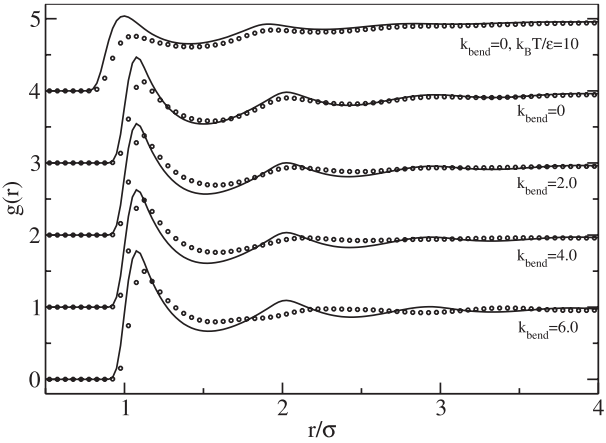

Fig. 4. Intermolecular radial distribution functions from SC/PRISM (*lines*) and MD simulations (*symbols*) for melts of semiflexible polymers of varying bending stiffnesses for N=50 beads. All results are for $k_BT/\epsilon = 1$ except the top curve where $k_BT/\epsilon = 10$. Density $\rho\sigma^3 = 0.85$ for all cases [108]

reasonable agreement between SC/PRISM and MD whereas stiffer chains result in progressively worse agreement for the separation distance between solvation shells. In particular, the shift of the second peak is less pronounced using SC/PRISM theory, which is also true for PRISM theory [107]. This may be due to a tendency for local ordering that increases with chain stiffness. This is not captured by PRISM theory, which assumes that the structure is isotropic.

In Fig. 4 we also compare the radial distribution functions for two values of k_BT/ϵ: $k_BT/\epsilon = 1.0$ often employed in bead-spring MD studies [76, 49], and $k_BT/\epsilon = 10.0$ that is more typical of polyolefin melts, as seen in Table 1 [109]. At $k_BT/\epsilon = 10.0$, SC/PRISM predicts that intermolecular sites have a tendency to be closer together than found in the MD simulation. This result shows that, as expected, SC/PRISM theory for bead-spring melts works better when the repulsive barrier is strong and the potential is closest to a hard core. In previous studies [59] PRISM theory was solved using the "exact" $\hat{\Omega}(k)$ obtained from MD simulation rather than from a self-consistent solution as in Fig. 4. This leads to an intermolecular g(r) in better agreement with MD than seen in Fig. 4. This demonstrates the approximate form of the solvation potential used.

4.2 United Atom Model Melts

One of the powerful features of PRISM theory is that it can be applied to more realistic polymer models than just the bead-spring model. In fact, to the authors' knowledge this is the only theory that has been applied in this manner. Let us first consider the simple case of the united atom model of polyethylene. Like the bead-spring

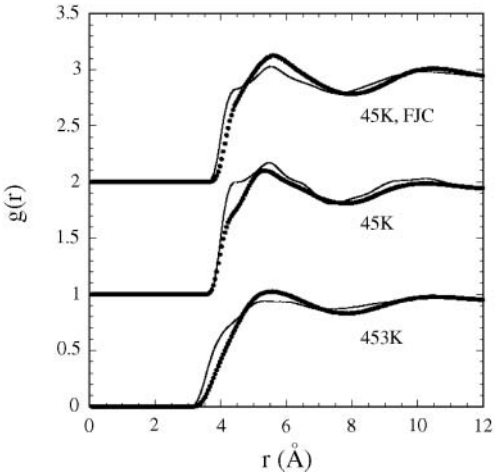

Fig. 5. The intermolecular radial distribution functions obtained from SC/PRISM theory (*lines*) and MD simulations (*points*) for a system of 3200 united atom polyethylene chains with 48 CH_x sites per chain at a density 0.03282 $Å^{-3}$ at the temperatures indicated. All results are for a repulsive Lennard-Jones nonbond potential with the TraPPE parameters in Table 1. The curves were displaced vertically for clarity

model there is only one independent site (a CH_2 unit) and the PRISM equations are scalar in the long chain limit. In Fig. 5 we display the theoretical and simulated intermolecular radial distribution functions of polyethylene melts (N=48) at the same values of k_BT/ϵ as in Fig. 4. Both the SC/PRISM and MD results are for purely repulsive non-bonded interactions. The general agreement is reasonable, except that PRISM theory predicts more structure in g(r) than is seen from MD, particularly at low k_BT/ϵ.

At 453K it can be seen in Fig. 5 that $g(r)$ from the MD simulations [59] is smoothly varying near contact in the 3.4—5.4 Å range. By contrast, the SC/PRISM theory shows a hint of a shoulder in $g(r)$ at ∼3.9 Å corresponding to a slight preference for nearest neighbor sites in contact. The main peak near ∼5.5 Å in both the theory and simulation is due to preferred packing of a pair of sites on different macromolecules with an intervening covalently bonded site. At low temperature, the "contact shoulder" becomes more pronounced in the PRISM generated $g(r)$. Interestingly, the MD results at 45K also seem to show the contact shoulder, but not to the extent as predicted from the theory. It appears that the shape of the theoretical and MD radial distribution functions are somewhat different at both high and low temperatures.

To isolate the source of this discrepancy we also performed theoretical calculations and MD simulations for a hypothetical FJC polyethylene model for which both the bond angle and torsional constraints are turned off. Therefore, the only difference between this FJC polyethylene model and the bead-spring model is the overlapping site aspect. It should be pointed out that this is a somewhat artificial model since

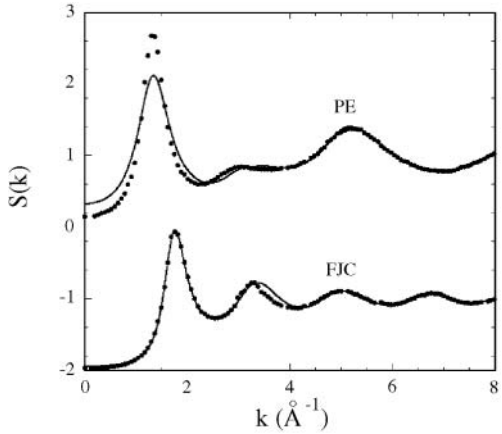

Fig. 6. Structure factor generated from PRISM (*curves*) and MD simulations (*points*) [59] for a freely-jointed chain, bead spring model and for polyethylene (N = 24, $\rho = 0.03104$ Å^{-3}, T = 405K). $\sigma = 3.93$ Å, $\epsilon = 0.092$ kcal mol^{-1}. Results for PE were determined from SC/PRISM while those for FJC were determined using the $\hat{\Omega}(k)$ from MD as input to PRISM. The results are displaced vertically for clarity

Lennard-Jones interactions are only applied between sites separated by more than three bonds. Hence, some unphysical intramolecular overlap is allowed in both the theory and simulation. Nevertheless, this model allows us to isolate the effect of bond angle and torsional constraints from the effect of the bond length being much less than the effective site diameter. It can be seen from Fig. 5 that the agreement between theory and simulation is somewhat better, but the contact shoulder is still more pronounced in the theory.

The fact that the agreement is somewhat better in this FJC polyethylene model indicates that internal constraints cause some difficulty in SC/PRISM theory. As seen in the semiflexible chain model, the bending and torsion constraints probably cause some local nematic ordering in the melt which cannot be captured in the present theory [59].

In Fig. 6 we plot the dimensionless structure factors $S(k)$ $(= \hat{S}(k)/\rho)$ for the FJC bead-spring model and for polyethylene from both theory and MD simulation. As expected from Figs. 3 and 4, reasonable agreement is seen between theory and simulation for the bead-spring model. For the case of polyethylene, PRISM predicts the zero wave vector structure factor to be too high relative to MD. This finding is consistent with the general trend of both PRISM theory of polymers, and RISM theory of small molecules, to overpredict the magnitude of the isothermal compressibility κ_T $(S(0) = \rho k_B T \kappa_T)$.

The basic approximation in the Percus-Yevick closure is that the direct correlation function is short range. In Fig. 7 we can observe that indeed $C(r)$ for both the bead-spring model and polyethylene are short range approaching zero on a scale of ~5 Å. However, $C(r)$ from self-consistent PRISM theory is even shorter range and

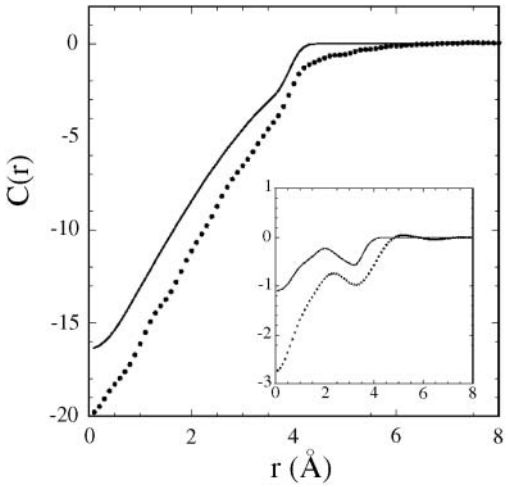

Fig. 7. The PRISM (*curves*) and MD (*points*) generated direct correlation functions [59] C(r) for a bead-spring model liquid with repulsive Lennard-Jones interactions. $\sigma = 3.93$ Å, $\epsilon = 0.092$ kcal mol^{-1}. The PRISM results were determined using the $\hat{\Omega}(k)$ from MD as input to PRISM. The inset shows the corresponding results for polyethylene (N = 24 sites, $\rho = 0.03104$ Å^{-3}, T = 405K)

tends to zero on a scale of σ (~4 Å). It is also evident from the areas under the curves in Fig. 7 that the theoretical compressibility is higher than the simulation values since

$$S(0) = \frac{N}{1 - \rho N \hat{C}(0)} \cong \frac{-1}{4\pi\rho \int_0^\infty r^2 C(r) dr} \tag{37}$$

It is possible to empirically modify PRISM theory for polyethylene [59] by making the direct correlation longer range by simply adding a power law tail to $C(r)$ beyond some hard core diameter. The power law exponent can then be adjusted to force the theory to yield the correct compressibility. This procedure led [59] to almost quantitative agreement of the theoretical $g(r)$ with MD for polyethylene. Unfortunately, this modification to PRISM theory is not useful for atomistic polymer models involving more than a single site since constraints, in addition to the compressibility, are needed to fix the exponents of the various direct correlation functions.

In Eqs. (19), (24), and (30), self-consistent PRISM theory is formulated in a general manner to allow for the modeling of polymer mixtures and polymer models containing an arbitrary number of interaction sites. A range of polymers of various complexities have been analyzed using PRISM theory. Pütz et al. [60] studied isotactic and syndiotactic polypropylene, head-to-head syndiotactic polypropylene, poly(ethylene propylene), and polyisobutylene using PRISM theory and MD simulations. In Figs. 8a, 8b we plotted the six independent pair correlation functions between intermolecular sites for isotactic polypropylene (iPP).

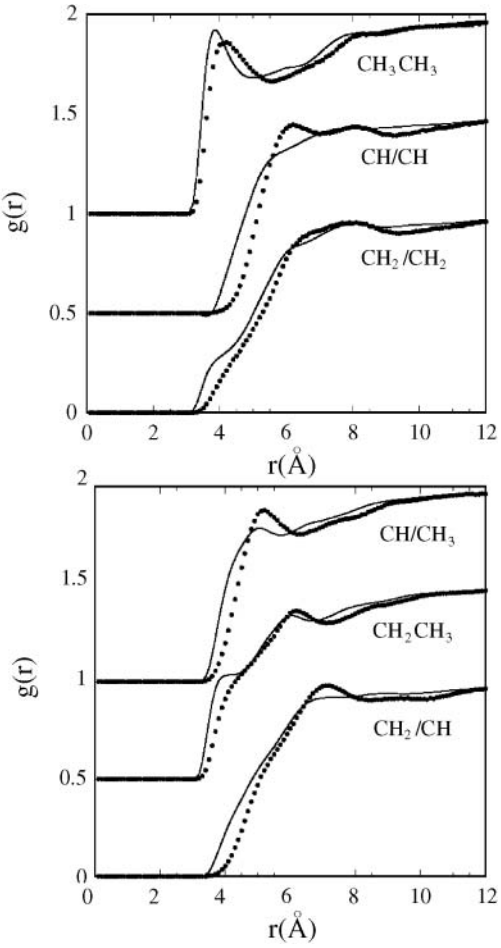

Fig. 8. The six intermolecular site-site radial distribution functions [60] for iPP (N = 48 CH_x sites, $\rho = 0.03282$ Å^{-3}, T = 453K). g(r) between sites of the same type (a) and between sites of different type (b). SC/PRISM theory used repulsive Lennard-Jones nonbond potentials, and the MD used the full Lennard-Jones potential with a 12 Å cutoff. The *curves* were displaced vertically for clarity

It is interesting to examine the individual $g_{\alpha\gamma}(r)'s$ for this vinyl polymer in light of the molecular architecture of iPP. In Fig. 8a it can be seen that the $g(r)$ between CH_3 groups is high near their point of closest approach in the 4 Å region. This reflects the fact that methyl groups can easily come in contact in the melt since they are on the outside of the chain. By contrast, other pairs of sites, such as between CH groups, are shielded from each other at short distances. This shows up clearly in Fig. 8a where it can be seen that the $g(r)$ between CH groups is essentially zero near 4 Å. It can be seen that both theory and simulation are able to account, at least qualitatively,

Table 3. Cohesive energy densities (MPa)

Polymer	T(K)	E_{PRISM}	E_{MD}	E_{exp} (440K)
Polyethylene	448	161	187	312
i-Polypropylene	453	131	155	252

for these subtle shielding effects. The agreement between theory and simulation is good for the $g(r)$ between CH_3 groups. In fact, the shape of this correlation function is closer to the simulation than for polyethylene and does not contain the contact shoulder feature. Not surprisingly, the agreement between SC/PRISM theory and MD is not as good for the other pair correlations where the sites are highly shielded.

These intermolecular radial distribution functions can be employed to compute the cohesive energy density E using

$$E = 2\pi \int_0^\infty \sum_{\alpha\gamma} \rho_\alpha \rho_\gamma U_{\alpha\gamma}(r) g_{\alpha\gamma}(r) r^2 dr, \tag{38}$$

where $U_{\alpha\gamma}(r)$ is the full Lennard-Jones interaction potential between sites α and γ, or equivalently the solubility parameter, $\delta = \sqrt{-E}$. Typical results are shown for polyethylene and iPP in Table 3 from both theory and simulation. It can be seen that PRISM predicts a smaller cohesive energy than MD simulation. This is a consequence of the theoretical $g_{\alpha\gamma}(r)$'s that tend to predict more intermolecular overlapping of sites than from MD. Also shown in Table 3 are experimental estimates of the cohesive energy density based on the internal pressure defined as

$$\Pi = \left(\frac{\partial E}{\partial V}\right)_{N,T} \tag{39}$$

Although the PRISM estimate of E is lower than the MD values, and both are lower than the experimental estimates, the theoretical and simulated predictions for the relative values are in good agreement with experiment for all the polyolefins studied by Pütz et al. [60].

In Fig. 9 we compared theory and simulation directly with the x-ray scattering experiments of Londono et al. [110]. The data is plotted as H(k) defined on a monomer basis according to

$$H_{iPP}(k) = \frac{3\left[\sum_{\alpha\gamma} b_\alpha b_\gamma \hat{S}_{\alpha\gamma}(k)/\rho_\alpha - \sum_\alpha b_\alpha^2\right]}{\left[\sum_\alpha b_\alpha\right]^2} \tag{40}$$

where the summations are over the three types of sites CH_3, CH_2, and CH. It can be seen that the agreement between the x-ray experiments for iPP and MD simulations is very good. As expected, SC/PRISM predicts the compressibility to be high as

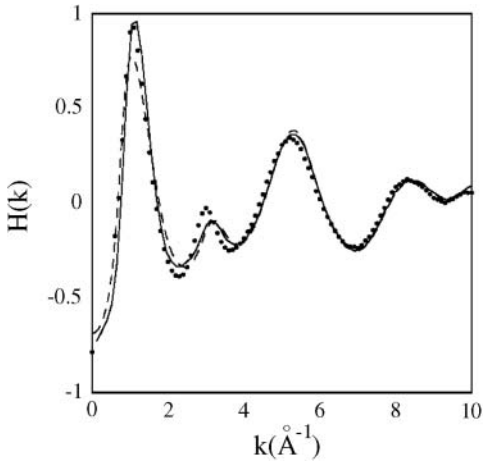

Fig. 9. X-ray scattering function H(k) [60] of iPP (N = 48 CH_X sites, $\rho = 0.03282$ Å^{-3}, T = 453K) computed from SC/PRISM theory (*dashed curve*) and MD simulations (*solid curve*). SC/PRISM theory used repulsive Lennard-Jones nonbond potentials, and the MD used the full Lennard-Jones potential with a 12 Å cutoff. The experimental data of Londono et al. [110] is shown as points

seen from the figure at zero wave vector. Note that both theory and simulation fail to quantitatively reproduce the second peak seen experimentally. This trend is generally observed in all the polyolefin systems we have studied and is probably a consequence of the neglect of the hydrogen atoms in our united atom model.

Very similar trends presented here for iPP were seen for the other polyolefin melts [60]. Sides et al. [63] studied the silicon containing polymer poly(dimethyl siloxane) (PDMS). Architecturally, PDMS has the same structure as polyisobutylene (PIB)with Si and O replacing C and CH_2 in the chain backbone. Because the bond lengths and angles are larger in PDMS than in PIB, the physical properties of these two polymers are dramatically different. For example, the diffusion constant for gases is lower for crosslinked PIB (butyl rubber) than for any other polyolefin based elastomer. By contrast, the gaseous diffusion is very high in PDMS. The six radial distribution functions of PDMS are presented in Fig. 10. Shielding effects qualitatively similar to iPP are seen in both the theory and simulation for the PDMS melt. Furthermore, the agreement between PRISM and MD is comparable to the iPP results shown in Figs. 8a and 8b and to PIB studied by Pütz et al. [60]. Comparison of Figs. 8 and 10 reveals that features in $g(r)$ for PDMS are shifted to larger r relative to iPP because of the differences in bond lengths and angles.

4.3 Explicit Atom Melts

The SC/PRISM theory as formulated in Eq. (19) is completely general and capable of treating explicit atom models where the hydrogen atoms are considered as

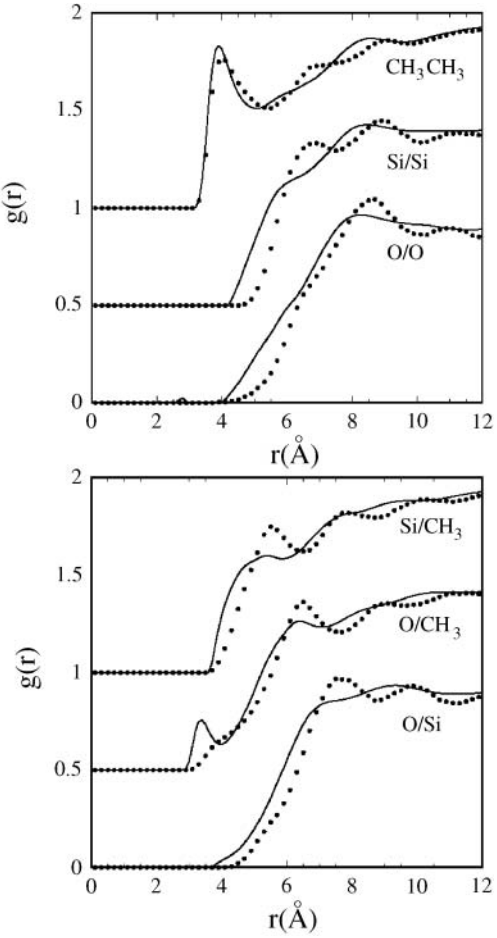

Fig. 10. The six intermolecular site-site radial distribution functions [63] for methyl terminated PDMS (20 Si per chain, $\rho = 0.98$ g cm^{-3}, T = 300K). g(r) between sites of the same type (a) and between sites of different type (b). SC/PRISM theory used repulsive Lennard-Jones nonbond potentials, and the MD used the full Lennard-Jones potential with a 12 Å cutoff. The *curves* were displaced vertically for clarity

separate sites. Of course the complexity of the calculation increases because it involves more integral equations. The only explicit atom calculation carried out thus far was by Tsige et al. [64] for polyethylene. The motivation for such a calculation was based on the fact that the pair correlation function between hydrogens can be directly measured by wide angle neutron scattering measurements on hydrogenated and deuterated alkanes [111].

The explicit atom potential of Eq. (14) was used for polyethylene in SC/PRISM calculations and MD simulations with the parameters in Table 2. A comparison between theory and simulation is given in Fig. 11 for each of the intermolecular pair

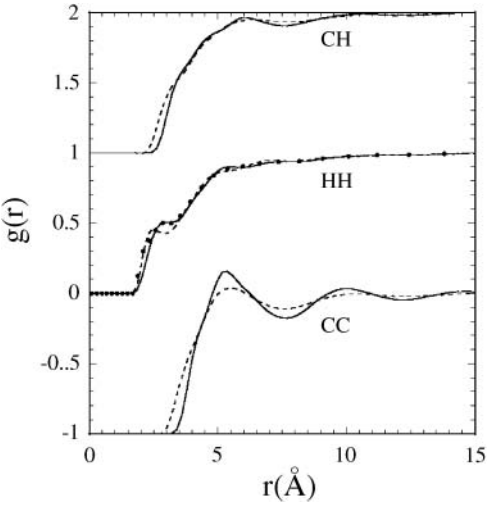

Fig. 11. The intermolecular radial distribution functions for $C_{20}H_{42}$ obtained from MD simulations (*solid curves*) and SC/PRISM theory (*dashed curves*) at T = 323K and ρ = 0.7888 g cm^{-3}. The experimental $g_{HH}(r)$ obtained from neutron scattering [111] is given by the points

correlation functions $g_{CC}(r)$, $g_{HH}(r)$, and $g_{CH}(r)$for the linear C_{20} alkane liquid at 323K. It can be seen that the agreement for $g_{CC}(r)$ is about the same as for the united atom model of polyethylene. Both theory and simulation show a shoulder near $\sim$ 2.9 Å due to preferred packing of the hydrogens in contact. Both theory and simulation predict the structure of $g_{HH}(r)$ to be very similar to the correlation function extracted from wide angle neutron scattering experiments of Londono et al. [111].

In principle, explicit atom potentials can be deduced from quantum calculations whereas one must rely on experiment to obtain united atom potentials. It would be useful if one could derive a united atom potential of a given site from the explicit atom potentials of the atoms making up that site. McCoy and Curro [112] suggested an approximate mapping of united and explicit atom potentials. In this scheme, the united atom potential is extracted from a Monte Carlo simulation of two chain fragments interacting with a full explicit atom potential. Tsige et al. [64] found almost exact agreement between $g_{CC}(r)$ obtained from MD simulations with the explicit atom potential and the united atom mapping of McCoy and Curro [112]. In order to match the pressure of the two models, Tsige et al. found it necessary to add an attractive tail to the united atom potential. Recently, a similar explicit to united atom mapping procedure has been suggested by Reith et al. [113].

5
Polymer Blends

Blends of two or more polymers provide an inexpensive means of combining the desirable properties of each type of polymer into one material. However, blending polymers presents new difficulties in processing due to the immiscibility of even very similar polymers. Compared to simple liquids, the entropy of mixing is small for chain molecules. Also, a slightly unfavorable energetic interaction between monomers can lead to a large energy of mixing per molecule for large N. Understanding how subtle effects control the miscibility of polymer blends is fundamental in the development of improved materials.

With the development of molecular closures, PRISM theory has shown the ability to predict a χ parameter with composition and degree of polymerization dependence that is consistent with simulation results [114]. Studies of symmetric block copolymer liquids show qualitative agreement with Monte Carlo simulation, but both the R-MMSA and R-MPY closures fail to predict a point of spinodal decomposition for finite degrees of polymerization [73, 74]. These results are for the somewhat unrealistic system of a symmetric blend model where each species has the same chain length and site diameter and the interactions between monomers of the same type are purely repulsive while the cross term has an attractive tail.

Studying the structure of polymer blends is much more difficult than the melt. The composition fluctuations present in polymer blends are more difficult for theories to handle than the density fluctuations that dominate in melts. This requires replacing the chain models with something more realistic to capture the subtle local composition deviations caused by combining chains of different types. The first attempt at this used intramolecular correlation functions, $\omega(r)$, from MD simulations of polymer blends in PRISM theory [77, 78]. Comparing these results to simulations, Fig. 12, shows that the radial distribution functions, including the local non-random mixing behavior, are in excellent agreement. However, the computational expense of MD simulations prohibit the use of this approach to study a wide range of polymer blends.

Over the past several years there has been significant effort in studying the subtle differences between a polymer chain in a homopolymer melt compared to a blend. Small changes in the structure of the polymer chain in the blend lead to major changes in the thermodynamic properties and phase behavior of the blend. Comparing PRISM results to MD simulations has proven to be a useful first approach towards quantifying the effects that assumptions in PRISM theory have on the local blend structure, and thus the bulk properties of polymer blends.

Continuing with the approach of including attractive interactions via perturbation theory, Tillman et al. [115, 116] compared the structure obtained from PRISM theory and MD simulation for blends of flexible chains of Lennard-Jones beads. They examined the radial distribution functions of blends of type A and type B chains with effective hard core diameters of $\sigma_A = 1.0$ and $\sigma_B = 1.2$. By incorporating progressively stronger attractive interaction strengths, they find only slight differences in the pair correlation functions. Although this has little effect on the compressibility factor

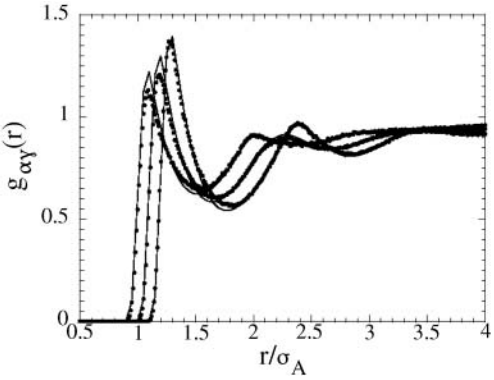

Fig. 12. Comparison between SC/PRISM theory (*lines*) and MD simulations (*symbols*) for the intermolecular radial distribution functions of an equimolar blend of N=50 semiflexible chains using a repulsive Lennard-Jones potential where $\sigma_A = 1.0$ and $\sigma_B = 1.2$ [78]

of the blend, the enthalpic χ parameter is much more sensitive to small changes in $g(r)$ and the blend is able to stabilize itself through slight changes in its structure.

5.1 Immiscibility of Isomeric Blends of Polypropylene

Self-consistent PRISM calculations and single-chain Monte Carlo simulations have been used to study blends of isotactic polypropylene (iPP) with syndiotactic polypropylene (sPP) [117]. These calculations use the repulsive form of the LJ potential in solving the PRISM equation with the PY closure. For $N = 36$ CH_x sites per chain, the packing in the blend is found to be very similar to the packing in the melt for each component. The pair correlation functions, Fig. 13, shows that backbone sites on sPP chains showed a slight preference for methyl groups on iPP chains while backbone sites on iPP chains showed a slight aversion for methyl groups on sPP chains. Correlations between backbone sites were screened by the presence of the methyl side groups. No significant favorable packing configurations were observed for either component in the blend, indicating that the mixture is miscible at this low molecular weight.

Since attractions are very important in determining the thermodynamic properties, the attractive part of the LJ potential, Eq. (2) is added to the repulsive form to calculate the cohesive energy densities. The heat of mixing of the blend is calculated from the PRISM results using Eq. (38) for the cohesive energy density. Applying Eq. (38) to both pure component melts and the blend gives the heat of mixing according to

$$\frac{\Delta H_{mix}}{N k_B T} = \frac{E(x)}{\rho(x)} - \left(\frac{x_{iPP} E_{iPP}}{\rho^0_{iPP}} + \frac{(1-x) E_{sPP}}{\rho^0_{sPP}} \right) \tag{41}$$

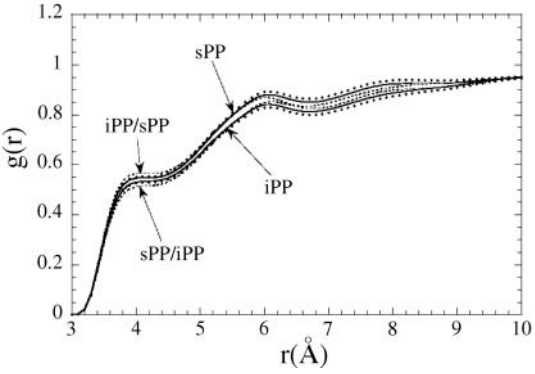

Fig. 13. Radial distribution functions between CH_3 and CH_2 sites for pure component liquids (*solid lines*) and the 50/50 blend (*points*). The two dotted curves represent the cross-correlations between chains of different tacticity in the blend [117]

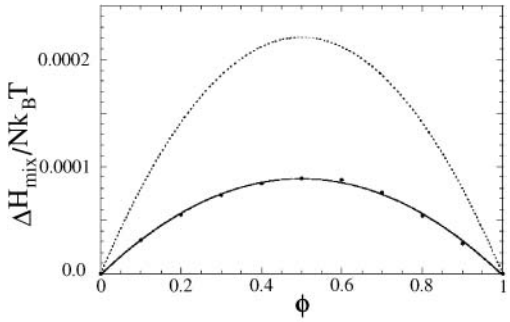

Fig. 14. Heat of mixing per monomer divided by $k_B T$ of the iPP/sPP blend for N = 36 CH_x sites per chain at T = 453K versus volume fraction of iPP monomers, ϕ [117]. The *points* are from SC/PRISM theory using Eq. (41). The *solid curve* is a guide to the eye. The dotted curve is an estimate based on the solubility parameters of the pure components

where x is the mole fraction of iPP in the blend, $\rho(x)$ is the number density of monomers in the blend of composition x, and ρ^0_{iPP} and ρ^0_{sPP} are the densities of pure component melts of iPP and sPP, respectively. The heat of mixing curve, shown in Fig. 14, is positive for the entire composition range. The Monte Carlo simulations also find a positive mixing energy, qualitatively consistent with experimental observations [118, 119, 120] that iPP and sPP are immiscible in the melt.

5.2 Isotactic Polypropylene and Polyethylene Blends

Self-consistent PRISM and MD simulations have also been used to study blends of isotactic polypropylene and polyethylene [121]. Here, we utilize the same approach of applying the repulsive LJ potential with the PY closure to the PRISM equation and applying the full LJ potential to the calculation of thermodynamic quantities.

For the iPP/PE blend, there are ten independent intermolecular radial distribution functions between the four types of interaction sites. Seven of these are also present in either the iPP or PE melt. Figure 15 shows the change in these seven radial distribution functions as the chains go from the melt to the blend. Both the PRISM results (Fig. 15a) and the MD results (Fig. 15b) show a decrease in g(r) for the iPP sites going from the melt to the blend in the region from 3 to 10 Å. The PE intermolecular radial distribution function actually increases in the 3 to 10 Å region. Figure 15a shows that these shifts are balanced by a increase for iPP and an decrease for PE in the region above 10 Å.

The changes in the intramolecular radial distribution functions are displayed in a similar manner in Fig. 16. Sharp peaks are evident for the three pairs that are covalently bonded with a bond distance of 1.54 Å, and these peaks were reduced in magnitude to declutter the figure. These three pairs also show doublet peaks between 3 and 5 Å, which correspond to the Gauche and anti torsional conformations. We see that $\omega(r)$ decreases for iPP and increases for PE in the 3 to 15 Å region, and the opposite is true in the region beyond 15 Å. This behavior for both $g(r)$ and $\omega(r)$ indicates that there is a favorable packing between iPP and PE molecules that allows them to adopt lower energy configurations in the blend than in the melt. We show below that this is the origin of the experimentally observed miscibility between iPP and PE.

Note that without scaling $\Delta g(r)$ and $\Delta\omega(r)$ by r^2, the magnitudes of the changes in the radial distribution functions in Figs. 15 and 16 are roughly 1% and 0.1% of the magnitude of the correlation functions themselves. This demonstrates the need for particularly high precision in the simulation results.

Instead of only considering the intermolecular van der Waals energy of each system, contributions from intramolecular van der Waals, torsional, bending, and bond energies are also included. The intermolecular van der Waals energy, E_{inter}, is calculated using Eq. (38). The intramolecular component is obtained using

$$E_{intra} = 2\pi \frac{\rho}{N} \int_0^\infty \sum_{\alpha\gamma} U_{\alpha\gamma}(r)\omega'_{\alpha\gamma}(r)r^2 dr \tag{42}$$

where $U_{\alpha\gamma}(r)$ is the full Lennard-Jones potential. In Eq. (42), $\omega'_{\alpha\gamma}(r)$ is the intramolecular correlation function excluding all pairs that are separated by less than three bonds since the energy contribution of pairs separated by less than three bonds is contained in the bond, bending, and torsional potential parameters. Combining these four contributions to get the total energy at a given composition, $E(x)$, the heat of mixing is calculated as in Eq. (41).

Table 4 lists the contributions to the heat of mixing for three different chain lengths for both SC/PRISM and MD. The two approaches show general agreement, particularly for the change in torsion and bending energies, but they still show some disparities beyond the uncertainty estimates. It is evident that a SC/PRISM heat of mixing calculation based only on the intermolecular contributions would result in a negative heat of mixing for the N = 48 and N = 96 blends, implying that these blends

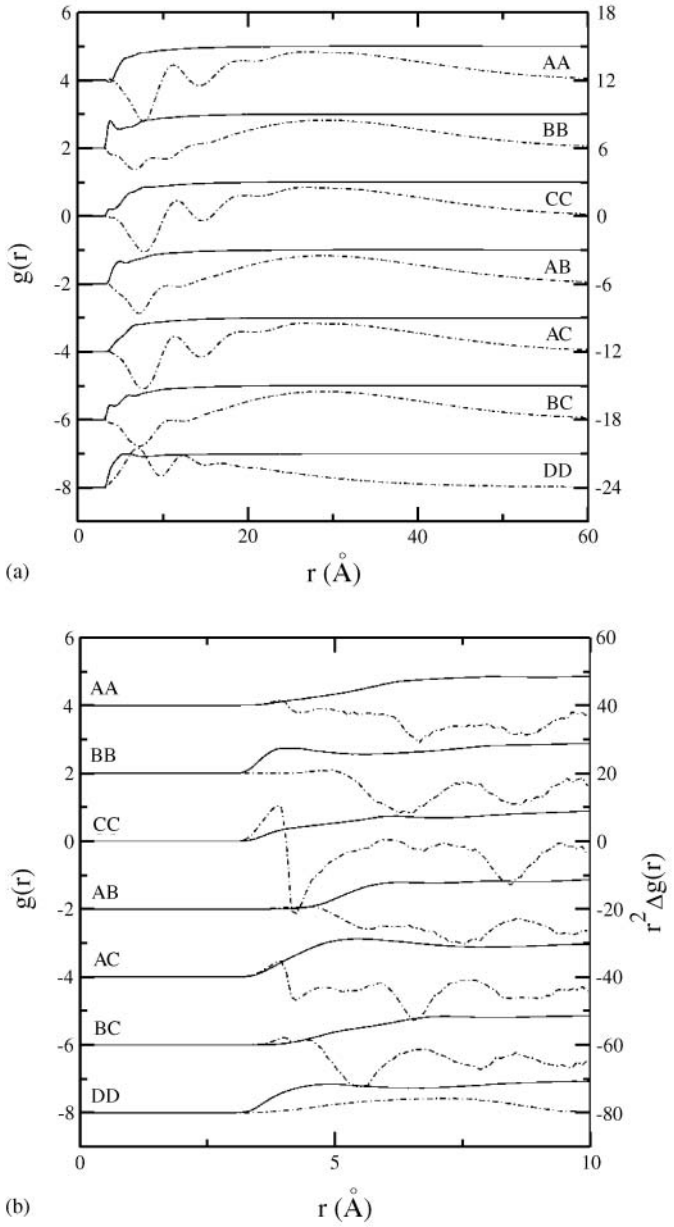

Fig. 15. Intermolecular radial distribution functions (*solid lines*) and difference between radial distribution functions (*dot dash*, rescaled) of the blend and the melt for iPP and PE obtained from (a) SC/PRISM and (b) MD simulations [121]. A, B, and C refer to the CH, CH_3, and CH_2 united atoms of iPP, respectively, and D refers to the CH_2 united atom of PE. The data sets are shifted for clarity. N = 96, $x_{iPP} = 0.5$, T = 453K, $\rho = 0.03282$ Å^{-3}

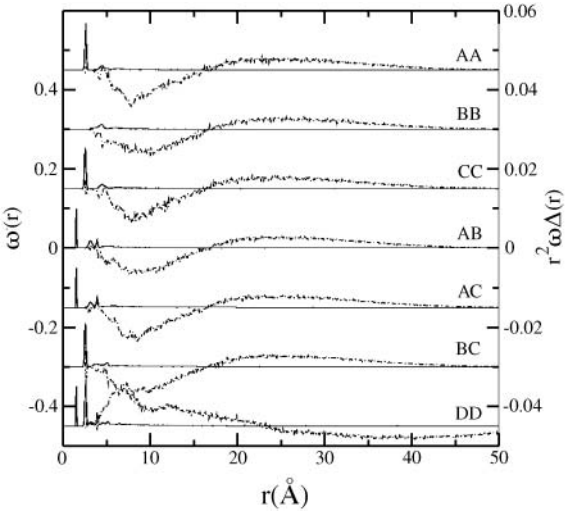

Fig. 16. Intramolecular radial distribution functions (*solid lines*) and difference between intramolecular radial distribution functions (*dot dash*, rescaled) of the blend and the melt for iPP and PE [121]. A, B, and C refer to the CH, CH_3, and CH_2 united atoms of iPP, respectively, and D refers to the CH_2 united atom of PE. The data sets are shifted for clarity. N = 96, $x_{iPP} = 0.5$, T = 453K, $\rho = 0.03282$ Å^{-3}

Table 4. Energy of mixing summary for iPP/PE blend at various N. T = 453K, $\rho = 0.03282$ sites/Å^3. Energy is expressed on a per site basis in units of $10^{-3} k_B T$

	N	x_s	Inter vdW	Intra vdW	Torsion	Bend	Bond	Total
PRISM	24	0.5	0.31	−1.04	1.79 ± 0.69	-0.12 ± 0.63	0	0.94
	48	0.5	−0.03	−0.62	0.61 ± 0.51	0.78 ± 0.46	0	0.73
	96	0.5	−1.13	0.81	0.76 ± 0.37	0.23 ± 0.33	0	0.67
MD	24	0.5	0.36 ± 0.14	0.11	0.57 ± 0.13	-0.02 ± 0.12	-0.25 ± 0.12	1.25 ± 0.23
	48	0.5	0.11 ± 0.10	0.25	0.30 ± 0.10	-0.07 ± 0.08	-0.04 ± 0.09	0.53 ± 0.17
	96	0.5	1.48 ± 0.15	−0.46	1.10 ± 0.15	0.02 ± 0.11	-0.01 ± 0.10	2.10 ± 0.22
	96	0.25	0.68 ± 0.15	0.06	0.57 ± 0.14	-0.03 ± 0.10	0.06 ± 0.10	1.30 ± 0.21
	96	0.75	0.90 ± 0.14	0.41	1.48 ± 0.13	0.14 ± 0.11	-0.07 ± 0.10	2.83 ± 0.21

are miscible. The internal energy components are sufficiently positive to give an overall positive heat of mixing, in agreement with experimental observations [122]. Although the change in intermolecular van der Waals energies based on MD results are all positive, the sum of the internal components are always greater than the intermolecular component.

The enthalpic χ parameter can be estimated from the heat of mixing using

$$\chi_{\Delta H} = \frac{\Delta H_{mix}}{x_{iPP}\,(1 - x_{iPP})\,N k_B T}. \tag{43}$$

The SC/PRISM and MD results are shown for several compositions in Fig. 17.

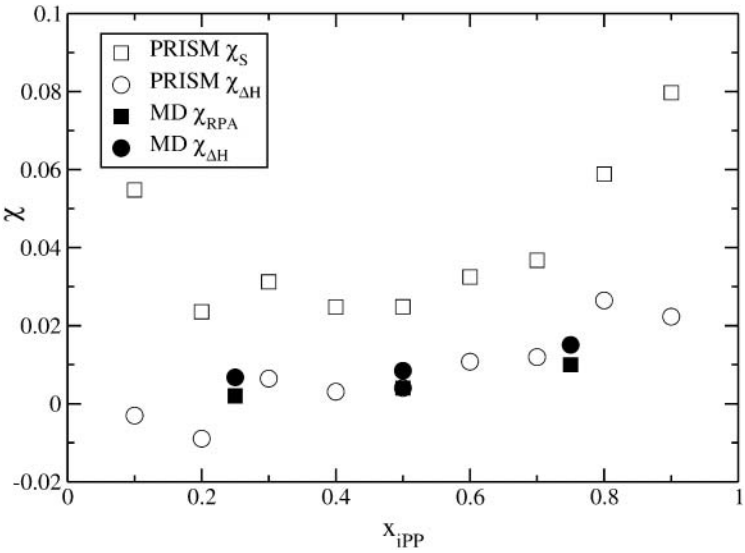

Fig. 17. Flory χ parameter as a function of composition based on SC/PRISM calculations (*open symbols*) and MD simulations (*closed symbols*) for the $N = 96$ iPP/PE blend at $T = 453$ K. The ΔH_{mix} values are obtained from the excess energy of the blend. The χ_S from SC/PRISM is the sum of the athermal χ_{ath}, Eq. (44), and $\chi_{\Delta H}$, Eq. (43), while χ_{RPA} is obtained by fitting the partial structure factor to the RPA formula

The athermal χ parameter can be calculated from the partial structure factors, defined in Eq. (22), from the equation

$$\chi_{ath} = \frac{1}{2}\left[\frac{1}{(1-x_{iPP})N_{PE}} + \frac{1}{x_{iPP}N_{iPP}}\right] - \frac{\rho k_B T}{2}\left[9\,(1-x_{iPP})^2\,\hat{S}_{CC}(0) - 6x_{iPP}\,(1-x_{iPP})\,\hat{S}_{CD}(0) + x_{iPP}^2\hat{S}_{DD}(0)\right]^{-1}, \tag{44}$$

where C and D correspond to iPP and PE CH_2 groups as in Fig. 16. Since the SC/PRISM calculations use only the repulsive part of the potential, this form neglects any enthalpic contributions to the χ parameter.

The χ parameter that one would measure from a scattering experiment is related to these two forms by [89]

$$\chi_S = \chi_{ath} - \frac{1}{2}\frac{\partial^2}{\partial x_{iPP}^2} x_{iPP}\,(1-x_{iPP})\,\chi_{\Delta H}, \tag{45}$$

which simplifies to $\chi_S = \chi_{ath} + \chi_{\Delta H}$ provided we neglect the composition dependence of $\chi_{\Delta H}$. The χ parameter is determined experimentally by fitting S(k) to the RPA scattering equation [3],

$$\hat{S}(k) = (b_{iPP}(k) - b_{PE}(k))^2 \left\{ \frac{1}{x_{iPP}\omega_{iPP}(k)} + \frac{1}{(1-x_{iPP})\omega_{PE}(k)} - 2\chi_{RPA} \right\}^{-1}. \quad (46)$$

Here, $b_i(k)$ is the scattering form factor for site i. χ_S can be calculated from the SC/PRISM estimates of χ_{ath} and $\chi_{\Delta H}$ and χ_{RPA} can be extracted from the RPA fit of the structure factor obtained from MD. These results are also shown in Fig. 17. The $\chi_{\Delta H}$ values obtained from the heat of mixing show remarkably good agreement between SC/PRISM and MD. However, the χ_S values obtained from SC/PRISM theory are consistently higher than the χ_{RPA} values. This is most likely due to the tendency [18, 59, 60] of SC/PRISM theory to predict compressibilities that are too high, resulting in higher values for $\hat{S}_{ij}(0)$ in Eq. (44).

MD simulations have also been performed for other polyolefin blends. Good agreement was found with small angle neutron scattering data of Krishnamoorti et al. [123, 124] on blends of poly(isobutylene) (PIB) with head-to-tail and head-to-head polypropylene (hhPP) [125]. In addition, MD simulations have been performed on all of the binary blends of PIB, iPP, sPP, hhPP, and PE [125].

6 Future Work

Studies of polyolefin blends have shown that SC/PRISM can handle the difficult problem of calculating the heat of mixing to within qualitative agreement with MD simulations and experimental observations. These studies have provided insight as to how specific polymer chains pack with their neighbors in the blend. They have also revealed that internal energy changes that occur as the chains rearrange themselves in the blend play a significant role in the thermodynamics of the blend. Other PRISM based theories have been developed to study highly branched polymers such as stars and combs [126, 127] as well as anisotropic systems such as liquid crystals and strained melts or rubbers [128, 129].

Currently, there is much interest in developing an effective means of coarse-graining the results of integral equation theories to study more complex systems such as polymer solutions in confined geometries or in the presence of colloids. Many attempts have been made to represent polymer coils [130, 131, 132, 133] or star polymers [134, 135] as soft, penetrable particles. Recently, the center-of-mass structure factor has been related to the monomer-monomer structure factor for dilute or semi-dilute polymer solutions using the PRISM formalism [136]. This allows an effective pair potential to be defined for interactions between polymers by inverting the center-of-mass pair distribution functions [137]. The resulting pair potentials generally depend on the polymer concentration, temperature, and degree of polymerization, but the structure agrees well with Monte Carlo simulation data at intermediate temperatures and under good solvent conditions. The agreement diminishes at very high temperatures and below the θ temperature (poor solvent conditions).

SC/PRISM theory has also been applied to solutions of polyelectrolytes modeled as rigid rods [138, 139]. Here, SC/PRISM accurately reproduces the long-range

structure, but is in qualitative error for the short-range structure. For flexible polyelectrolytes [140, 141], the results were largely dependent on the manner in which self-consistency was implemented. Poor results were obtained for the system of rigid rod polyelectrolytes with explicit counterions [142].

As discussed above, our implementation of SC/PRISM theory makes use of a single chain simulation and hence is nearly exact for a given solvation potential for the intramolecular part of the problem. An alternative to SC/PRISM theory, exact at zero density, is the "two-chain" equation for $g(r)$ [95, 143]. This equation was originally suggested by Laria, Wu, and Chandler (LWC) [95] and later derived by Donley, Curro, and McCoy (DCM) [143] using density functional techniques. For a single site model, they showed that g(r) can be written in the form

$$g(r) = \left\langle\!\left\langle \exp\left\{ -\sum\nolimits_{\alpha\gamma} \left[V(r_{\alpha\gamma}) + \Delta V(r_{\alpha\gamma}) \right] / k_B T \right\} \right\rangle\!\right\rangle \tag{47}$$

where the double bracket corresponds to a two chain average of a Boltzmann factor, holding a pair of sites on each of the two chains fixed at a distance r. The exponential involves a "bare" pair interaction (e.g., Lennard-Jones) $V(r)$ plus a pairwise-additive medium-induced correction term, $\Delta V(r)$, that mimics the effect of the other chains in the system. The pairwise additivity of the medium-induced potential is the only approximation needed to yield Eq. (47). This potential $\Delta V(r)$ can have many forms, but the most accurate at present is the HNC-style used by LWC and derived by DCM:

$$\Delta V(r) \cong -C \star S \star C(r) \tag{48}$$

where the stars denote convolution integrals. Thus Eqs. (47) and (48), together with the generalized Ornstein-Zernike equation, Eq. (19), provide a closed set of equations for computing $g(r)$ that is exact at the two chain level. Note that this theory for $g(r)$ is the direct analog of the one used in Sect. 3.3 to compute the intramolecular correlation function $\Omega(r)$. Solution of these equations requires a two chain simulation, but with reweighting techniques should still be orders of magnitude faster than simulation of the full many chain problem. The DCM theory was found to be very accurate for diatomic molecule liquids [143]. Yethiraj et al. [144] used the two-chain equation with a medium-induced potential obtained from weighted density functional theory to study tangent site chain liquids and likewise found good agreement with simulation. However, weighted density functional methods usually require knowledge of the liquid equation of state [145, 146], which is usually a goal of liquid theories, so such approaches are limited. LWC developed a mean-field approximation to the two-chain equation and applied it with success to the study of solvated electrons in water [95]. Yethiraj et al. applied this LWC theory to examine polyelectrolytes in solution and found that the theory works well in describing liquid structure as a function of density [138, 139]. However, recent work by Donley, Heine, and Wu showed that the theory performs poorly at large, experimentally relevant interaction energies and charge densities [147]. Donley, Rajasekaran and Liu recently also developed an

approximation to the two-chain equation [150, 148, 149]. This theory seems to perform properly at large interaction energies and charge densities for polyelectrolytes, but presently only for purely repulsive systems [147]. DRL have argued that this limitation stems from the use of the HNC-style medium-induced potential, Eq. (48), rather than any further approximation that they employed [150, 148, 149]. In spite of this limitation, it is of much interest to determine how well the two-chain theory will perform for soft repulsive or hard-core liquids. Current efforts are underway to apply the two-chain equation to polyethylene melts.

An alternative theory for describing systems that contain strong repulsive and attractive interactions is the recent range optimized random phase approximation (RO-RPA) of Donley, Heine, and Wu [147]. This theory is much closer in spirit to RISM and PRISM, yet, for the cases examined to date, seems to describe well the properties of polyelectrolyte solutions at high charge densities and interaction energies while also handling attractive interactions.

7 Conclusions

In this work we demonstrated that self-consistent PRISM theory is in reasonable agreement with simulations for bead-spring, united and explicit atom models. The intermolecular pair correlation functions from theory are qualitatively similar to the simulation, and the same trends are seen with changes in chain length, temperature and backbone stiffness. Generally the theory is most accurate in describing correlations between exposed sites along the chain but has difficulty in describing correlations between sites that are highly shielded. Furthermore, the theory works best at high density with strongly repulsive potentials. Accuracy in predicting the packing diminishes somewhat with increasing chain stiffness, presumably because chain stiffness tends to promote the tendency for local nematic ordering in the melt. Overall, self-consistent PRISM theory is comparable in accuracy for the structure of polymer liquids to the RISM theory of Chandler and Andersen [9, 11, 10] applied to small molecule liquids.

If the goal is to simply obtain accurate radial distribution functions or thermodynamics properties, then MD or Monte Carlo simulations can provide formally exact results, although statistical noise can cause difficulties in achieving high accuracy. Depending on the problem, large computer resources and multiple processors may be required, however, these are readily available today. Integral equation theory can provide approximate results with far less computer time. In fact, for some properties, theory may be the only feasible way to obtain results over a wide parameter space. One example is the calculation of the zero wave vector structure factor of polymer blends. To achieve low wave vector properties requires the simulation of very large systems. In the case of polyolefin blends, we have recently found [125] that to reach $k = 0.04$ Å^{-1}, which is on the high end of the experimentally relevant range of interest, requires a system of greater than 150,000 sites and a month of cpu time on 64 processors. Of course, theory can provide additional physical insights beyond those

attainable in simulation. This is frequently the case when analytical approximations can be made as in Eq. (36). In many problems in complex fluids, the most effective approach to achieving a full understanding may very well involve a combination of both theory and simulation integrated closely with experiment.

Acknowledgement

Sandia is a multiprogram laboratory operated by Sandia Corporation, a Lockheed Martin Company, for the United States Department of Energy's National Nuclear Security Administration under Contract No. DE-AC04-94AL85000. Research sponsored by the Division of Material Sciences and Engineering, Office of Basic Energy Sciences, U.S. Department of Energy, under contract No. DE-AC05-00OR22725 with Oak Ridge National Laboratory, managed and operated by UT-Battelle, LLC.

References

1. Flory PJ (1953) Principles of Polymer Chemistry. Cornell University, Ithaca 210, 221, 222
2. Doi M, Edwards SF (1986) The Theory of Polymer Dynamics. Oxford University Press, London 210, 219
3. deGennes PG (1979) Scaling Concepts in Polymer Physics. Cornell University Press, London 210, 218, 226, 242
4. Freed KF (1987) Renormalization Group Theory of Macromolecules. Wiley, New York 210
5. Hill TL (1956) Statistical Mechanics. McGraw Hill, New York 210
6. Hansen JP, McDonald IR (1976) Theory of Simple Liquids. Academic Press, London 210, 211, 217, 220, 221
7. Percus JK, Yevick GJ (1958) Phys Rev **110**:1 210, 218
8. Stell G (1963) Physica **29**:517 210, 220, 221
9. Chandler D, Andersen HC (1972) J Chem Phys **57**:1930 210, 218, 245
10. Chandler D (1982) Studies in Statistical Mechamics, vol. VIII. North-Holland, Amsterdam 210, 218, 245
11. Lowden LJ, Chandler D (1973) J Chem Phys **59**:6587 210, 218, 245
12. Lowden LJ, Chandler D (1974) J Chem Phys **61**:5228 210, 218
13. Lowden LJ, Chandler D (1975) J Chem Phys **62**:4246 210, 218
14. Curro JG, Schweizer KS (1987) Macromolecules **20**:1928 210, 217, 218, 219
15. Curro JG, Schweizer KS (1987) J Chem Phys **87**:1842 210, 218, 219
16. Schweizer KS, Curro JG (1987) Phys Rev Lett **58**:246 210, 218, 219
17. Schweizer KS, Curro JG (1994) Adv Poly Sci **116**:321 210, 218
18. Schweizer KS, Curro JG (1997) Advances in Chemical Physics, vol. XCVIII. Interscience, New York 210, 211, 218, 223, 226, 243
19. Freed KF, Dudowicz J (1992) Theor Chim Acta **82**:357 211
20. Dudowicz J, Freed KF (1993) Macromolecules **26**:213 211
21. Dudowicz J, Freed KF (1995) Macromolecules **28**:6625 211
22. Wertheim MS (1984) J Stat Phys **35**:1935 211
23. Wertheim MS (1986) J Stat Phys **42**:459477 211
24. Wertheim MS (1986) J Chem Phys **85**:2929 211

25. Wertheim MS (1987) J Chem Phys **87**:7323 211
26. Wertheim MS (1988) J Chem Phys **88**:1145 211
27. Eu BC, Gan HH (1993) J Chem Phys **99**:4084 211
28. Gan HH, Eu BC (1993) J Chem Phys **99**:4103 211
29. Gan HH, Eu BC (1994) J Chem Phys **100**:5922 211
30. Gan HH, Eu BC (1995) J Chem Phys **102**:2261 211
31. Gan HH, Eu BC (1995) J Chem Phys **103**:2140 211
32. Taylor MP, Lipson JEG (1995) J Chem Phys **102**:2118,6272 211
33. Attard P, (1995) J Chem Phys **102**:5411 211
34. Barker JA, Henderson D (1976) Rev Mod Phys **48**:587 211, 221
35. Andersen HC, Chandler D, Weeks JD (1976) Adv Chem Phys **34**:105 212, 221, 225
36. Weeks JD, Chandler D, Andersen HC (1971) J Chem Phys **54**:5237 212
37. Grest GS, Kremer K (1986) Phys Rev A **33**:3628 212
38. Carmesin I, Kremer K (1988) Macromolecules **21**:2819 212
39. Deutsch HP, Binder K (1991) J Chem Phys **94**:2294 212
40. Paul W, Binder K, Heermann DW, Kremer K (1991) J Phys II **1**:37 212
41. Jorgensen WL, Madura JD, Swenson CJ (1984) J Am Chem Soc **106**:813 212
42. Siepmann JI, Karaborni S, Smit B (1993) J Am Chem Soc **115**:6454 212
43. Siepmann JI, Karaborni S, Smit B (1993) Nature **365**:330 212
44. Han J, Gee RH, Boyd RH (1994) Macromolecules **27**:7781 212
45. Paul W, Yoon DY, Smith GD (1995) J Chem Phys **103**:1702 212
46. Sorensen RA, Liau WB, Kesner L, Boyd RH (1988) Macromolecules **21**:200 212, 216, 217
47. Kaminski G, Jorgensen WL (1996) J Phys Chem **100**:18010 212, 216
48. Chen B, Martin MG, Siepmann JI (1998) J Phys Chem B **102**:2578 212, 216
49. Kremer K, Grest GS (1990) J Chem Phys **92**:5057 213, 227
50. Everaers R, Kremer K (1995) Macromolecules **28**:7291 213
51. Grest GS (1996) J Chem Phys **105**:5532 213
52. Honnell KG, Curro JG, Schweizer KS (1990) Macromolecules **23**:3496 213
53. Faller R, Müller-Plathe F, Heuer A (2000) Macromolecules **33**:6602 213
54. Auhl R, Everaers R, Grest GS, Kremer K, Plimpton SJ (2003) J Chem Phys **119**:12718 213
55. Martin MG, Siepmann JI (1998) J Phys Chem B **102**:2569 213, 216
56. Martin MG, Siepmann JI (1999) J Phys Chem B **103**:4508 213, 215, 216
57. Sok RM, Berendsen HJC, van Gunsteren WF (1992) J Chem Phys **96**:4699 214
58. Frischknecht AL, Curro JG (2003) Macromolecules **36**:2122 214
59. Curro JG, Webb III EB, Grest GS, Weinhold JD, Pütz M, McCoy JD (1999) J Chem Phys **111**:9073 214, 215, 227, 228, 229, 230, 243
60. Pütz M, Curro JG, Grest GS (2001) J Chem Phys **114**:2847 215, 224, 230, 231, 232, 233, 243
61. Tuckerman M, Berne BJ, Martyna GJ (1990) J Chem Phys **92**:5057 215
62. Andersen H (1983) J Comput Phys **52**:24 215
63. Sides SW, Curro JG, Grest GS, Stevens MJ, Soddemann T, Habenschuss A, Londono JD (2002) Macromolecules **35**:6455 215, 233, 234
64. Tsige M, Curro JG, Grest GS, McCoy JD (2003) Macromolecules **36**:2158 215, 216, 234, 235
65. Smith GD, Yoon DY (1993) J Chem Phys **100**:649 216
66. Ornstein LS, Zernike F (1914) Proc Akad Sci (Amsterdam) **17**:793 217
67. Chandler D (1978) Faraday Disc Chem **66**:74 218

68. Sullivan DE, Gray CG (1981) Mol Phys **42**:443 218
69. Schweizer KS, Curro JG (1988) Macromolecules **21**:3070 218
70. Schweizer KS, Curro JG (1988) Macromolecules **21**:3082 218
71. Flory PJ (1949) J Chem Phys **17**:303 218
72. Donley JP, Rajasekaran JJ, McCoy JD, Curro JG (1995) J Chem Phys **103**:5061 219
73. David EF, Schweizer KS (1994) J Chem Phys **100**:7767 219, 236
74. David EF, Schweizer KS (1994) J Chem Phys **100**:7784 219, 236
75. Curro JG (1994) Macromolecules **27**:4665 219
76. Curro JG, Schweizer KS, Grest GS, Kremer KJ (1989) J Chem Phys **91**:1357 219, 225, 227
77. Stevenson CS, McCoy JD, Plimpton SJ, Curro JG (1995) J Chem Phys **103**:1200 220, 236
78. Stevenson CS, Curro JG, McCoy JD, Plimpton SJ (1995) J Chem Phys **103**:1208 220, 236, 237
79. Percus JK (1962) Phys Rev Lett **8**:462 220
80. Percus JK (1964) The Equilibrium Theory of Classical Fluids. Benjamin, New York 220
81. Chandler D, Silbey R, Ladanyi BM (1982) Mol Phys **46**:1335 220
82. Richardson DM, Chandler D (1984) J Chem Phys **80**:4484 220
83. Lebowitz JL, Percus JK (1966) Phys Rev **144**:251 221
84. Gehlsen MD, Rosedale JH, Bates FS, Wignall GD, Hansen L, Almdal K (1992) Phys Rev Lett **68**:2452 221
85. Deutsch HP, Binder K (1992) Europhys Lett **17**:697 221
86. Deutsch HP, Binder K (1992) Macromolecules **25**:6214 221
87. Yethiraj A, Schweizer KS (1992) J Chem Phys **97**:1455 221, 225, 226
88. Chandler D, Weeks JD, Andersen HC (1983) Science **220**:787 221, 225
89. Rajasekaran JJ, Curro JG, Honeycutt JD (1995) Macromolecules **28**:6843 222, 242
90. Schweizer KS, Yethiraj A (1993) J Chem Phys **98**:9053 222
91. Weinhold JD, Curro JG, Habenschuss A, Londono JD (1999) Macromolecules **32**:7276 223
92. Schweizer KS, Honnell KG, Curro JG (1992) J Chem Phys **96**:3211 223
93. Chandler D, Singh Y, Richardson DM (1984) J Chem Phys **81**:1975 223
94. Nichols AL, Chandler D, Singh Y, Richardson DM (1984) J Chem Phys **81**:5109 223
95. Laria D, Wu D, Chandler D (1991) J Chem Phys **95**:4444 223, 244
96. Melenkevitz J, Schweizer KS, Curro JG (1993) Macromolecules **26**:6190 223
97. Mendez S, Curro JG, Pütz M, Bedrov D, Smith GD (2001) J Chem Phys **115**:5669 223
98. Grayce CJ, Schweizer KS (1994) J Chem Phys **100**:6846 223
99. Swendsen RH, Ferrenberg RH (1988) Phys Rev Lett **61**:2635 224
100. Elliot JR, Kanetar US (1990) Mol Phys **71**:871 225
101. Yethiraj A, Hall CK, Honnell KG (1990) J Chem Phys **93**:4453 225
102. Yethiraj A, Hall CK (1992) J Chem Phys **96**:797 225, 226
103. Dodd LR, Theodorou DN (1994) Adv Poly Sci **116**:289 225
104. Yethiraj A, Hall CK (1990) J Chem Phys **93**:5315 226
105. Cummings PT, Morriss GP, Wright CC (1981) Mol Phys **43**:1299 226
106. Cummings PT, Morriss GP, Stell G (1984) Mol Phys **51**:289 226
107. Yethiraj A (1994) J Chem Phys **101**:9104 227
108. Heine DR, Curro JG, Grest GS (in prep) 227
109. In the MD simulation, the average bond length did not change as ϵ was reduced. Only the non-bonded LJ interaction was reduced for $k_B T/\epsilon = 10.0$. 227
110. Londono JD, Habenschuss A, Curro JG, Rajasekaran JJ (1996) J Polym Sci B **34**:3055 232, 233

111. Londono JD, Annis BK, Turner JZ, Soper AK (1994) J Chem Phys **101**:7868 234, 235
112. McCoy JD, Curro JG (1998) Macromolecules **31**:9362 235
113. Reith D, Pütz M, Müller-Plathe F (2003) J Comp Chem **24**:1624 235
114. Yethiraj A, Schweizer KS (1993) J Chem Phys **98**:9080 236
115. Tillman PA, Rottach DR, McCoy JD, Plimpton SJ, Curro JG (1997) J Chem Phys **107**:4024 236
116. Tillman PA, Rottach DR, McCoy JD, Plimpton SJ, Curro JG (1998) J Chem Phys **109**:806 236
117. Clancy TC, Pütz M, Weinhold JD, Curro JG, Mattice WL (2000) Macromolecules **33**:9452 237, 238
118. Thomann R, Kressler J, Setz S, Wang C, Mülhaupt R (1996) Polymer **37**:2627 238
119. Thomann R, Kressler J, Rudolf B, Mülhaupt R (1996) Polymer **37**:2635 238
120. Maier RD, Thomann R, Kressler J, Mülhaupt R, Rudolf B (1997) J Polym Sci B **35**:1135 238
121. Heine DR, Wu DT, Curro JG, Grest GS (2003) J Chem Phys **118**:914 238, 240, 241
122. Wignall GD, Child HR, Samuels RJ (1982) Polymer **23**:957 241
123. Krishnamoorti R, Graessley WW, Fetters LJ, Garner RT, Lohse DJ (1995) Macromolecules **28**:1252 243
124. Krishnamoorti R, Graessley WW, Dee GT, Walsh DJ, Fetters LJ, Lohse DJ (1996) Macromolecules **29**:367 243
125. Jaramillo E, Wu DT, Grest GS, Curro JG (2004) J Chem Phys **120**:8883 243, 245
126. Grayce CJ, Schweizer KS (1995) Macromolecules **28**:7461 243
127. Patil R, Schweizer KS, Chang TM (2003) Macromolecules **36**:2544 243
128. Pickett GT, Schweizer KS (2000) J Chem Phys **112**:4869,4881 243
129. Oyerkun FT, Schweizer KS (2004) J Chem Phys **120**:475 243
130. Louis AA, Bolhuis PG, Hansen JP, Meijer EJ (2000) Phys Rev Lett **85**:2522 243
131. Bolhuis PG, Louis AA, Hansen JP, Meijer EJ (2001) J Chem Phys **114**:4296 243
132. Pagonabarraga I, Cates ME (2001) Europhys Lett **55**:348 243
133. Fuchs M, Schweizer KS (2002) J Phys Cond Matter **14**:239 243
134. Dzubiella J, Jusufi A, Likos CN, von Ferber C, Löwen H, Stellbrink J, Allgaier J, Richter D, Schofield AB, Smith PA (2001) Phys Rev E **64**:010401 243
135. Jusufi A, Dzubiella J, Likos CN, von Ferber C, Löwen H (2001) J Phys: Condens Matter **13**:6177 243
136. Krakoviack V, Hansen JP, Louis AA (2002) Europhys Lett **58**:53 243
137. Krakoviack V, Rotenberg B, Hansen JP (2004) J Phys Chem B **108**:6697 243
138. Yethiraj A, Shew C (1996) Phys Rev Lett **77**:3937 243, 244
139. Yethiraj A (1997) Phys Rev Lett **78**:3789 243, 244
140. Shew CY, Yethiraj A (1999) J Chem Phys **110**:5437 244
141. Shew CY, Yethiraj A (2000) J Chem Phys **113**:8841 244
142. Shew CY, Yethiraj A (1999) J Chem Phys **110**:11599 244
143. Donley JP, Curro JG, McCoy JD (1994) J Chem Phys **101**:3205 223, 244
144. Yethiraj A, Fynewever H, Shew CY (2001) J Chem Phys **114**:4323 244
145. Woodward CE (1991) J Chem Phys **94**:3183 244
146. Woodward CE (1992) J Chem Phys **97**:4525 244
147. Donley JP, Heine DR, Wu DT (2004) Macromolecules (in press) 244, 245
148. Donley JP (2002) J Chem Phys **116**:5315 245
149. Donley JP (2004) J Chem Phys **120**:1661 245
150. Donley JP, Rajasekaran JJ, Liu AJ (1993) J Chem Phys **109**:849 245

Index

Author Index Volumes 101 – 173

Author Index Volumes 1 – 100 see Volume 100

Subject Index